Advancing thermogalvanic cells using a combination of fundamental investigations and developing novel, sustainable redox couples

Buckingham, Mark

Awarding institution:
King's College London

Advancing thermogalvanic cells using a combination of fundamental investigations and developing novel, sustainable redox couples

Mark A. Buckingham, MChem (Hons)

King's College London

Department of Chemistry,

Faculty of Natural, Mathematical and Engineering Sciences

A Thesis Submitted Towards the Degree of Doctor of Philosophy in Chemistry

Submitted August 2021.

Acknowledgments

This thesis is the culmination of almost 4 years of research conducted at the Chemistry Department of King's College London. Four years of hard work, long hours and not a small amount of stress, particularly given the global COVID-19 disruption from March 2020 – August 2021 (and thereafter).

I initially want to dedicate this thesis (and moreover my two degrees as a whole) to my parents. Having lost my mother aged 5 and father during my masters' degree aged 21 neither have been around to witness me achieving these degrees. However, the memory of them has always been a driving force in everything I have done to date and will continue to do in the future.

Having to go through these hardships I was never alone, and as such I am eternally grateful to the rest of my family. In particular my Aunties Mo, and Jill and late auntie Ann and uncles Ed and Roy and numerous cousins that are too many to name. I would like to wholeheartedly thank them for everything they have done for me throughout my life.

I would also wholeheartedly like to thank Dr. Leigh Aldous for his guidance, supervision, and mentorship during my Ph.D. We have struck up a very productive working partnership during my time here. We do not agree on everything, from experiments to written story, but in discussing our different opinions in an open and constructive way I have always felt that we improved everything we discussed through this, and our joint work has significantly benefitted from the open working dialogue. I also feel that through this process, I have significantly benefitted and improved in numerous ways as a researcher.

As a new first year undergraduate student at the University of Bath, I would never have dreamt that I would be here at the end of a Ph.D. - after 8 years of university study - receiving a doctorate degree. I would like to thank two of my supervisors at the University of Bath, without whom I would certainly not have been here many years later. I would firstly like to thank my personal tutor and long-term supervisor and mentor Prof. Frank Marken. It was due to Frank that I initially got a taste of novel academic research doing a summer project, where I certainly caught the research bug, and have been hooked ever since! I would also like to thank Prof. Mike Hill. Mike was supervising me during the most difficult period of my life when my father was losing his battle with cancer and his supervision and chats in the office was immensely helpful during this period. I am sure neither of them know just how valuable their contribution is to my successes to date but here it is in writing for everyone to know and also to know how eternally grateful I am to the pair of them.

I would also like to thank my many collaborators during both my summer undergraduate and masters project (in particular all the members of Prof. Frank Marken's group). I have gained many more collaborators during my Ph.D. both at King's, with Dr's Anastasia Zaleska and Wayne Dickson from the Department of Physics, and abroad in Prof. Jun Chen's group, in particular Shuai Zhang, Dr. Yuqing Liu, and Yuetong Zhou at the University of Wollongong. A place where I had the absolute pleasure to spend a couple of months visiting during my Ph.D. I would also like to thank other collaborators Prof. Patrick Phelan at Arizona State University and again Prof. Frank Marken at the University of Bath, who I continue to collaborate with.

I have been very fortunate during my Ph.D. to have been able to work with some wonderful people within the group, both Dr. Hassan Alzahrani in my early years

in the group and Dr. Kristine Laws in my later years in the group. I have particularly enjoyed the time in the lab with both of these wonderful people.

I would also like to thank my colleagues at KCl, in particular Kristine, Georgia, Hassan, Ryan, Dan, Rosanna, Laszlo and Nick. Also, the many members of the office who have made coming to work a lot of fun over the last 4 years, including all the aforementioned, plus Ines, Ed, Callum.

I would also like to acknowledge my Ph.D. cohort, in particular Ryan and Steven. We made it 4 years of Ph.D. including over 18 months of pandemic-related restrictions, making it extra tough but also extra rewarding. Finally, I want to thank the KCl football crew, it was a blast playing 4 – 7 a side with you guys and thank you for all the good times on the pitch!

Finally, I would like to thank Dr. Eamonn Reading for being the virtual viva facilitator and Prof's Douglas MacFarlane and Katherine Holt for the thoroughly enjoyable discussion in the viva itself.

Publications from this Ph.D.

1. The thermoelectrochemistry of the aqueous iron(ii) | iron(iii) redox couple: significance of the anion and pH in thermogalvanic thermal-to-electrical energy conversion.

   Mark A. Buckingham, Frank Marken & Leigh Aldous, *Sustainable Energy and Fuels*, 2018, 2, 2717. (a 2018 *Sustainable Energy and Fuels* HOT article)

2. Success and failure in the incorporation of gold nanoparticles inside ferri/ferro-cyanide thermogalvanic cells.

   Hassan A. H. Alzahrani, **Mark A. Buckingham**, Frank Marken & Leigh Aldous, *Electrochemistry Communications*, 2019, 102, 41.

3. Gold nanoparticles immobilised in a superabsorbent hydrogel matrix: Facile synthesis and application for the catalytic reduction of toxic compounds.

   Hassan A. H. Alzahrani,[†] **Mark A. Buckingham**,[†] William P. Wardley, Richard D. Tilley, Nicholas Ariotti & Leigh Aldous, *Chemical Communications*, 2020, 56, 1263.

4. A fundamental study of the thermoelectrochemistry of ferricyanide/ ferrocyanide: Cation, concentration, ratio and heterogeneous and homogeneous electrocatalytic effects in thermogalvanic cells.

   Mark A. Buckingham,[†] Samer Hammoud,[†] Huanxin Li, Conor J. Beale, Jason T. Sengel & Leigh Aldous, *Sustainable Energy and Fuels*, 2020, 4, 3388. (a 2020 *Sustainable Energy and Fuels* HOT article)

5. Thermogalvanic cells: A side-by-side comparison of measurement methods.

Mark A. Buckingham & Leigh Aldous, *Journal of Electroanalytical Chemistry*, 2020, 872, 114280.

6. Using iron sulphate to form both n-type and p-type *pseudo*-thermoelectrics: non-hazardous and 'second-life' thermogalvanic cells.

Mark A. Buckingham, Kristine Laws, Jason T. Sengel and Leigh Aldous, *Green Chemistry*, 2020, 22, 6062. (a 2020 *Green Chemistry* HOT article)

7. Advanced wearable thermocells for body heat harvesting.

Yuqing Liu, Shuai Zhang, Yuetong Zhou, **Mark A. Buckingham**, Leigh Aldous, Peter C. Sherrel, Gordon G. Wallace, Gregory Ryder, Shaikh Faisal, David L. Officer, Stephen Beirne and Jun Chen, *Advanced Energy Materials*, 2020, 10, 2002539.

8. The significance of supporting electrolyte on poly(vinyl alcohol)-iron (ii)/iron(iii) solid-state electrolytes for wearable thermo-electrochemical cells.

Yuetong Zhou, Yuqing Liu, **Mark A. Buckingham**, Shuai Zhang, Leigh Aldous, Stephen Beirne, Gordon G. Wallace and Jun Chen, *Electrochemistry Communications*, 2021, 124, 106938.

9. Thermogalvanic cells demonstrate inherent physiochemical limitations in redox-active electrolytes at water-in-salt concentrations.

Mark A. Buckingham, Kristine Laws, Huanxin Li and Leigh Aldous, *Cell Reports Physical Sciences*, 2020, 2, 100510.

10. Thermogalvanic and thermocapacitive behaviour of superabsorbent hydrogels for combined low-temperature thermal energy conversion and harvesting.

Mark A. Buckingham, Shuai Zhang, Yuqing Liu, Jun Chen, Frank Marken and Leigh Aldous, *ACS Applied Energy Materials*, 2021, 4, 10, 11204. (Supplementary journal cover associated with this publication)

11. Developing iron-based anionic redox couples for thermogalvanic cells: towards the replacement of the ferricyanide/ferrocyanide redox couple.

Mark A. Buckingham, Kristine Laws, Edwards Cross, Andrew J. Surman and Leigh Aldous, *Green Chemistry*, 2021, 23, 8901. (a 2021 *Green Chemistry* HOT article)

12. Nanostructuring electrode surfaces and hydrogels for enhanced thermocapacitance.

Mark A. Buckingham, Florence Stoffel, Shuai Zhang, Yuqing Liu, Frank Marken, Jun Chen and Leigh Aldous, *ACS Applied Nano Materials*, advanced article, 2022, DOI:10.1021/acsanm.1c03273.

Other publications from Mark A. Buckingham

1. Ion flow in a zeolitic imidazolate framework results in ionic diode phenomena. Elena Madrid, **Mark A. Buckingham**, James M. Stone, Adrian T. Rogers, William J. Gee, Andrew D. Burrows, Paul R. Raithby, Veronica Celorrio, David J. Fermin and Frank Marken, *Chemical Communications,* 2016, 52, 2792.

2. Aerosol-Assisted Chemical Vapor Deposition of CdS from Xanthate Single Source Precursors.
   Mark A. Buckingham, Amanda L. Catherall, Michael S. Hill, Andrew L. Johnson and James D. Parish, *Crystal Growth and Design,* 2017, 17, 907.

3. Electrochemically Driven C-H Hydrogen Abstraction Processes with the Tetrachloro-Phthalimido-N-Oxyl (Cl_4PINO) Catalyst.
   Mark A. Buckingham, William Cunningham, Steven D. Bullm Antoine Buchard, Andrea Folli, Damien M. Murphy and Frank Marken, *Electroanalysis,* 2018, 30, 1706.

4. Microscale Ionic Diodes: An Overview.
   Budi R. Putra, Luthando Tshwenya, **Mark A. Buckingham**, Jingyuan Chen, Klaus Mathwig, Koichi, Aoki, Omotayo Arotiba, Abigail Thompson, Zhongkai Li and Frank Marken, *Electroanalysis,* 2021, 33, 1398.

Contents

Chapter 1:

Introduction to thermogalvanic thermal-to-electrical energy conversion using iron-based redox couple

Chapter 1: Introduction

1.1 – Waste heat as an unexploited energy source

The rapidly growing global population, coupled with the rapidity of recent industrial development for many non-western nations has led to a significant demand for energy on a global level.[1] As most nations currently rely on non-renewable sources such as coal, oil and gas to generate this energy, a significant energy crisis is currently occurring.[2] This current energy crisis is two-fold. Firstly, it is an energy generation crisis, where sustainable sources of clean energy need to be exploited in order to meet the growing global demand, without emitting significant quantities of greenhouse gases. Secondly, the energy efficiency of all processes associated with energy, from harvesting, conversion, transport, storage, and utilisation need to be significantly increased. It is currently predicted that for every joule of energy utilised by humanity, two joules of energy is lost as waste heat.[3,4] Thus we actually need to produce triple the quantity of energy that we currently require. If the efficiency of these processes is improved, and we lose significantly less energy as waste heat we would require significantly less energy resources, which could be met by renewable sources. Therefore, exploiting alternative sources of energy that can be sustainably harvested without producing greenhouse gases are of paramount importance to balancing the growing demand for energy, while preventing both global warming and the over-exploitation of the ecosystem.

As mentioned, thermal energy is currently produced (and wasted) in vast quantities on a global scale, if waste thermal energy can be converted sustainably, cleanly, and cheaply to usable energy (such as electricity), it has the potential to become a significant energy source. If a sustainable method of thermal-to-electrical energy conversion can be developed, there are many potential sources of thermal

energy, such as industrial processes,[5–9] transportation vehicles,[10] geothermal,[11] human habitation,[12,13] and the human body itself,[14–17] among many others. Some of these potential sources of thermal energy are shown in Figure 1.

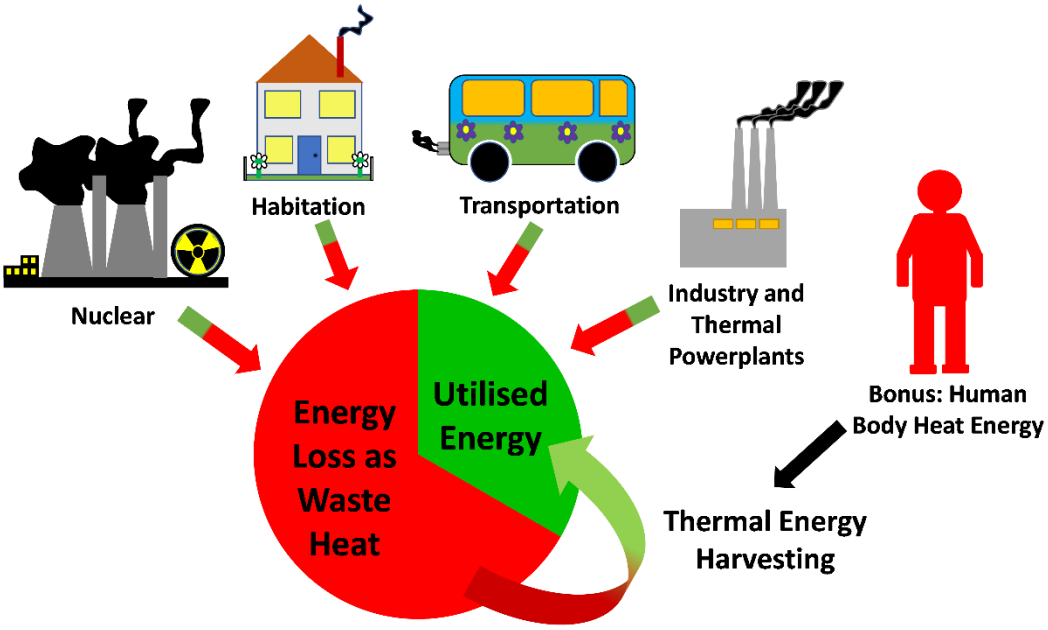

Figure 1 – Schematic representation of various sources of unexploited waste thermal energy.

Thermal energy is quantified in three grades, where low grade (<200 °C), medium grade (200 – 500 °C) and high grade (>500 °C) can be harvested *via* different methods to generate electricity.[18,19] High-grade heat utilisation is currently well-developed as the steam Rankine cycle.[20] This method has an initial step where thermal energy vaporises water, resulting in high-pressure steam, which is subsequently used to turn a turbine, generating electricity. This process is used in both fossil-fuel and nuclear power plants and is a very efficient method of generating electricity. However,

with obvious disadvantages from a sustainability perspective relying on non-renewable sources and producing greenhouse gases.

Rankine cycles based on organic liquids, rather than water have also been developed. These systems utilise lower temperatures by employing volatile organic compounds as the fluid.[21–23] Waste heat sources such as those in Figure 1 are generally classed as low-grade (<200 °C).[19] Currently this potential source of energy is almost completely un-exploited.

Thermogalvanic cells can sustainably convert temperature (in the form of a temperature gradient) directly into electricity.[24,25] These exploit a difference in entropy between two redox states of a redox couple. Once a temperature gradient is applied to a thermocell, a continuous generation of current is produced by this thermodynamically driven process. The fundamental aspects of thermogalvanic cells using an imaginary redox couple $A + e^- = B$ is initially discussed. In the interest of space, the fundamental processes of thermogalvanic cells are discussed along with aqueous iron-based redox couples.

1.2 – Introduction to thermogalvanic energy conversion

Thermogalvanic cells (also known as thermocells) are either liquid or gelled state devices which convert thermal energy directly into electrical energy.[24,25] Thermogalvanic cells are a sub-class of thermoelectrochemical cells, which have historically been referred to as “liquid thermoelectrics”, and were initially characterised in the late 19th century.[26–28] These devices convert thermal energy to electrical energy by a thermodynamically-driven redox process that is analogous to the

classic Seebeck effect experienced by solid-state thermoelectric devices.[29] This process is commonly referred to as the thermogalvanic Seebeck effect.[30]

The application of a temperature gradient (ΔT) between the two electrodes of a thermogalvanic cell results in the production of a voltage (ΔV). This is quantified as a temperature coefficient (known as the Seebeck coefficient, S_e). This coefficient quantifies the ability of the system to convert heat to electricity and follows the equation:

$$S_e = \frac{\Delta V}{\Delta T} \quad (1)$$

A thermogalvanic cell is simply a redox-active electrolyte, either in a solution or gelled state, sandwiched between two electrodes which are held at dissimilar temperatures (this is shown schematically in Figure 2).[24,25] Typically, thermogalvanic cells utilise a redox couple of electrolytes such as the $[Fe(CN)_6]^{3-/4-}$,[17,31–35] $Fe^{2+/3+}$,[36–40] or $[Co(bpy)_3]^{2+/3+}$.[41–46] However, thermocells have also been reported using metal to ion transition such as the $Cu^{0/2+}$ and $Li^{0/+}$ redox couples.[47–50] However, it has been demonstrated that almost any redox couple will exhibit a thermogalvanic temperature coefficient.[51] These redox ions act as charge carriers to the electrodes, where they either undertake an oxidation or reduction at the electrode surface (Figure 2).

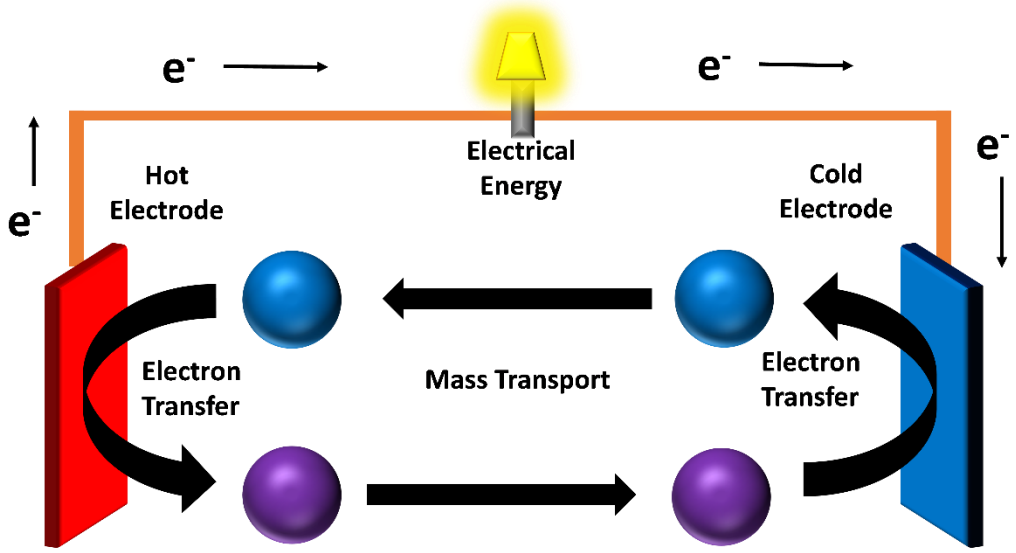

Figure 2 – Schematic of a thermogalvanic cell where the reduction is occurring at the cold electrode and the oxidation is occurring at the hot electrode with an imaginary redox couple.

Thermogalvanic cells have been increasingly investigated for thermal energy conversion due to many inherent advantageous properties. These include: 1) Thermogalvanic cells typically utilise earth-abundant metals such as Fe in sustainable solvents such as water, this also aids in cost-effectiveness;[30] 2) Thermogalvanic cells can be made of flexible materials and shaped to fit the source of waste heat, this has been demonstrated with heat sources such as a hot-water pipe[52] or commonly the human body.[14–17] 3) As liquid devices, thermogalvanic cells also have inherently low thermal conductivity, which can even be improved by gelling the liquid electrolyte to a gelled electrolyte (discussed in section 1.5).[53] Finally 4) The thermogalvanic Seebeck coefficient is typically one to two orders of magnitude higher than those of thermoelectric devices.[24,25,47,54] For these reasons, thermogalvanic cells are being

increasingly investigated as a cheap and sustainable alternative for low grade waste heat harvesting devices.

1.3 – The driving force of thermogalvanic cells

In the previous section, the Seebeck effect was introduced as a way of quantifying the driving force for thermogalvanic cells, as in Equation 1 (expanded in Equation 2). This is an entropically driven process, where the difference in entropy between two redox active species (ΔS_{rc})[51,55,56] is the actual driving force for thermogalvanic cells, once a difference in temperature is applied.

$$S_e = \frac{\Delta V}{\Delta T} = \frac{\Delta S_{rc}}{nF} \tag{2}$$

where n is the number of electrons transferred, and F is Faraday's constant. With respect to the entropy, several distinct entropic components combine to the overall ΔS_{rc}.[31,51,57–59]:

$$\Delta S_{rc} = \left(S_B + \hat{S}_B\right) - \left(S_A + \hat{S}_A\right) - n\bar{\bar{S}}_e \tag{3}$$

where S, $\hat{S}$ and $\bar{\bar{S}}$ are the partial molar entropy of redox species, the Eastman entropy of transport of ions in solution and the entropy of transport of electrons through the external circuit, respectively.[31] The entropy of transport of electrons though copper connections is typically negligible, (*ca.* 2 μV K^{-1}) and can be discounted.[31] The Eastman entropy refers to the interaction of the solvated ion and the bulk solvent as the solvated ion is travelling through the solvent. (*i.e.* minor perturbation in bulk solvent as a polarised solvation shell is driven from one electrode to the other by the

thermodynamic driving force in a thermogalvanic cell), which can also be considered negligible compared to the partial molar entropy.[24]

To demonstrate this, previous investigations have been undertaken to measure the Seebeck coefficient while allowing sufficient time to reach Soret equilibrium ($S_{e(\infty)}$).[31,60] The Soret effect is a combination of the accumulation of ions at one electrode upon the application of a temperature gradient (a kinetic factor) and the difference in Eastman entropy of transport, driving a potential (a thermodynamic factor).[58,59,61–64] These factors combine to result in an accumulation of species at each electrode, generating a high potential difference.[65,66] However, the Soret effect typically only has a minor impact on ΔS_{rc}, compared to the Seebeck effect when a redox-active couple are present, and can also be discounted in redox-active electrolyte thermogalvanic cells.[25,31] Therefore, a simplified but relatively accurate approximation of Equation 3 can be:

$$\Delta S_{rc} = S_B - S_A \tag{4}$$

In thermogalvanic cells, the ΔS_{rc} is based on the solvent polarisation around each ionic species, and can therefore be either positive or negative, depending on whether the oxidation or reduction in the redox process results in a net gain of entropy. For example, upon reduction of Fe^{3+} to Fe^{2+}, a less charge dense ion is formed, whereas upon reduction of $[Fe(CN)_6]^{3-}$ to $[Fe(CN)_6]^{4-}$ a more charge dense ion is formed. Thus, the same process (a reduction) results in the opposite change in entropy. Upon formation of a less charge dense ion, formerly polarised solvent is lost to the bulk. This gives a positive entropy change and thus, a positive S_e.[36] The effect on polarised aqueous solvent is shown in Figure 3.[35,67] Despite the ability to either gain or lose

entropy upon reduction, the laws of thermodynamics constitute that there must always be a net gain of entropy to the system.[68] To achieve this, the reduction in a thermocell can occur at either the hot electrode (n-type) or the cold electrode (p-type) in order to always gain entropy. Please note that Figure 3 is just meant to be a visual representation of the gain and loss of 'fixed' solvating water molecules in the inner solvation shell, this is not meant to be an accurate approximation of the number of solvated molecules; for simplicity, it excludes the outer solvation shell and the bulk solvent.

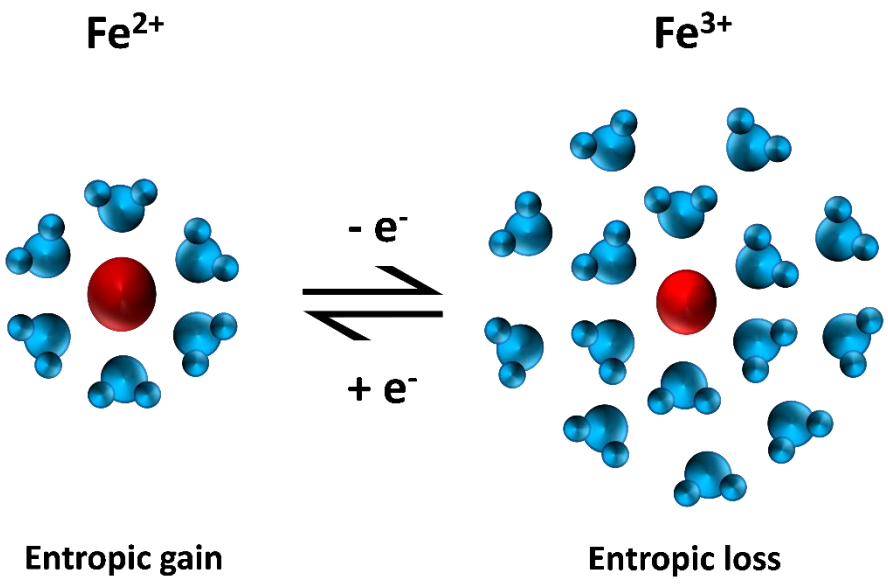

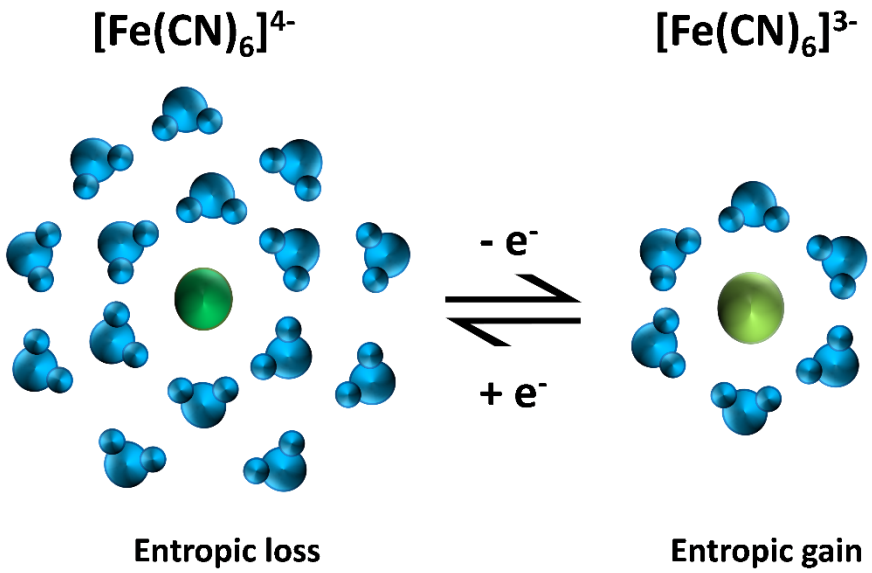

Figure 3 – Visual representation of the change in inner solvation sphere with reduction / oxidation of the $Fe^{2+/3+}$ and $[Fe(CN)_6]^{3-/4-}$ redox couples. Where the solvation increases with increasing charge density of the ions.

1.4 – The fundamental thermodynamics of thermogalvanic cells

As the ΔS_{rc} of a redox couple determines the Seebeck coefficient of the redox couple, the ΔS_{rc} is also directly related to the voltage output possible by a thermocell, at any given temperature difference (as in Equation 1). As discussed in the next section this is also hugely important towards the power output of a thermogalvanic cell. To this end, predicting the ΔS_{rc} for any given redox couple, in any given solvent is highly desirable for the advancement of thermogalvanic cells.

Fundamental studies have been undertaken on a wide variety of redox couples at low concentrations in a range of aqueous and organic solvents. This research has been conducted in an attempt to determine an equation that can be used to predict the ΔS_{rc} of a particular redox couple based on ionic radius, ionic charge and the

solvent.[69-73] Two equations have typically been used for this purpose, one is the Born model:[74,75]

$$(\Delta S_{rc}) = \frac{e^2 N_A}{2\varepsilon r T}\left(\frac{d ln\varepsilon}{dT}\right)(Z_{Ox}^2 - Z_{Red}^2) \quad (5)$$

Where e is the electronic charge, N_A is Avogadro's constant, ε is the dielectric constant, r the ionic radii, T the temperature and Z_{Ox} and Z_{Red} the ionic charge of the oxidised and reduced species, respectively. This model has been compared to experimental values for ΔS_{rc} of a range of redox couples, with varying degrees of success.[70] Further and more comprehensive studies determined the relationship:

$$\Delta S_{rc} = K_1 + K_2(AN) + K_3\frac{(Z_{Ox}^2 - Z_{Red}^2)}{r} \quad (6)$$

Where $K_{1\text{-}3}$ are all constants depending on the solvent and *AN* is the acceptor number of the solvent,[76] which reflects a combination of the electrophilicity and polarity of the solvent.[77] This relationship has been shown to correlate well with ΔS_{rc} using a variety of redox couples, in a variety of solvents.[76] These equations can easily be simplified into a predictive relationship:

$$\Delta S_{rc} \propto \frac{(Z_{Ox}^2 - Z_{Red}^2)}{r} \quad (7)$$

which has been used to model speciation of redox couples in thermogalvanic cells.[30,78,79] This therefore can be used as a useful tool in predicting redox couple S_e, based only on the ionic radius and charge. This also allows a significant insight into potential improvements of the Seebeck coefficient of redox couples in thermocells, in the absence of additives into the thermocell. This is clearly observed as, small, highly charged and highly charge dense redox couples are ideal candidates for high Seebeck coefficients.

1.5 – Enhancing voltage in thermogalvanic cells

The application of a temperature gradient to a thermogalvanic cell generates a voltage, which is equivalent to:

$$\Delta V = \frac{\Delta S_{rc} \Delta T}{nF} \quad (8)$$

Typical Seebeck coefficients in thermogalvanic cells are in the range of 0.1 – 2 mV K^{-1}.[24] To put this into context, under modest applied temperature differences, (of *ca.* 20 K between body heat and the typical ambient environmental temperature) and a S_e of 1 mV K^{-1}, this correlates to an 'overpotential' ($0.5V_{OCP}$) across the thermocell of *ca.* 20 mV. This overpotential is the electrochemical driving force behind the redox processes in the thermogalvanic cell, but is very low for typical electrochemical processes.[80] It should also be noted in Equation 8 that moving from a 1 electron process to a 2 electron process halves the driving force (as n is a denominator in Equation 8). There are a number of methods employed in order to increase observed S_e in thermocells, such as addition of organic co-solvents,[81,82] solvent structure breaking electrolytes[83] or host-guest complexation additives like cyclodextrins.[84–87] As these are not relevant to this thesis these methods will not be discussed.

These methods can also be either expensive, complicated, or detrimental to the current generation ability of the thermocell. Therefore, another, simpler method of obtaining high voltage in thermogalvanic cells is routinely employed. This is achieved by creating a device which comprises of both positive S_e (commonly known as n-type thermogalvanic cells) and negative S_e (commonly known as p-type thermogalvanic cells) thermocells wired electrically in-series, as in Figure 4.[14,15] This arrangement avoids a thermal short circuit by maintaining these thermocells thermally in-parallel.[88]

This is possible as the direction of electron transport is the opposite direction in n-type thermocells to their p-type counterpart (as demonstrated in Figure 4 for the n-type $Fe^{2+/3+}$ and p-type $[Fe(CN)_6]^{3-/4-}$ systems). This method has been employed to produce thermocell devices which generate voltages in the order of 100s of mV to several V's, along with output currents in the mA and output power in the μW ranges.[14–17,89] These factors all combine to determine the output voltage of the thermogalvanic cell. However, for the thermocell to generate power, the thermocell needs to generate both voltage and current. The power generation ability of a thermocell is further discussed in the next section.

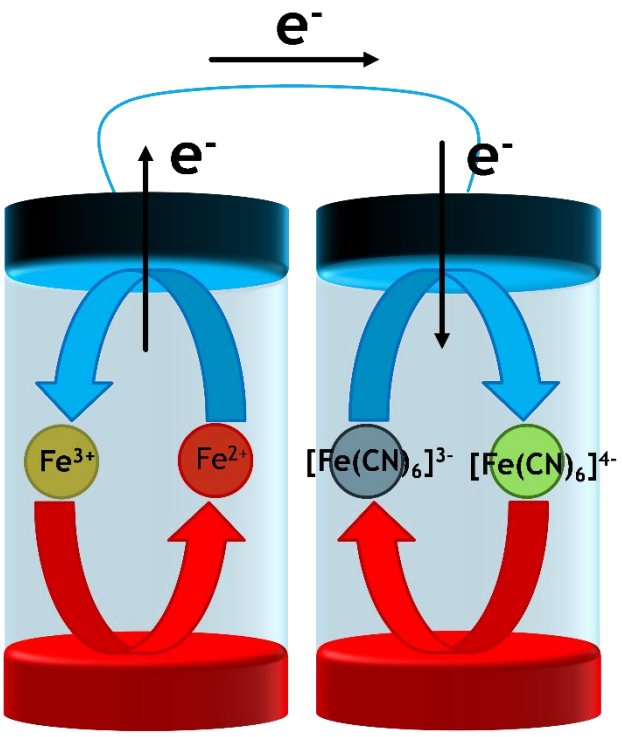

Figure 4 – Figure showing a schematic of the n-type $Fe^{2+/3+}$ thermocell and the p-type $[Fe(CN)_6]^{3-/4-}$ thermocell connected electrically in series, to enhance output voltage of the device.

1.6 – The fundamental kinetics of thermogalvanic cells

Thermodynamics are the driving force for the thermocell overpotential,[35,90] stemming from the Seebeck effect observed in the presence of a temperature difference between the two electrodes. However, this does not yield any insight into the kinetics of a thermogalvanic cell, namely the nature of electron transfer at the electrode surface. To generate power density, both voltage and current are required.

Because the electrolyte in thermogalvanic cells undergo a redox process, current can be drawn from the thermogalvanic cell when a voltage lower than the open circuit voltage (*i.e.* voltage when no current is allowed to pass) is applied.[3] The ability of an electrochemical system to generate current is often called the kinetics of the electrochemical cell.[80] As power is a combination of current and voltage (as discussed in section 1.7), the kinetics of current generation in thermogalvanic cells is hugely important.

In electrochemical systems that have an inherent overpotential (such as an ohmic overpotential) the Butler-Volmer equation is typically used to predict current generation in the system, such as in Equations 9 and 10:

$$j = j_0 \left(exp \left[\frac{\alpha_a n F \eta}{RT} \right] - exp \left[- \frac{\alpha_c n F \eta}{RT} \right] \right) \quad (9)$$

$$\text{where } j_0 = F k^0 ({C_{Ox}}^{\alpha} {C_{Red}}^{\alpha}) \quad (10)$$

and j is the current density, j_0 the exchange current density, α_a and α_c the anodic and cathodic charge transfer coefficients, respectively, n the number of electrons transferred, F the Faraday's constant, η the activation over-potential, R the universal

gas constant, T is the temperature, k^0 the electron transfer constant, C_{Ox} and C_{Red} the oxidised and reduced concentration, respectively.

As thermocells are electrochemical cells that have inherent overpotential resistances, the Butler-Volmer equation has often been used to describe the electrode kinetics of thermocells.[35,90–92] Another important factor from this equation is the importance of concentration of electrolyte (both redox states in a redox couple). In thermogalvanic cells, there have been many investigations into concentration of electrolyte,[35,67,93–95] these will be discussed further in Chapter 3 – where concentration is the main focus of investigation.

At high concentrations of electrolyte, improving the kinetics (and therefore current output) of thermocells has typically been achieved in two ways, by either improving heterogeneous or homogeneous electrocatalysis. Heterogeneous electrocatalysis has often been achieved by modifying the electrode surface, by either employing noble-metal electrodes,[32,33,67] or surface modification of the electrode with nanomaterials.[40,96] Homogeneous electrocatalysis has been achieved through catalytic pathways due to the presence of additional species (such as H^+)[38,39] in the thermocell solution.

Understanding the fundamental aspects of both the thermodynamics and kinetics of thermogalvanic cells is hugely important towards improving thermocell efficiency. How power can be generated and measured in a thermogalvanic cell, and how thermocell efficiency is measured is discussed in the next section.

1.7 – Power generation in a thermogalvanic cell

To measure power in a thermogalvanic cell, a variety of methods can be utilised.[3] The two most common are to measure the open-circuit voltage, and apply fixed resistances to the thermogalvanic cell. The drop in voltage ΔV would then be measured, and the current calculated from Ohm's law:

$$V = IR \tag{11}$$

where V is voltage, I is current, and R is resistance.[3]

The other common method commonly employed to measure power of a thermocell is through measuring an IV curve through a combination of chronoamperometry and chronopotentiometry.[3] IV curves are highly dependent on inherent resistances observed in an electrochemical cell.

Thermogalvanic cells are limited by several inherent resistances.[91,97] There are three main internal resistances: 1) the ohmic resistance (R_O), 2) the electron transfer resistance (R_{ET}) and 3) the mass transport resistance (R_{MT}). These three resistances describe the ohmic (or iR) drop through the electrochemical system, resistance in transferring an electron from the electrode to the redox ion, and the resistance of the ion transport between the electrodes, respectively.[24,32] Due to these inherent resistances, a thermocell essentially acts as a perfect resistor when measuring an IV curve, therefore a linear IV curve is almost exclusively observed (such as in Figure 5(a)), following Ohm's law. From a linear IV curve, a classic parabolic power curve (Figure 5(b)) can be calculated following Watt's power law:

$$P = IV \tag{12}$$

$$P_{max} = 0.5V_{OCP}.\,0.5j_{SC} \quad (13)$$

where P is power. From this, the maximum power output P_{max}, is observed at exactly $0.5V_{OCP}$ and $0.5j_{SC}$ (Equation 13). From Equation 12, it is also clear that a linear IV curve would expect to observe a parabolic power curve, as shown in Figure 5(b).

In thermogalvanic cells, voltage is generated from the Seebeck effect and reaches a maximum (known as the open circuit voltage or V_{OCP}) dependent on the Seebeck coefficient of the redox couple, and the applied temperature in the thermocell.[3] Under an applied load, such as an applied voltage lower than the V_{OCP} or an applied resistance to the thermocell while measuring the open circuit voltage, a current can be drawn (or calculated).[3,24,47] Maximum current is reached when V = 0 (known as the short-circuit current, I_{SC} or when divided by the electrode area, short-circuit current density j_{SC}).[3,92]

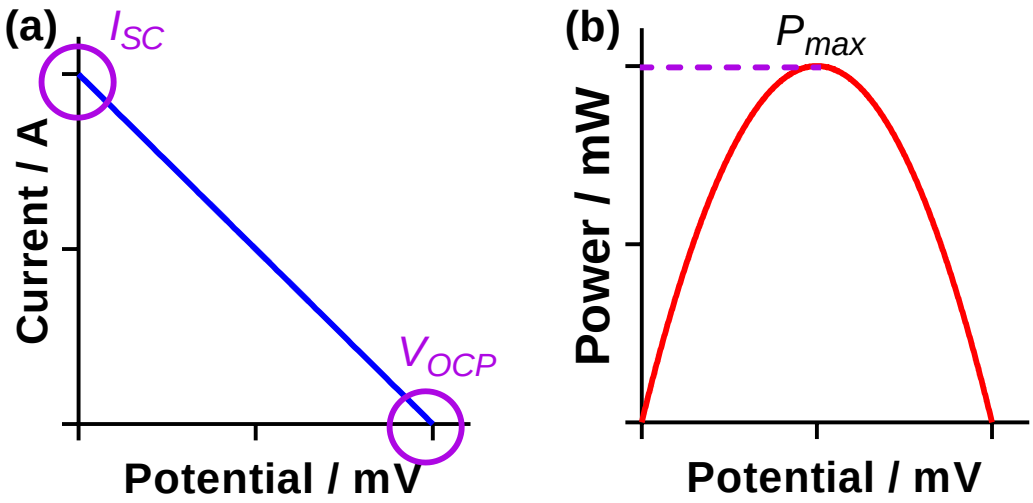

Figure 5 – Simulated data displaying the performance of a thermocell which is dominated by a single, fixed inherent resistance, R (which acts as a resistor following the V= IR relationship), where (a) a linear V= IR response results; the highest potential

difference and current are the V_{OCP} and I_{SC}, respectively, and (b) the resulting power curve, shown as power *vs* potential, with P_{max} achieved at $0.5V_{OCP}$ and $0.5I_{SC}$. This figure has been reused with permission from: Buckingham, *Journal of Electroanalytical Chemistry*, 2020, 872, 114280.[3]

It is noteworthy here that a thermocell is a galvanostatic, rather than a potentiostatic system. This is observed by the 'opposite' direction of the IV curve than expected, a potentiostatic measurement with a limiting resistance would increase proportionately away from V = 0 and I = 0 and an increase in V from 0 would be the observed overpotential. In a galvanostatic measurement, a linear IV curve is observed (such as in Figure 5(a)) from V = OCP (which is not 0) where I = 0 and the overpotential is observed in the galvanostatic system away from V = OCP.

This section has discussed how both voltage and current output of a thermogalvanic cell relate to the output power of the same thermocell. However, one of the most important aspects of a thermogalvanic cell is related to the accuracy of measuring the thermocell performance. This is discussed further below.

1.8 – Accurate thermogalvanic measurements:

1.8.1 – The importance of equipment

One of the main current limitations in thermogalvanic cells is the low S_e (in the mV K^{-1}). Due to this, and the low applied ΔT (also commonly investigated), low thermogalvanic overpotentials are observed. These low overpotentials lead to low currents drawn from these individual cells. Therefore, the method, instrument and time used to measure the voltage and current (and therefore power) of these thermocells

must have sufficiently high impedance to be able to accurately measure these fundamental parameters of the thermocell.

With respect to voltage, this has been measured qualitatively with a Source Measure Unit (SMU), potentiostat, and various voltmeters to measure the voltage output on the same thermocell.[3] This report suggested that voltage could be easily measured with both the SMU and potentiostat, but a high quality 4-digit multimeter was the minimum required to accurately measure the voltage.[3] The reason this is important is because a voltmeter, combined with a variable resistor box is arguably the most commonly employed method of measuring power density in thermocells.[3] This should also be the same for current, but has not been tested beyond comparing an SMU and potentiostat, which both measured an equivalent current from the same thermogalvanic cell.[3] As both voltage and current combine to demonstrate the output power of a thermogalvanic cell. Accurate measurement of both of these parameters is vital. However, even with high impedance equipment for accurate potential and current measurements, the time taken in measuring these properties may also lead to inaccurate measurements.

1.8.2 – The importance of measurement technique and time

There are several methods of measuring a thermogalvanic cell based on the three parameters in Ohm's law (V = IR). The thermocell can be measured by application of either constant voltage, current or resistance, whilst measuring the current (constant voltage) or voltage (constant current or resistance), respectively. Power density can then be calculated from the $P = IV = V^2/R = I^2/R$ relationships.[3]

A fundamental and thorough investigation into thermocell measurement methods has been reported.[3] This investigation compared many different methods of measuring thermogalvanic power density, utilising several different methods. It was found that by using previously reported techniques such as applying a fixed *R* and measuring *V*,[31,41] a fixed *V* and measuring *I*,[36,98] or fixed *I* and measuring *V*[67,99] that equivalent power densities of the thermocell can be observed, if given sufficient time to reach 'steady-state'.[3] The variation in time taken for these techniques to reach steady-state was also observed using the first derivative of the raw data (shown in Figure 6). This demonstrates that using different techniques required different times to reach steady-state and the 'true' thermogalvanic power density, where all steady-state measurements observed equivalent power (Figure 6(g)).

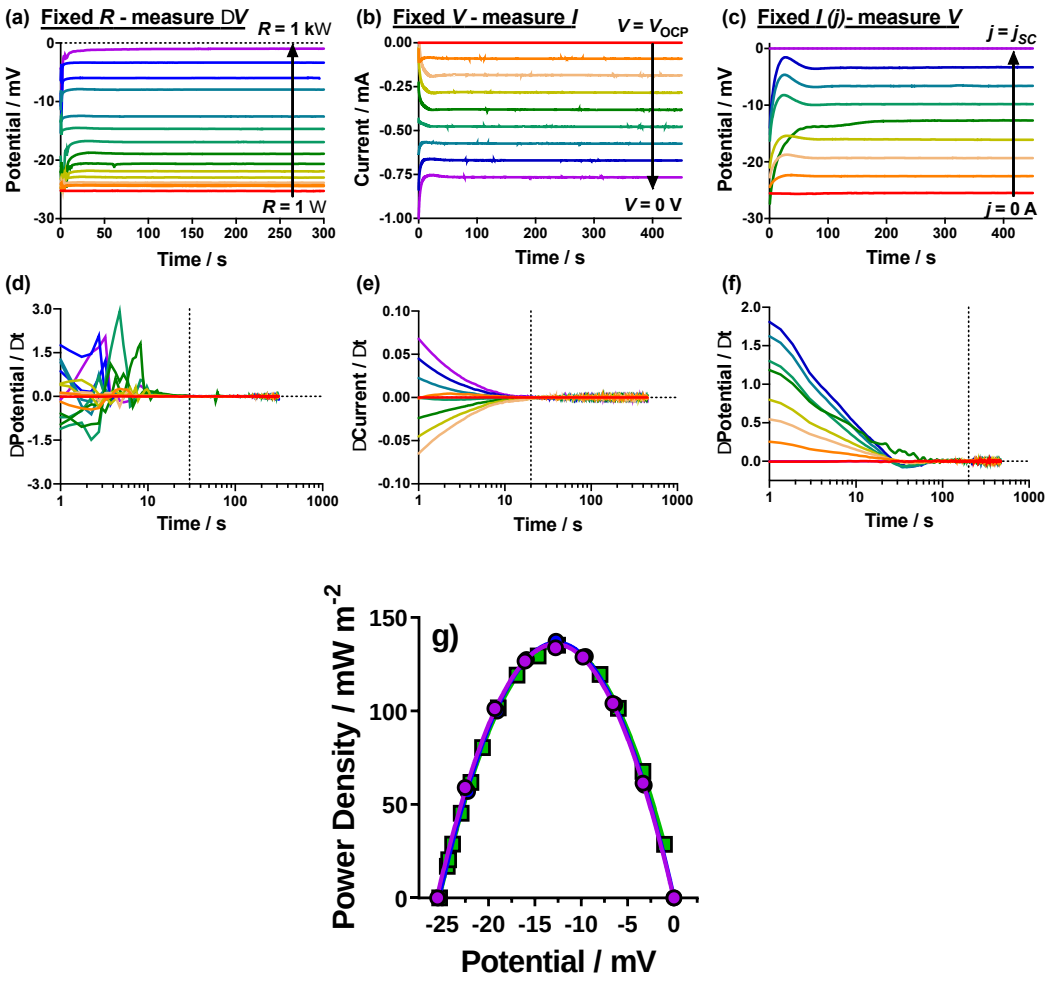

Figure 6 – Figure showing (a) the sequence of constant resistances method (with applied resistances between 1 Ω and 1000 Ω), (b) the sequence of constant potentials method (with applied potentials between V_{OCP} and 0 V), and (c) the sequence of constant currents method (with applied currents between j_{SC} and 0 A). The arrows indicate the order of the sequence of measurements, from first to last. Also shown below are the first order derivatives of the raw data, for constant resistance, voltage and current in (d), (e) and (f), respectively. The vertical dashed lines indicate the equilibration times (*i.e.* point at which there was no significant change *vs* time). Also shown in (g) is the corresponding power curves obtained by these three measurement methods (as averages of the steady state values) for the sequences of constant resistances (green squares), constant voltages (blue triangles) and constant currents (purple circles); the near-perfect overlay of these three power curves demonstrates these measurement methods yield equivalent values. These figures have been reused from: Buckingham, *Journal of Electroanalytical Chemistry*, 2020, 872, 114280.[3]

1.9 – Measuring and calculating the efficiency of a thermogalvanic cell

The maximum power density of a thermocell (P_{max}) is achieved at $0.5V_{OCP}$ and $0.5j_{SC}$. One method of measuring thermocell efficiency has been proposed using this parameter, as in Equation 14.[52,100]

$$\eta = \frac{0.25(V_{OCP} j_{sc})}{A\kappa\left(\frac{\Delta T}{d}\right)} \tag{14}$$

where η is the efficiency of the thermocell, V_{OCP} is the open circuit voltage, j_{sc} is the short-circuit current density, A is the electrode surface area, κ is the thermal conductivity, ΔT is the temperature difference between the two electrodes and d is the inter-electrode separation. In this equation, $0.25(V_{OCP}j_{SC})$ is the maximum output power (P_{max}) and $A\kappa(\Delta T/d)$ is the input thermal flux between the hot and cold electrodes.[25]

As mentioned previously, 2 of every 3 joules of energy produced by humanity, are lost as waste heat. In 1824 a theoretical engine was devised by Nicolas Léonard Said Carnot, and was proposed as the maximum efficiency device between two temperature reservoirs.[101] This engine is known as a Carnot engine and has been used as a comparative measure of efficiency in both thermoelectric and thermoelectrochemical systems as in Equation 15[25]:

$$\eta_{carnot} = \frac{Power\ efficiency\ of\ the\ device\ (\eta)}{Power\ efficiency\ of\ the\ Carnot\ engine\ at\ the\ same\ temperatures} \tag{15}$$

where the Carnot efficiency (η_{Carnot}) is calculated from the proportion of the efficiency of a device (η) relative to the efficiency of the Carnot engine (*i.e.* 100%).[33] It has been proposed that a thermogalvanic cell with a modest Carnot efficiency of between 2 and 5% is high enough to be commercially viable.[25]

The efficiency of thermogalvanic cells relative to the Carnot engine are determined from Equation 16.

$$\eta_{Carnot} = \frac{\eta}{\frac{(T_h - T_c)}{T_h}} \quad (16)$$

where T_h and T_c are the hot and cold electrode temperatures, respectively. And η_{Carnot} is the efficiency of a device relative to the Carnot engine.

This method of measuring thermocell efficiency has been extensively used, particularly when novel electrode materials have been investigated in thermocells.[16,40,52,93,96,100,102–110] These investigations have reported a wide range of efficiencies from 0.001%,[93] up to a recently reported 11%.[34] Some of the highest efficiencies relative to Carnot have been reported utilising high surface area carbon nanotube-reduced graphene oxide nanocomposite,[96] carbon nanotube-graphene hybrid aerogel,[104] or Pt-nanoparticle-decorated orientated carbon nanotube aerogel[100] electrodes, or through utilising thermocrystilisation of $[Fe(CN)_6]^{4-}$.[34]

As the fundamental aspects of thermogalvanic cells, the governing fundamental driving forces behind these aspects and the importance in measurement method time and technique of these thermocells has been discussed and evaluated. More practical aspects of thermogalvanic cells relevant to this thesis will next be discussed, namely the iron-based redox couples which have currently been reported and the current applications which have been either demonstrated or proposed.

1.10 – Iron redox couples in thermogalvanic cells

The three main factors regarding thermocell performance are the redox couple,[25,47] electrode[54] and solvent.[24,111] In this thesis, neither electrode materials or solvent are significantly investigated and in the interest of space neither will be discussed here. However, fundamental electrochemical behaviour is heavily investigated, alongside development of novel iron redox couples based on the principles of green chemistry. Iron-based redox couples are exclusively investigated or developed in this thesis; therefore, it is prudent to discuss all currently reported iron redox couples in thermocells, and the effect solvent has on these redox couples.

Iron is a highly appealing metal to use due to its significant earth-abundance, low cost, and easy recyclability. Because of this, a wide range of Fe-based redox couples have been investigated in thermocells. Redox couples such as the $Fe^{2+/3+}$, $[Fe(CN)_6]^{3-/4-}$ and $[Fe(cp)_2]^{0/+}$ have been explored in aqueous, ionic liquid and organic solvents, generating a wide range of both n-type (positive S_e) and p-type (negative S_e) systems. These are all discussed further below.

1.10.1 - $Fe^{2+/3+}$

The $Fe^{2+/3+}$ redox couple is an n-type thermocell, with a redox couple which exhibits a S_e between +0.3 and +1.76 mV K^{-1}.[36,38,39] This redox couple is generated through the solvation of iron salts, almost exclusively as either an aqueous or gelled electrolyte. Several iron salts have been investigated for this purpose, namely; $FeCl_{2/3}$,[14,15,67,112] $Fe(SO_4)_{1/1.5}$,[30,36,39,88] and $Fe(ClO_4)_{2/3}$.[38,39] The $Fe^{2+/3+}$ redox couple is

dominated by anion co-ordination, therefore the iron salt, supporting electrolyte and pH of the thermocell is vitally important to both the S_e and power output.[36,39,112]

The ideal redox couple generated from these iron salts is $[Fe(H_2O)_6]^{2+/3+}$, which is predicted to observe a redox couple entropy (ΔS_{rc}) equivalent to +1.8 mV K^{-1}, under very dilute conditions.[71] The reason for the significant deviation in observed (S_e) compared to the predicted value is due to discrepancies of the species present in solution. This is due to significant differences in cation-anion coordination strength, where the $[SO_4]^{2-}$, $[HSO_4]^-$ and $[Cl]^-$ anions are all found to strongly associate to the Fe ion.[113] This is also demonstrated by the lower observed Seebeck coefficients.[30,36,39]

The ionic charge of the redox couple has a significant effect on the observed redox couple entropy.[76] Therefore, strongly co-ordinating anions such an $[SO_4]^{2-}$ and $[Cl]^-$ will undertake an equilibrium such as (17) below, which will decrease not only the observed charge density of the redox couple, but also the redox couple entropy (and observed S_e).

$$[Fe(H_2O)_6]^{2+/3+} + [A]^{x-} \rightleftharpoons [Fe(H_2O)_5(A)]^{2+/3+-x} \quad (17)$$

This equilibrium has been demonstrated with $[A]^{x-}$ being either $[SO_4]^{2-}$,[30,36,39] or $[Cl]^-$,[39] resulting in the $[Fe(SO_4)(H_2O)_5]^{0/+}$ or $[Fe(Cl)(H_2O)_5]^{+/2+}$ redox couples, respectively. This is not the case for less strongly coordinating anions such as $[ClO_4]^-$, which fully-dissociates to the $[Fe(H_2O)_6]^{2+/3+}$ species, particularly at low pH.[36,39]

Anionic iron redox couples have also been reported in ionic liquid[78,114,115] solvents, observing p-type S_e. The ionic liquid solvent facilitates the addition of $[Cl]^-$ or $[Br]^-$ anions, resulting in the $[Fe(Cl)_4]^{-/2-}$ or $[Fe(Br)_4]^{-/2-}$ redox couples. These have been found to observe negative Seebeck coefficients (due to the negatively charged

nature of these redox couples) of -0.48 and -0.42 mV K^{-1} respectively.[114] This is an interesting contrast to aqueous $FeCl_{2/3}$, which demonstrates a positive Seebeck (discussed above).

Iron salts are not the only iron redox couples investigated in thermocells, iron-ligand complexes have also been reported. The most common of these is the hexacyanoferrate ($[Fe(CN)_6]^{3-/4-}$), which is further discussed below.

1.10.2 - $[Fe(CN)_6]^{3-/4-}$

The hexacyanoferrate complex, commonly known as ferricyanide ($[Fe(CN)_6]^{3-}$) and ferrocyanide ($[Fe(CN)_6]^{4-}$) is the most extensively explored redox couple in thermogalvanic cells, due to the high Seebeck coefficient of -1.4 mV K^{-1} and fast, reversible redox kinetics.[25,31–33,67] The $[Fe(CN)_6]^{3-/4-}$ redox couple has become the benchmark in thermoelectrochemistry, this is typified by being the typical comparison when novel redox couples are reported, such as the $[Co(bpy)_3]^{2+/3+}$,[116] and $Fe(ClO_4)_{2/3}$.[38,39] The $[Fe(CN)_6]^{3-/4-}$ redox couple has also been the subject of both fundamental and theoretical investigations, such as both equimolar[35,67] and non-equimolar[35,95,117] concentration studies, thermocell orientation,[33] inter-electrode separation,[32] temperature effect,[3] and different techniques for measuring the power density of the thermocell[3] (some of these are discussed in chapters 2 and 3). $[Fe(CN)_6]^{3-/4-}$ is also almost exclusively used as the redox couple of choice in novel electrode reports.[40,52,93,96,100,102,104,106]

The $[Fe(CN)_6]^{3-/4-}$ redox couple is typically obtained from the potassium salts.[25,35,67] The 0.4 M $K_3[Fe(CN)_6]$ & $K_4[Fe(CN)_6]$ (or $K_{3/4}[Fe(CN)_6]$) redox couple

yields a Seebeck coefficient of *ca.* -1.4 mV K^{-1},[67] demonstrating a redox couple entropy of *ca.* -135 J K^{-1} mol^{-1}. However, the $K_{3/4}[Fe(CN)_6]$ redox couple has a solubility limit <<1 M,[35,118] limited by the $K_4[Fe(CN)_6]$.[35] It has been demonstrated that simply increasing the concentration of a redox couple in a thermocell directly increases the power density of the thermocell.[35,67] Therefore, it is desirable to increase the solubility of $[Fe(CN)_6]^{3-/4-}$, this has been demonstrated by substituting the $K_4[Fe(CN)_6]$ with $(NH_4)_4[Fe(CN)_6]$,[39,40] This substitution has significantly increased the power density with increasing electrolyte concentration.[39,40] However, one significant shortcoming of utilising $(NH_4)_4[Fe(CN)_6]$ is the instability of $[Fe(CN)_6]$ to acids,[30] resulting in the formation of highly toxic $HCN_{(g)}$.[30,119] Therefore this combination should be avoided and a more benign method of increasing redox couple concentration should be developed.

The $[Fe(CN)_6]^{3-/4-}$ redox couple was also the redox couple of choice for several seminal reports in thermogalvanic cells.[17,34,100,120] One of these has exploited the significantly reduced solubility of the $[Fe(CN)_6]^{4-}$ ion with high concentration of guanidinum salts.[120] This report has demonstrated 'thermosensitive crystallisation' of the $[Fe(CN)_6]^{4-}$ to increase the S_e of the $[Fe(CN)_6]^{3-/4-}$ redox couple to -3.73 mV K^{-1}.[34] Thermosensitive crystallisation has also significantly enhanced the efficiency of the thermocell.[34] This highly efficient and highly powerful thermocell has been demonstrated as a 20-unit cell, which has been capable of powering small electronic devices such as an electric fan, an array of LEDs and even charging a mobile phone, all over short timescales.[34]

The other seminal work using the $[Fe(CN)_6]^{3-/4-}$ redox couple exploits the Soret effect to significantly increase the S_e. This combination of Seebeck and Soret effect

has increased the S_e from the usual *ca.* -1.4 mV K^{-1}, up to -17 mV K^{-1}.[17] This has been achieved by utilising a high concentration of KCl, along with the typical $[Fe(CN)_6]^{3-/4-}$ electrolyte, but hosted in a gelatin environment. The use of gelatin, rather than a simple aqueous environment facilitates the ability to exploit the Soret (or 'thermodiffusion') effect to significantly increase the Seebeck coefficient.[17] This thermocell has been demonstrated as a 25-cell (all p-type) wearable device which is capable of generating 2.2 V from body heat.[17]

1.10.3 – Other Fe(ligand) complexes

There are also other Fe(ligand) complexes that have been investigated in thermogalvanic cells, the most common of these is the ferrocene / ferrocenium $[Fc]^{0/+}$ redox couple.[78,114,121–125] This redox couple has been the subject of several fundamental investigations such as enhanced S_e by either covalently tethering charged moieties,[121] through synergistic combined redox couples,[122] or host guest complexation with cyclodextrines.[125] These investigations are undertaken in ionic liquid solvent due to the instability of the ferrocenium ion in aqueous solvent.[122]

Other Fe(ligand) complexes have also been investigated, two of these are substitutions of the $[Fe(CN)_6]^{3-/4-}$ redox couple, namely the $[Fe(phen)(CN)_4]^{-/2-}$ and $[Fe(bpy)(CN)_4]^{-/2-}$ complexes, which observe p-type S_e of 1.05 mV K^{-1},[31] and between -0.24 and -1.21 mV K^{-1}, respectively.[70] Other n-type redox couples have also been investigated, the $[Fe(bpy)_3]^{2+/3+}$ and Fe(salcyclamide) have been reported to have S_e of between +0.33 and +0.51 mV K^{-1} and +1.25 mV K^{-1}, respectively.[78,114,115] However, all these investigations have mainly focussed on the thermodynamics alone and have

not assessed the kinetics. When both thermodynamics and kinetics were assessed, such as for the $[Fe(phen)(CN)_4]^{-/2-}$ redox couple, the power efficiency was found to be two orders of magnitude less than the standard $[Fe(CN)_6]^{3-/4-}$.

Having discussed the fundamental parameters governing thermogalvanic cells and the Fe-based redox couples used in them. It is important to discuss both the proposed and utilised thermal energy sources and current applications for thermocell devices. This is discussed further below.

1.11 – Current applications of thermogalvanic cells

There has been significant advancement in understanding the fundamental aspects and driving forces in thermoelectrochemical cells. Ultimately, the real drive for research in this field should be concerned with the application of cheap, large-scale low-grade thermal energy harvesting. In this, heat can be either thermogalvanically converted directly to electricity,[24,25] or stored as either a *pseudo*-capacitor[126] or thermogalvanic charging of an electronic capacitor.[14,16,40,127]

Thermoelectrochemistry has already been either proposed or demonstrated to utilise thermal energy in several 'real-world' applications. Flexible thermocells[16,52,128] are required to harvest waste heat from sources such as hot pipes,[52,129] automobiles,[130] data centres,[131] mobile phone batteries,[127] photovoltaics[132] and human body heat.[14–17] Another important trait that thermocells require in order to be implemented on large scale is durability, the ability to continuously operate for months, or even years. Bromine-based thermocells have been measured over an almost 2-year timeframe,[133]

and have been found to even increase performance over 180 days.[134] The potential applications that have been proposed or investigated are discussed in this section.

One current limitation in thermocells is the low output voltage from limited S_e and low-grade heat sources. Arrays of n-type and p-type thermocells have therefore routinely been employed in series in order to generate higher voltages.[14,15,30,38–40,88,89] Higher voltage thermocells have also been reported from increased Seebeck coefficients. These thermocells employ synergistic relationships with thermocrystallisation,[34] thermodiffusion[17] or evaporation-condensation[98] reactions, driving significant entropic advantages. These systems have shown huge potential by demonstrating applications such as lighting LEDs, powering small electronic devices and charging a mobile phone, but only over very short timescales (up to 10s of seconds).[34]

1.11.1 – Wearable thermocells

One of the areas of research currently driving thermogalvanic cells is the ability to develop small, wearable devices that utilise the human body as a heat source. These are typically arrays of both n-type and p-type thermocells,[14,15,40,88,89] but have also been demonstrated as an all p-type array.[16,17] This type of system was first demonstrated using a novel electrode material and an all p-type $[Fe(CN)_6]^{3-/4-}$ redox couple, as a modest array generating *ca.* 120 mV.[16]

Further development in this area yielded significantly higher output voltage by using the combination of gelled $Fe^{2+/3+}$ and $[Fe(CN)_6]^{3-/4-}$ in-series. This thermocell utilised 59 pairs of n-p- thermocells to generate 0.85 V, with an output power of *ca.* 2

μW from body heat. This report also demonstrated commercial capacitor charging; where both 10 μF and 100 μF capacitors were charged to 0.7 and 0.55 V, respectively.[14] More recent developments in this area have demonstrated illumination of a commercial LED using body heat alone. This was achieved using a watch-strap design where 30 n-p- pairs were connected in series to a 470 mF supercapacitor, which was charged by the thermogalvanic cells harvesting body heat. Upon removal of the charged capacitor a green LED was illuminated using a voltage booster.[15]

The highest output voltage generated from a wearable device has been achieved as a gelled thermocell, using a synergistic combination of the Seebeck and Soret effects. In this device 25 individual p-type thermocells were utilised in-series to generate 2.2 V from body heat.[17] Due to the increased S_e of this system, this device was also smaller than those previously reported. The significant output voltage and power of this thermocell device has been proposed as a power source for small 'internet-of-things' devices.[17] Some of the reported wearable thermocell devices are shown in Figure 7.

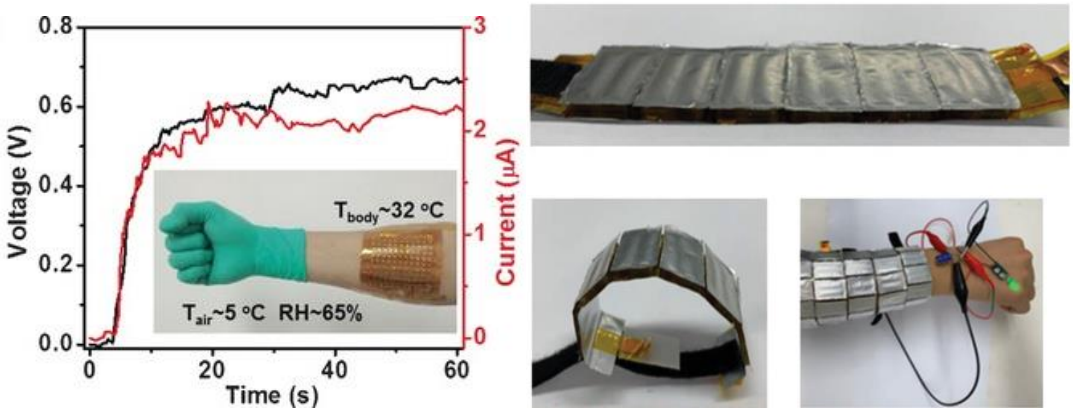

Figure 7 – Figure showing wearable thermocells, both reused with permission from (a) Yang *et. al., Angewandte Chemie International Edition*, 2016, 55, 12050.[14] and (b) Liu *et. al., Advanced Energy Materials*, 2020, 10, 2002539.[15]

1.11.2 - Solar Energy Harvesting

Another important future real-world application for thermogalvanic cells is through synergy with other energy devices. This has been demonstrated previously using solar as an energy source. One such synergistic technique is through the combined thermogalvanic energy harvesting, generating electricity as an 'open-interfacial' thermocell.[135] This method uses solar energy to drive a temperature gradient from the open-top of the thermocell, where the closed-bottom of the thermocell is colder, driving the thermogalvanic cell. This thermocell uses the cyclodextrin-complexed I^-/I_3^- redox couple. The synergy of this process comes from the evaporation of the saline aqueous solvent, which is distilled as pure water elsewhere. This therefore acts as a hybrid desalination-thermogalvanic thermocell for smart-energy conservation.

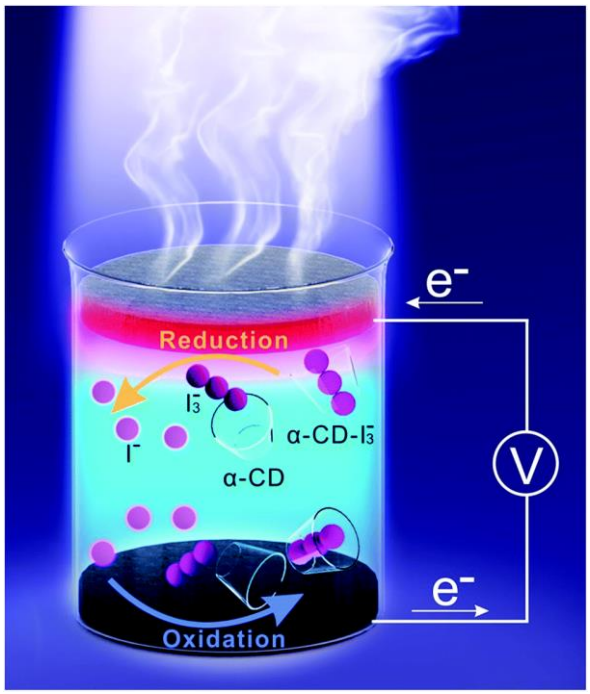

Figure 8 – Schematic representation of the combined thermogalvanic, desalination cell. Reused with permission from Shen *et. al.*, *Journal of Materials Chemistry A*, 2019, 7, 6514.[135]

1.11.3 - Other Applications of thermogalvanic cells

Thermogalvanic cells have also shown their versatility outside of directly generating electricity. This has been achieved by exploiting the thermogalvanic effect to act as surface temperature[136] and force[137] sensors. Thermogalvanic cells have also been proposed for cooling applications,[131,138] with the added bonus of harvesting electricity.

It should also be mentioned here that this is far from an exhaustive list of all the fundamental parameters governing thermogalvanic power generation. The effect of altering solvent as both liquid and gelled electrolytes, and the significant role electrode materials, in particular nanomaterials can have has not been discussed in this brief introduction to thermogalvanic cells. For a more complete (but by no means comprehensive) outlook of thermogalvanic cells, the reader is directed towards the good reviews in this field.[24,25,54,139,140]

Experimental Chapter:

Chemicals, experimental and accurately measuring a thermogalvanic cell

Measuring thermoelectrochemical power density:

Thermogalvanic characterisation measurements were all undertaken using a Keysight B2901A Source Measure Unit (SMU, Keysight, UK). Temperature control was maintained by copper heat exchangers that were regulated by RS-TX150 thermostatic circulator baths (Grant Instruments Ltd, UK). The thermocell was setup as per the schematic shown in Figure E1.

In our setup, the thermocell was connected as a two-electrode cell to an SMU, the working and sense electrodes were combined and connected to the hot electrode *via* copper tape, and the counter and reference electrodes were combined and connected to the cold electrode *via* copper tape. This was consistent throughout the entire thesis for thermogalvanic characterisation.

The thermogalvanic cell:

The thermogalvanic cell used was a tailor made poly(methyl methacrylate) (PMMA) cell, made in-house by Jason T. Sengel of King's College London chemistry department. CAD drawings of the cell was made using SolidWorks 2006 SP4.1 and prepared on a Roland MDX-40 CNC (computer numerical control) vertical milling machine using 1–3 mm square end mills. The method of forming one-chamber goes as follows: first, a rectangular cell of predetermined size was machined from cast PMMA. Subsequently, a cylinder was formed (through the 8.4 mm deep section); a 10 mm diameter lip (0.5 mm deep) was then machined at each opening. Finally, two smaller holes were drilled to allow direct injection of the electrolyte into the transparent PMMA cell.

There were two types of thermogalvanic cell used in this thesis, either a 2-chamber cell, or a 6-chamber cell. The dimensions of the two-chamber cell block are 30 mm (width) x 20 mm (height) x 8.4 mm (depth). The dimensions of the six-cylinder cell block are (30 mm (width) × 44 mm (height) × 8.4 mm (depth)). Each chamber was a 6.7 mm diameter cylinder giving a geometric electrode surface area of 35 mm^2, this area was consistently used to calculate both current and power densities. The inter-electrode separation was also fixed at 7.4 mm. A schematic cross-section of the thermogalvanic cell with electrodes in the heating and cooling system is shown in Figure E1.

Solid gold and solid platinum disc electrodes with a diameter of 10 mm were purchased from Surepure Chemetals, USA.

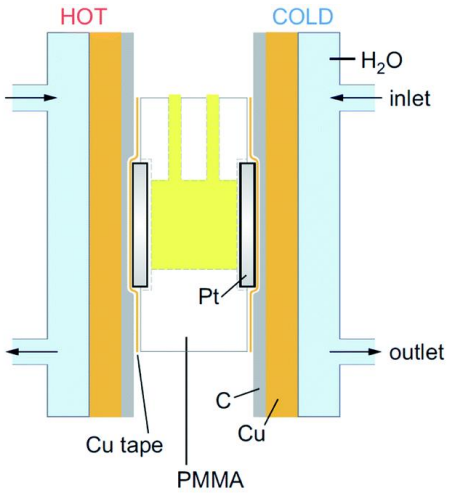

Figure E1 – Schematic representation of the thermocell (with Pt electrodes as an example) employed in this report (approximately to scale), where the cell is PMMA-based. Pt, Au, and graphite electrodes have all been used in this thesis and the dimensions of these electrodes were equivalent to fit in the designed electrode slot within the thermocell, either side of the solution. These were temperature-controlled by copper (Cu) heat-exchangers in direct contact with thermostatically controlled water (H_2O) *via* the indicated inlets and outlets.

Measuring the thermogalvanic characteristics of a thermocell:

There are four main characteristics of a thermogalvanic cell which need to be fully characterised, the Seebeck coefficient (S_e), the open-circuit voltage (V_{OCP}), the short-circuit current density (j_{SC}) and the maximum power density (P_{max}).

The V_{OCP} and Seebeck coefficient: The open-circuit voltage of the thermocells was measured by using choropotentiometry over a set timeframe. Typically, either 300 s or 600 s was used. In aqueous thermogalvanic cells (which are exclusively investigated in this thesis) this was always sufficient time to reach steady state, as shown in Figure E2 for a typical (a) $[Fe(CN)_6]^{3-/4-}$ and (b) $Fe^{2+/3+}$ (generated from $Fe(CF_3SO_3)_{2/3}$).

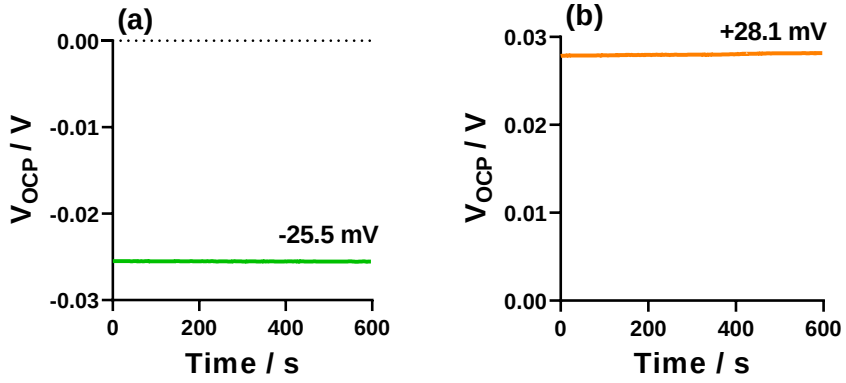

Figure E2 – Figure showing raw data for open circuit voltage obtained for (a) the 0.4 M $K_3/K_4[Fe(CN)_6]$ thermocell on Pt electrodes, and (b) the 0.4 M $Fe(CF_3SO_3)_{2/3}$ thermocell at Au electrodes. Both at a ΔT of 20 K, obtained from a T_{hot} of 40°C and a T_{cold} of 20°C.

If a thermocell has a perfect thermal interface, an 'applied ΔT' will be equivalent to an 'observed ΔT'. In this instance, the open circuit voltage (ΔV) measured from the thermogalvanic cell is directly equivalent to the S_e, as in Equation 1:

$$S_e = \frac{\Delta T}{\Delta V} \quad (1)$$

In our thermogalvanic cell, we measured the classic 0.4 M $K_3/K_4[Fe(CN)_6]$ solution, and observed a V_{OCP} for an applied ΔT of 20 K (where T_{hot} was 40°C and T_{cold} was 20°C) of -25.6 mV. The Seebeck coefficient of this solution is known to be -1.4 mV K^{-1},[67,93] therefore our 'observed' temperature was lower than the 'applied' temperature (at 91% of expected, relating to an 'observed' ΔT of *ca.* 18 K at this difference in temperature). This is further explored in chapter 2. In this thesis, the S_e calculated from each thermocell system has been calculated by using the corrected ΔT (note this discrepancy in temperature was not always known to us, so our publications may report where the 'applied' ΔT was used).

The j_{SC}: The j_{SC} of each thermocell solution was measured using chronoamperometry. Again this was measured over either 300 or 600 s, both of which allow sufficient time to reach steady-state, shown in Figure E3 again for (a) $[Fe(CN)_6]^{3-/4-}$ and (b) $Fe^{2+/3+}$.

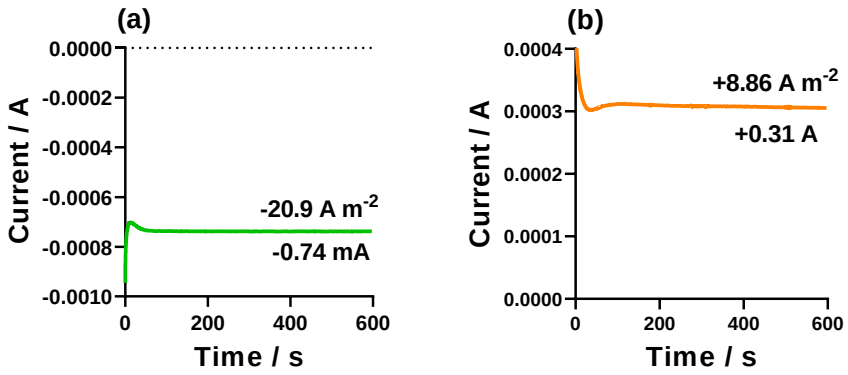

Figure E3 – Figure showing raw data for short-circuit current obtained for (a) the 0.4 M $K_3/K_4[Fe(CN)_6]$ thermocell on Pt electrodes, and (b) the 0.4 M $Fe(CF_3SO_3)_{2/3}$ thermocell at Au electrodes. Both at a ΔT of 20 K, obtained from a T_{hot} of 40°C and a T_{cold} of 20°C.

Thermogalvanic power density: Having measured the V_{OCP} and j_{SC}, the maximum power of the thermogalvanic cell can be calculated from the equation:

$$P_{max} = 0.5V_{OCP}\ x\ 0.5j_{SC} \quad (13)$$

this is known as a '2-point' measurement of a thermocell and has been used to successfully measure all four of the fundamental thermogalvanic characteristics of the investigated systems in this thesis.

Power curves of thermogalvanic cells have also been measured throughout this thesis, these were measured in succession where: The V_{OCP} was initially measured using chronopotentiometry (applying 0 A) as above. Next, 0.75, 0.5, 0.25 of the V_{OCP} was applied to the thermocell through chronoamperometry, measuring the current. Finally, 0 V was applied to the thermocell and the short-circuit current measured. Then the power of each point was calculated from the equation:

$$Power = Voltage\ x\ Current \quad (12)$$

This resulted in a power curve as shown below for the 0.4 M $K_3/K_4[Fe(CN)_6]$ system at platinum electrodes under a ΔT of 20 K (where T_{hot} was 40°C and T_{cold} was 20°C).

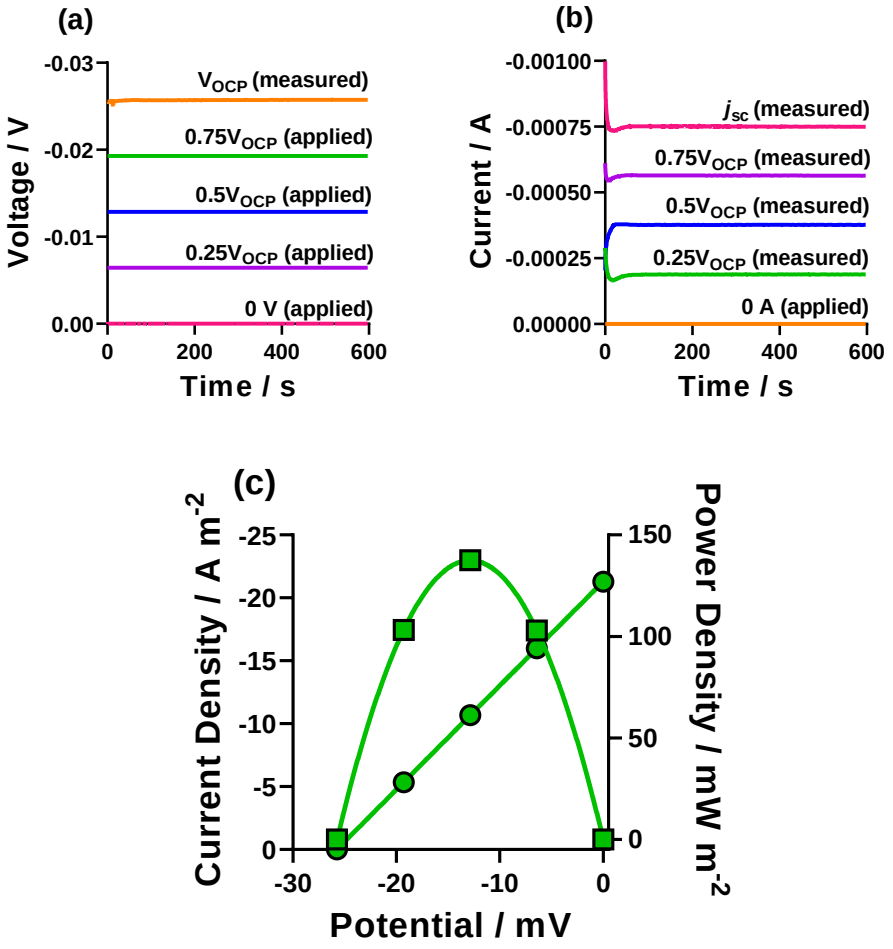

Figure E4 – Figure showing (a) the various voltages (both measured and applied), (b) the various currents (both measured and applied) to a 0.4 M $K_3/K_4[Fe(CN)_6]$ thermocell on Pt electrodes. These measurements combined result in (c) a linear IV curve (circles) and a polynomial power curve (squares).

A note on electrolyte concentration

Throughout this thesis, electrolyte concentration was accurately prepared in molality (mol kg^{-1}), rather than molarity (mol dm^{-3}). It was assumed that this value was not

significantly different to the actual molarity value. In chapter 3, concentrations (in molarity) of electrolytes were needed to be accurately calculated for the specific analysis conducted. Accurate determination of molarity was achieved through measuring the density of the solutions and from this calculating the molarity. It was also found during this analysis that low concentration (*ca.* 400 mM) electrolytes were roughly equivalent in both molarity and molality, therefore our assumption that low concentration electrolytes (in both m and M) are roughly interchangeable was confirmed. This is why molarity is almost always used throughout this thesis rather than molality, unless it is important to distinguish between the two (such as in Chapter 3 when such high concentrations are used).

Chemicals:

All chemicals were purchased from UK suppliers and were used as received; these were:

Chapter 2: Potassium hexacyanoferrate tri-hydrate, (ferrocyanide, $K_4[Fe(CN)_6]$, ≥99.5%, Sigma Aldrich), potassium hexacyanoferrate (ferricyanide, $K_3[Fe(CN)_6]$, ≥99.0%, Sigma Aldrich), lithium chloride (LiCl, Fluorochem), lithium sulphate (Li_2SO_4, 99%+, Acros Organics), sodium chloride (NaCl, ≥99.5%, Sigma Aldrich), sodium sulphate (Na_2SO_4, ≥99.0%, Sigma Aldrich), potassium chloride (KCl, ≥99.0%, Sigma Aldrich), potassium sulphate (K_2SO_4, ≥99.0%, Sigma Aldrich), rubidium chloride (RbCl, Fluorochem), rubidium sulphate (Rb_2SO_4, 99.8%, Sigma Aldrich), caesium chloride (CsCl, Fluorochem) and caesium sulphate (Cs_2SO_4, 99%, Alfa Aesar). All water used was ultra-purified, with a resistivity of 18.2 MΩ cm.

Chapter 3: Potassium ferrocyanide trihydrate, ($K_4[Fe(CN)_6]$, ≥99.5%, Sigma Aldrich), potassium ferricyanide ($K_3[Fe(CN)_6]$, ≥99.0%, Sigma Aldrich), sodium ferrocyanide decahydrate, ($Na_4[Fe(CN)_6]$, ≥99.5%, Sigma Aldrich), rubidium chloride (RbCl, Fluorochem) and caesium chloride (CsCl, Fluorochem), potassium chloride (KCl, ≥99.0%, Sigma Aldrich), potassium sulphate (K_2SO_4, ≥99.0%, Sigma Aldrich), potassium fluoride (KF, Alfa Aesar, 98%), citric acid (≥99.5%, Sigma), and sodium hydroxide (NaOH, pellets, ChemCruz).

Chapter 4: Ammonium iron(ii) sulphate hexahydrate ($([NH_4])_2Fe(SO_4)_2$, ≥98%, Sigma Aldrich), ammonium iron(iii) sulphate dodecahydrate ($[NH_4]Fe(SO_4)_2$, ≥99%, Sigma Aldrich), iron(iii) nitrate nonahydrate ($Fe(NO_3)_3$, ≥99.95%, Sigma Aldrich), iron(ii) sulphate heptahydrate ($FeSO_4.7H_2O$, 99%, Acros Organics), iron(iii) sulphate pentahydrate ($Fe(SO_4)_{1.5}.5H_2O$ 97%, Acros Organics), iron(ii) trifluoromethanesulfonate, ($Fe(CF_3SO_3)_2$, ≥85%, Sigma Aldrich), iron(iii) trifluoromethanesulfonate ($Fe(CF_3SO_3)_3$, 90%, Sigma Aldrich), nitric Acid (HNO_3, 70%, Fisher Scientific), sulfuric acid (H_2SO_4, 1 M volumetric standard, Honeywell), trifluoromethanesulfonic acid (CF_3SO_3H, 98+%, Alfa Aesar).

Chapter 5: Iron(ii) sulphate heptahydrate ($FeSO_4.7H_2O$, 99%, Acros Organics), iron(iii) sulphate pentahydrate ($Fe(SO_4)_{1.5}.5H_2O$ 97%, Acros Organics), sodium sulphate (Na_2SO_4, 98%, Sigma Aldrich), potassium carbonate (K_2CO_3, Santa Cruz Biotechnology) and sodium hydrogen sulphate ($NaHSO_4$, Sigma Aldrich).

Chapter 6: Iron(ii) chloride tetrahydrate ($FeCl_2.4H_2O$, sigma, ≥99.0%), iron(iii) chloride hexahydrate ($FeCl_3.6H_2O$, Honeywell, 97%), iron(ii) sulphate heptahydrate ($FeSO_4.7H_2O$, 99%, Acros Organics), iron(iii) sulphate pentahydrate

($Fe(SO_4)_{1.5}.5H_2O$ 97%, Acros Organics), Acetic acid (Alfa, 99+%), sodium acetate (sigma, ≥99%), malonic acid (Sigma, 99%), sodium malonate dibasic monohydrate (sigma), citric acid (sigma, ≥99.5%), sodium citrate tribasic dehydrate (sigma, ≥99.0%), 2-[(carboxymethyl)amino]acetic acid ($IDAH_2$, Fluorochem), 2,2',2"-nitriloacetic acid ($NTAH_3$, Fluorochem), ethylenediaminetetraacetic acid disodium salt dehydrate ($EDTANa_2H_2$, Sigma, 99.0-101.0%), ethylene glycol-bis(β-aminoethylether)-N,N,N',N'-tetraacetic acid tetrasodium salt ($EGTANa_4$, sigma, ≥97%), diethylenetriaminepentaacetic acid ($DEPTAH_5$, Acros, 98+%), sodium hydroxide (pellets, chemcruz), potassium carbonate, (chemcruz), sodium sulfate (sigma, ≥99.0%) and hydrochloric acid (~37%, fischer).

Synthesis:

Chapter 2, 3 and 5: These chapters were all conducted entirely with commercially available materials.

Chapter 4: This chapter with completed with commercially available materials with the exception of $Fe(NO_3)_2$, which could not be purchased. Since iron(ii) dinitrate was not commercially available, it was synthesised *in situ* by preparing an aqueous solution containing 0.2 M iron(ii) chloride tetrahydrate (≥98%, Honeywell) and 0.4 M silver nitrate (99.5%, Acros Organics). This was stirred overnight until metathesis was complete. The solution was then filtered using a Sartorius biotech Minisart® syringe filter to remove the silver chloride precipitate. Yielding an aqueous solution of 0.2 M iron(ii) nitrate; cyclic voltammetry was used to confirm the absence of residual silver. Subsequently, solid iron(iii) nitrate was dissolved to form a mixture of 0.2 M iron(ii)

nitrate and 0.2 M iron(iii) nitrate, which was used directly. Since iron(ii) nitrate is known to slowly decompose, these solutions were prepared immediately before use.

Chapter 6: Preparation of the Fe(ligand) solutions was achieved using one of the three methods below, all using ultrapure water:

Method 1 (Ac, Mal and Cit): The solutions were prepared from stock solutions of $Fe(ii)Cl_2$ (0.5 M) and $Fe(iii)Cl_3$ (0.5 M), whereas the carboxylic acid and alkali metal carboxylate salts were used as solids; the exception was acetate where the acid was handled as the neat liquid.

Firstly, Fe(ii) (1 mL of 0.5 M stock, 1 equivalent) and Fe(iii) (1 mL of 0.5 M stock, 1 equivalent) were diluted with ultrapure water (8 mL) to form a 10 mL aqueous solution. Initially, the desired carboxylic acid ligand was added as the solid (to make it a 200 mM solution, 2 equivalents per Fe) and stirred until dissolved. Then the corresponding carboxylate ligand was added as a solid (to make it a 200 mM solution, 2 equivalents per Fe). As the ratio of carboxylic acid : carboxylate was varied, the corresponding equivalents were altered by changing the mass of solid(s) added.

Method 2 (IDA only): The solutions were prepared from stock solutions of $Fe(ii)Cl_2$ (0.5 M) and $Fe(iii)Cl_3$ (0.5 M), whereas the IDA carboxylic acid was handled as the solid.

Firstly, Fe(ii) (1 mL of 0.5 M stock, 1 equivalent) and Fe(iii) (1 mL of 0.5 M stock, 1 equivalent) were diluted with ultrapure water. Then, the IDA carboxylic acid ligand was added as a solid (to make it a 400 mM solution, 4 equivalents) and stirred until dissolved, the pre-neutralised IDA-dicarboxylate was then added from a stock solution (1 M). As the ratio of carboxylic acid : carboxylate was varied the various amounts of

added water and neutralised IDA stock were varied to always end up with a 10 mL solution.

Method 3 (NTA, EDTA, EGTA, DEPTA): The solutions were prepared from stock solutions of Fe(ii)Cl_2 (0.5 M), Fe(iii)Cl_3 (0.5 M) and the sodium salt of the carboxylate ligands (1.0 M). This latter solution had to be prepared by stirring the nearly insoluble carboxylic acids in water, and solid NaOH was slowly added; enough NaOH was added to achieve near complete deprotonation (*ca.* 0.95 – 0.99 equivalents of NaOH per RCOOH group), by which point all solid had dissolved to yield a *ca.* 1.0 M solution. Complete neutralisation was avoided due to the sensitivity of the Fe(ii/iii) species to $[OH]^-$.

Firstly, Fe(iii) (1 mL of 0.5 M stock, 1 equivalent) was diluted with ultrapure water. Next, the desired carboxylate ligand was added (2 mL of the 1.0 M stock, 4 equivalents) and stirred, to give an orange solution. Finally, Fe(ii) (1 mL of 0.5 M stock, 1 equivalents) was added with stirring, resulting in a red solution. As the ratio of carboxylate was varied, the relative volume of the 1.0 M stock solution and ultrapure water was varied to adjust the equivalents of carboxylate added to finish with a 10 mL solution.

For the pH optimisation study on Fe(NTA), Fe(EDTA) and Fe(DEPTA), solid K_2CO_3 was added to this solution to achieve the desired pH.

Electrochemical measurements

All electrochemical measurements in all chapters were conducted using a PGSTAT204 potentiostat and NOVA 2.0 software (Metrohm Autolab, the Netherlands).

Quiescent (static) electrochemistry: Quiescent electrochemical experiments were carried out using either a 1.6 mm Au or Pt disc electrode as a working electrode, a 1.6 mm Pt disc as a counter electrode and a 3 M NaCl Ag/AgCl electrode as a reference electrode. All electrodes were purchased from BASi, USA. The various scan rate and solution compositions for each individual experiment are reported in the respective figure legends.

Rotating disc electrochemistry (Chapter 3): Rotating disc electrochemistry was also performed as per the static cyclic voltammetry setup. However, the working electrode was a 3 mm diameter Pt electrode as part of the Autolab RDE module. All displayed measurements were obtained using a rotation speed of 1600 rpm.

Electrochemical impedance spectroscopy:

Electrochemical impedance spectroscopy (ESI) was performed as:

Chapter 4: Electrochemical impedance was performed on solutions of 0.2 M of both Fe(ii) and Fe(iii) in the presence and absence of 1 M conjugate acid in the same setup as thermoelectrochemical measurements in the absence of supporting electrolyte. The impedance measurements were performed by a Solartron 1286/1250 system with Zplot/Zview software (Solartron, UK). The impedance spectra were obtained at the

equilibrium potential with a frequency range from 50,000 Hz to 1 Hz and with an amplitude of 20 mV.

Chapter 5: Electrochemical impedance spectroscopy measurements were carried out using a PGSTAT204 potentiostat with NOVA software (Metrohm, UK). These were performed *in situ* inside the thermocell at non-isothermal temperatures, where ΔT = 20 K (T_h = 40 °C; T_c = 20 °C). EIS was performed on both gold and graphite electrodes. Typically, the hot electrode was employed as the working electrode and the cold electrode employed as the counter electrode, unless otherwise specified (see discussion in the appendix). Impedance spectra was recorded from 20,000 to 0.1 Hz with an amplitude of 10 mV.

Chapter 6: Electrochemical impedance spectroscopy measurements were carried out using a PGSTAT204 potentiostat with NOVA software (Metrohm, UK). These were performed *ex-situ* at ambient temperature (*ca.* 22 °C) using a 1.6 mm Pt disc working electrode, a 1.6 mm diameter Pt disc counter electrode, and an Ag/AgCl (3 M NaCl) reference electrode (all BASi, USA). Impedance spectra was recorded from 20,000 to 0.1 Hz with an amplitude of 10 mV.

All of these measurements were fitted using the same fitting model (shown below in Figure E5). All Nyquist plots and resultant fitting data can also be found in the appendix.

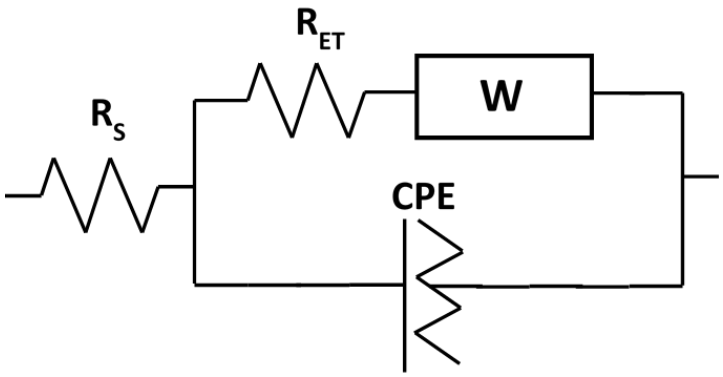

Figure E5 – Model used to fit the Nyquist plots in this thesis, where R_S, R_{ET} and C all correspond to the solution resistance (R_S), electron transfer resistance (R_{ET}) and electrode capacitance (C) (fitted as a constant phase element (CPE)). W here refers to a Warburg element.

UV-Vis:

All UV-Vis spectroscopy measurements were performed using a Cary 100 UV-Vis and WinUV software (Agilent, UK) between 200–800 nm, with a crossover wavelength of 400 nm. The specific details are thus:

Chapter 4: A Quartz cuvette with a path length of 100 μm were used (FireflySci, USA). Temperature was either left at ambient (*ca.* 25 °C) or controlled using an integrated Peltier temperature control block. All spectrums were obtained using solutions containing 20 mM of the Fe(iii) salt only, in the presence and absence of 100 mM of the conjugate acid (*i.e.* a 10-fold dilution of the thermogalvanic solutions).

Chapter 5: A Quartz cuvette with a path length of 100 μm were used (FireflySci, USA). Temperature was left at ambient (*ca.* 20 °C). All spectra were obtained on solutions containing 30 mM of the Fe(iii) sulphate only, in the presence or absence of 75 mM Na_2SO_4, or $NaHSO_4$. (*i.e.* a 10-fold dilution on the thermogalvanic solutions).

Chapter 6: A Quartz cuvette with a path length of 1 mm were used (FireflySci, USA). The temperature was fixed to 20 °C, which is representative of the cold electrode in the thermogalvanic cell. All spectra were obtained using solutions containing either 2.5 mM of the Fe(ii)L, 2.5 mM of the Fe(iii)L or 1.25 mM Fe(ii)L and 1.25 mM Fe(iii)L, where L represents the various ligands investigated in this chapter (*i.e.* a 20-fold dilution of the thermogalvanic solutions).

Conductivity:

The conductivity of each solution was measured using a platinum conductivity electrode (CON-1, cell constant = 10 cm^{-1}, Sciquip UK Ltd, UK). All measurements were performed at ambient temperatures of 22°C.

Density and Viscosity:

Density and Viscosity measurements were performed using a DMA 4100M Density meter and Lovis 2000 M/ME Microviscometer (Anton Paar, UK). All measurements were performed at a temperature of 20°C, as this is the cold electrode (and therefore assumed limiting) temperature in the thermogalvanic cell.

pH:

All pH measurements were taken using a digital pH meter (SciQuip Benchtop 9 Series pH and conductivity meter, SciQuip, UK). These were measured at ambient temperature.

Chapter 2:

Fundamental insights into the $[Fe(CN)_6]^{3-/4-}$ thermogalvanic cell

A fundamental study of the thermoelectrochemistry of ferricyanide/ferrocyanide: temperature, cation, concentration, ratio, and homogeneous electrocatalysis effects in thermogalvanic cells

The results of this chapter have been jointly published in:

Journal of Electroanalytical Chemistry, 2020, **872**, 114280.[3] &

Sustainable Energy and Fuels, 2020, **4**, 7, 3388.[35]

Chapter 2: Fundamental insights into the $[Fe(CN)_6]^{3-/4-}$ thermogalvanic cell

2.1 – Aims and Objectives

In this chapter, there were several main aims and objectives:

- We initially set out to fundamentally investigate a 'model' thermogalvanic cell (the $K_3/K_4[Fe(CN)_6]$ with Pt electrodes) with respect to changing the temperature difference, changing the absolute temperature but maintaining the temperature difference, and altering both the equimolar and non-equimolar (ratio of oxidised : reduced species) concentrations.
- Once this was achieved, we set out to understand the fundamental equations governing thermogalvanic cells; this was undertaken by modelling the outcomes of these investigations for both the thermodynamic (voltage) and kinetic (current) outputs and comparing this modelled data to our experimental results.
- Once the fundamental investigations were complete and the fundamental equations understood, the effect of altering counter-cation on the $[Fe(CN)_6]^{3-/4-}$ redox couple was investigated, with respect to both the electrochemical and thermoelectrochemical effects.
- Finally, we set out to undertake a cost-analysis on selected investigations of these systems, to observe if any benefit in cost can be obtained by altering the parameters.

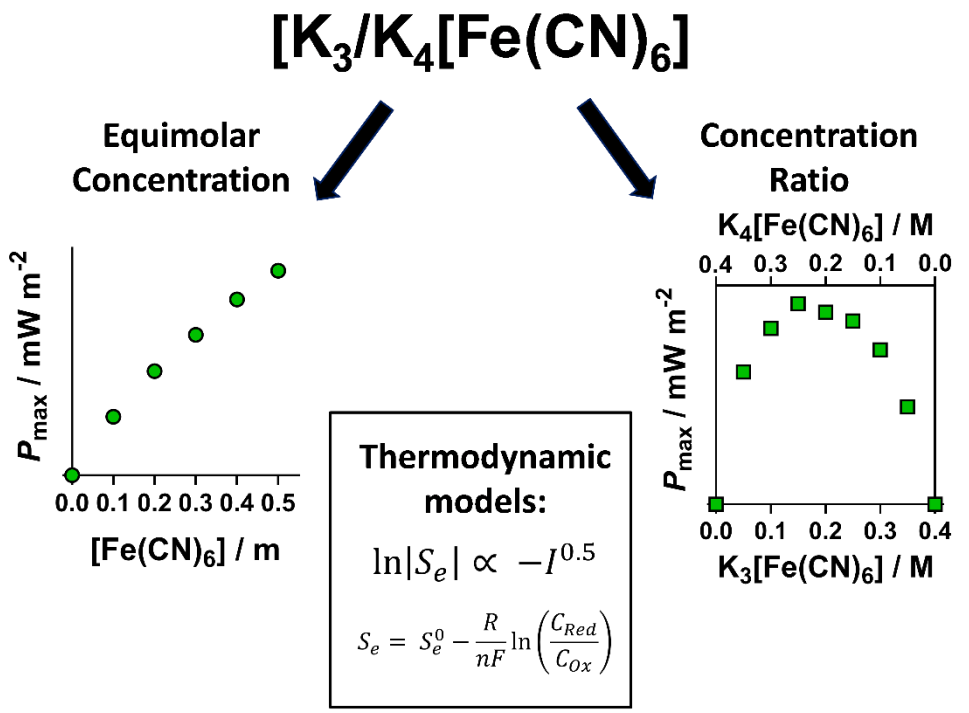

Kinetic model:

$$j_{SC} = k_{agg} F ({C_{Ox}}^{\alpha} {C_{Red}}^{\alpha}) \left(exp \frac{0.5 V_{OCP} \alpha_a nF}{RT_{cold}} \right) - \exp\left(-\left(\frac{0.5 V_{OCP} \alpha_c nF}{RT_{cold}} \right) \right)$$

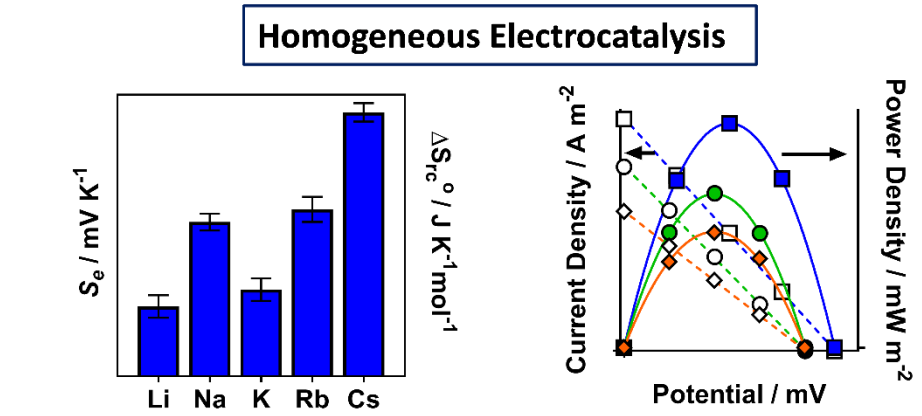

Chapter 2: Fundamental insights into the $[Fe(CN)_6]^{3-/4-}$ thermogalvanic cell

2.2 – Introduction

A plethora of redox couples, thermocell designs, measuring techniques, solvents and temperatures have all been investigated in thermoelectrochemical cells.[24,54,139] All of which have a significant impact on measured thermoelectrochemical properties, namely the Seebeck coefficient (S_e), short-circuit current density (j_{SC}) and maximum power density (P_{max}).

By far the most widely reported redox couple employed in thermo-electrochemical cells is ferricyanide/ferrocyanide ($[Fe(CN)_6]^{3-/4-}$), which is often obtained from the potassium salts.[35] This redox couple is routinely reported as either an aqueous,[31,67] or gelled[14,53] electrolyte. Early reports using this redox couple investigated both the thermodynamics,[141] and kinetics[31,67] in thermogalvanic cells, stating a S_e of -1.4 mV K^{-1}.[67] This redox couple has also been extensively utilised when novel electrode materials have been investigated.[40,93,96,100]

Despite the heavy utilisation of the $[Fe(CN)_6]^{3-/4-}$ redox couple, it is still at the forefront of thermogalvanic cells currently being explored.[17,34,35,95] Recently, two seminal works have been reported using $[Fe(CN)_6]^{3-/4-}$. Firstly, $[Fe(CN)_6]^{3-/4-}$ has been employed as gelled electrolyte in an agar-agar environment, a high concentration of supporting potassium chloride was also present in this thermocell. This has led to a synergistic combination of both Seebeck and Soret effects, culminating in a record high S_e of *ca.* -17 mV K^{-1}.[17]

The other seminal work reported additive electrolytes such as guanidinium in the aqueous $[Fe(CN)_6]^{3-/4-}$ redox couple to induce 'thermocrystallisation'. This

addition has been reported to yield a more modest increase in S_e up to *ca.* -4 mV K^{-1}. This system has been demonstrated as an in-series array (as 20 combined units) to generate 3.1 V, 120 mA and 96 mW at an applied ΔT of 50 K. This high-power output has been shown to power small devices such as an LED array, electric fan, and a thermohydrometer.[34]

There are also numerous other investigations utilising $[Fe(CN)_6]^{3-/4-}$ in thermogalvanic cells, these have mainly been concerned with improving the thermodynamics of the system. This has been proposed to be achieved by addition of organic co-solvent such as methanol or acetone, reporting S_e up to -2.9 mV K^{-1}.[81] However, later, and more thorough investigations have disputed this, demonstrating a much less significant increase and even a significant decrease in observed S_e.[82,94] Addition of supporting electrolyte such as Cs^+ and Rb^+ cations have also been demonstrated to have a synergistic effect on the thermodynamics of the $[Fe(CN)_6]^{3-/4-}$ redox couple, however this report focussed solely on the thermodynamics and did not investigate any kinetic factors.[83]

The $[Fe(CN)_6]^{3-/4-}$ thermocell has also been reported as an example for interesting applications, such as a thermogalvanic force sensor,[137] fast and sensitive surface temperature sensor,[136] and in wearable devices.[14–16] As a result of the extensive research into $[Fe(CN)_6]^{3-/4-}$ thermocells, coupled with the significant discrepancies between different thermocell designs, temperatures and measuring techniques, we therefore set out to conduct a comprehensive electrochemical and thermo-electrochemical investigation of the $[Fe(CN)_6]^{3-/4-}$ redox couple using our thermocell setup. Investigating equimolar and non-equimolar concentration, both absolute

temperature and temperature difference, homogeneous electrocatalysis and both simulating and modelling these experimental outcomes as to definitively determine the fundamental phenomena describing these various fundamental parameters.

2.3 – Results and Discussion

2.3.1 – Temperature effect on 0.4 m $K_3/K_4[Fe(CN)_6]$

There are a wide variety of differences in applied temperature in thermocell reports, both with respect to the temperature difference (ΔT) and the applied temperatures at equivalent ΔT. Previous reports using $[Fe(CN)_6]^{3-/4-}$ thermocells have used temperatures between -40 and >100 °C.[103,118] There has also been reports of 'temperature insensitive power densities', normalised by the square of the temperature difference, reported in W m^{-2} K^{-2} or mW m^{-2} K^{-2}.[17,40,52,93,142]

Initially, the effect of altering temperature difference was measured on the 0.4 M $[Fe(CN)_6]^{3-/4-}$ thermocell. This was achieved by maintaining the cold electrode temperature at 20 °C and increasing the hot electrode from 30 °C to 55 °C in 5 °C increments, increasing the ΔT from 10 to 35 K. The effect of increasing ΔT on the thermogalvanic properties was measured and is shown in Figure 9. From the resultant power curves, the open circuit voltage, short circuit current and power density are all found to increase, as expected. From measuring the change in V_{OCP} (ΔV) with changing temperature (ΔT), the S_e can be determined, as in Equation 1. The observed S_e in our thermogalvanic cell, at this applied temperature was found to be -1.28 mV K^{-1}. Which is lower than the expected and consistently reported -1.4 mV K^{-1}.[35,40,67,93]

Therefore, it was pertinent to investigate the effect of altering applied absolute temperature, whilst maintaining a constant ΔT.

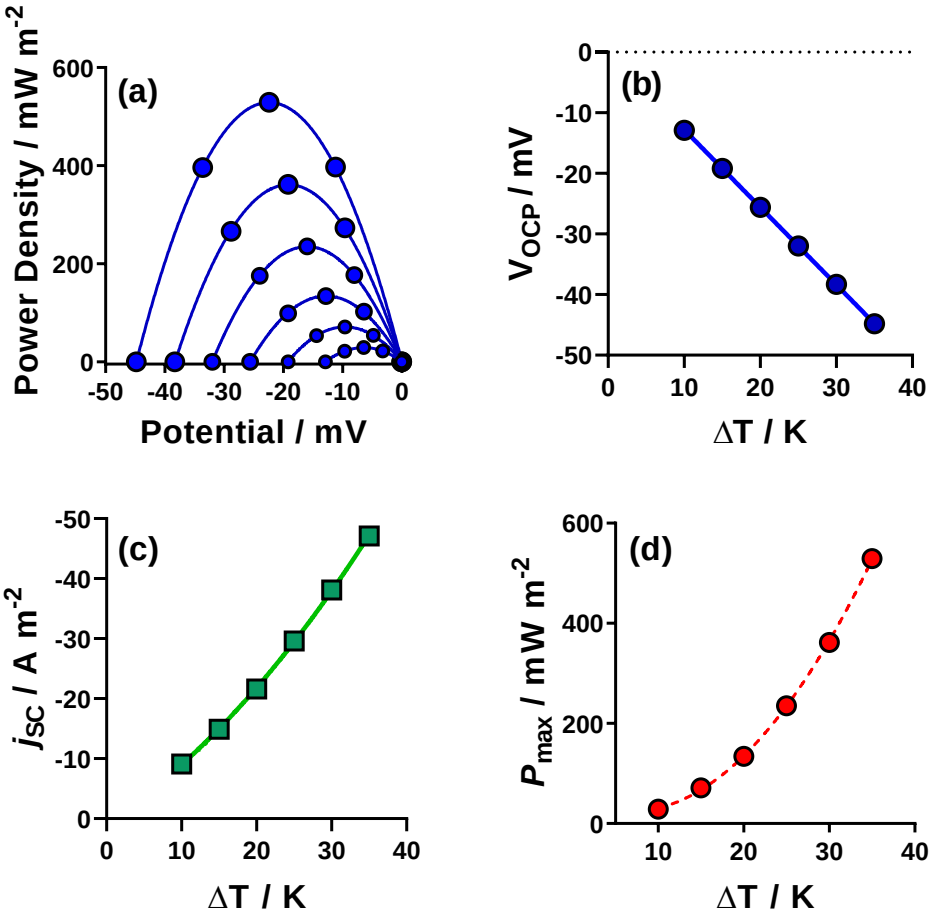

Figure 9 – Figure showing (a) power curves, (b) open circuit potential (V_{OCP}), (c) short-circuit current density (j_{SC}) and (d) maximum power density (P_{max}) of the 0.4 M $[Fe(CN)_6]^{3-/4-}$ thermocell. When the temperature difference (ΔT) between the electrodes was increased from 10 K (from a T_{cold} of 20 °C and a T_{hot} of 30 °C) to 35 K (from a T_{cold} of 20 °C and a T_{hot} of 55 °C).

Applied absolute temperature, whilst maintaining a constant ΔT was achieved by altering the applied temperature of T_{cold} (from 20 – 40 °C) and T_{hot} (from 30 – 50 °C) in parallel (*i.e.* maintaining a constant ΔT of 10 K). Figure 10 shows the effect of

altering applied temperature on the V_{OCP}, j_{SC} and P_{max}. At a T_{hot} and T_{cold} of 20 °C and 30 °C, the observed S_e is -1.23 mV K^{-1} (*ca.* 88% of the expected -1.4 mV K^{-1}). However, upon increasing the applied temperature of T_{cold} and T_{hot} to 40 °C and 50 °C, respectively, the observed S_e increased to -1.33 mV K^{-1} (*ca.* 96% of the expected -1.4 mV K^{-1}). This therefore simply demonstrates that the lower observed S_e in our thermocell is due to temperature loss through our thermocell setup. Interestingly, the current and power densities also significantly increased upon an increase of applied temperature. At a T_{cold} and T_{hot} of 20 °C and 30 °C, the current and power densities were observed as -8.51 A m^{-2} and 26.16 mW m^{-2}, respectively. However, at a T_{cold} and T_{hot} of 40 °C and 50 °C, the current and power densities were observed as -13.12 A m^{-2} and 42.54 mW m^{-2}, respectively, which equates to an increase of 154% and 166%.

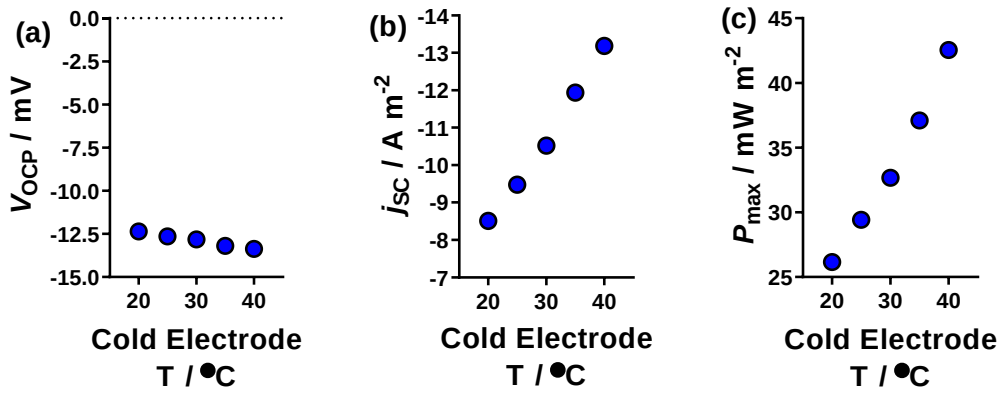

Figure 10 – Plots showing the effect of increasing temperature at a constant ΔT of 10 K on the (a) V_{OCP}, (b) j_{SC} and (c) P_{max}. Temperature was increased from a T_{cold} of 20 to 40 °C and a T_{hot} of 30 to 50 °C.

This increase in current and power, whilst maintaining a constant ΔT is problematic for the routinely reported temperature-normalised power density (mW m^{-2} K^{-2}). This normalisation is based on the assumption that both the V_{OCP} and j_{SC} increase linearly with ΔT. As demonstrated by Figure 9(b), V_{OCP} clearly increases linearly with ΔT. However, we observe here that the current density increases by a factor of 1.3 in Figure 9(c) and is clearly highly dependent on applied temperature, as demonstrated in Figure 10(b). Therefore, we expanded the investigation (Figure 11) for more temperatures and attempted to normalise the resulting data with respect to temperature.

In Figure 11(a & b), the effect of increasing T_{hot} was measured while maintaining T_{cold} at ●, 20 °C, ■, 25 °C and ◆, 30 °C. When the normalisation factor of ΔT^2 was applied, it was not found to accurately normalise the power density, as shown in Figure 11(a). As the current density was found to increase by a factor of 1.3, a new normalisation factor of $\Delta T^{2.3}$ was applied, which was found to accurately normalise the power density (Figure 11(b)). In order to test this theory further, the effect of reducing T_{cold} to increase ΔT was also investigated, where T_{hot} was maintained at ●, 55 °C and ■, 60 °C. Interestingly, the typical normalisation factor of ΔT^2 was found to accurately normalise the power density (Figure 11(c)). This decrease in required normalisation is likely due to the decrease in kinetics at the cold electrode with reducing temperature, which is assumed to be limiting.[35] This additional decrease in limiting electrode is not observed in Figure 11(a & b) due to the cold electrode (and thus the limitation) being constant.

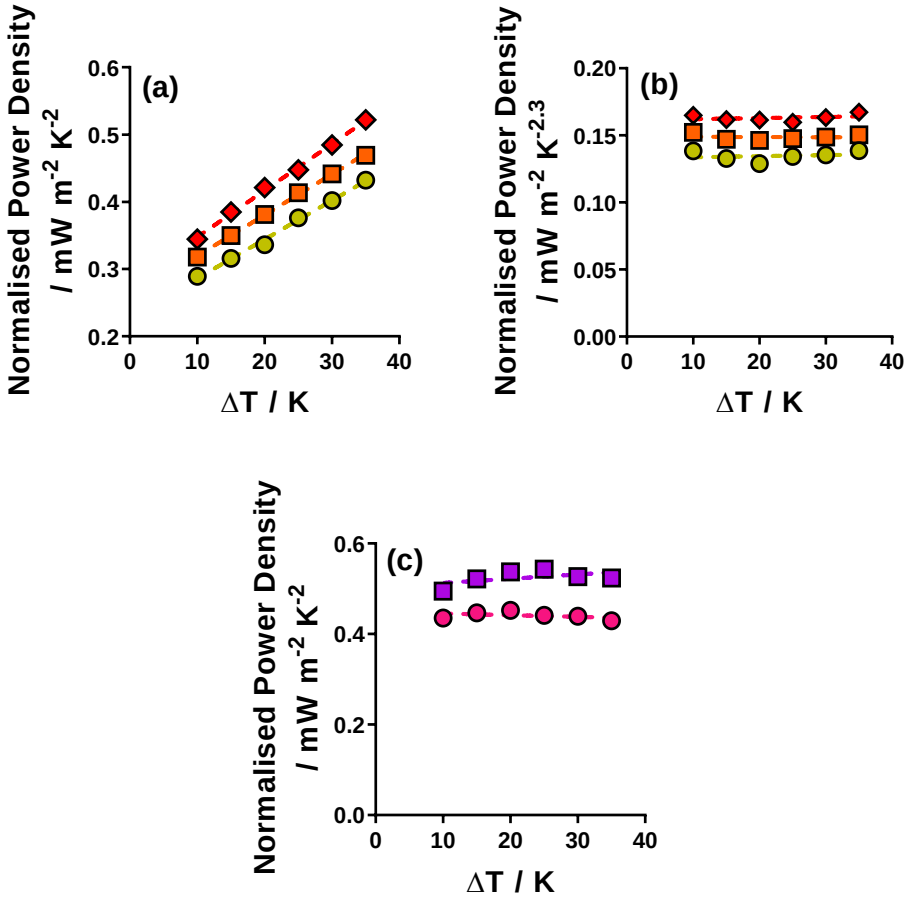

Figure 11 – Figure showing (a & b) data from Figure 9(d) normalised to (a) ΔT^2 and (b) $\Delta T^{2.3}$. Where T_{cold} values were set to ●, 20 °C, ■, 25 °C and ◆, 30 °C and T_{hot} was increased to increase ΔT. Also shown is (c) P_{max} / ΔT^2 where T_{hot} was fixed at ●, 55 °C and ■, 60 °C, and T_{cold} decreased to increase ΔT.

This investigation clearly demonstrates that a 'normalisation' factor of ΔT^2 is not universally valid, but is valid only under certain conditions. The effect of altering temperature clearly has a substantial impact on power generation ability of the thermocell. However, other factors such as thermocell orientation,[33,143] inter-electrode separation,[32] and numerous other factors (both internal and external of the thermocell)

will also have a significant impact on performance. With the effect of temperature critically assessed, the effect of concentration of electrolyte was next investigated.

2.3.2 – Equimolar concentration of $K_3/K_4[Fe(CN)_6]$

Measuring the effect of altering concentration of equimolar $[Fe(CN)_6]^{3-/4-}$ is not a novel investigation and has been reported several times previously.[31,35,67] However, differing measurement times, techniques, and temperatures of the same thermogalvanic cell yield significantly different observed power densities.[3] Therefore, this simple study (increasing $[Fe(CN)_6]^{3-/4-}$ concentration in an equimolar ratio) was investigated here using our thermocell setup.

Initially, the concentration of $[Fe(CN)_6]^{3-/4-}$ was incrementally increased in an equimolar ratio of $K_3/K_4[Fe(CN)_6]$ (in 0.1 M increments) from a total $[Fe(CN)_6]$ concentration of 0.1 to 0.5 M. Figure 12 shows the effect this has on the (a) observed S_e, (b) j_{SC} and (c) P_{max} (tabulated values are shown in Table 1). The benchmark 0.4 M $K_3/K_4[Fe(CN)_6]$ system has been reported to have a Seebeck coefficient of -1.4 mV K^{-1}.[93,102,106,107] We have demonstrated that increasing the applied temperature, at equivalent temperature differences has increased the 'observed S_e' of our 0.4 M $[Fe(CN)_6]^{3-/4-}$ thermocell.[3] This was found to occur by increasing the 'observed temperature difference', and that our thermocell observes a ΔT of 18 K, as opposed to the applied 20 K.[3] All Seebeck coefficients measured have therefore been given a compensation factor of 1.11 to account for this discrepancy in our thermocell design. Figure 12(a) also shows that as the concentration decreases, the observed S_e increases, which is also consistent with previous reports.[35,93,144]

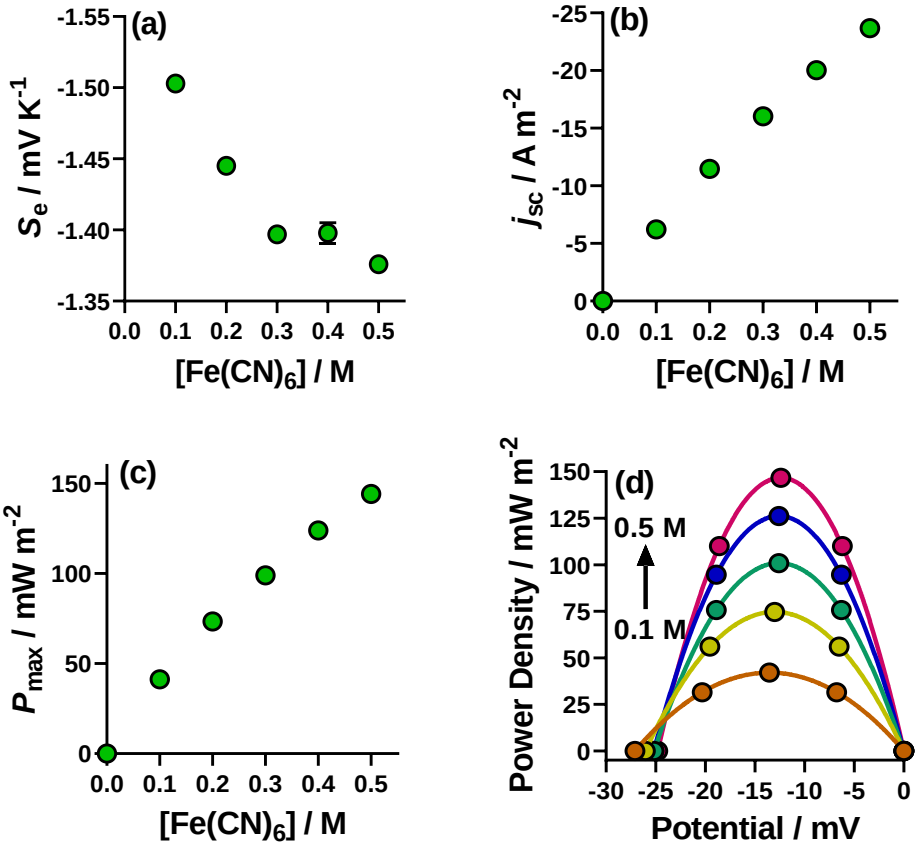

Figure 12 – Figure showing the effect of increasing equimolar $K_3/K_4[Fe(CN)_6]$ in increments of 0.1 m from 0.1 m to 0.5 m total $[Fe(CN)_6]$ concentration has on (a) the S_e, (b) the j_{SC}, (c) the P_{max} and (d) the power curves of each respective system.

Table 1 – Table of data for Figure 12(a-c).

Concentration / M	S_e / mV K^{-1}	j_{SC} / A m^{-2}	P_{max} / mW m^{-2}
0.1	-1.50 ± 0.01	-6.21 ± 0.45	41.3 ± 0.3
0.2	-1.45 ± 0.01	-11.5 ± 0.3	73.3 ± 0.2
0.3	-1.40 ± 0.01	-16.0 ± 0.6	99.1 ± 0.5
0.4	-1.40 ± 0.01	-20.0 ± 0.2	125 ± 2
0.5	-1.38 ± 0.01	-23.7 ± 0.7	144 ± 1

Both current and power densities increased almost linearly with concentration (Figure 12(b & c)), as expected, and previously reported.[67] The power curves of these five systems was calculated using Equation 12 and are shown in Figure 12(d).

$$Power = V.I \tag{12}$$

Having (re)evaluated the effect of equimolar concentration of the $K_3/K_4[Fe(CN)_6]$ redox couple, whilst obtaining equivalent trends to previously reported studies, we can therefore be confident in the robust nature of our thermocell setup and measuring technique (technique of measuring critically assessed and reported previously[3]). This allowed us to conduct a far less common investigation, altering the concentration ratio of $K_3[Fe(CN)_6]$:$K_4[Fe(CN)_6]$.

2.3.3 – Non-equimolar concentration of $K_3/K_4[Fe(CN)_6]$

Equimolar concentration studies of redox couples are common in thermogalvanic reports, not only for the $[Fe(CN)_6]^{3-/4-}$ redox couple, but also for other redox couples such as the $Fe^{2+/3+}$,[15,38,39] and I^-/I_3^-.[145] To date, there has only been a finite number of studies into concentration ratio of a redox couple in thermogalvanic cells, which were all conducted on $[Fe(CN)_6]^{3-/4-}$.[35,95,117,146] These older investigations demonstrate a parabolic curve in both conductivity[117] and power density[146] with altered ratio of redox couple, along with an increased Seebeck coefficient associated with higher $K_4[Fe(CN)_6]$ concentrations.[117] Therefore, this intriguing study was also conducted on our thermocell setup.

The non-equimolar concentration ratio study was conducted using a total concentration of 0.4 M $[Fe(CN)_6]$, which was obtained by altering the ratio of $K_3[Fe(CN)_6]$: $K_4[Fe(CN)_6]$. The respective concentrations were incrementally increased or decreased by 50 mM, to maintain 0.4 M $[Fe(CN)_6]$. Figure 13(a) shows that at higher concentrations of $K_4[Fe(CN)_6]$, we also observe a higher S_e, contrary to the Debye-Hückel relationship which states that increasing ionic strength decreases the Seebeck coefficient (discussed in the next section). It is observed that a general linear decrease in S_e occurs with increasing $K_3[Fe(CN)_6]$ in the ratio.

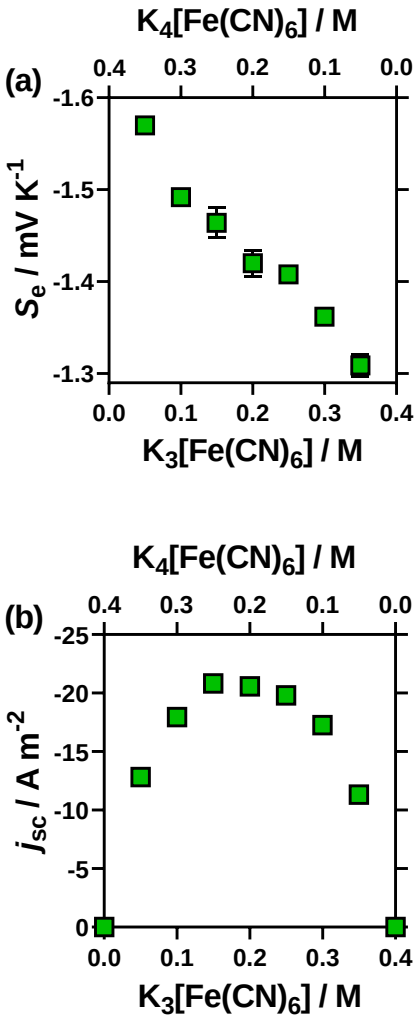

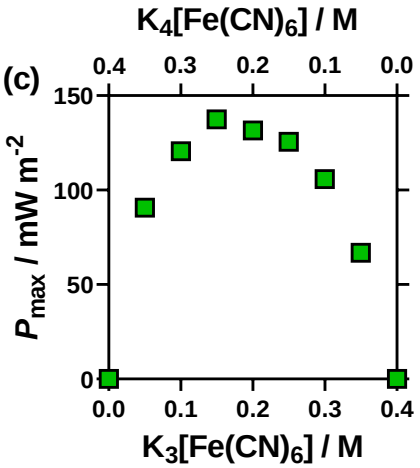

Figure 13 – Figure showing the effect of altering concentration ratio of $K_3[Fe(CN)_6]$: $K_4[Fe(CN)_6]$ has on (a) the S_e, (b) the j_{SC} and (c) the P_{max}, whilst containing a total $[Fe(CN)_6]$ concentration of 0.4 m

With respect to the current and power densities of these systems, they both display parabolic curves, consistent with those previously reported.[146] The current density is generally equivalent to a perfect parabola, where the peak current density is roughly equivalent at ratios of K_3 : K_4 between 0.15 : 0.25 to 0.25 : 0.15 (Figure 13(b)). The power density parabola is more complicated. As power is calculated from both voltage and current, and the voltage increases at higher concentration ratios of $K_4[Fe(CN)_6]$, the peak in power density is centred on a concentration ratio of K_3 : K_4 at 0.15 : 0.25 (Figure 13(c)), not the expected and consistently reported 0.2 : 0.2 M. This is potentially significant as the cost of $K_3[Fe(CN)_6]$ and $K_4[Fe(CN)_6]$ are not equivalent, and could result in a cost-benefit (discussed in section 2.3.7). Tabulated data of Figure 13 is shown in Table 2.

Table 2 – Tabulated data from Figure 13.

$K_3[Fe(CN)_6]$: $K_4[Fe(CN)_6]$ ratio / M	S_e / mV K^{-1}	j_{SC} / A m^{-2}	P_{max} / mW m^{-2}
0.05 : 0.35	-1.57 ± 0.01	-12.8 ± 0.1	90.7 ± 0.6
0.10 : 0.30	-1.49 ± 0.01	-17.9 ± 0.1	120.6 ± 1.2
0.15 : 0.25	-1.46 ± 0.02	-20.8 ± 0.3	137 ± 3
0.20 : 0.20	-1.42 ± 0.01	-20.6 ± 0.3	132 ± 3
0.25 : 0.15	-1.41 ± 0.01	-19.8 ± 0.3	126 ± 2
0.30 : 0.10	-1.36 ± 0.01	-17.3 ± 0.1	106 ± 1
0.35 : 0.05	-1.31 ± 0.02	-11.3 ± 0.2	66.8 ± 2.0

Both these studies yielded interesting results, where the increase in ionic strength of solution can either decrease (equimolar concentration) or increase (non-equimolar concentration) the observed S_e. In order to further understand the governing equations behind both these studies, both the thermodynamics (Seebeck) and kinetics (current) have been modelled and are discussed in turn in the next sections.

2.3.4 – Thermodynamic modelling of the S_e

The equimolar concentration study observed a decrease in Seebeck coefficient with increasing concentration. This is commonly observed in electrochemical systems as a Debye-Hückel relationship,[93,141,144] where a lowering in activity coefficient (γ) is

observed with an increase in ionic strength (I), quantified by Equation 18 (simplified for thermoelectrochemical systems in Equation 19).

$$\ln(\gamma) = -Az_i^2 I^{0.5} \tag{18}$$

$$\ln|S_e| \propto -I^{0.5} \tag{19}$$

Where A is a constant that depends on temperature and z is ionic charge. Figure 14 shows both the equimolar ● and non-equimolar ■ studies shown modelled by Equation 19. It can clearly be seen that the equimolar concentration ratio demonstrates that $\ln|S_e|$ is proportional to $-I^{0.5}$, consistent with the Debye-Hückel relationship. It is also clear that the ratio study follows the opposite trend, where $\ln|S_e|$ actually increases with increasing I. This curious result, which clearly does not fit the same trend, required a different model.

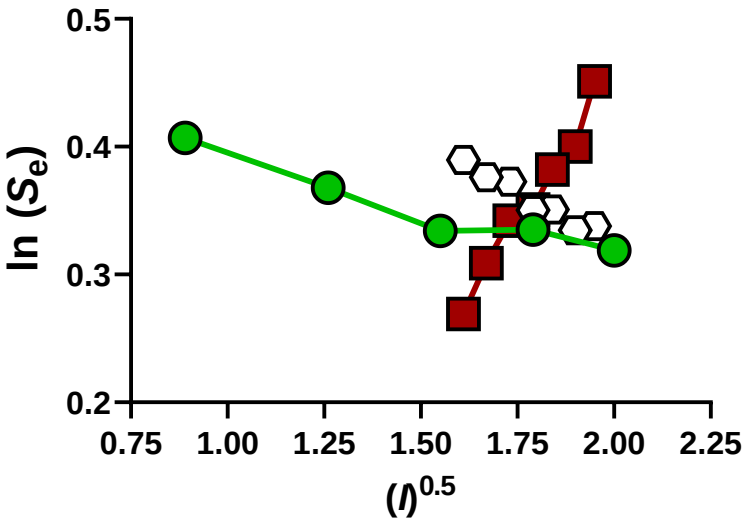

Figure 14 – Figure showing the S_e as a function of ionic strength for the equimolar ● and non-equimolar ■ concentration studies from Figure 12(a) and Figure 13(a), respectively. Also shown is the non-equimolar concentration data with a 'Nernstian-

correction' to account for the non-equimolar nature of the electrolyte (hollow hexagons).

Non-equimolar electrochemical systems are generally described by the Nernst equation (Equation 20), which can account for different concentrations of oxidised and reduced species in the system. This model was therefore adapted to thermoelectrochemical, rather than electrochemical systems (where E_{cell} was substituted to S_e by dividing E_{cell} (as ΔE_{cell}) by T (as ΔT)).

$$E_{cell} = E^0_{cell} - \frac{RT}{nF}\ln\left(\frac{C_{Red}}{C_{Ox}}\right) \quad (20)$$

$$S_e = S^0_e - \frac{R}{nF}\ln\left(\frac{C_{Red}}{C_{Ox}}\right) \quad (21)$$

Where E_{cell} is the cell potential, E^0_{cell} is the standard cell potential, S_e the Seebeck coefficient at any given concentration ratio, S^0_e the standard Seebeck coefficient (taken as the extensively reported -1.4 mV K^{-1}), R the gas constant, T the temperature, n the number of electrons transferred, F the Faraday constant and C_{Red} and C_{Ox} the concentration of reduced and oxidised species, respectively.

As demonstrated in Figure 14, once the Nernstian correction was applied from this model to the ratio study (shown as hollow hexagons), it too followed the expected Debye-Hückel trend of $\ln|S_e|$ being proportional to $-I^{0.5}$. With the success of ascertaining the fundamental parameters guiding the thermodynamic aspects for both the equimolar and non-equimolar concentration studies, the kinetics was then investigated.

2.3.5 – Kinetic modelling of j_{SC}

In an attempt to determine the fundamental phenomena governing the observed kinetics (generating current) of the system, a new model was required. The kinetics of previously reported thermocells has been attributed to the Butler-Volmer model.[91] Therefore, this model was investigated here. The Butler-Volmer equation predicts the current, as a function of exchange current density, based on the overpotential in the system and the reversibility of the redox couple,[80] as in Equation 22.

$$j = j_0 \left(exp \left[\frac{\alpha_a n F \eta}{RT} \right] - exp \left[- \frac{\alpha_c n F \eta}{RT} \right] \right) \quad (22)$$

$$j_0 = F k^0 ({C_{Ox}}^{\alpha} {C_{Red}}^{\alpha}) \quad (23)$$

Where j is the current density, j_0 the exchange current density, α_a and α_c the anodic and cathodic charge transfer coefficients, respectively, n the number of electrons transferred, F the Faraday's constant, η the activation over-potential, R the universal gas constant, T is the temperature, k^0 the electron transfer constant, and C_{Ox} and C_{Red} the oxidised and reduced concentration, respectively. This can be adapted to model the short-circuit current density of the thermocell (j_{SC}) as:

$$j_{SC} = k_{agg} F ({C_{Ox}}^{\alpha} {C_{Red}}^{\alpha}) \left(exp \frac{0.5 V_{OCP} \alpha_a n F}{R T_{cold}} \right) - \exp \left(- \left(\frac{0.5 V_{OCP} \alpha_c n F}{R T_{cold}} \right) \right) \quad (24)$$

Here, the overpotential (η) is expressed as $0.5V_{OCP}$, T was set to the cold electrode temperature, T_{cold}, which is assumed to be kinetically limiting,[35] and the charge transfer constant (α) of the $[Fe(CN)_6]^{3-/4-}$ redox couple, where $\alpha_a = \alpha_c$ was set to 0.5.[147] One important factor to highlight is that the electron transfer coefficient has

been reattributed as an aggregated rate constant k_{agg}, this is to account for all three forms of mass transport (diffusion, migration and convection), along with the fact that steady-state (*operando*) measuring would lead to a non-uniform concentration gradient across the whole system (*i.e.* the electrode surface would have a depleted or enhanced concentration to the bulk of one redox state at one electrode, with the opposite concentration gradient at the opposite electrode). As the k_{agg} is the only unknown in the equation, a value for this aggregated rate constant would need to be determined.

To attain a value for k_{agg}, this model was initially applied to the equimolar 0.2 M $[Fe(CN)_6]^{3-}$ and 0.2 M $[Fe(CN)_6]^{4-}$ system only, to obtain a k_{agg} value that could accurately model this commonly utilised system. The value obtained was 2.06 x10^{-4} cm^2 s^{-1} on the Pt electrodes and was subsequently exclusively employed in this chapter. This value is significantly lower than the literature values reported for k^0 of this redox couple (*ca.* 0.20 to 0.02 cm^2 s^{-1}).[147,148] But is consistent with simulated kinetic rate constants for a cyclic voltammetric study of $[Fe(CN)_6]^{3-/4-}$,[94] and slightly higher than the same model applied on a gasket graphite electrode material.[35] It should also be noted that k^0 is the kinetic rate constant under ideal conditions *i.e.* low concentrations of redox electrolyte with high concentrations of supporting electrolyte, whereas in this report high concentrations of redox electrolyte are used, in the absence of any supporting electrolyte.

With a value obtained for k_{agg} at equimolar 0.4 M $[Fe(CN)_6]^{3-/4-}$, the rest of the concentration study was modelled and as can be seen in Figure 15(a), an excellent fit with the experimental data is obtained. This model can be extended to the experimentally obtained power data, by calculating the power from the measured V_{OCP}

and the modelled j_{SC} values, which is also found to be an excellent fit (Figure 15(b)). To test the validity of the k_{agg} value, and more widely the model as a whole, the equimolar concentration study was used as an example with the same values used in the ratio model. Figure 15(c) demonstrates that the experimental data obtained in the equimolar concentration study can also be successfully modelled. Confirming the validity of the predicted k_{agg} value.

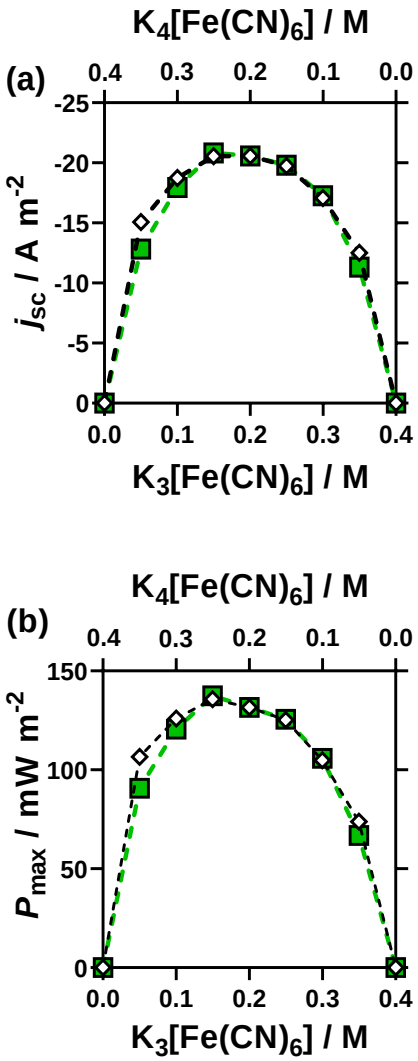

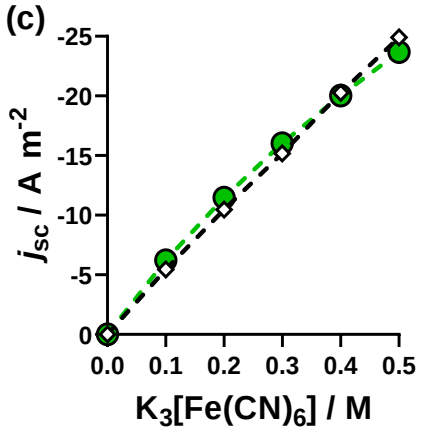

Figure 15 – Figure showing the experimental data (■) of (a) the j_{SC} and (b) P_{max} from the non-equimolar ratio study taken from Figure 13(b) and (c), respectively. The modelled Butler-Volmer values are overlayed (white diamonds). Also shown in (c) is the experimental (●) and modelled (white diamonds) data for the equimolar concentration study (experimental data taken from Figure 12(b)).

2.3.6 – Homogeneous electrocatalysis through alkali metal salts

2.3.6.1 – Electrochemistry

Having investigated and modelled the fundamental driving forces for both the thermodynamics and kinetics of the $K_3/K_4[Fe(CN)_6]$ thermocell at altered concentrations of both equimolar and non-equimolar systems, attempts were then made to improve both of these aspects through homogeneous electrocatalysis.

The $[Fe(CN)_6]^{3-/4-}$ redox couple is known to ion-pair in the presence of high concentrations to alkali metal cations such as K^+.[149] This ion-pairing has previously explained the increasing equilibrium potential (E_{eq}) in fundamental cyclic voltametric investigations.[149] Recently, an investigation into altering the alkali-metal cation in the $[Fe(CN)_6]^{3-/4-}$ redox couple has been reported. This work demonstrated that by

changing the alkali-metal cations down group 1, the ΔS_{rc} of these systems increased. However, this was purely a thermodynamic investigation and offered no insight into the kinetics. We therefore set out to test both the thermodynamic and kinetic effects of altering the alkali-metal cation using all 5 of the group 1 metals (Li, Na, K, Rb & Cs) in a thermogalvanic context.

This was initially investigated in an electrochemical context, cyclic voltammograms of 10 mM concentration of $K_3/K_4[Fe(CN)_6]$ were measured in the presence of a large excess of alkali-metal salts (namely 0.4 M X_2SO_4). This can therefore be essentially viewed as the Li, Na, K, Rb and Cs equivalents of $[Fe(CN)_6]^{3-/4-}$.

Firstly, the E_{eq} was measured, and found to significantly increase whilst decreasing down group 1 (from Li to Cs, Figure 16(b)). This is strongly suggesting an increase in ion-pairing in the presence of larger, less charge dense Cs^+ cations than in the presence of smaller, highly charge dense Li^+ cations. Secondly, the ΔE was taken from the CVs, and was found to generally decrease down the group (Figure 16(c)), which is indicative of faster redox kinetics at the electrode surface.

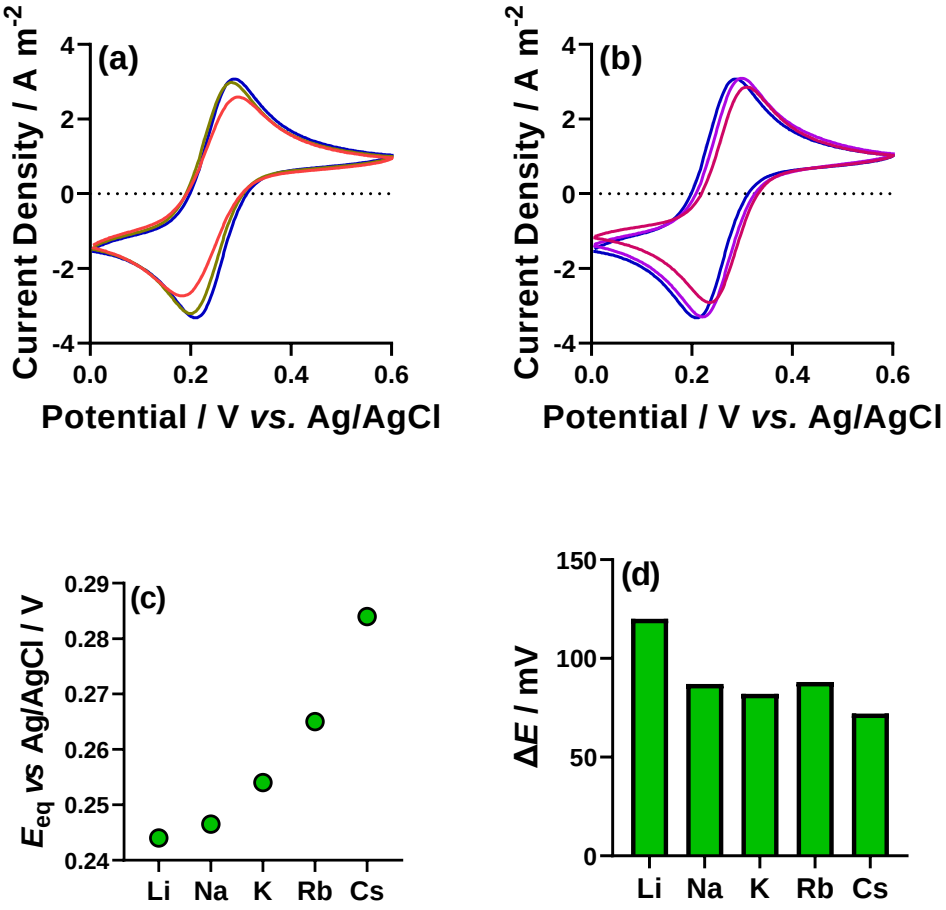

Figure 16 – Figure showing (a & b) CVs of 10 mM $K_3/K_4[Fe(CN)_6]$ in the presence of 0.4 M X_2SO_4 (yellow, dashed line), where in (a) Li (red), Na (yellow) and KCl (blue) are shown and in (b) K (blue), Rb (purple) and CsCl (pink) are all shown. Also shown are (c) the measured E_{eq} and (d) the measured ΔE of each alkali metal salt system taken from the CVs.

With very encouraging indications of electrocatalytic ion pairing down group 1, these systems were measured for their thermoelectrochemical properties, which are discussed further below.

2.3.6.2 – Thermoelectrochemistry

It has previously been reported that altering the alkali metal cation has a beneficial effect on the redox entropy of the $[Fe(CN)_6]^{3-/4-}$ redox couple, down group 1.[83] Having already observed the electrocatalytic effect of this trend in the electrochemistry (*vide supra*) the thermoelectrochemical properties of these systems were measured. This was initially measured purely in a thermodynamic context. The Seebeck coefficient was measured by measuring the open circuit voltage whilst altering the difference in temperature between the two electrodes, starting with a ΔT of 20 K, reducing this to 0 K in 5 K increments, and re-increasing the ΔT back to 20 K.

For this study, the *pseudo*-alkali metal cation $[Fe(CN)_6]^{3-/4-}$ was again achieved by having a large excess of alkali metal salt combined with lower concentrations of $K_3/K_4[Fe(CN)_6]$.* Figure 17(a) shows the observed S_e for each alkali-metal cation in the presence of the alkali metal chloride (blue, left) and sulphate (purple, right) respectively. The trend experimentally observed here does not correlate perfectly with those observed previously,[83] as the Na^+ observes a higher S_e than the K^+. However, it must be noted that this system contains a combination of K^+ and Na^+, and this combination is known to have a beneficial effect to the redox entropy of this redox couple.[94] Tabulated values of the S_e and corresponding ΔS_{rc} are shown in Table 3.

* This excess was achieved through having 10 mM $K_3/K_4[Fe(CN)_6]$ and either 0.4 M or 1 M of the chloride or sulphate salt of the alkali metal cation, respectively. Yielding a ratio of 23:1 and 29:1 for alkali metal cation : inherent potassium for the chloride and sulphate salts, respectively.

As mentioned, the previous investigation into the redox couple with different alkali metal cations only interrogated the redox couple entropy.[83] Therefore, we set out to perform a novel investigation into these systems by investigating the thermogalvanic power density. As both the kinetics (as observed by the electrochemistry Figure 16) and the thermodynamics (as observed by the S_e, Figure 17(a)) both improved by altering the alkali-metal cation down group 1, the power was also expected to increase.

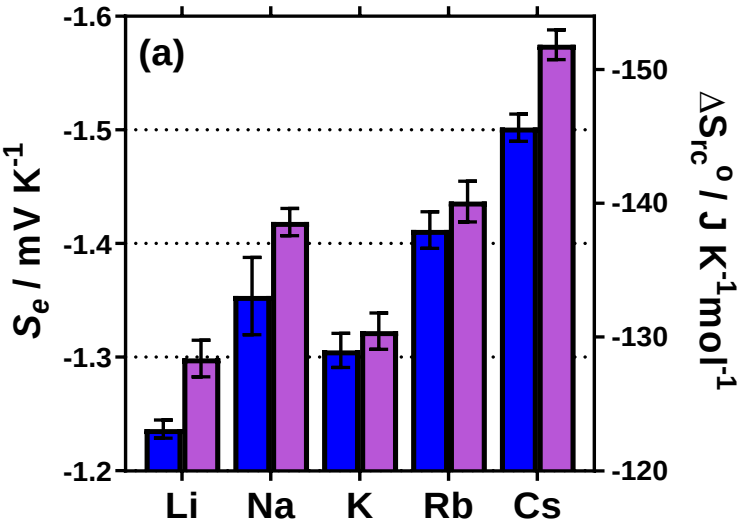

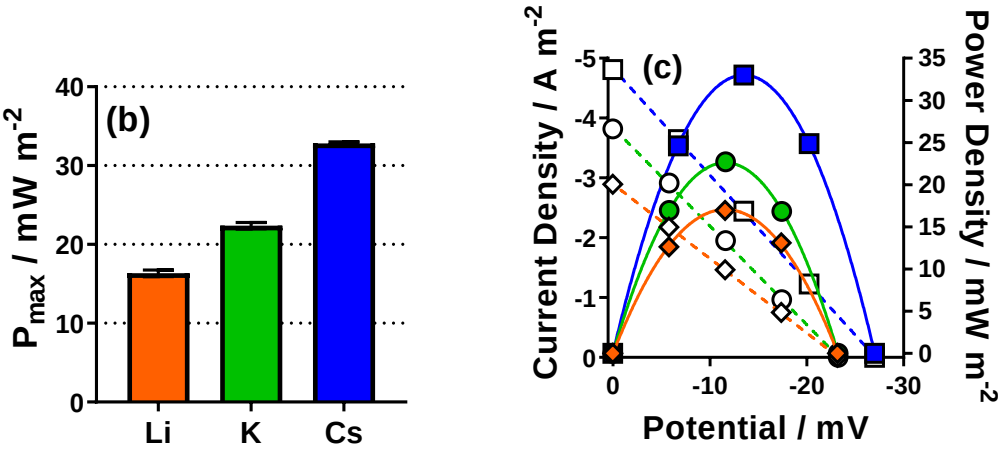

Figure 17 – Figure of (a) the measured S_e of the $K_3/K_4[Fe(CN)_6]$ with a large excess of XCl (blue, left) or X_2SO_4 (purple, right) for each alkali-metal cation. (b) the P_{max} of the Li, K and Cs $[Fe(CN)_6]^{3-/4-}$ systems generated from a large excess of alkali-metal cations from addition of either Li, K or Cs chloride, and (c) representative power curves for (b) where the Li system (diamond) K system (circle) and Cs (square) are all shown. The coloured shapes represent the power density, and the hollow shapes represent the current density, respectively.

Table 3 – Tabulated of data from Figure 17(a).

Alkali Metal	S_e (XCl Salt) / mV K^{-1}	ΔS_{rc} / J K^{-1} mol^{-1}	S_e (X_2SO_4 Salt) / mV K^{-1}	ΔS_{rc} / J K^{-1} mol^{-1}
Li	-1.30 ± 0.02	-129 ± 2	-1.24 ± 0.01	-123 ± 1
Na	-1.42 ± 0.01	-141 ± 1	-1.35 ± 0.03	-134 ± 2
K	-1.32 ± 0.02	-131 ± 1	-1.31 ± 0.02	-130 ± 1
Rb	-1.44 ± 0.02	-142 ± 2	-1.41 ± 0.02	-140 ± 2
Cs	-1.58 ± 0.01	-156 ± 1	-1.50 ± 0.01	-149 ± 1

This different investigation was undertaken with a larger concentration of $K_3/K_4[Fe(CN)_6]$ (50 mM) in the presence of 1.5 M LiCl, KCl or CsCl. Figure 17(b) demonstrates that the expected increase in power density down group 1 is indeed observed, as shown by the *pseudo*-Li, K and Cs $[Fe(CN)_6]^{3-/4-}$ systems. The power curves also show this trend (Figure 17(c)), but as the output voltage is proportional to the S_e, the power curve of the Cs system has both a higher output voltage and power density, demonstrating both enhanced thermodynamic and kinetic effects from the presence of Cs^+ cations.

Having fundamentally investigated the $[Fe(CN)_6]^{3-/4-}$ redox couple for concentration and homogeneous electrocatalysis effects, a provisional cost-comparison of the equimolar, non-equimolar and electrocatalysis effects have been investigated and are discussed further below.

2.3.7 – Cost-comparison of relative $[Fe(CN)_6]^{3-/4-}$ systems

The primary motivation behind the ratio study was to understand if the almost exclusively employed equimolar 0.2 M $K_3[Fe(CN)_6]$: 0.2 M $K_4[Fe(CN)_6]$ generated the highest power density. This assumption was not actually observed, due to the higher S_e with increasing $K_4[Fe(CN)_6]$, producing a higher overpotential driving slightly higher power density in the $K_4[Fe(CN)_6]$-rich systems. This non-ideality in polynomial power density could potentially have other important implications, such as a more cost-effective ratio of obtaining power density than the equimolar universally employed 0.2 : 0.2 M.

This was investigated using the observed absolute power (in mW) of the ratio study from Figure 13. Using the cost per weight of $K_3[Fe(CN)_6]$ and $K_4[Fe(CN)_6].2H_2O$ from Sigma Aldrich.[†] Figure 18 shows the cost analysis in £ / mW for each ratio using two different grade reagents, each one of which favours the opposite redox state as the cheaper one (orange hexagon for ACS grade and blue diamond for ReagentPlus grade, respectively). Both of these therefore show a cost-benefit favouring either a higher $K_3[Fe(CN)_6]$ or $K_4[Fe(CN)_6]$ system, respectively.

Using the best cost of the two different grades analysed allowed further cost-effectiveness to be obtained in the ratio analysis. This analysis also shown in Figure 18 displays the same trend as the observed power ratio study, where a small ratio in favour of the $K_4[Fe(CN)_6]$ was found to be the most cost-effective system.

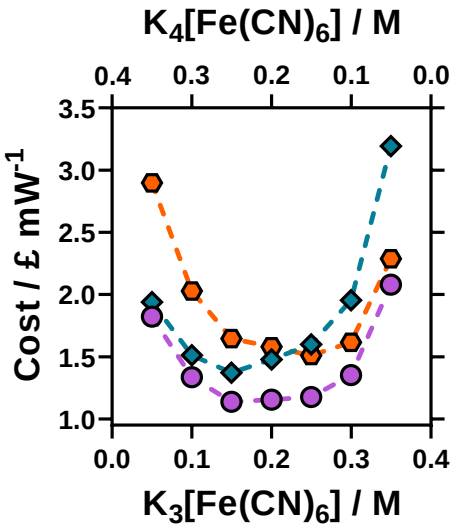

Figure 18 – Figure showing the cost-effectiveness of the power densities of the ratio study shown in Figure 13, showing the cost of each ratio using the ACS (orange

[†] This was done using both the ACS reagent and the ReagentPlus grades, as these had significantly different £ / g of the $K_3[Fe(CN)_6]$ (0.136 and 0.222 respectively) and the $K_4[Fe(CN)_6].2H_2O$ (0.222 and 0.134, respectively).

hexagons) and ReagentPlus (blue diamonds) grades from Sigma Aldrich as of 26th December 2020. Also shown is the most cost-effective of these two reagent grades for the $K_3[Fe(CN)_6]$ and $K_4[Fe(CN)_6].3H_2O$ (purple circles).

One final cost-analysis was undertaken with these systems, it was clearly demonstrated that addition of Cs salts increased both the thermodynamics and kinetics of the $K_3/K_4[Fe(CN)_6]$ thermocell. So a cost-analysis of the $K_3/K_4[Fe(CN)_6]$ system was undertaken in the presence of 0.7 M CsCl. As expected, the power density increased from 124 ± 2 mW m^{-2} to 153 ± 1 mW m^{-2} upon addition of the Cs salt. However, CsCl is expensive, and the cost per mW increased from *ca.* 2 £ mW^{-1} to *ca.* 16 £ mW^{-1}. This final analysis clearly demonstrates that increases in power are not necessarily cost-competitive and should be approached with caution when attempting to scale-up this type of system.

2.4 – Conclusions

To conclude, herein a fundamental study of potassium ferri/ferrocyanide ($K_3/K_4[Fe(CN)_6]$) was conducted. This was undertaken with respect to both equimolar and non-equimolar concentration studies, and the effect of introducing alkali-metal salts into the system for their homogeneous electrocatalytic ability. In these systems, the Seebeck coefficient can be modelled by the Debye-Hückel relationship once a Nernstian correction has been applied to the non-equimolar study. The current generating ability of these systems can be modelled using the Butler-Volmer equation, where an aggregated rate constant (k_{agg}) for the *operando* thermocell was found to be 2.06 $x10^{-4}$ cm^2 s^{-1} at Pt electrodes, which is consistent with previous investigations at gasket graphite electrodes, and the k^0 of simulated cyclic voltammograms (CVs).

The observed S_e, current density and power density of the system can be significantly improved upon addition of electrocatalytic alkali-metal cations such as Rb^+ or Cs^+. This increase was also observed in the E_{eq} of the CVs which increased in the same order as group 1, namely Li < Na < K < Rb < Cs. Finally, a provisional cost-comparison was drawn between the ratio study, using a variety of price and grade materials. The most cost-effective system was found to be simply the most powerful, namely 0.15 M $K_3[Fe(CN)_6]$: 0.25 M $K_4[Fe(CN)_6]$. A further cost-analysis demonstrated that despite the higher power density of the Cs^+-enhanced system, the high price of Cs salts was significantly detrimental to cost-effective power density.

Chapter 3:

Inherent limitations with concentration

Inherent limitations in redox-active 'water-in-salt' electrolytes: Using the thermoelectrochemistry of $[Fe(CN)_6]$ as a model example

The results of this chapter have been published in:

Cell Press Journal: *Cell Reports Physical Sciences*, 2021, 2, 100510.[94]

3.1 – Aims and Objectives

In the previous chapter, a concentration study of both equimolar and non-equimolar ratios of the $K_3/K_4[Fe(CN)_6]$ redox couple was investigated. With respect to increasing equimolar concentration, both current and power density was found to linearly increase with concentration (Figure 12), while the observed S_e was found to decrease proportionately to the square root of the ionic strength. The $K_3/K_4[Fe(CN)_6]$ system is the most widely employed redox couple in thermocells and is routinely employed when novel electrode materials are the focussed area of research.[40,52,93,96,100] This is due to the $[Fe(CN)_6]^{3-/4-}$ redox couple still being state-of-the-art, despite being first investigated in the 1960s and 1970s.[60,67]

Therefore, in this chapter we set out to achieve:

- The highest concentration of $[Fe(CN)_6]^{3-/4-}$ in a thermogalvanic cell.
- To investigate the fundamental physiochemical, electrochemical and thermoelectrochemical properties of these highly concentrated 'salt-in-water' and beyond the 'water-in-salt' transition.
- To understand why there was an observed plateau in power density, quiescent and rotating disc cyclic voltametric current density and conductivity. This inherent limitation observed by several significantly different methods was further investigated for diffusion coefficients of the redox species.
- Attempts to overcome this inherent limitation by several methods i) introducing electrocatalytic alkali-metal cations, ii), introducing less viscous organic co-solvent or iii) inducing mass convection within the thermocell were all ultimately unsuccessful.

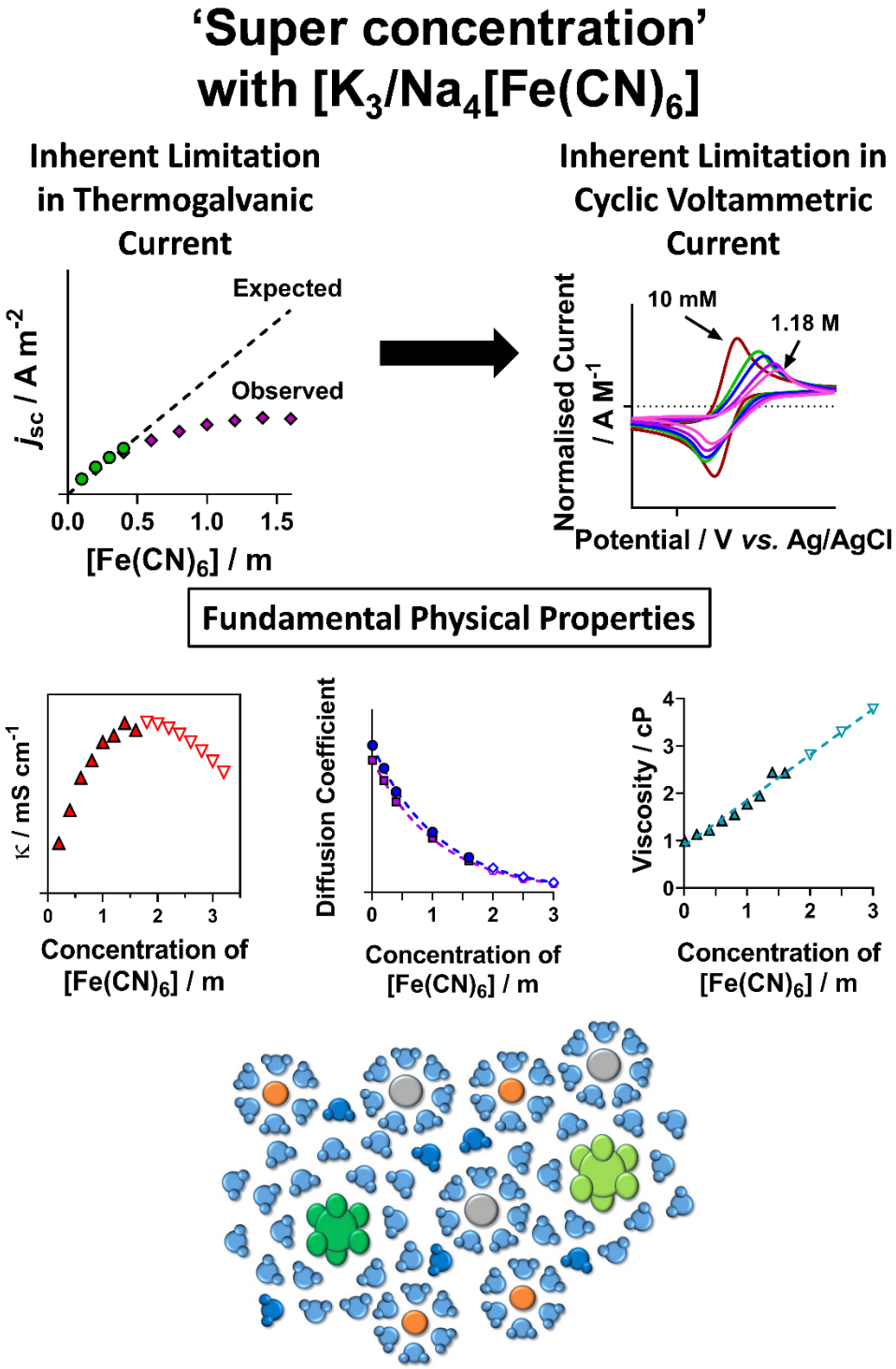
'Super concentration'
with [K3/Na4[Fe(CN)6]
Inherent Limitation in Thermogalvanic Current
Expected
Observed
jsc / A m-2
0.0 0.5 1.0 1.5
[Fe(CN)6] / m
Inherent Limitation in Cyclic Voltammetric Current
10 mM
1.18 M
Normalised Current / A M-1
Potential / V vs. Ag/AgCl
Fundamental Physical Properties
κ / mS cm-1
Concentration of [Fe(CN)6] / m
Diffusion Coefficient
Concentration of [Fe(CN)6] / m
Viscosity / cP
Concentration of [Fe(CN)6] / m

3.2 – Introduction

The previous chapter described a fundamental investigation of the $K_3[Fe(CN)_6]/K_4[Fe(CN)_6]$ redox couple, which has been extensively discussed in the introduction of the previous chapter and will not be repeated here. This salt combination has been extensively employed as 0.4 M $[Fe(CN)_6]$, due to the solubility limit of the $K_4[Fe(CN)_6]$ salt.[35] Concentrations of $[Fe(CN)_6]$ have been increased to 0.9 M by utilising a combination of the $K_3[Fe(CN)_6]$ and $[NH_4]_4[Fe(CN)_6]$.[39,40] Although in most of the reported $[Fe(CN)_6]^{3-/4-}$ thermocells, it is unclear from the sample preparations whether this is genuine molarity or molality.

We have previously reported the potentially hazardous nature of the acidic n-type $Fe^{2+/3+}$ system utilised in series with the p-type $[Fe(CN)_6]^{3-/4-}$, due to the possibility of these solutions mixing and the instability of $[Fe(CN)_6]$ to acidic conditions.[30] Which could result in significant quantities of severely toxic $HCN_{(g)}$[30] (discussed further in Chapter 5). Due to this inherent acidic instability, the utilisation of $[NH_4]_4[Fe(CN)_6]$ yields an inherently hazardous, rather than potentially hazardous system.[30] A combination of K^+ and Na^+ salts offer a benign alternative. The combination of K^+ and Na^+ cations have previously demonstrated a significant increase in solubility for the $[Fe(CN)_6]^{4-}$ anion, for energy storage applications.[150] Another $[Fe(CN)_6]^{3-/4-}$ thermocell has been reported for 'beyond-saturated' concentrations in the presence of salts such as guanidinium, which results in selective 'thermocrystalisation' of the $[Fe(CN)_6]^{4-}$ ion, which re-dissolves at the higher temperature in a thermocell as the $[Fe(CN)_6]^{3-}$, yielding high S_e and power densities.[34]

Concentration effects of redox couples in thermocells are routinely investigated, where high concentrations of commonly employed redox couples have been reported up to 1.5 M using $Fe(ClO_4)_{2/3}$[38,39] and 2 M for $Fe(Cl)_{2/3}$.[15] However, as these ions have an ionic charge > 1, the ionic strengths of these systems are significantly higher. The ionic strength of a 1.5 M $Fe(ClO_4)_{2/3}$ and 2 M $Fe(Cl)_{2/3}$ are 6.75 M and 9 M respectively. Other fundamental properties of the high-concentration $Fe^{2+/3+}$ thermocells have also been investigated, such as the ionic and thermal conductivities.[38]

This high ionic strength is comparable to recently reported 'water-in-salt' solutions, which have been proposed for energy storage applications, namely, aqueous lithium-ion batteries.[151–153] Reported 'water-in-salt' systems have used alkali metal salts such as Li^+,[151,152] and Na^+.[152] Recently, a 'water-in-salt' system has been reported using the redox active $K_3[Fe(CN)_6]$ as an electrochemical probe for a high concentration of KF (up to 17 M).[154] This investigation reports that at the 'salt-in-water' to 'water-in-salt' transition, the diffusion coefficient of the redox-active $[Fe(CN)_6]^{3-}$ species is severely decreased, due to a significant increase in viscosity.[154]

Despite many investigations into 'water-in-salt' systems using low charge metal salts, and several investigations into high charge salts at high concentrations. There is still a missing link between 'water-in-salt' solutions obtained from high charge redox active electrolytes. We therefore set out to undertake a fundamental investigation of high-concentration, high charge, redox active electrolyte, namely the $[Fe(CN)_6]^{3-/4-}$.

3.3 – Results and Discussion

3.3.1 – Effect of increasing concentration on the thermoelectrochemical properties

We set out to undertake further fundamental investigations of a thermogalvanic cell, this time at the super-concentrated electrolyte region (within the total saturation limit). This was undertaken by using the combination of $K_3[Fe(CN)_6]$ and $Na_4[Fe(CN)_6]$ to dissolve high-concentration solutions. Ultimately this was successful, where a total concentration of 1.6 m‡ $[Fe(CN)_6]$ was achievable using mechanical stirring. The thermoelectrochemical properties of increasing concentration of equimolar $K_3/Na_4[Fe(CN)_6]$ was investigated, increasing incrementally in 0.2 m intervals from 0.2 m to 1.6 m total $[Fe(CN)_6]$ concentration.

As the previous equimolar investigation demonstrated that both current and power density increased proportionately to concentration,[35] this was also expected to occur here. Therefore, increasing the concentration from 0.5 m (from the $K_3/K_4[Fe(CN)_6]$ in the previous chapter) to 1.6 m (maximum concentration achieved with the $K_3/Na_4[Fe(CN)_6]$) would be assumed to increase the power density by >3 times. However, this was not the case.

With respect to the S_e, the general decrease with increasing concentration was again observed (Figure 19(a)). However, the S_e of the K_3/Na_4 combination was found to be consistently higher than the equivalent K_3/K_4 combination, consistent with our previous results.[35] With respect to the current density, at lower concentrations the

‡ Molality (g kg^{-1}) has been used as a measure of concentration here due to the ease of sample preparation, more accurate concentrations in molarity (mol dm^{-3}) has been calculated from the density and are discussed in turn.

expected proportional increase was observed. Although, at higher concentrations this proportionality was reduced, reaching a plateau *ca.* 1.4 m (Figure 19(b)).

Figure 19(c) shows the power density of these solutions mirroring the plateau of the current density, observing a plateau *ca.* 1.2 – 1.6 m concentration of $[Fe(CN)_6]$. Also shown in Figure 19(c) is the increase in power density expected if the proportional increase with respect to K_3/K_4 equimolar concentration was observed (shown as a dotted line). This increase in power density would result in an expected 495 mW m^{-2} at 1.6 m. The actual power observed was 203 mW m^{-2}, only 41% of the expected value. The power curves obtained from 0.4 m K_3/K_4 and 1.6 m K_3/Na_4 are also shown in Figure 19(d). Tabulated values of the S_e, j_{SC} and P_{max} of all concentration solutions of $K_3/Na_4[Fe(CN)_6]$ are shown in Table 4.

This significant reduction in power density between the expected increase and the actual observed value is intriguing, this plateau in power density has also been observed previously in $Fe^{2+/3+}$ systems.[15,38] However, the $Fe^{2+/3+}$ redox couple is known to be significantly affected by pH and presence of anions in the solution.[36] The Fe^{3+} ion is also known to be highly reactive to the solvating H_2O molecules, hydrolysing the inner solvation sphere[36,39] (these aspects are all discussed further in chapters 4, 5 and 6). The $[Fe(CN)_6]^{3-/4-}$ redox couple is known to be far more inert with respect to these factors, therefore it is interesting that this redox couple also observes this behaviour, and requires further investigation into the fundamental physical and electrochemical properties.

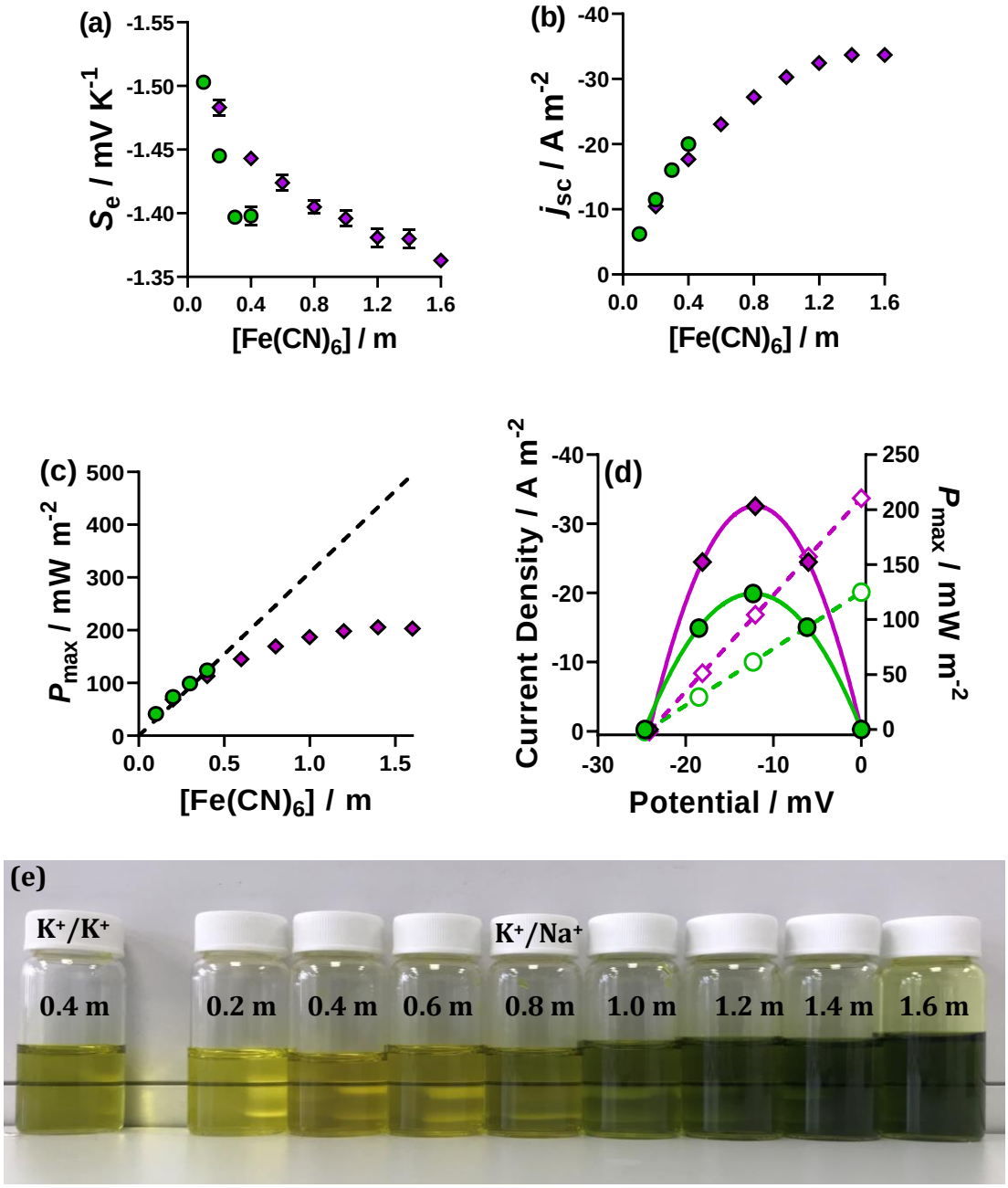

Figure 19 – Figure showing (a) the observed S_e, (b) the j_{SC} and (c) the P_{max} of the $K_3[Fe(CN)_6]/Na_4[Fe(CN)_6]$ redox couple increasing incrementally (in 0.2 m increments) from 0.2 to 1,6 m total $[Fe(CN)_6]$ concentration, alongside the $K_3/K_4[Fe(CN)_6]$ data from the previous chapter. Also shown in (d) is representative power curves of the 0.4 m $K_3/K_4[Fe(CN)_6]$ (●) and the 1.6 m $K_3/Na_4[Fe(CN)_6]$ (◆) where power is filled and current is hollow and (e) an image of the various concentration $K_3/Na_4[Fe(CN)_6]$ solutions.

Table 4 – Tabulated values of Figure 19(a-c)

Concentration / m	S_e / mV K^{-1}	j_{SC} / A m^{-2}	P_{max} / mW m^{-2}
0.2	-1.48 ± 0.01	-10.4 ± 0.1	69.5 ± 0.4
0.4	-1.44 ± 0.01	-17.7 ± 0.1	113 ± 1
0.6	-1.42 ± 0.01	-23.1 ± 0.3	145 ± 3
0.8	-1.41 ± 0.01	-27.2 ± 0.3	169 ± 2
1.0	-1.40 ± 0.01	-30.3 ± 0.3	187 ± 3
1.2	-1.38 ± 0.01	-32.4 ± 0.5	198 ± 4
1.4	-1.38 ± 0.01	-33.7 ± 0.3	206 ± 2
1.6	-1.36 ± 0.01	-33.7 ± 0.3	203 ± 3

3.3.2 – Static electrochemistry

In order to gain further insight into these various concentration $[Fe(CN)_6]^{3-/4-}$ systems, we investigated their electrochemical properties. Cyclic voltammograms (CVs) were recorded for the 0.01, 0.1, 0.2, and 0.4 m $K_3/K_4[Fe(CN)_6]$ and 0.01, 0.2, 0.4, 1 and 1.6 m $K_3/Na_4[Fe(CN)_6]$ systems. Figure 20(a & c) demonstrate the expected increase in current density with increasing concentration in both the K_3/K_4 and K_3/Na_4 systems. However, when these CVs are concentration normalised[§] (as shown in Figure 20(b & d)) they observe a decrease with increasing concentration. This is due to a significant increase in peak-to-peak separation (ΔE, Figure 20(f)), which is a manifestation of slower electron transfer at the electrode surface.

[§] Here the concentration is reported in true molarity (mol dm^{-3}), this was accurately calculated as the density of each solution was measured. Yielding a true and accurate concentration in molarity.

Interestingly, the E_{eq} of the CVs also increase with increasing concentration of the redox couple, this has previously been attributed to increased ion-pairing of the K^+ ion to the $[Fe(CN)_6]^{3-/4-}$ anion.[149,154,155] The experimentally observed results are indicative of increased ion-pairing and slower electron transfer at the electrode surface, to obtain further insight and quantitative information from these CVs, they were simulated using DigiElch software. This enables the extraction of more quantitative information of fundamental parameters such as kinetic rate constants and diffusion coefficients.

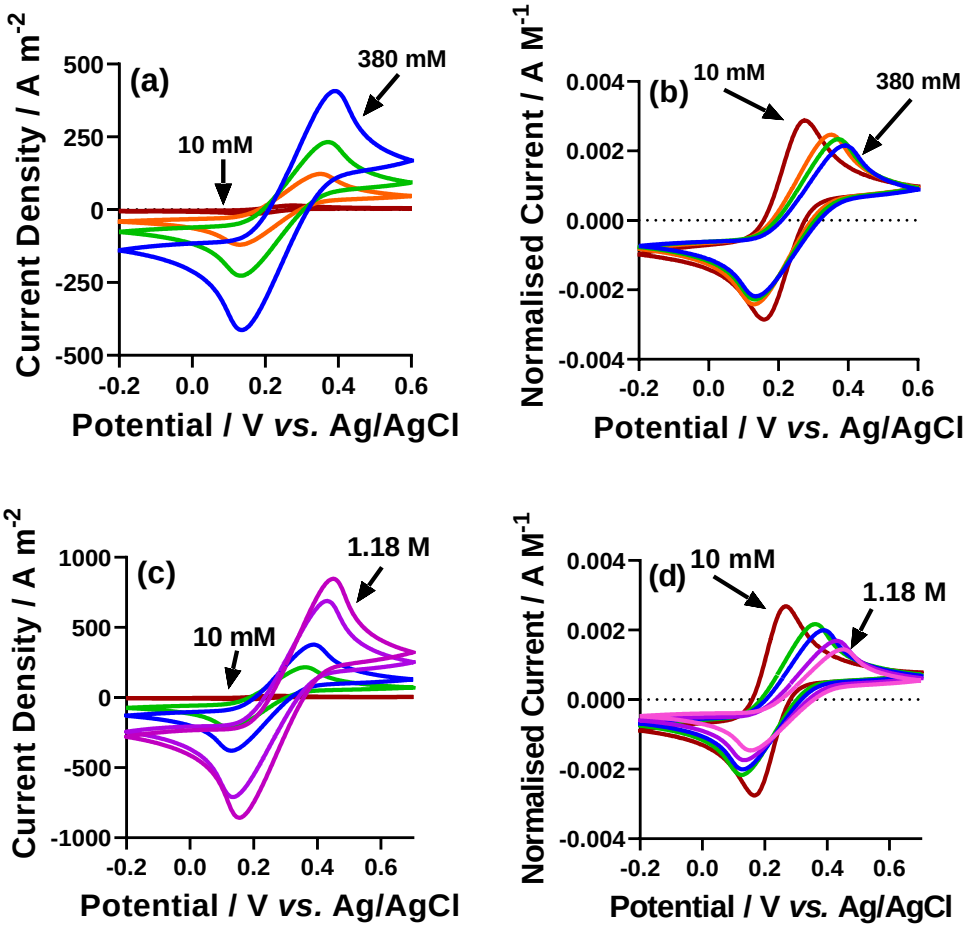

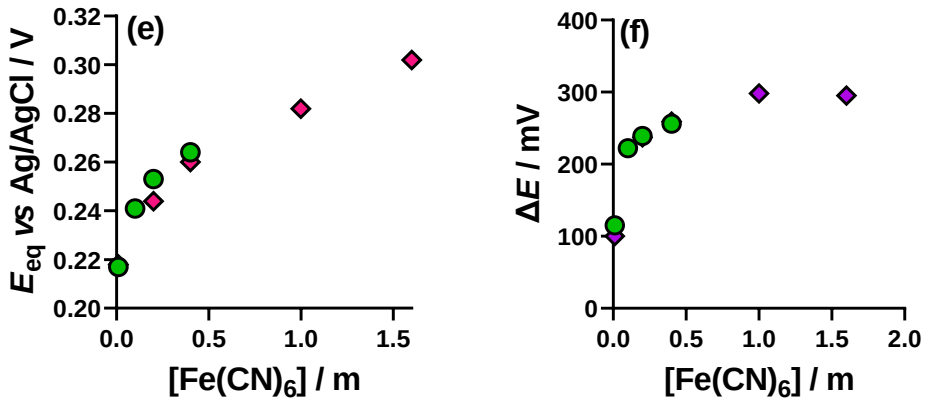

Figure 20 – Figure showing the CVs of 0.01, 0.1, 0.2 and 0.4 m $K_3/K_4[Fe(CN)_6]$ as (a) current density and (b) concentration normalised current. Also shown is 0.01, 0.2, 0.4, 1 and 1.6 m of the $K_3/Na_4[Fe(CN)_6]$ system as (c) current density and (d) concentration normalised current. The (e) E_{eq} and (f) ΔE of these CVs are also shown, respectively.

The various concentration systems were therefore simulated, and the lowest (0.01 m) and highest (0.4 m for K_3/K_4 and 1.6 m for the K_3/Na_4) concentration simulated voltammograms are shown in Figure 21(a-d). Simulating the CVs allowed the determination of the simulated diffusion coefficients (shown in Figure 21(e)) and kinetic rate constants (shown in Figure 21(f)). As expected, the diffusion coefficients and kinetic rate constants both clearly decrease with increasing concentration. These two factors combine to explain the lower concentration normalised current for the CVs shown in Figure 21(b & d).

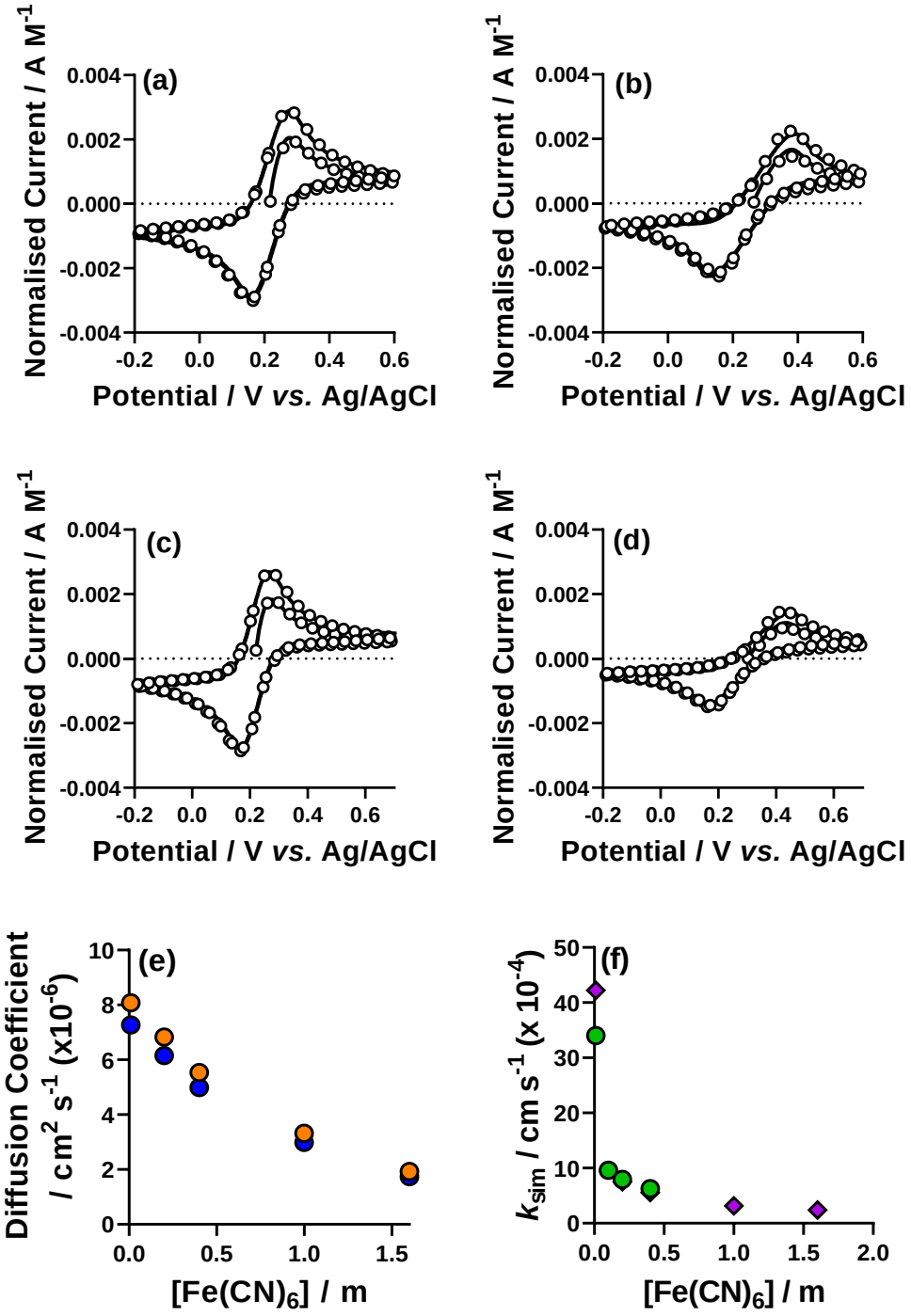

Figure 21 – Figure showing (a-d) cyclic voltammograms of experimental (solid line) and simulated (circled datapoints) of (a) 0.01 m $K_3/K_4[Fe(CN)_6]$, (b) 0.4 m $K_3/K_4[Fe(CN)_6]$, (c) 0.01 $K_3/Na_4[Fe(CN)_6]$ and (d) 1.6 m $K_3/Na_4[Fe(CN)_6]$. Also shown is (e) the simulated rate constants (k_{sim}) of the $[Fe(CN)_6]^{3-}$ (orange) and $[Fe(CN)_6]^{4-}$ (blue) for the $K_3/Na_4[Fe(CN)_6]$ at all investigated concentrations. And (f) the simulated

rate constant for the $K_3/K_4[Fe(CN)_6]$ (green circles) and $K_3/Na_4[Fe(CN)_6]$ purple diamonds.

One thing to note from the simulated kinetic rate constants obtained at higher concentrations (anything above 10 mM) is that the simulated k^0 (or k_{sim}) is of the same order of magnitude as the k_{agg} proposed from the Butler-Volmer model in the previous chapter.[35] Again reinforcing the validity of the previously utilised model. These static electrochemical investigations allow a fascinating insight into the $[Fe(CN)_6]^{3-/4-}$ systems interrogated in this chapter. But they offer no insight into the limitation inherently observed, and no explanation for the reduced diffusion coefficient and kinetic rate constant. Therefore, CVs were also recorded at a rotating disc electrode.

Table 5 – Table of data for DigiElch simulations of $K_3/K_4[Fe(CN)_6]$ and $K_3/Na_4[Fe(CN)_6]$ CVs of various concentrations.

$[Fe(CN)_6]$ concentration / m	E_{eq} / V vs Ag/AgCl	ΔE / mV	k_{sim} / x10^{-4} cm s^{-1}	D_{ox} / x10^{-6} cm^2 s^{-1}	D_{red} / x10^{-6} cm^2 s^{-1}
$K_3/K_4[Fe(CN)_6]$					
0.01	0.217	115	34.0	9.76	8.79
0.10	0.241	222	9.61	8.62	7.76
0.20	0.253	239	7.95	7.99	7.19
0.40	0.264	256	6.26	6.87	6.18
$K_3/Na_4[Fe(CN)_6]$					
0.01	0.218	100	42.2	8.08	7.27
0.20	0.244	237	7.54	6.83	6.15
0.40	0.260	259	5.56	5.54	4.99
1.00	0.282	298	3.15	3.32	2.99
1.60	0.302	295	2.39	1.93	1.74

3.3.3 – Rotating disc electrochemistry

Electrochemistry undertaken at a rotating disc electrode (RDE), rather than a static electrode allows electrochemistry to be studied in the absence of the typical mass-transport limitation (*i.e.* more kinetic independent analysis). Figure 22(a & b) show the difference between a static and rotating disc electrode for both the current density and concentration normalised current. RDE CVs were measured for all the K_3/Na_4 solutions investigated. Generally, the same trend was observed as the CVs in the previous section, where the current density increases with concentration, but the concentration normalised current decreases (Figure 22(b & c)).

Further insight can be obtained when the peak current density at the static CV (j_p) and limiting current density at the rotating disc (j_{lim}) are both plotted as a function of concentration. Interestingly, the same trend was observed in both j_p and j_{lim} as the j_{SC} of the thermoelectrochemistry measured in section 3.3.1. This is visually demonstrated in Figure 22(f) where the j_{lim} and j_{SC} are overlayed. To further demonstrate the perfect overlay, they have also been plotted against each other, which shows an excellent linear relationship (Figure 22(f, inset)).

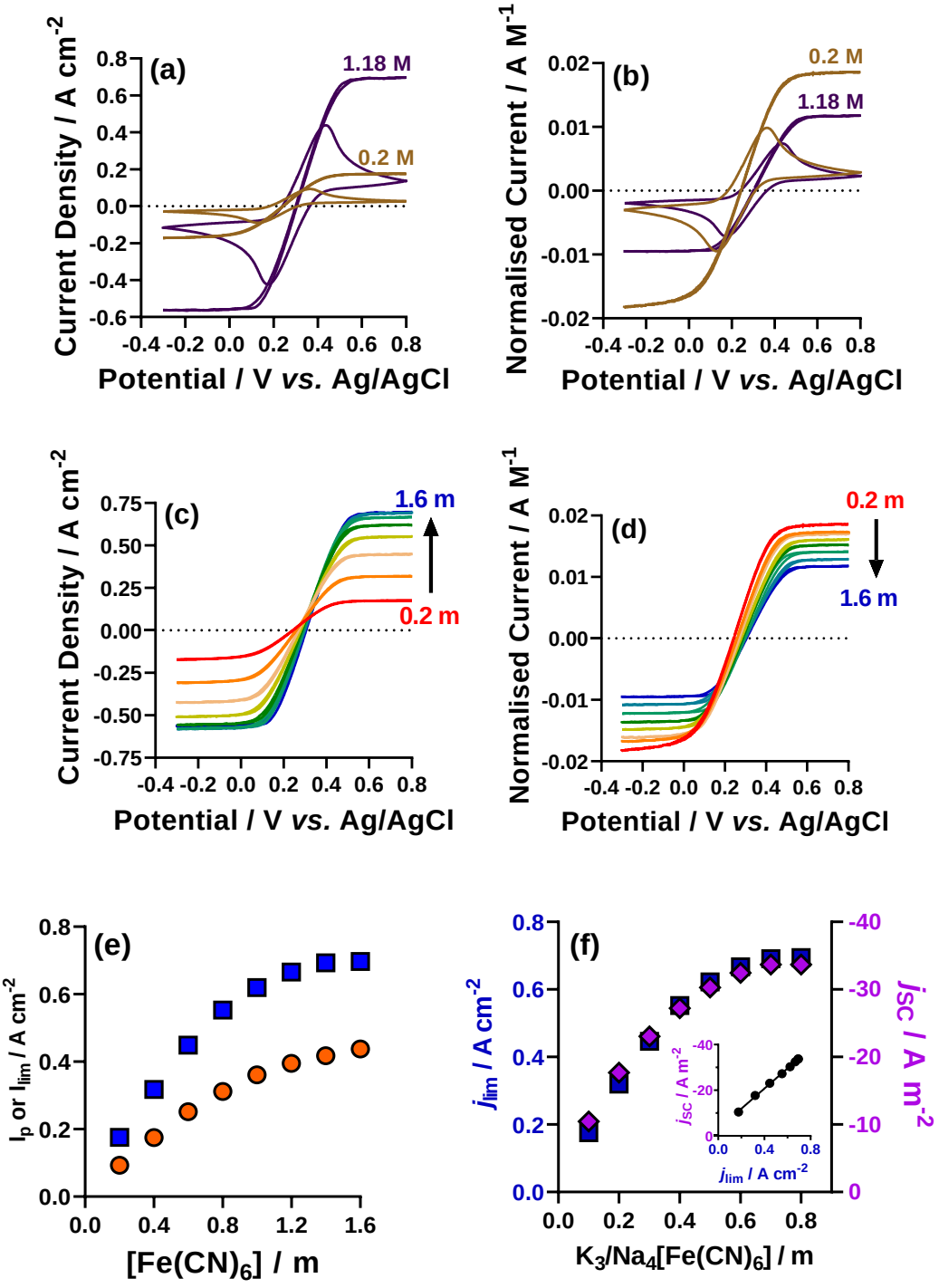

Figure 22 – Figure showing the static CV *vs* rotating-disc CV for the 0.2 M and 1.18 M $[Fe(CN)_6]^{3-/4-}$ systems as (a) current density and (b) concentration normalised current. Also shown is the rotating-disc CVs for every $[Fe(CN)_6]^{3-/4-}$ concentration investigated in Figure 21 shown as (c) current density and (d) concentration normalised current. (e) the j_p from static CV (orange circles) and j_{lim} from the rotating disc CV (blue squares) shown as a function of increasing concentration of $[Fe(CN)_6]^{3-/4-}$ and (f)

an overlay of the RDE j_{lim} and thermogalvanic j_{SC} *vs* concentration of $[Fe(CN)_6]^{3-/4-}$, inset: j_{SC} *vs* j_{lim}.

It is interesting that the j_{lim} should follow the same trend as the j_{SC} and j_p. For these are three significantly different measurement techniques under significantly different conditions. It does however demonstrate that the limitation causing the plateau in j_{SC} is not alleviated by removing the mass transport limitation in the solution, but is caused by some other fundamental property. As both static and dynamic electrochemical investigations offered significant insight into the properties of the solution, but also followed the same trend as the thermogalvanic current density, deeper insight into the solution properties were investigated, starting with the conductivity.

3.3.4 – Experimental and predicted conductivity

With the same inherent limitation observed in j_{SC}, j_p and j_{lim}, the conductivity of these various concentration $K_3/Na_4[Fe(CN)_6]$ solutions was measured in an attempt to gain further insight into the fundamental physiochemical properties of these high salt concentration environments. The experimentally determined conductivity (κ) with increasing concentration are displayed in Figure 23(a, (▲)) which was found to also observe a plateau at the same concentration as the j_{SC} (also shown in Figure 23(a)). Conductivity of strong electrolyte solutions such as $[Fe(CN)_6]^{3-/4-}$ are expected to observe a linear decrease in molar conductivity (Λ_m) with respect to increasing the square root of concentration ($c^{0.5}$) in line with Kohlrausch's law[94,156]:

$$\Lambda_m = \Lambda_m^o - K\sqrt{c} \tag{25}$$

Where Λ_m^o is the limiting molar conductivity (*i.e.* at infinite dilution) and K is an empirical constant. This relationship has been previously applied to moderately concentrated solutions of $K_3[Fe(CN)_6]$ and $K_4[Fe(CN)_6]$.[156]

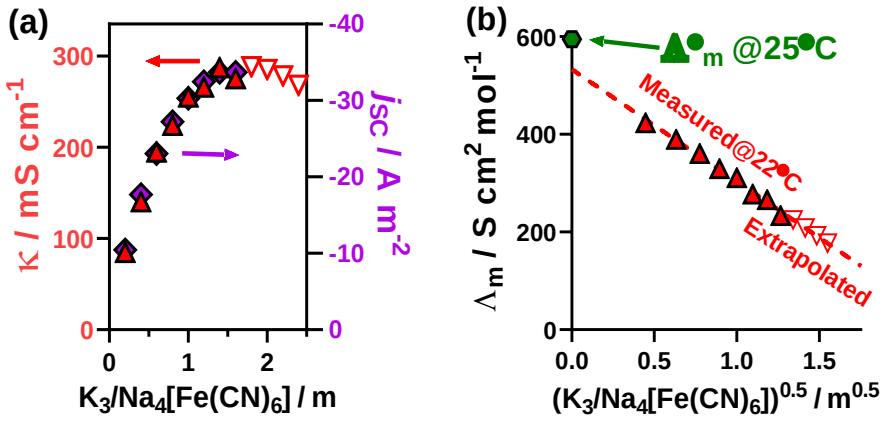

Figure 23 – Figure showing (a) the experimentally measured conductivity between 0.2 and 1.6 m $[Fe(CN)_6]$ (κ, ▲), overlaying the j_{SC} data from Figure 19(b) (◆), also shown is the Kohlrausch's law predicted conductivity values between concentrations of 1.8 and 2.4 m $[Fe(CN)_6]$ (▽). (b) shows the Kohlrausch's law molar conductivity (Λ_m) *vs* the square root of concentration for both experimental (▲) and extrapolated (▽) values.

As demonstrated in Figure 23(b) the experimentally determined conductivity (▲) is found to be a good fit to Kohlrausch's law, and have therefore been extrapolated to higher concentrations (▽), up to 2.4 m. Upon reverting these extrapolated values back to conductivity *vs* concentration, it can be observed that conductivity beyond 1.6 m is predicted to decrease (Figure 23(a, ▽)). This predicted decrease would be severely detrimental to thermocells, and would result in a reduction of both current and power densities with concentrations of $[Fe(CN)_6]$ beyond 1.6 m.

The molar conductivity (Λ_m) and viscosity (η) of a system can be used to determine a further fundamental property of a system. These two parameters share an approximate inverse correlation such that $\Lambda_m\eta \approx$ constant. This relationship is frequently referred to as the Walden product.[94] The Walden product as a function of $K_3/Na_4[Fe(CN)_6]$ concentration is shown in Figure 24. The Walden product increased from 0.48 S cm^2 Pa mol^{-1} s^{-1} at 0.4 m to 0.57 S cm^2 Pa mol^{-1} s^{-1} at 1.6 m; this increase is likely indicative of increasing ion pairing with increasing concentration. This partially mirrors the minor decreases in the Seebeck coefficient with increasing concentration (*cf.* Figure 19(a)), with Seebeck coefficients typically being highly sensitive to ion pairing.[36]

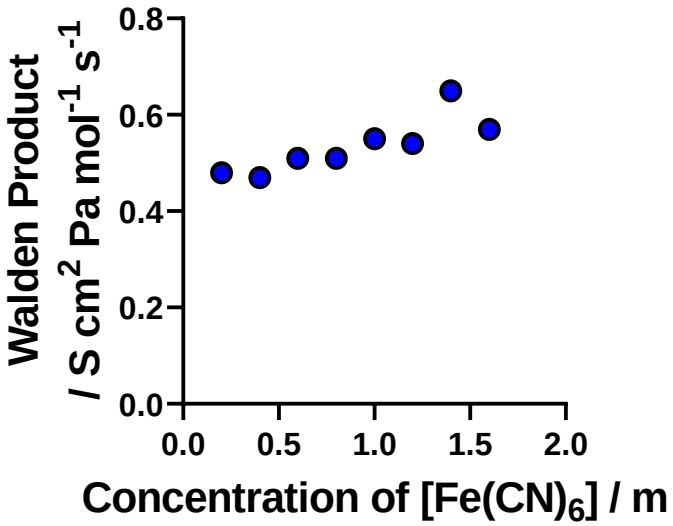

Figure 24 – Plot of the Walden product as a function of the combined concentration of $K_3/Na_4[Fe(CN)_6]$

3.3.5 – Attempting to overcome the inherent limit in thermogalvanic power density

3.3.5.1 – Homogeneous electrocatalysis

Having determined that the inherent limit in thermogalvanic current and power density is also present in the inherent electrochemistry (as shown by the j_p and j_{lim}) and conductivity (as discussed above) of the solution. We next attempted to overcome this limit several methods: i) homogeneous electrocatalysis, ii) adding organic co-solvent, and iii) induced convection in the thermocell.

Firstly, homogeneous electrocatalysis was employed to try and overcome the inherent limitation in thermogalvanic current (and therefore power) density. In the previous chapter, it was demonstrated that addition of large, alkali metal cations (such as Rb^+ and Cs^+) observed a benefit to both the thermodynamics and kinetics of the $[Fe(CN)_6]^{3-/4-}$ redox couple. Therefore, this was again employed on both the $K_3/K_4[Fe(CN)_6]$, and the $K_3/Na_4[Fe(CN)_6]$ systems. Figure 25(a) shows the expected increase in current density of the 0.4 m $K_3/K_4[Fe(CN)_6]$ with addition of 0.7 m CsCl. CsCl was also added to the 0.4 m $K_3/Na_4[Fe(CN)_6]$, however, this system suffered severe solubility issues and resulted in a precipitate which could not be measured.

Swapping the 0.7 m CsCl to 0.7 m RbCl was found to retain the solubility of the $K_3/Na_4[Fe(CN)_6]$, whilst maintaining the electrocatalytic ability on the thermogalvanic performance, as shown in Figure 25(b). Subsequently, 0.7 m RbCl was added to the 1 m $K_3/Na_4[Fe(CN)_6]$ system. However, this did not improve the observed current density, demonstrating that the limit is not caused by a kinetic effect and the significant decrease in kinetic rate constant observed in section 3.3.2 is caused by the

as yet unknown limitation inherent within the super concentrated electrolyte solution. Representative power curves of these systems are also shown in Figure 25.

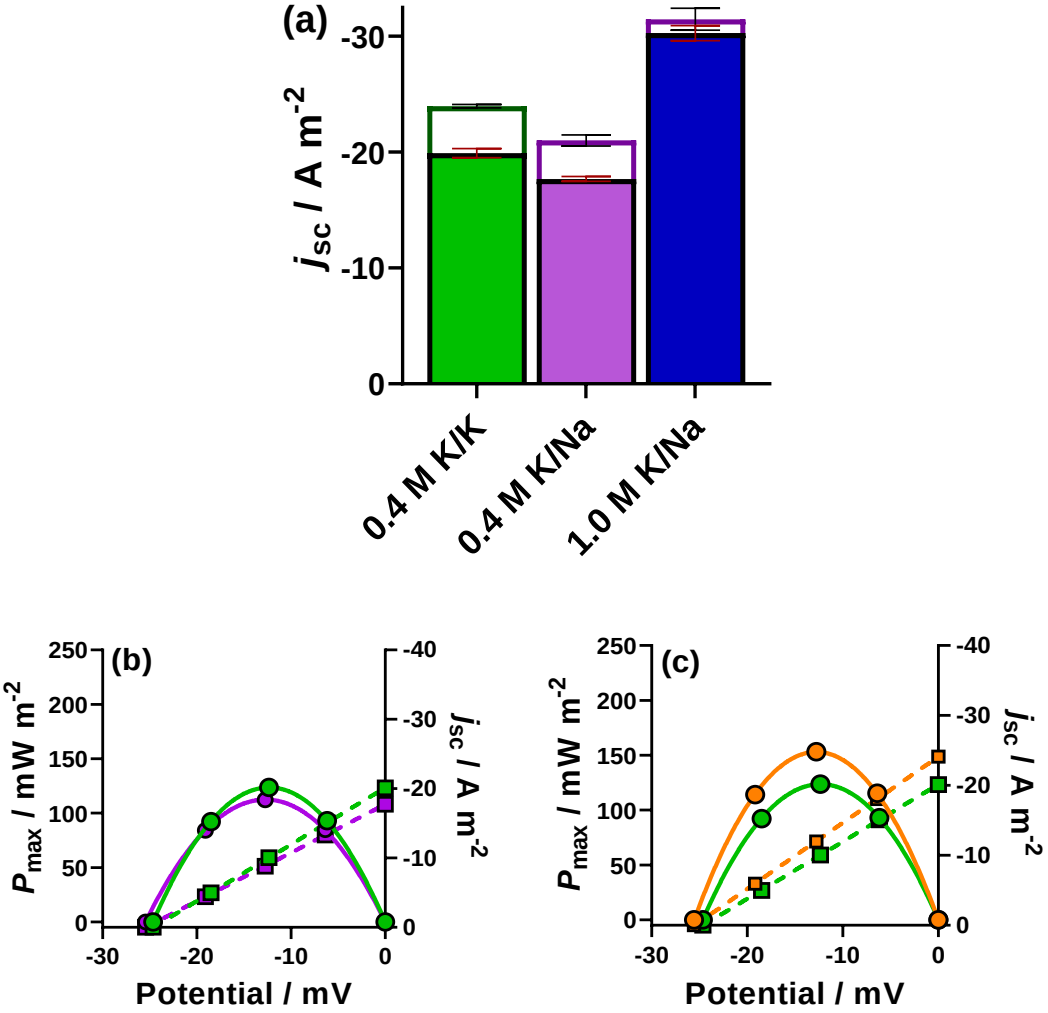

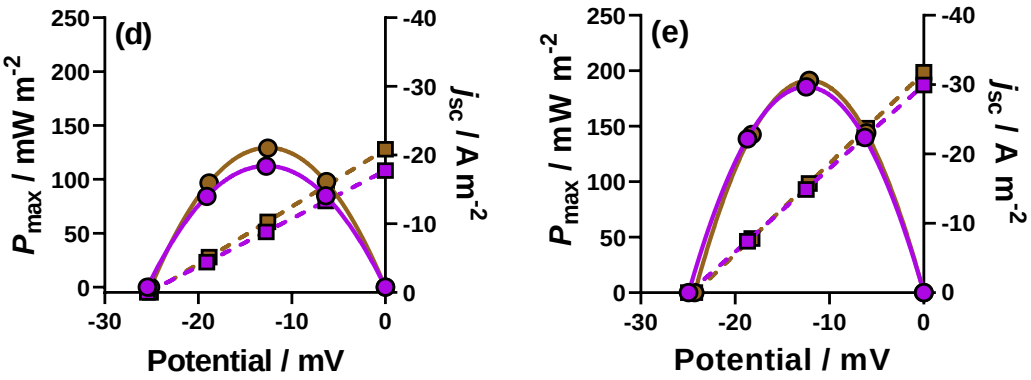

Figure 25 – Figure showing (a) the observed current density of the 0.4 m $K_3/K_4[Fe(CN)_6]$, $K_3/Na_4[Fe(CN)_6]$ and 1 m $K_3/Na_4[Fe(CN)_6]$ in the absence of presence of 0.7 M CsCl in the K_3/K_4 system and 0.7 M RbCl for the K_3/Na_4 systems. Also shown is power curves for (b) the 0.4 m $K_3/K_4[Fe(CN)_6]$ (green) and $K_3/Na_4[Fe(CN)_6]$ (purple) systems (c) the 0.4 m K_3/K_4[Fe(CN6] in the absence (green) and presence (orange) of 0.7 M CsCl. (d) the 0.4 m $K_3/Na_4[Fe(CN)_6]$ in the absence (purple) and presence (brown) of 0.7 M RbCl and (e) the 1 m $K_3/Na_4[Fe(CN)_6]$ in the absence (purple) and presence (brown) of 0.7 M RbCl.

3.3.5.2 – Investigating the addition of organic co-solvent

Next, the effect of adding organic co-solvent to the higher concentrated systems was investigated. This was undertaken using methanol, ethanol, and acetone at a ratio of 10 % v/v of organic to aqueous solvent. This investigation was undertaken as addition of organic co-solvent has been previously reported to increase the S_e of the $[Fe(CN)_6]^{3-/4-}$ redox couple.[81] The other added benefit is that the organic co-solvent was assumed to decrease the viscosity of the solution, enabling faster mass transport of the electrolyte through the solution.

Addition of organic co-solvent was achieved by diluting the 1.4 m $K_3/Na_4[Fe(CN)_6]$ system with methanol, and the 1.2 m $K_3/Na_4[Fe(CN)_6]$ system with either ethanol or acetone. These concentrations were found to be the highest capable

of being diluted with the respective organic co-solvent, without forming precipitates of $[Fe(CN)_6]$. Diluting the 1.4 m to 1.2 m and 1.2 m to 1.0 m systems, respectively.

Figure 26 shows the effect of adding organic co-solvent to the $[Fe(CN)_6]$ for the observed (a) S_e, (b) j_{SC} and (c) P_{max}. As can clearly be observed, addition of organic co-solvent had little to no effect on the observed S_e, (Figure 26(a)), but had a significant but detrimental effect on the current and power densities (Figure 26(b & c)). This was a curious result as the literature has reported a significant benefit to the S_e using methanol. Where addition of 10 % methanol increased the S_e from -1.4 to -2.7 mV K^{-1}.[81] However, another investigation using organic co-solvents has reported significantly more minor effects on observed S_e with alcohols.[82] Our results here clearly support the latter, where no effect observed from the former could be observed.

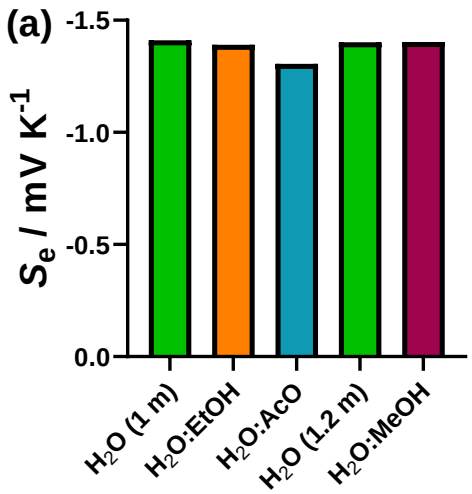

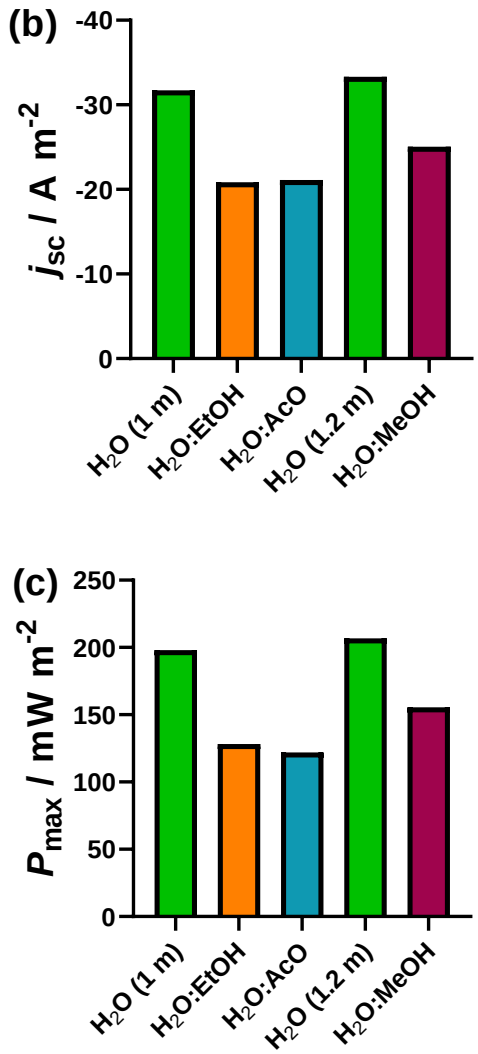

Figure 26 – Figure showing the effect of adding organic co-solvent (methanol, (MeOH, red), ethanol (EtOH, orange) and acetone (AcO, blue)) on the 1 m (for ethanol and acetone) and 1.2 m (for methanol) for the observed (a) S_e, (b) the j_{SC} and (c) the P_{max}.

3.3.5.3 – Inducing mass transfer within the thermocell

Finally, the effect of 'inducing' mass transport within the thermocell was explored, this was achieved by introducing a spherical magnetic bead into our thermocell, which was subsequently stirred using an external magnetic field as the thermocell performance was being measured. The effect of increasing rotation speed

was assessed from 0 rpm to 2000 rpm on the thermogalvanic properties of both the 0.4 m $K_3/K_4[Fe(CN)_6]$ and 1.6 m $K_3/Na_4[Fe(CN)_6]$ thermocells.

In short, and can clearly be observed in Figure 27, inducing mass transport within the thermocell has no effect on any thermogalvanic property on either solution. Since we apparently could not overcome the unknown inherent limitation in the thermocell by any of the attempted methods, further fundamental physiochemical investigations were required. Therefore, the viscosity of the solutions were assessed with increasing concentration, the diffusion coefficients of the redox ions was also re-evaluated and is discussed further below.

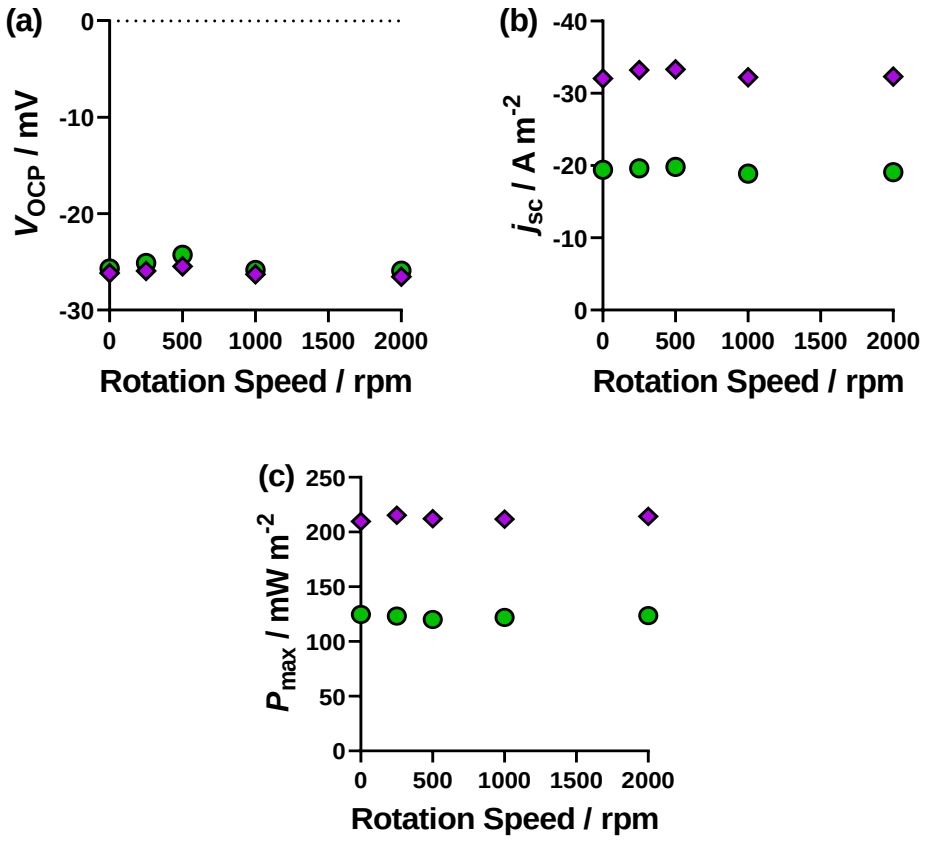

Figure 27 – Figure showing the effect of rotation of a magnetic bead within the thermogalvanic cell stirred by an externally applied magnetic field. This shows the

effect on (a) V_{OCP}, (b) j_{SC} and (c) P_{max} for (green circles) the 0.4 m $K_3/K_4[Fe(CN)_6]$ and (purple diamonds) the 1.6 m $K_3/Na_4[Fe(CN)_6]$.

3.3.6 – Viscosity and modelling the diffusion coefficient beyond 1.6 m $[Fe(CN)_6]^{3-/4-}$

As discussed previously, the cyclic voltammograms of the $K_{3/4}[Fe(CN)_6]$ and $K_3/Na_4[Fe(CN)_6]$ systems at various concentrations were modelled using DigiElch software (Figure 21). This analysis determined that the simulated kinetic rate constant of the redox reaction decreased with increasing concentration, concurrent with a decrease in the diffusion coefficients of both the oxidised and reduced species, but at different rates of decrease. Therefore the viscosity of each solution of $K_4/Na_4[Fe(CN)_6]$ was measured, this is plotted along with the simulated diffusion coefficients in Figure 28. Viscosity clearly demonstrates a linear increase with increasing concentration of electrolyte (in molality).

'Water-in-salt' electrolytes have recently received significant attention due to their great promise for aqueous battery applications.[151–154,157,158] However, there are discrepancies in the literature about the exact definition at which an electrolyte reaches 'water-in-salt' conditions. The original definition reports that at 5 m (*ca.* 5 M) lithium salts have become 'water-in-salt'.[151] More recently, 10 m has become the benchmark value.[152,154] As these previous reports describe alkali-metal salt electrolytes, the concentration is equivalent to the ionic strength, so even though our highly-charged redox-active system has a much lower overall concentration (1.6 m), it has equivalent ionic strength to reported 'water-in-salt' systems (13 m).

In an attempt to gain a better understanding of these systems at concentrations beyond the 1.6 m limit, the viscosity and diffusion coefficients were both modelled and extrapolated, up to 2.4 m. Equivalent to the conductivity model using Kohlrausch's law (Figure 23(a)). Figure 28(a) shows the excellent fit of the model using an exponential decrease in both diffusion coefficients and linear increase in viscosity beyond 1.6 m. Previously, the reduction in the diffusion coefficient of 5 mM $K_3[Fe(CN)_6]$ has been directly attributed to the increase in viscosity once 'water-in-salt' level electrolytes have been achieved.[154] This trend was broadly observed here, despite the disproportional nature of the decrease in *D* (exponential decrease) and the increase in viscosity (linear increase).

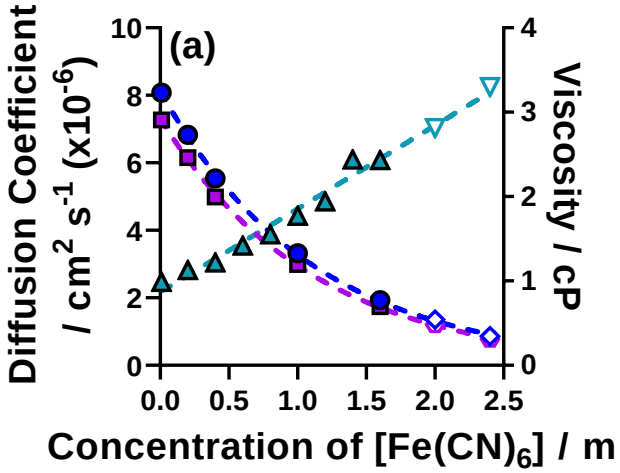

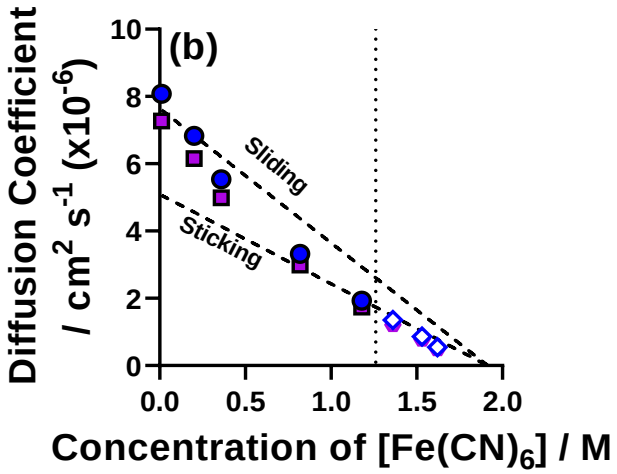

Figure 28 – Figure showing (a) the relationship of both diffusion coefficient, with the oxidised (●) and reduced (■) species are shown independently and viscosity with increasing concentration of $[Fe(CN)_6]$ (in molality). Both of these parameters have their experimentally measured (viscosity) or simulated based on experimental (diffusion coefficient) values (solid fill) and the extrapolated values (hollow). Also shown in (b) the change in diffusion coefficient with increasing concentration (in molarity) of $[Fe(CN)_6]$, shown in this figure is the predicted trend based on the Stokes-Einstein equation for the 'sticking' and 'sliding' models (both labelled).

To better understand the mass transport of the ions with respect to the solvent, the Stokes-Einstein model was used. The Stokes-Einstein equation (Equation 26) is used to characterise the mass transport of particles in liquids.[154,159,160] This model can be applied to ions in solution that have a fixed solvation sphere, to determine if these are 'sliding' or 'sticking' with respect to the associated bulk solvent.[154]

$$D = \frac{k_B T}{(X\pi)\eta r} \tag{26}$$

Where D is the diffusion coefficient, k_B the Boltzmann constant, T the temperature, $X\pi$ is either 4π or 6π depending on the sliding or sticking model respectively, η is the viscosity and r is the radius of the spherical particle (taken as

4.22 nm).[154] In the sticking model, with 6π as the denominator, the solvated ion experiences a pressure force from the front of the particle (equivalent to 4π) and a frictional force parallel to the particle surface (equivalent to 2π). This particle is experiencing the "frictional coefficient" ($6\pi\eta r$). In the sliding model, the particle does not experience the frictional force, and the particle (in this case a solvated ion) experiences the "Sutherland coefficient" ($4\pi\eta r$). With less force hindering mass transport, the ion thus move faster in solution.[159,160]

This model has previously been demonstrated to show that, at low concentrations of redox-inactive supporting electrolyte, $K_3[Fe(CN)_6]$ was found to fit the 'sliding' model, and at higher concentrations the diffusion coefficient is much lower than expected from the 'sticking' model.[154] Figure 28(b) shows the experimentally simulated diffusion coefficients of both the oxidised and reduced species, along with the predicted trends based on the 'sliding' and 'sticking' models, using the experimentally determined viscosity from Figure 28(a).

At low concentrations of $K_3/Na_4[Fe(CN)_6]$, the 'sliding' characteristic is clearly observed. As the concentration increases, the $[Fe(CN)_6]^{3-}$ and $[Fe(CN)_6]^{4-}$ ions are found to transition from the 'sliding' model to observe 'sticking' characteristics. Moreover, when the diffusion coefficients and viscosity are extrapolated to 2.4 m (*ca.* 1.5 M, ionic strength of 12.1 M, or 19.3 m), the model clearly demonstrates the 'sticking' characteristic of both the oxidised and reduced species. Another interesting outcome of this model was the prediction of 'zero diffusion coefficient' for the redox ions, which is proposed to be *ca.* 1.6 M. Due to the significant ionic strength of these experimental and predicted solutions, and the severely hindered diffusion of the redox

ions in solution, the system investigated here can be classed as a true 'water-in-salt' system. This analysis also demonstrates that the limitation inherent within our thermogalvanic cell is due to severely restricted mass transport with increasing concentration of electrolyte. This inherent limitation is also likely to be present for all aqueous electrochemical systems where high concentrations of electrolyte are desirable.

3.3.8 – Mimicking the concentration with redox-inactive electrolytes

Having ascertained the inherent limitation of the high concentration $[Fe(CN)_6]$ thermocell, we next set out to investigate whether these properties were unique to high concentration redox-active electrolytes or whether they were universal to all high concentration electrolytes. To achieve this, the electrochemical parameters of $K_3/K_4[Fe(CN)_6]$ and $K_3/Na_4[Fe(CN)_6]$ were investigated as either the only electrolyte (with a low 0.1 M KCl supporting electrolyte, discussed further below) or a low concentration of 10 mM $[Fe(CN)_6]$ was investigated with high concentration of supporting electrolytes. The effect of charge on the supporting electrolyte was also investigated using a range of charged potassium salts with various charged anions (KCl, K_2SO_4 and K_3Citrate).

Cyclic voltammograms of various concentration $K_3/K_4[Fe(CN)_6]$ and $K_3/Na_4[Fe(CN)_6]$ have already been recorded and are discussed in section 3.3.2. The ionic strength of these solutions was calculated (in molality) and attempts to replicate this ionic strength using additional supporting electrolytes (KCl, K_2SO_4 and K_3Citrate) was made.

As previously discussed, with increasing concentration of $[Fe(CN)_6]^{3-/4-}$, the peak-to-peak separation (ΔE) increases, consistent with a significant reduction in kinetic rate constant (as shown in Figure 21). To determine if this is a uniquely redox-active electrolyte or simply just an electrolyte effect, equivalent ionic strength CVs of low concentration $[Fe(CN)_6]^{3-/4-}$ were recorded. The concentration normalised CVs of $K_3/K_4[Fe(CN)_6]$ and $K_3/Na_4[Fe(CN)_6]$ are again shown in Figure 29(a & b), also shown are the concentration normalised CVs for $K_3/K_4[Fe(CN)_6]$ with various concentrations of KCl (Figure 29(c)) and K_3Citrate (Figure 29(d)) for the $K_3/Na_4[Fe(CN)_6]$ system with various concentrations of KF (Figure 29(d)) and K_3Citrate (Figure 29(e)).

Interestingly, the ΔE of the CVs with ionic strength mimic were found to decrease with increasing concentration, consistent with an increase in kinetic rate constant. This is likely due to a reduction in ohmic resistance due to the extremely high concentration of supporting electrolyte.[80] However, this is contrary to the high ionic strength $[Fe(CN)_6]$ systems, which demonstrate a reduction in the kinetic rate constant.

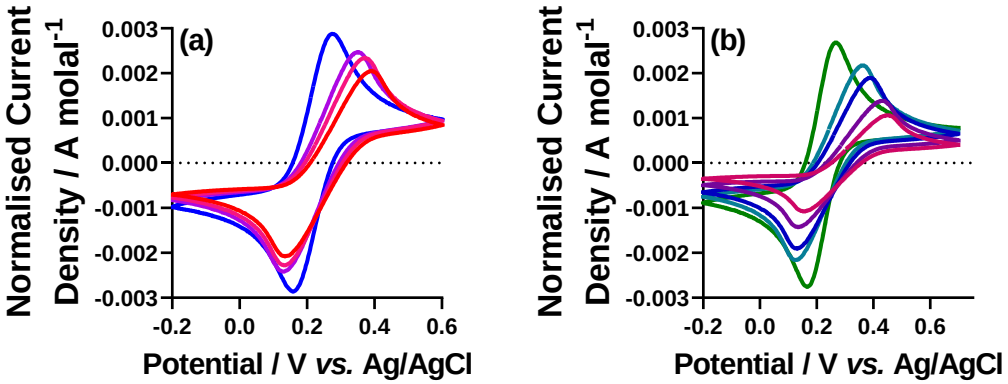

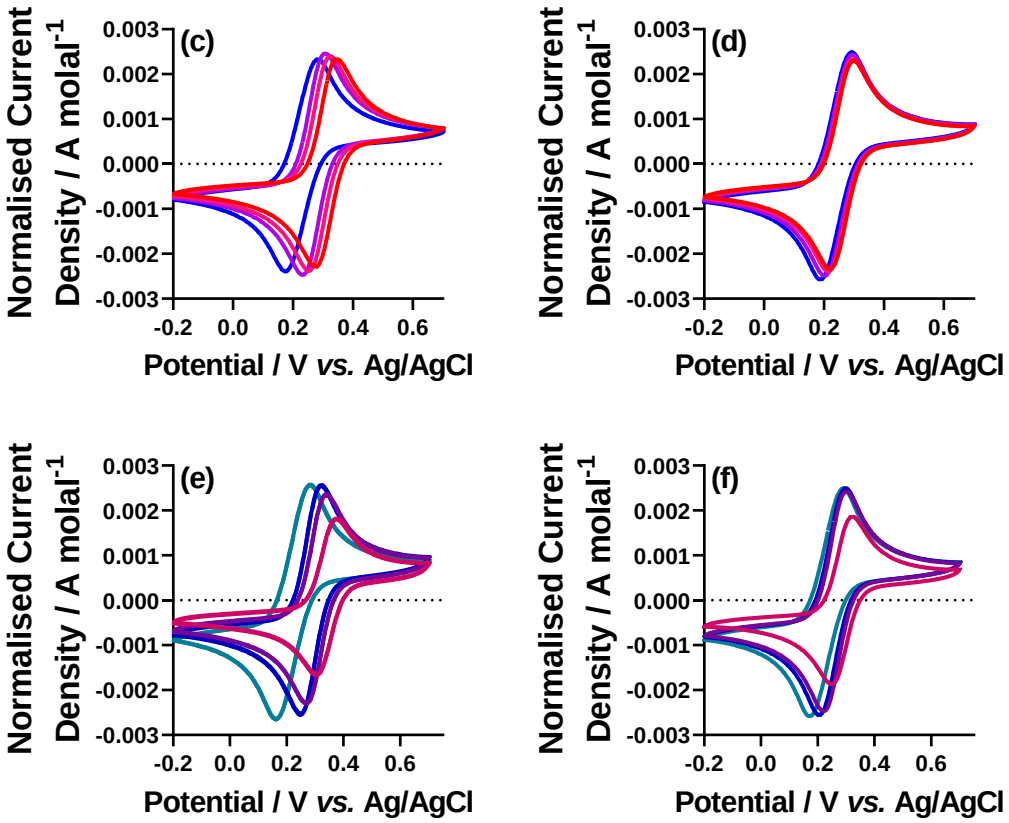

Figure 29 – Figure showing cyclic voltammograms of (a) the $K_3/K_4[Fe(CN)_6]$ (at 0.01, 0.1, 0.2 and 0.4 m), (b) $K_3/Na_4[Fe(CN)_6]$ (at 0.01, 0.2, 0.4, 1, 1.6 m). (c, d) 0.01 m $K_3/K_4[Fe(CN)_6]$ with concentrations of (c) KCl (0.10, 0.82, 1.62 and 3.22 m) and (d) K_3Citrate (0.10, 0.15, 0.23 and 0.30). (e, f) 0.01 m $K_3/Na_4[Fe(CN)_6]$ with concentrations of (e) KF (0.1, 1.62, 3.22 and 8.00 m) and (f) K_3Citrate (0.1, 0.3, 0.5 and 1.5).

Another interesting effect of this investigation is on the observed equilibrium potential (E_{eq}). Figure 30 shows the E_{eq} of the CVs with increasing ionic strength, which demonstrates an increase in E_{eq} with ionic strength for all systems, but to varying degrees. It is apparent that the rate of increase of E_{eq} occurs in the order: KCl ~ KF > K_2SO_4 > K_3Citrate ~ $[Fe(CN)_6]$, which is equivalent to the increase in charge of the anions: -1 > -2 > -3 ~ -3.5 (the average between $[Fe(CN)_6]^{3-}$ and $[Fe(CN)_6]^{4-}$).

The increase in E_{eq} has previously been attributed to increases in ion pairing between the K^+ and $[Fe(CN)_6]^{3-/4-}$ ions.[149,154,155] This ion-pairing appears to be hindered using higher charge anion salts such as $[citrate]^{3-}$, which is potentially competing with the $[Fe(CN)_6]^{3-/4-}$ for the K^+ ions. This result indicates that the formation of ion-paired species such as $[KFe(CN)_6]^{2-/3-}$ occurs more readily with electrolytes such as KCl and KF, which should thus be avoided in thermocells as this appears to decrease the observed S_e.

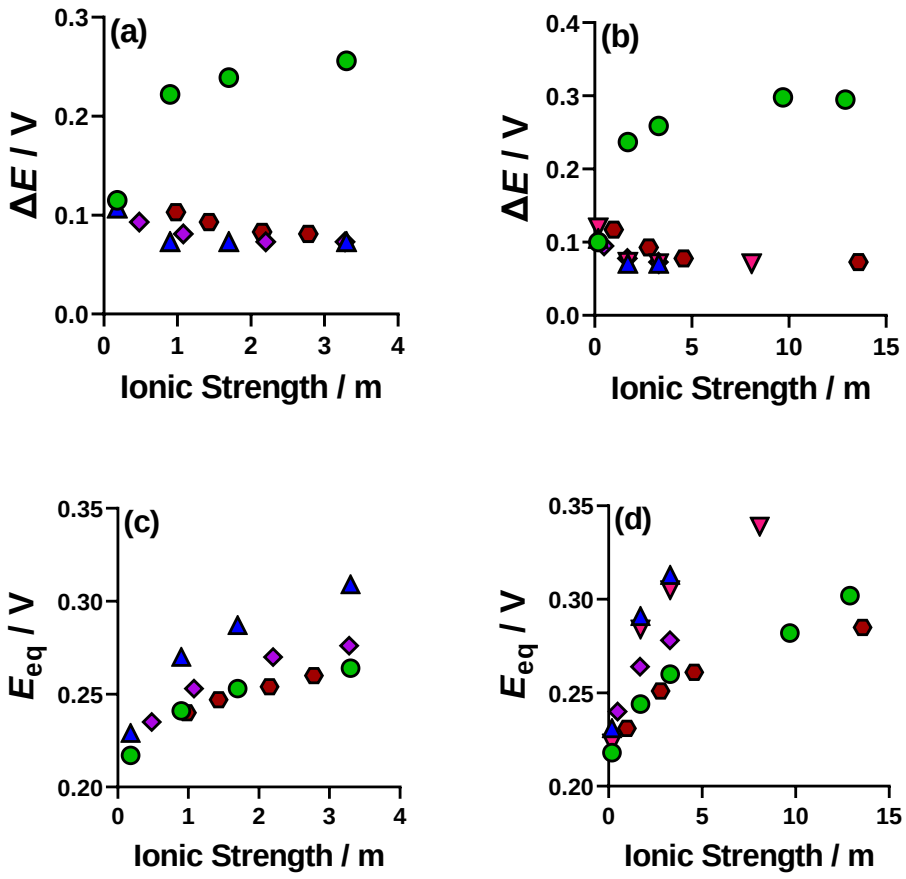

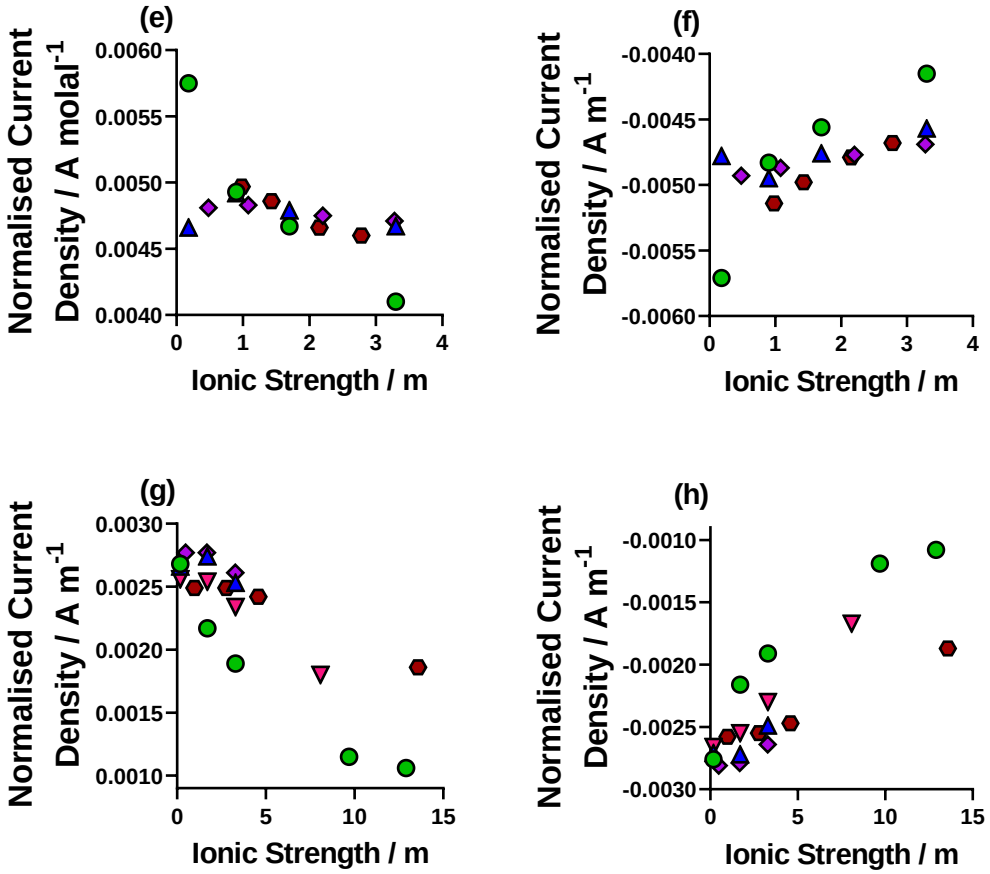

Figure 30 – Figure showing the ΔE for these CVs in Figure 20 for the (a) $K_3/K_4[Fe(CN)_6]$ (b) $K_3/Na_4[Fe(CN)_6]$ and the E_{eq} for the (c) $K_3/K_4[Fe(CN)_6]$ and (d) $K_3/Na_4[Fe(CN)_6]$ where KCl (blue triangle), KF (pink inverted triangle), K_2SO_4 (purple diamond) K_3Cit (red hexagon) and $[Fe(CN)_6]$ (green circle) are all shown. Also shown are the peak current observed from the cyclic voltammetry data shown in Figure 20. This is shown for (e) oxidation current and (f) reduction current for the $K_3/K_4[Fe(CN)_6]$ and (g) oxidation current and (h) reduction current for $K_3/Na_4[Fe(CN)_6]$. Where KCl (blue triangle), KF (pink inverted triangle), K_2SO_4 (purple diamond) K_3Cit (red hexagon) and $[Fe(CN)_6]$ (green circle) are all shown.

Further information can be obtained from the cyclic voltammetry data, where the normalised peak current (normalised to concentration of $[Fe(CN)_6]$ in molality) has been determined and is shown in Figure 30. It can clearly be seen that the normalised

peak current in both K_3/K_4- and K_3/Na_4-only systems decrease faster than the supporting electrolyte mimicked systems. This is due to the synergistic detrimental combination of a reduction in both kinetic rate constant and diffusion coefficients. Whereas in the ionic strength mimic the detrimental effect is from a purely mass transport aspect. Further work will need to be undertaken in the future to determine this more clearly using both higher concentration $[Fe(CN)_6]$ in the ionic strength mimic, and other (possibly less inert) redox couples such as $Fe^{2+/3+}$ or redox couples that utilise the grotthuss hopping mechanism such as I^-/I_3^-.

3.3.9 – Beyond 1.6 m $[Fe(CN)_6]^{3-/4-}$ through ultrasonication-mediated dissolution of solute

Upon attempting to solubilise concentrations of $[Fe(CN)_6]$ above 1.6 m, it was observed that ultrasonication was a method capable of achieving higher concentration solutions of $K_3/Na_4[Fe(CN)_6]$. Therefore, 1.2, 1.6, 2 and 2.4 m solutions were all prepared *via* this method and the thermoelectrochemical properties measured. These solutions were compared to the mechanically solvated equivalent at 0.4, 0.8, 1.2 and 1.6 m. Figure 31 shows that the power density drops after a plateau observed at 1.6 m. This peak in power density, followed by a subsequent decrease was already predicted by the Kohlrausch's law conductivity (Figure 23).

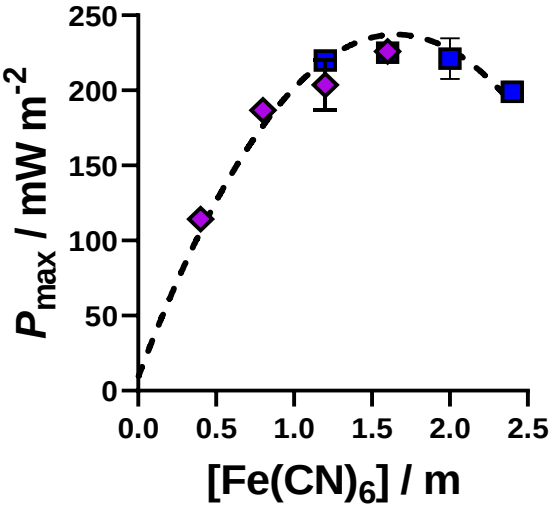

Figure 31 – Figure showing the observed power density of the $K_3/Na_4[Fe(CN)_6]$ from the mechanically solubilised systems (purple diamond) and the ultrasonication mediated solubilised systems (blue squares).

These 2 and 2.4 m solutions are predicted to have total $[Fe(CN)_6]$ concentrations of 1.36 and 1.50 M. The density of the 2 m solution could be measured, this allows the accurate determination of the molarity, which was determined at 1.37 M. The predicted viscosity of this solution was 2.81 cP, the experimentally determined value was 2.86 cP, both of these results demonstrating the effectiveness of the models. Inherent instability with respect to precipitation didn't allow the measurement by conductivity or electrochemistry of the systems >1.6 m.

Concentrations of 2.0 and 2.4 m, corresponding to concentrations of 1.37 and 1.50 M have ionic strengths of 16 and 19 m, (11 and 12 M). The predicted solvation number of K^+, Na^+, $[Fe(CN)_6]^{3-}$ and $[Fe(CN)_6]^{4-}$ are 7,[161,162] 6,[161,162] 11[163] and 17[163]

respectively.[**] At these high concentrations, we calculated there are less water molecules present than can fully solvate the ions (as shown visually in Figure 32 for the 0.4, 1.6 and 2.4 m solutions). Decreasing to 90 % and 77 % of complete solvation for the 2 and 2.4 m solutions, (*i.e.* 10% and 23% less water present than to fully solvate the ions), respectively. This lack of complete solvation of ions is presumed to be the cause of the inherent instability of these solutions to precipitation. These systems can be classified as true 'water-in-salt' systems, but as clearly observed, using high concentration of redox-active electrolytes such as $[Fe(CN)_6]^{3-/4-}$ to achieve this are significantly different from the typical water in salt electrolytes investigated from high-concentration alkali metal electrolytes. The table of data for this calculation is shown in Table 6.

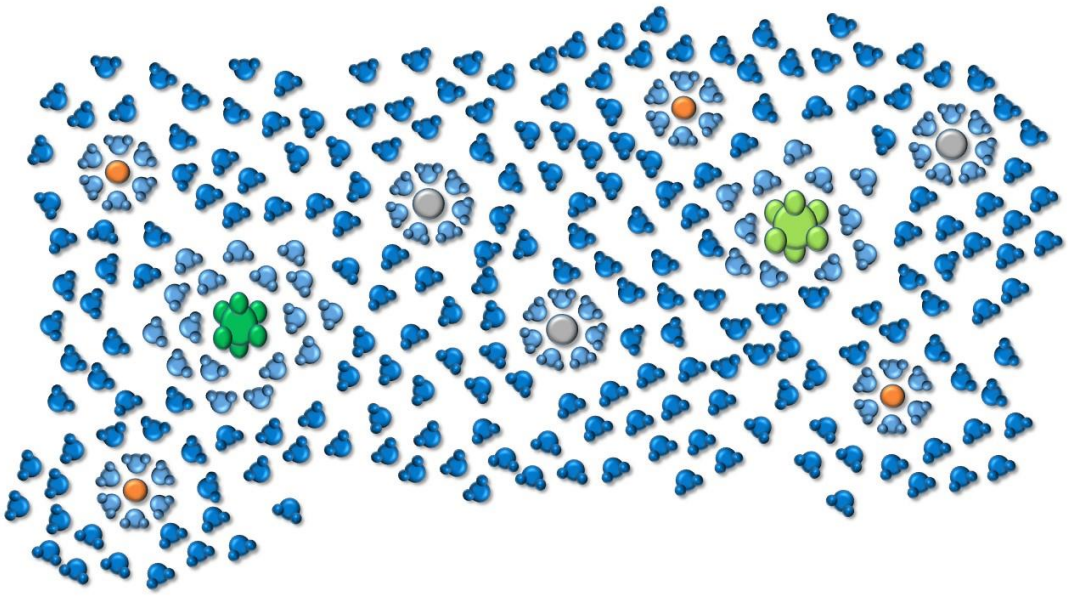

[**] It should be noted here that the water molecules predicted to be solvating the $[Fe(CN)_6]^{3-}$ and $[Fe(CN)_6]^{4-}$ are taken from the solvation number within 5 Å, it is assumed that the full number solvating will be even larger than this.

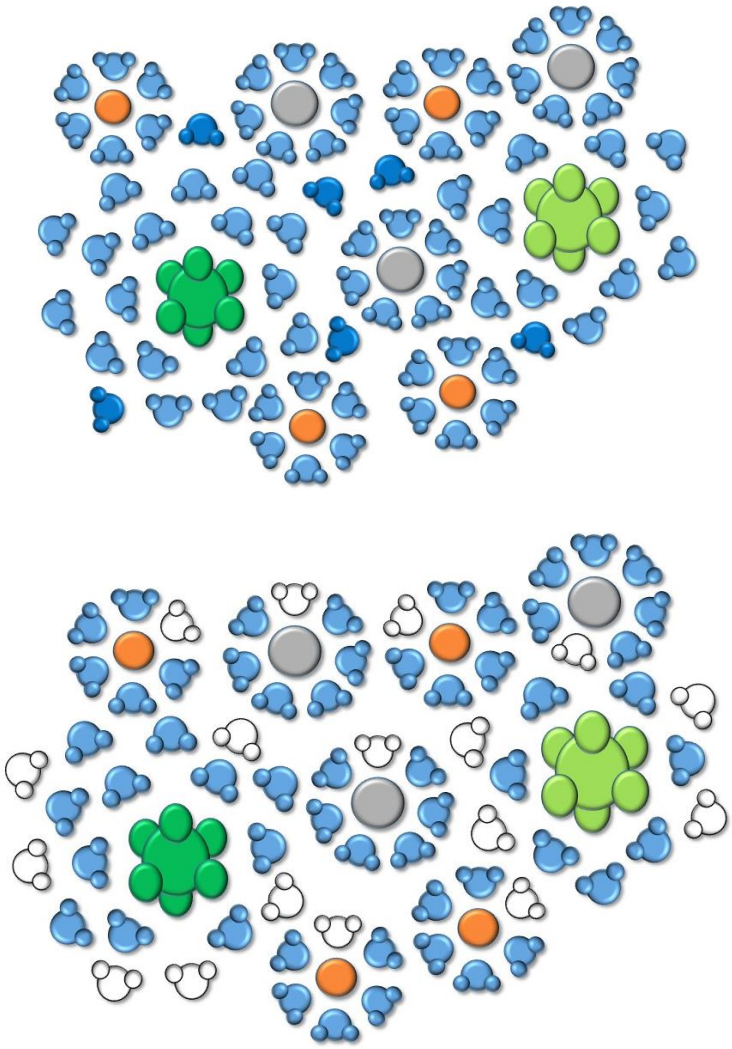

Figure 32 – Visualisation of three concentration $[Fe(CN)_6]^{3-/4-}$ solutions at (top) 0.4 m, (middle) 1.6 m and (bottom) 2.4 m. The ions of $[Fe(CN)_6]^{3-}$ (light green), $[Fe(CN)_6]^{4-}$ (dark green), Na^+ (orange) and K^+ (grey) have all been shown.

Table 6 - Table of data for water of solvation calculation.

Ionic Species	Number of water molecules in the inner hydration sphere (based upon literature values)					Total H_2O molecules (per one $K_3[Fe(CN)_6]$ and $Na_4[Fe(CN)_6]$ molecules)	'Free' H_2O
	$[Fe(CN)_6]^{3-}$	$[Fe(CN)_6]^{4-}$	K^+	Na^+	Total		
0.4 m	11	17	21	24	73	288	215
1.6 m	11	17	21	24	73	79	6
2.4 m	11	17	21	24	73	56	-17

3.4 – Conclusions

In this chapter we have investigated the fundamental electrochemical, thermoelectrochemical, and inherent physiochemical properties of highly concentrated $[Fe(CN)_6]$ solutions. The solubility of $[Fe(CN)_6]$ has been significantly increased by utilising a benign combination of $K_3[Fe(CN)_6]$ and $Na_4[Fe(CN)_6]$, where 1.6 molal total $[Fe(CN)_6]$ was achieved using mechanical stirring. The thermogalvanic properties demonstrated a plateau in observed current and power densities. This plateau was also observed in the electrochemical properties, namely the peak current j_p at static CV and j_{lim} under rotating disc electrode, and the conductivity of the solution. Attempts to improve the current and power of these systems were undertaken using several methods: i) homogeneous electrocatalysis, ii) addition of organic co-solvent, and iii) inducing convection through the introduction of a spinning magnetic stirrer, which were all ultimately unsuccessful.

Chapter 3: Inherent limitations with concentration

Using Kohlraush's law and other models the experimentally measured conductivity, viscosity, and experimentally simulated diffusion coefficients were extrapolated beyond the 1.6 m mechanically stirred limit. Using the Stokes-Einstein equation the low concentration systems were found to fit the "sliding" model, but the higher concentration systems were found to fit the "sticking" model, with significantly reduced diffusion coefficients. Solutions with concentration beyond 1.6 m were found to be achievable using ultrasonication-mediated dissolution. 2.4 m $[Fe(CN)_6]$ was achieved, which was found to reduce in power density beyond the 1.6 m previously observed. This limitation appears to be inherent in redox-active super concentrated electrolytes, but further work on other redox couples will need to be undertaken in order to ascertain if this is a universal limitation.

Chapter 4:

$Fe^{2+/3+}$ - pH and anion effect

The thermoelectrochemistry of the aqueous iron(ii) | iron(iii) redox couple: significance of the anion and pH in thermogalvanic thermal-to-electrical energy conversion

The results of this chapter have been published in:

Royal Society of Chemistry: *Sustainable Energy and Fuels*, 2018, **2**, 2717–2726.[36]

4.1 – Aims and Objectives

In the previous two chapters, a model redox couple (the $[Fe(CN)_6]^{3-/4-}$) was fundamentally investigated for a wide range of electrochemical, physiochemical and thermoelectrochemical properties. High concentrations of electrolyte were also achieved up to water-in-salt levels, but showed no significant benefit, and even detrimental effects in thermocells. These comprehensive and detailed studies were highly informative towards the inherent driving forces and limitations in this thermocell. However, $[Fe(CN)_6]^{3-/4-}$ is a p-type (negative S_e) redox couple, to be able to generate devices with high voltage output, an n-type redox couple (positive S_e) will also need to be developed, ideally with equivalent S_e and power density to the p-type redox couple.

Therefore, in this chapter we set out to:

- Fundamentally investigate the $Fe^{2+/3+}$ redox couple, generated from a range of salts namely: $FeSO_4$, $[NH_4]FeSO_4$, $FeNO_3$ and $FeCF_3SO_3$.
- Investigate the effect of acid to these systems in the thermocell, with respect to both electrochemical and thermoelectrochemical properties.
- Investigate the speciation of the $Fe^{2+/3+}$ using thermoelectrochemical, electrochemical and spectroscopic analysis.
- Undertake an analysis of the green chemistry and sustainability aspects of the various salts, acids, and species present in each thermocell solution.
- To undertake a cost-analysis of these unacidified and acidified systems to determine the most cost-effective thermocell system.

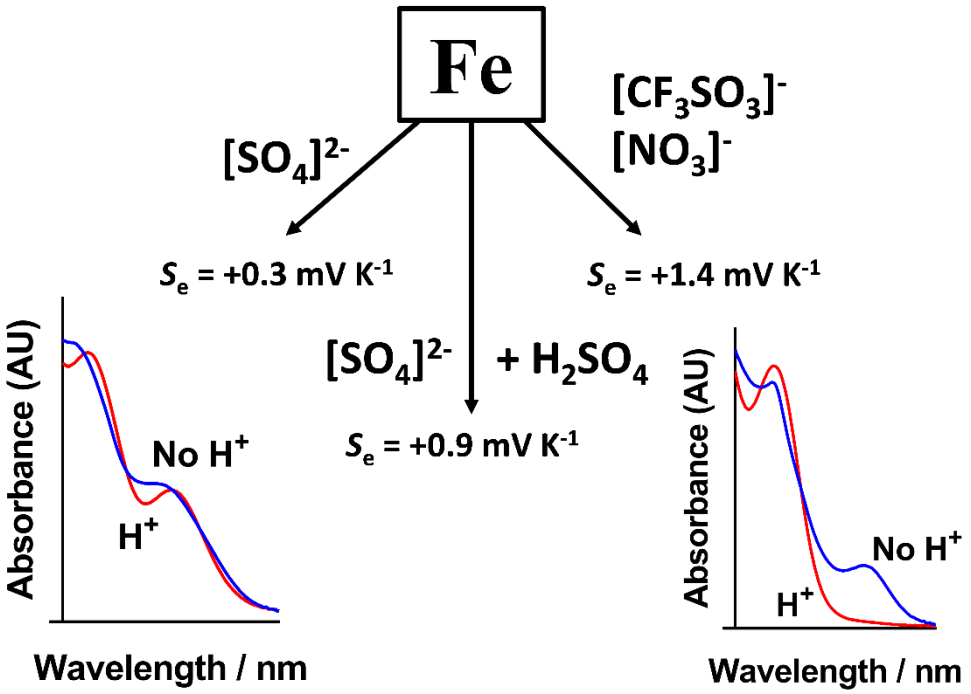

$$[Fe(SO_4)]^{0/+} + H^+ \rightleftharpoons [Fe(HSO_4)]^{+/2+}$$

$$[Fe(OH)_x]^{2+/3+-x} + H^+ \rightleftharpoons [Fe(H_2O)]^{2+/3+}$$

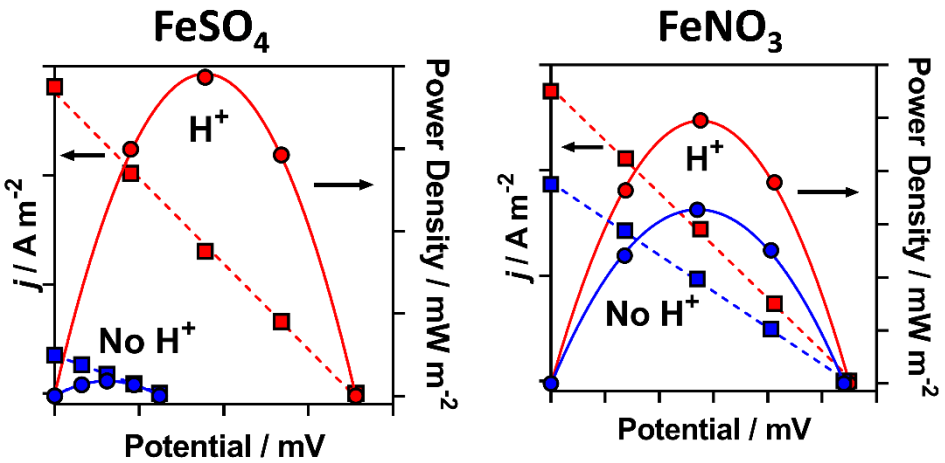

4.2 – Introduction

The $Fe^{2+/3+}$ redox couple is routinely employed as an aqueous n-type (positive Seebeck) thermogalvanic redox couple.[15,36,39,67,88,112] Several iron salts have been investigated for this purpose, in either acidified or un-acidified thermocells. Iron salts such as the iron sulphate,[40,88] iron chloride,[14,15,37,164] and iron perchlorate[38,39] have all been reported. Different iron salts are observed to yield significantly different Seebeck coefficients, ranging from +0.3 mV K^{-1} for the un-acidified $FeSO_4$ redox couple[30,88] to +1.76 mV K^{-1} for the acidified $FeClO_4$ redox couple.[39]

The reason for this substantial difference in Seebeck coefficient is due to the significant differences in co-ordination ability of the anion in the iron salt to the metal centre, significantly altering the charge density of the overall redox couple.[30,36] The co-ordinating ability of a range of anions has previously been compared in lanthanide salts,[165] where anions such as $[Cl]^-$ and $[SO_4]^{2-}$ were found to be strongly coordinating, and anions such as $[ClO_4]^-$ and $[CF_3SO_3]^-$ were found to not be strongly coordinating.[165]

In iron complexes, this difference in coordination ability of anions can result in different species. Non-coordinating anions such as $[ClO_4]^-$, $[NO_3]^-$ and $[CF_3SO_3]^-$ would likely yield the fully-dissociated iron hexaaqua complex ($[Fe(H_2O)_6]^{2+/3+}$).[36,39] Fundamental thermodynamic investigations has determined the $[Fe(H_2O)_6]^{2+/3+}$ redox couple has an entropy difference between the redox couple (ΔS_{rc}) equivalent to a S_e of *ca.* +1.87 mV K^{-1}, at both low ionic strength and under acidic conditions.[69] However, another investigations have reported a ΔS_{rc} equivalent to +1.12 mV K^{-1}, calculated under standard conditions in the absence of anions.[166] More strongly coordinating

anions such as $[SO_4]^{2-}$ and $[Cl]^-$ have been proposed to yield semi-coordinated species in solution, such as the $[Fe(SO_4)(H_2O)_5]^{0/+}$,[30,36,39,113] and $[Fe(Cl)(H_2O)_5]^{+/2+}$.[39]

The iron chloride redox couple has been extensively investigated in aqueous,[99,118,167] gelled,[14,15,164] and ionic liquid solvents.[114] With respect to the aqueous systems, high concentration FeCl has been found to display a Seebeck coefficient of between +0.6 mV K^{-1},[1,99,118] to +0.96 mV K^{-1},[31] and high power densities (of several W m^{-2}) at high ΔT of 150°C.[118] With respect to the gelled electrolyte, the FeCl redox couple has been employed in a PVDF polymer with 10 wt% HCl, yielding a S_e of +1.02 mV K^{-1}, which has been utilised in a thermocell array with the p-type $[Fe(CN)_6]^{3-/4-}$ thermocell.[14] In ionic liquid solvent both FeCl and FeBr actually observe a negative S_e of *ca.* -0.4 mV K^{-1}, proposed to be the $[FeCl_4]^{-/2-}$ and $[FeBr_4]^{-/2-}$ redox couples.[114]

The iron sulphate thermocell has also been demonstrated as a viable n-type candidate to be utilised in-series with the p-type $[Fe(CN)_6]^{3-/4-}$ thermocell.[40,88] However, both the Seebeck coefficient and the power density are considerably lower than the $[Fe(CN)_6]^{3-/4-}$ thermocell, with an observed S_e between +0.3 and +0.54 mV K^{-1} for the un-acidified and acidified iron sulphate systems, respectively.[88] The in-series $[Fe(CN)_6]^{3-/4-}$ and acidified $[Fe(SO_4)]^{0/+}$ thermocells have been utilised to charge various-sized capacitors.[40]

Iron perchlorate is a much more recently explored redox couple, being first reported in 2019.[38,168,169] The Seebeck of the iron perchlorate thermocell is reported to be between +1.65 – +1.76 mV K^{-1}.[38] Almost reaching the theoretical maximum S_e of +1.87 mV K^{-1}.[69] Due to the slightly higher Seebeck coefficient and greater solubility

of the $FeClO_4$ *vs* the $K_{3/4}[Fe(CN)_6]$ thermocell, the iron perchlorate is found to display higher power density.[38]

Herein investigated are four different iron salts, two with strongly coordinating anions: ammonium iron sulphate and iron sulphate, and two much less strongly coordinating anions: iron triflate and iron nitrate. An investigation into the Seebeck coefficient and power density of the four redox couples in presented, along with discussion related to both temperature and pH related speciation of the redox couples in the thermocell. The electrochemistry and electrochemical impedance spectroscopy of the thermocells have also been explored, determining the comparative resistances of the thermocells. Additionally presented is a provisional techno-economic evaluation of the systems, and the relative sustainability of the redox couples assessed.

4.3 – Results and Discussion

4.3.1 – A note on nomenclature used in this chapter

In this chapter, two iron salts are dissolved in water solvent to form solutions of the combined 0.2 M Fe(ii) and 0.2 M Fe(iii) salts (*i.e.* a 0.4 M Fe solution in total with a 50:50 ratio of Fe(ii) and Fe(iii)). The four iron salts investigated are: ammonium iron sulphate, iron sulphate, iron triflate and iron nitrate. For simplicity to both the reader and in writing, these 0.4 M solutions of either ammonium iron sulphate, iron sulphate, iron triflate or iron nitrate have been abbreviated to **$[NH_4]FeSO_4$**, **$FeSO_4$,** **$FeCF_3SO_3$** and **$FeNO_3$**, respectively. These abbreviations represent the solutions of Fe generated from the salt dissolved in aqueous solvent and will be used throughout the rest of the chapter.

4.3.2 – Seebeck and entropy of the iron redox couples

The thermodynamics of four iron salt redox couples: **$[NH_4]FeSO_4$**, **$FeSO_4$**, **$FeCF_3SO_3$** and **$FeNO_3$** either in the presence or absence of 1 M of the anions' conjugate acid (H_2SO_4, CF_3SO_3H and HNO_3 respectively) were all investigated. The observed Seebeck coefficient (S_e) and the calculated redox couple entropy (ΔS_{rc}) are both displayed in Figure 33 and are also tabulated in Table 7. Here it is worth noting that these values have been corrected for our 'observed' ΔT of 18 K, rather than the 'applied' ΔT of 20 K.

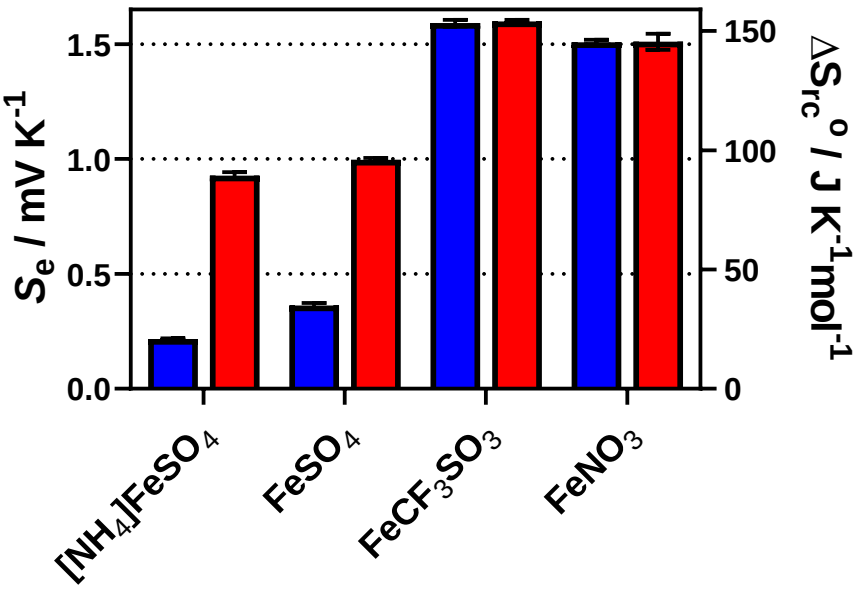

Figure 33 - Bar chart showing the Seebeck coefficient (S_e) and redox couple entropy (ΔS_{rc}) for various Fe(ii)/Fe(iii) systems, in the presence (red) and absence (blue) of 1 M of the anions conjugate acid. The counter-ion is specified for clarity. All are reported at ΔT = 20°C (T_{hot} = 35°C and T_{cold} = 15°C) and error bars are 1 SD of triplicate measurements. All Fe(ii)/Fe(iii) redox couples were present in a 50 : 50 ratio, and the solutions prepared to contain 0.2 M of the Fe(ii) salt and 0.2 M of the Fe(iii) salt (total redox active concentration 0.4 M).

Table 7 - Table of data showing the apparent Seebeck Coefficients, S_e, and corresponding difference in entropy between the redox couple (ΔS_{rc}). Values are reported in the absence and presence of 1 M of the anions' conjugate acid. All only apply for 0.2 M of the Fe(ii) salt and 0.2 M of the Fe(iii) and when measured at ΔT = 20°C (T_{hot} = 35°C; T_{cold} = 15°C) given the significant temperature and concentration sensitivities of these systems. Error values are the standard deviation of triplicate measurements.

Fe system	Seebeck coefficient / mV K^{-1}		ΔS_{rc} / J K^{-1} mol^{-1}	
	Un-acidified	Acidified	Un-acidified	Acidified
$[NH_4]FeSO_4$	0.22 ± 0.01	0.93 ± 0.01	20.9 ± 0.3	89.6 ± 1.4
$FeSO_4$	0.36 ± 0.01	1.00 ± 0.01	35.0 ± 1.0	96.1 ± 0.9
$FeCF_3SO_3$	1.59 ± 0.01	1.60 ± 0.01	153 ± 1	154 ± 0.7
$FeNO_3$	1.51 ± 0.01	1.51 ± 0.04	146 ± 1	146 ± 3

In the absence of acid, the observed S_e of the two sulphate-based redox couples (**$[NH_4]FeSO_4$** and **$FeSO_4$**) were found to observe the expected and previously reported S_e of *ca.* +0.3 mV K^{-1}.[88] However, both these systems observed significantly lower S_e than that of the triflate or nitrate-based redox couples (**$FeCF_3SO_3$** and **$FeNO_3$** respectively, Figure 33). With the highest observed S_e for the **$FeCF_3SO_3$** system reaching *ca.* +1.6 mV K^{-1}, and the S_e of the **$FeNO_3$** system observed a S_e of *ca.* +1.5 mV K^{-1}.

The Seebeck coefficient of redox couples is known to be highly dependent on ionic strength.[35,94] Therefore it is important to note that the four investigated systems (**$[NH_4]FeSO_4$**, **$FeSO_4$**, **$FeCF_3SO_3$** and **$FeNO_3$**) consist of a total concentration of 0.4 M, made up of 0.2 M of the Fe(ii) and 0.2 M of the Fe(iii) salt in solution. This represents a high ionic strength, which is also significantly increased by addition of 1

M of the conjugate acids. It should also be noted that the Fe(ii)(NO_3) could not be purchased, and had to be synthesised *in-situ* from $FeCl_2$ and $AgNO_3$.

The observed S_e of the **$FeCF_3SO_3$** and **$FeNO_3$** systems were found to be relatively independent of pH. Where systems in the presence of acid both display a S_e *ca.* +1.5 - +1.6 mV K^{-1}. Which at the time of publication was a record for aqueous iron-based n-type thermocell redox couples.[36] This is a significant observation as the high S_e is even higher in the n-type direction than the standard thermoelectrochemical redox couple, namely the p-type $[Fe(CN)_6]^{3-/4-}$, which has a high S_e of -1.4 mV K^{-1}.[35,67,94]

The Seebeck coefficient of both the **$[NH_4]FeSO_4$** and **$FeSO_4$** systems were found to be significantly dependent on pH. The S_e of both increase to *ca.* +0.95 mV K^{-1} from +0.22 and +0.36 mV K^{-1} for the **$[NH_4]FeSO_4$** and **$FeSO_4$** salts, respectively. Iron salts and iron complexes are known to have very strong dependence on speciation with regard to pH, where at a pH > *ca.* 2.5 iron forms insoluble $Fe(OH)_x$ complexes.[30,113] The Fe^{3+} species is also found to be significantly more reactive with respect to the solvent water molecules. This is demonstrated by the significantly more acidic (> 1 pH unit lower than the Fe^{2+}), nature of the Fe^{3+} solution in the absence of Fe^{2+}, which is caused by the Fe^{3+} ion undertaking hydrolysis of water, as in equilibrium 27.

Due to the significant dependence on speciation in the thermocell with respect to both the anion and $[OH]^-$, there are three competing equilibria present in the two sulphate systems. Where equilibrium (27) is also present for the **$FeNO_3$** and **$FeCF_3SO_3$** systems, but equilibrium (28) and (29) are not.

$$[Fe(H_2O)_6]^{3+} \rightleftharpoons [Fe(OH)(H_2O)_5]^{2+} + H^+ \quad (27)$$

$$Fe^{2+/3+} + [SO_4]^{2-} \rightleftharpoons [FeSO_4]^{0/+} \quad (28)$$

$$[Fe(SO_4)]^{0/+} + H^+ \rightleftharpoons [Fe(HSO_4)]^{+/2+} \quad (29)$$

The **$FeSO_4$** systems in the absence of acid observe low S_e, due to the strong association of the $[SO_4]^{2-}$ anion to the Fe ions, resulting in the low charge $[Fe(SO_4)]^{0/+}$ redox couple.[30,39] However, in the presence of acid the observed S_e increases dramatically, due to the protonation of $[Fe(SO_4)]^{0/+}$, forming the $[Fe(HSO_4)]^{+/2+}$ redox couple (Equilibrium 29). The $[HSO_4]^-$ anion is evidently still strongly coordinating compared to $[CF_3SO_3]^-$, $[NO_3]^-$ and $[ClO_4]^-$ due to the lower observed S_e. In order to evaluate the extent of the speciation of the redox couples, the effect of both temperature and pH with regard to UV-Vis spectroscopy of the redox couples was investigated.

4.3.3 – pH effect

Altering the pH of the **$[NH_4]FeSO_4$** and **$FeSO_4$** systems was found to display a significant change in S_e, increasing both systems to *ca.* $+0.95 \pm 0.05$ mV K^{-1}. This is caused by changes in speciation present within the thermocell, where process (28) and (29) are in competition. In a strongly acidic environment process (29) will be dominant, yielding slightly less strongly coordinating $[HSO_4]^-$ anions,[165] and a higher charge $[Fe(HSO_4)]^{+/2+}$ redox couple.[30,36]

In the absence of introduced acid, the four iron systems were found to have an inherent acidity that increased in the order: **$[NH_4]FeSO_4$** < **$FeSO_4$** < **$FeCF_3SO_3$** < **$FeNO_3$**. As mentioned previously, this acidity is due to the hydrolysis of water in

process (27), and is dominated by the Fe^{3+} species.[36] The highest concentration of H^+ generated was *ca.* 40 mM, (Figure 34) equivalent to 20 % of the total Fe^{3+} concentration in the thermocell. Therefore, despite hydrolysis of water occurring in these systems, the majority of the species in solution for the **$FeCF_3SO_3$** and **$FeNO_3$** systems are still expected to be $[Fe(H_2O)_6]^{2+/3+}$. It is also predicted that the $[Fe(H_2O)_{6-x}(OH)_x]^{3+-x}$ species are thermodynamically silent in the thermocell, as the S_e hardly changes with the addition of 1 M conjugate acid (Figure 34) in these systems. Clearly the $[Fe(H_2O)_6]^{2+/3+}$ redox couple dominates the observed S_e for both the **$FeCF_3SO_3$** and **$FeNO_3$** systems (observed by their equivalent S_e).

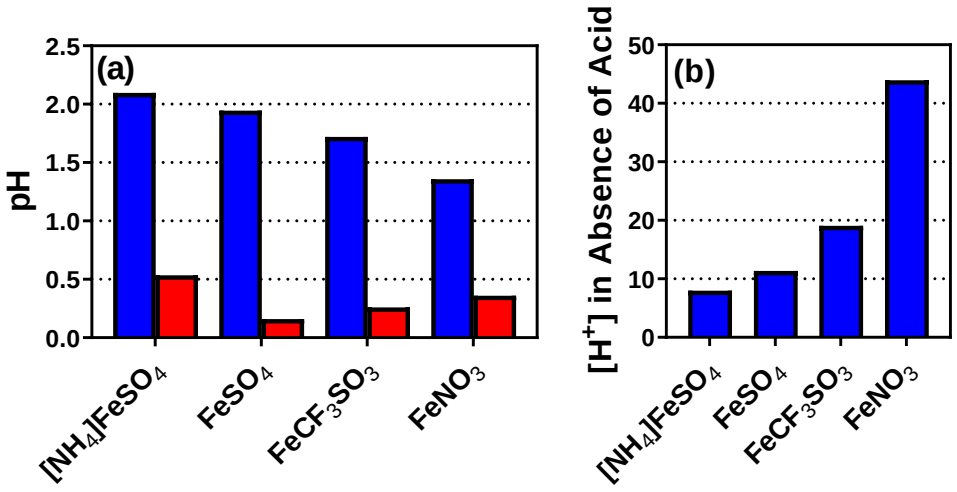

Figure 34 –Plots showing (a) the pH of the four different 0.4 M Fe(II)/Fe(III) systems, for their inherent pH (blue) and after addition of 1 M of their conjugate acid (red). Also shown, (b) is the concentration of protons, $[H^+]$, present in solution for the un-acidified systems; the concentration of $[H^+]$ present indicates the extent to which process **(27)** (*i.e.* $[Fe(OH)_x]^{3+-x} + H^+$) occurs.

The pH-dependence on the UV-Vis spectra of all four thermocell systems was also measured, where the UV-Vis spectra in both the absence and presence of 1 M of the anions' conjugate acid was recorded. Broadly, the **$[NH_4]FeSO_4$** system displayed the same spectra as the **$FeSO_4$**, and the **$FeNO_3$** system displayed a similar spectra to the **$FeCF_3SO_3$**, with the exception of a much greater intensity of the peak *ca.* 230 nm (Figure 35).

Figure 35 demonstrates that both the **$FeSO_4$** and **$[NH_4]FeSO_4$** observe the same spectra. Centred *ca.* 240 nm, and *ca.* 295 nm which can be attributed to $[Fe(H_2O)_6]^{3+}$[30,36,39,170] and $[FeSO_4]^{+}$,[30,36,39] respectively. The **$FeCF_3SO_3$** and **$FeNO_3$** observe a peak centred *ca.* 330 nm, which can be attributed to $[Fe(OH)_x]^{3+-x}$ species.[36,39,170] The **$FeCF_3SO_3$** system also observes the $[Fe(H_2O)_6]^{3+}$ peak at around the same intensity as the **$FeSO_4$** and **$[NH_4]FeSO_4$** systems. However, the **$FeNO_3$** system displays a peak centred around the same wavelength of a much higher intensity. The high intensity of the peak *ca.* 230 nm can be attributed to the $[NO_3]^-$ anion[36] (Figure A1).

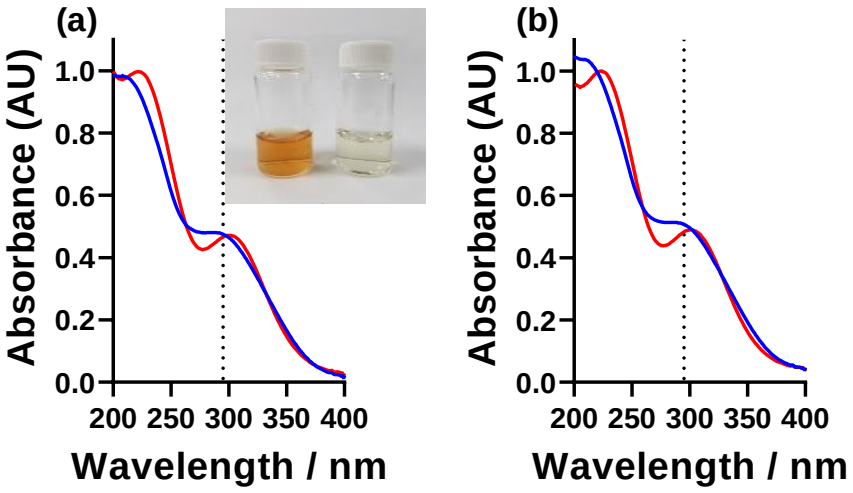

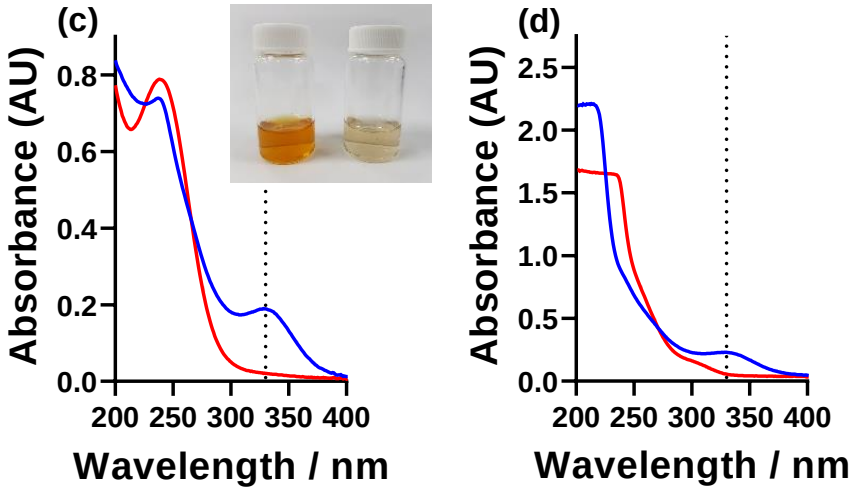

Figure 35 – (a-d) UV-Vis spectra of (a) **$FeSO_4$**, (b) **$[NH_4]FeSO_4$**, (c) **$FeCF_3SO_3$** and (d) **$FeNO_3$** solutions for concentrations of 0.02 M of the Fe(ii) and 0.02 M Fe(iii) salts in the absence (blue) and presence (red) of 1 M conjugate acid. Inset in (a) and (c) – photos of these systems at the 0.4 M Fe(ii)/Fe(iii) concentration used elsewhere, in the absence (left in inset) and presence (right in inset) of 1 M conjugate acid. The wavelength of (a & b) 295 nm and (c & d) 330 nm has been highlighted by a ticked line.

Next the effect of pH on the UV-Vis spectra for these systems was measured. For the **$[NH_4]FeSO_4$** and **$FeSO_4$** systems, the peaks centred *ca.* 220 nm and 290 nm both became sharper with the presence of acid (Figure 35(a & b)), consistent with a shift in a dynamic equilibrium. But neither peak was removed, or changed wavelength, so the species present in the absence of acid appeared to remain in the presence of acid. It is therefore difficult to distinguish between $[Fe(SO_4)]^+$ and $[Fe(HSO_4)]^{2+}$ through UV-Vis spectroscopy, as the introduction of a high concentration of acid is expected to increase the $[Fe(HSO_4)]^{2+}$ character of the system.[30] Due to this, it is also difficult to assess the extent of a shift in the two equilibria (28) and (29) with the introduction of acid.

For the **$FeCF_3SO_3$** system, addition of acid resulted in a sharpening of the $[Fe(H_2O)_6]^{3+}$ peak (centred at 220 nm). For the peak *ca.* 330 nm in both the **$FeCF_3SO_3$** and **$FeNO_3$** systems, introduction of acid resulted in the complete removal of the $[Fe(OH)_x]^{3+-x}$ peak (centred at 330 nm) (Figure 35(c & d)). Demonstrating a shift in process (27) completely to the left, removing all $[Fe(OH)_x]^{3+-x}$ species. This clearly has no effect on the observed thermodynamics of the thermocell, demonstrated by the equivalent S_e from both the acidified and un-acidified **$FeCF_3SO_3$** and **$FeNO_3$** systems. pH is not the only factor expected to have a significant impact on speciation, temperature is also expected to have an impact. Therefore, the temperature effect on both the S_e and the UV-Vis spectroscopy was measured.

4.3.4 – Temperature-dependent speciation

In ideal conditions, the Seebeck coefficient is a temperature-independent parameter,[3] therefore altering the temperature within the thermocell (whether that is with a constant ΔT or changing ΔT) should yield equivalent Seebeck coefficients. To measure this, reducing the ΔT of the thermocell by increasing the T_{cold} was investigated. Temperature-independent S_e were observed for both the un-acidified and acidified **$FeCF_3SO_3$** and **$FeNO_3$** systems, and the acidified **$FeSO_4$** and **$[NH_4]FeSO_4$** systems.

However, for both the un-acidified **$[NH_4]FeSO_4$** and **$FeSO_4$** systems, the S_e was found to be temperature-dependent, most significantly in the **$[NH_4]FeSO_4$** system (Figure 36(a)). At the lower T_{cold} temperature (high ΔT) the **$[NH_4]FeSO_4$** system has a significantly higher S_e than at higher T_{cold} temperature (low ΔT). The observed S_e

was +0.20 mV K^{-1} for the 20 K ΔT and +0.10 mV K^{-1} for the 5 K ΔT. This significant temperature-dependence on the S_e is due to the temperature-dependence of anion association to the iron metal centre.[30,36] It can be inferred from the observed change in S_e that the Fe-$[SO_4]^{2-}$ interactions are stronger at higher temperatures. Owing to a temperature-dependent shift in equilibrium (28) leading to a relative shift in speciation.

UV-Vis of the **$FeSO_4$** and **$FeCF_3SO_3$** systems were undertaken at various temperatures in order to gain a better understanding of the temperature-dependent speciation present. Initially, the Fe^{2+} and Fe^{3+} species were measured independently, but the Fe^{2+} system was found to display no appreciable signal,[30,36] therefore all discussion will be of the Fe^{3+} systems only.

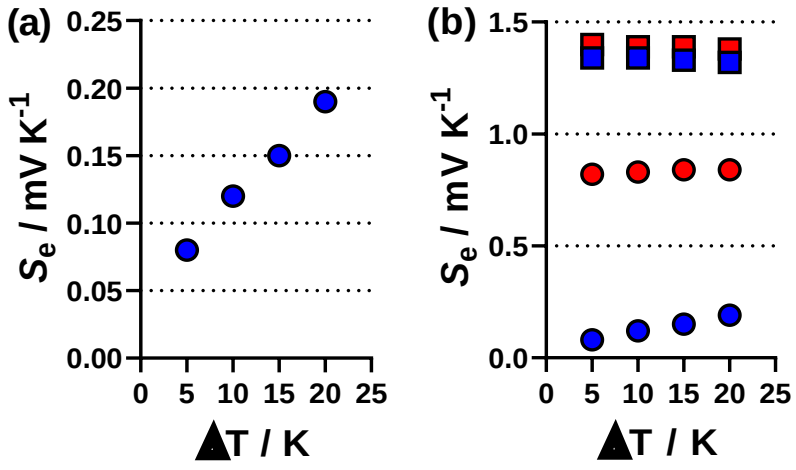

Figure 36 - Plots showing the variation in the apparent Seebeck coefficient (S_e), against ΔT (T_{hot} = 35°C, T_{cold} = 15 to 30°C), for (a) the un-acidified **$[NH_4]FeSO_4$** system, and (b) both the un-acidified (blue) and acidified (red) **$[NH_4]FeSO_4$** (circles) and **$FeNO_3$** (squares) systems. All other conditions match those in Figure 1. The high temperature sensitivity of the apparent S_e of the un-acidified **$[NH_4]FeSO_4$** system against ΔT is immediately apparent, as is the relatively more minor variations in the other three systems.

Both the $[Fe(SO_4)]^+$ and $[Fe(OH)_x]^{3+-x}$ peaks (at 295 nm and 330 nm respectively) were found to increase in intensity with increasing temperature (Figure 37). This does not demonstrate any specific change in speciation, simply shifting to the right of both equilibria (27) and (28) respectively (*i.e.* increasing both $[FeSO_4]^+$ and $[Fe(OH)_x]^{3+-x}$ character within solution). This is supported by the temperature dependent S_e of the **$[NH_4]FeSO_4$** system, where decreasing the ΔT from 20°C to 5°C (by increasing the temperature of the cold electrode from 15°C to 30°C) is found to decrease the Seebeck coefficient, which is likely caused by increasing the $[Fe(SO_4)]^+$ character of the system.[30,36,39] The observed increase in $[Fe(OH)_x]^{3+-x}$ character in the **$FeNO_3$** system is also consistent with the thermoelectrochemical results, where the $[Fe(OH)_x]^{3+-x}$ species appears to be thermodynamically inactive.

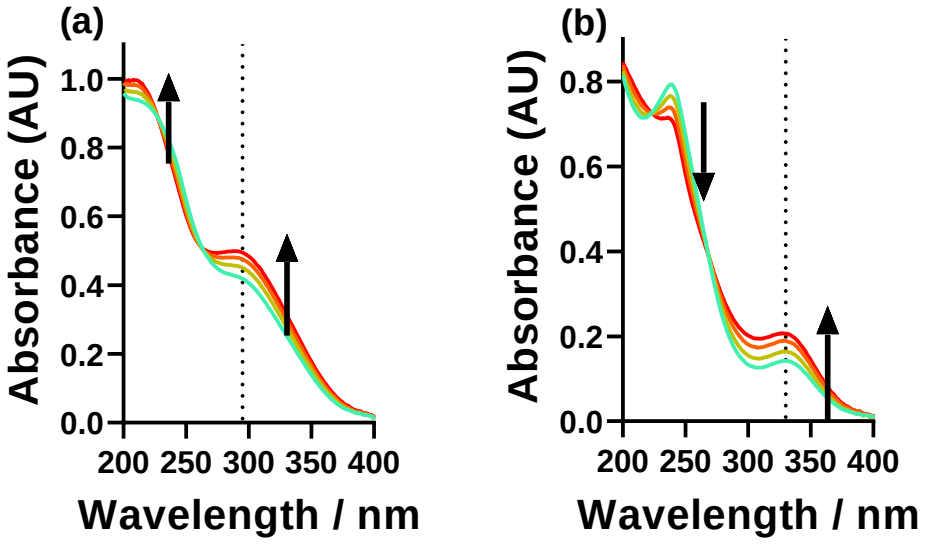

Figure 37 - UV-Vis spectra of (a) 20 mM **$FeSO_4$** and (b) **$FeCF_3SO_3$** recorded at temperature intervals of 10°C at 5°C (blue), 15°C (yellow), 25°C (orange) and 35°C (red); arrows indicate if absorption increased or decreased going from cold to hot. Dotted lines are added for clarity at peaks corresponding to a) 295 nm $[Fe(SO_4)]^+$ and b) 330 nm $[(Fe(OH)_x]^{3+-x}$.

The significant difference in speciation with both pH and temperature is assumed to have a significant impact upon the kinetics of the thermocell, even in the absence of having an impact on the thermodynamics of the thermocell. To assess this, thermogalvanic power of all four systems in the absence and presence of acid was measured.

4.3.5 – Power density of the iron redox couples

The power density of the four iron systems were investigated both in the presence and absence of acid. Figure 38 shows representative power curves of all the investigated systems, with the values tabulated in Table 8. As the voltage output of a thermocell is proportional to the S_e (Equation 8) the expected large increase in output voltage (expected for the significant increase in S_e) of the **[NH$_4$]FeSO$_4$** and **FeSO$_4$** systems was observed. Also observed in these systems was a significant increase in current density (and therefore power density as P = IV).[24,25]

The power density of the two un-acidified **[NH$_4$]FeSO$_4$** and **FeSO$_4$** systems were found to be equivalent (within error). However, upon acidification, the power density of **FeSO$_4$** was observed to be much higher than **[NH$_4$]FeSO$_4$**. In these systems, a 13-fold (from 0.48 ± 0.05 to 6.12 ± 0.90 mW m^{-2}) and 18-fold (from 0.56 ± 0.06 to 10.2 ± 2.0 mW m^{-2}) increase in power density was observed upon acidification of the **[NH$_4$]FeSO$_4$** and **FeSO$_4$**, respectively (Figure 38(a & b)). This discrepancy is initially surprising, given both these systems observe equivalent S_e when acidified. The higher power density of **FeSO$_4$** is therefore due to the significantly higher observed current

density. The reason for this significant difference in the two acidified systems is unknown and is discussed further in the next section (4.3.6).

With respect to **$FeCF_3SO_3$** and **$FeNO_3$**, the observed S_e does not change with acidification, therefore the output voltage at open circuit also does not change. For both systems, a significant increase in power density is observed from an increase in current density upon acidification (Figure 38(c & d)). This can easily be rationalised by the observed pH dependence on the UV-Vis (Figure 35(c & d)), where the complete removal of any hydroxide species is observed. From this, it is possible to postulate that the $[Fe(H_2O)_6]^{2+/3+}$ species are far more thermogalvanically active than the $[Fe(OH)_x]^{3+-x}$ species. This can be rationalised as an *ca.* 60 – 80 % increase in current, and the corresponding increase in power density of *ca.* 60 – 80 % is observed upon addition of acid.

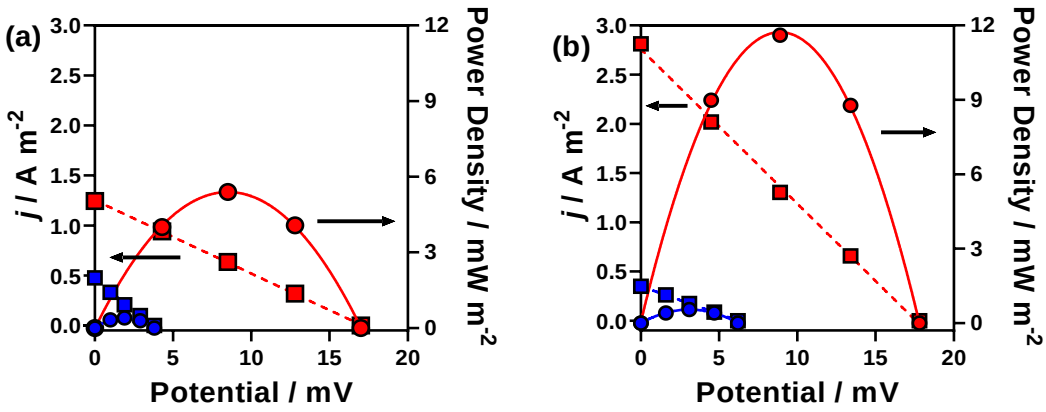

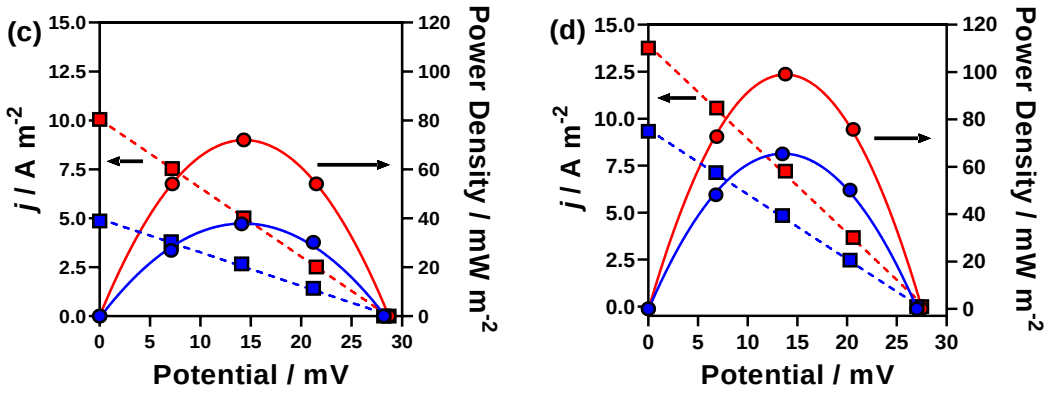

Figure 38 – Plots of both power density, and current density *vs.* potential for (a) **[NH₄]FeSO₄**, (b) **FeSO₄**, (c) **FeCF₃SO₃** and (d) **FeNO₃**. Current densities are shown as squares with dashed lines and power densities as circles with solid lines, in the absence (blue) and presence (red) of 1 M conjugate acid at $\Delta T = 20°C$.

The acidified **[NH₄]FeSO₄** was found to observe a much lower power density than the acidified **FeSO₄** system, also the **FeCF₃SO₃** systems (both un-acidified and acidified) were found to yield much lower power density than the equivalent **FeNO₃** thermocells. These observations cannot be easily rationalised by any of the previous investigations. Therefore, the four iron systems were electrochemically probed by cyclic voltammetry and electrochemical impedance spectroscopy.

Table 8 - Table of data showing the short circuit current density and maximum power density values for the four Fe(ii)/Fe(iii) systems (all for 0.2 M Fe(ii) and 0.2 M Fe(iii), recorded at Au electrodes with T_{hot} = 35°C and T_{cold} = 15°C. Error values are the standard deviation of triplicate measurements.

Fe system	Current Density (*j*) / A m^{-2}		Power Density / mW m^{-2}	
	Un-acidified	Acidified	Un-acidified	Acidified
$[NH_4]FeSO_4$	0.50 ± 0.05	1.47 ± 0.23	0.48 ± 0.05	6.12 ± 0.90
$FeSO_4$	0.34 ± 0.03	2.28 ± 0.46	0.56 ± 0.06	10.2 ± 2.0
$FeCF_3SO_3$	4.78 ± 0.84	8.56 ± 2.01	34.2 ± 6.0	61.6 ± 14.7
$FeNO_3$	8.84 ± 0.69	14.0 ± 1.3	60.0 ± 4.3	95.1 ± 7.0

4.3.6 – Cyclic voltammetry

Cyclic voltammograms (CVs) were recorded of the four iron systems, at equal concentration (400 mM total concentration) to the other measurements undertaken in this study. This represents extremely concentrated solutions and in the un-acidified systems a general absence of supporting electrolyte, but is consistent with typical thermoelectrochemical investigations.[30,35,36] Figure 39 displays the recorded CVs, along with the peak-to-peak separation (ΔE) of each redox couple. Generally, ΔE in the CVs correlate with the thermogalvanic power of the thermocell systems observed in Figure 38, where a decrease in ΔE is consistent with an increase in thermogalvanic power. Particularly with respect to the un-acidified and acidified comparison of the same species. A decrease in ΔE relates to faster electrode kinetics at the electrode surface.[80] However, from the CV data alone it isn't possible to determine whether this is an electrolyte effect (in the form of 1 M H^+) or whether the electrocatalysis of the electrode surface improves due to the removal of any $[Fe(OH)_x]^{3+-x}$, and the formation

of $[Fe(HSO_4)]^{+/2+}$. In order to further investigate this, Electrochemical impedance spectroscopy was employed.

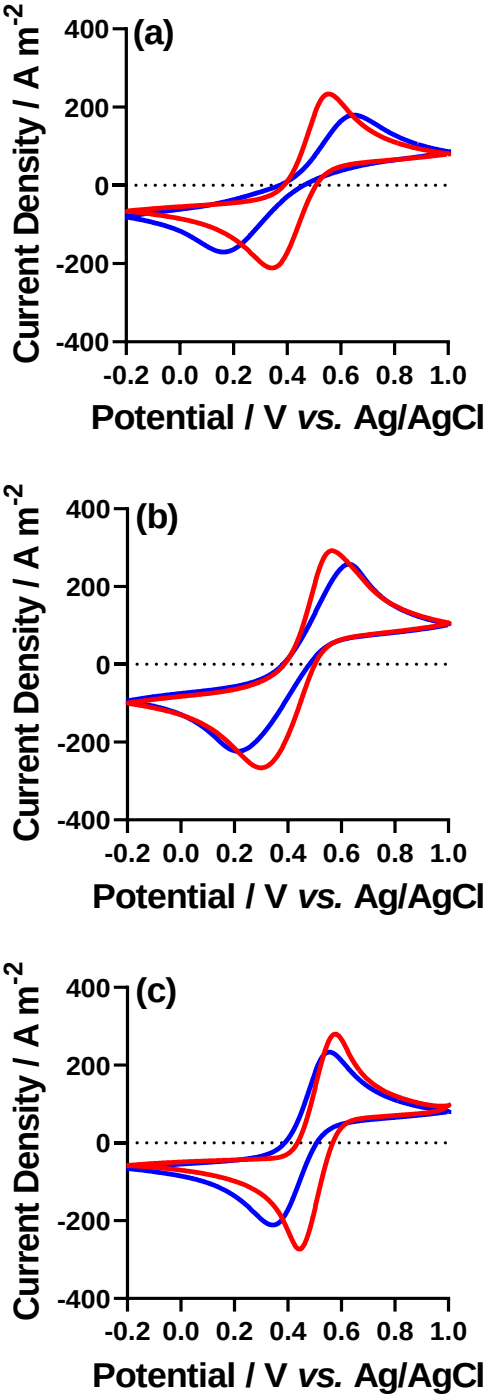

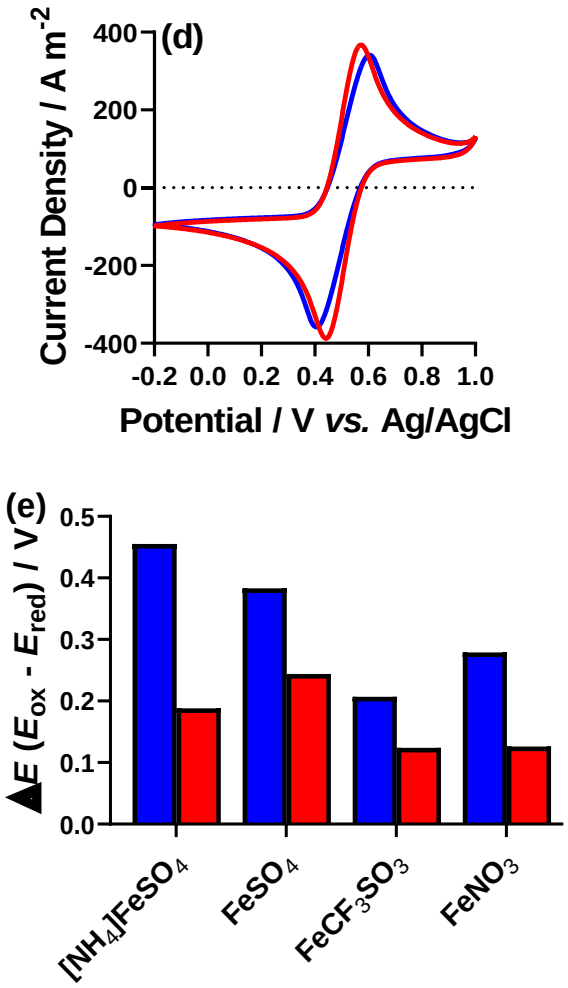

Figure 39 – Cyclic voltammograms recorded for (a) **NH_4FeSO_4** (b) **$FeSO_4$**, (c) **$FeCF_3SO_3$** and (d) **$FeNO_3$** both in the presence (red) and absence (blue) of 1 M conjugate acid with respect to the counter-anion. Recorded using a Au working electrode at 50 mV s^{-1}, *vs.* a Ag|AgCl reference electrode. e) plot of the peak-to-peak separation (ΔE) for all the four iron salts both in the absence (blue) and presence (red) of respective conjugate acid.

The peak current density of the CVs follow the expected trend from the thermogalvanic power, where **$FeSO_4$** observes a higher i_p than **$[NH_4]FeSO_4$** and **$FeNO_3$** observes a higher i_p than **$FeCF_3SO_3$**. This result offers insight into why the thermogalvanic current (and power) densities of the **$FeNO_3$** and **$FeSO_4$** systems are

higher of the two distinct types of systems. However, this does not explain why these systems out-perform their counterparts, to further investigate the cause of the lower thermogalvanic and cyclic voltametric current, electrochemical impedance spectroscopy was employed.

4.3.7 – Electrochemical impedance spectroscopy

Impedance spectroscopy was performed on the four thermocell systems. This was measured *ex situ* at isothermal temperature (*ca.* 25°C) in the presence and absence of acid. The resulting data was fitted using the simplest model possible (model shown in Figure E5). From this, the solution (or mass transport) (R_S) and electron transfer (or polarisation) (R_{ET}) resistances were determined and are displayed in Figure 40(a &b).

With respect to the R_S, the resistance is significantly lower in the presence of acid, due to supporting electrolyte effect of 1 M [H^+] within the solution. The high R_S of the **$FeSO_4$** system is likely a result of complex speciation, as in (28), and the ion association between the $Fe^{2+/3+}$ and $[SO_4]^{2-}$.[113] This is offset somewhat in the **$[NH_4]FeSO_4$** system, by the presence of extra $[NH_4]^+$ ions acting as an inherent supporting electrolyte.[36] Similar to the inherent charge of a super-absorbent polymer, reducing R_S for $FeCl_{2/3}$.[171]

With respect to the R_{ET}, the **$FeCF_3SO_3$** and **$FeNO_3$** systems have significantly lower R_{ET} than the **$[NH_4]FeSO_4$** and **$FeSO_4$** systems (Figure 40(b)). As with the R_S of these two systems, addition of acid was also found to decrease the R_{ET}, consistent with improved electron transfer kinetics. Surprisingly, for the two sulphate systems, the R_{ET} was found to be considerably higher when acidified. This is due to the presence of

large quantities of $[SO_4]^{2-}$ and $[HSO_4]^-$, which is known to have strong association ability to gold surfaces, poisoning the electrode surface by hindering the formation of electrocatalytic gold oxide,[172] and thus increasing the R_{ET}.[173]

As previously discussed, there is a difference in speciation of the thermocell solutions, where the two sulphate systems are either the $[Fe(SO_4)]^{0/+}$ in the absence of acid or $[Fe(HSO_4)]^{+/2+}$ in the presence of acid,[30,36] and the other two systems are the $[Fe(H_2O)_6]^{2+/3+}$ species in solution. Due to the difference in speciation of the iron-ions, pH-induced surface modification of the gold electrode surface could result in significantly different electrocatalytic ability of the electrode surface. Where formation or removal of oxides on gold electrodes is known to significantly alter the electrocatalytic ability of gold towards the $Fe^{2+/3+}$ redox couple.[172,174,175]

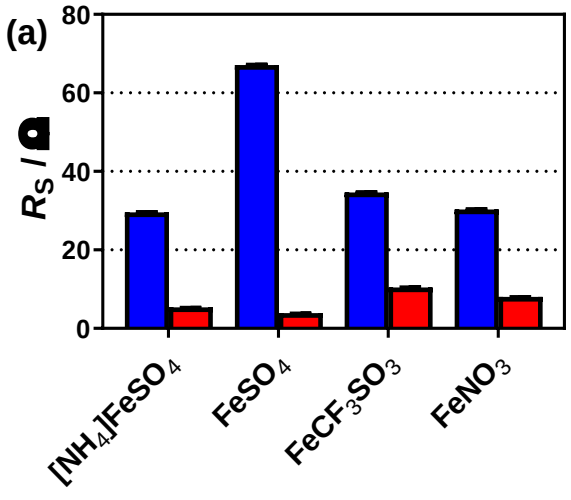

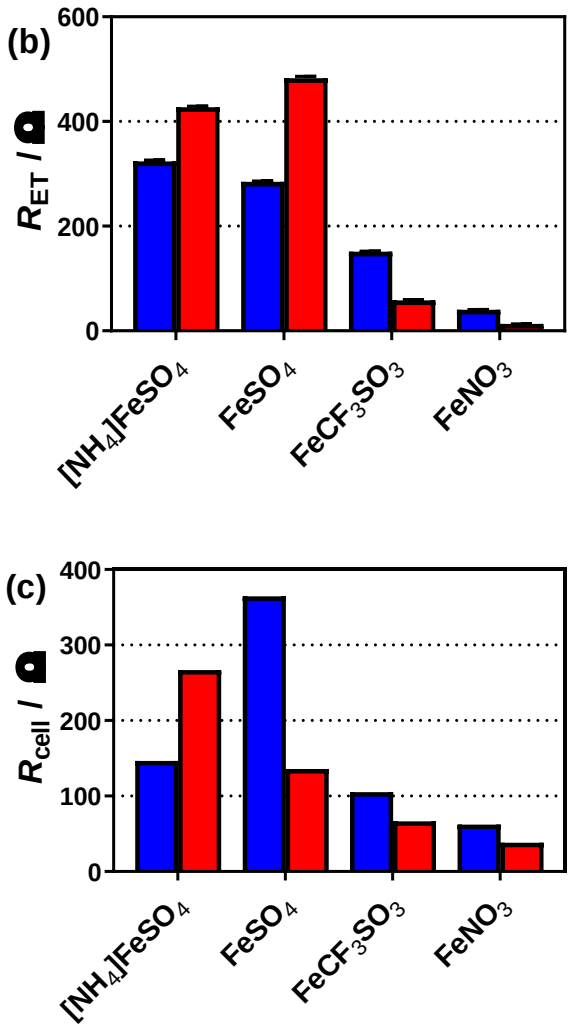

Figure 40 - Plots of the (a) solution (or mass transport) resistance (R_S), and (b) electron transfer (or polarisation) resistance (R_{ET}), measured under isothermal conditions using electrochemical impedance spectroscopy. Also shown is the (c) calculated internal resistance of the thermogalvanic cell (R_{cell}) at $\Delta T = 20°C$, R_{cell}, based upon Ohms law (V = IR) and the I–V plots shown in Figure 38, where for each system the unacidified (blue) and acidified (red) resistances are shown.

Also displayed in Figure 40 is the calculated overall resistance of the thermocell (R_{cell}) under *operando* conditions, calculated from the power density *I-V* curves. As these are two significantly different conditions, this comparison is not

meant to be quantitative, but comparisons in observed trends can still be informative.[††] Here, the **$FeCF_3SO_3$** and **$FeNO_3$** systems follow the expected trend from the isothermal impedance R_S and R_{ET} observations. However, in the *operando* thermocell, the acidified **$FeSO_4$** system has significantly lower R_{cell} than the un-acidified **$FeSO_4$** thermocell, demonstrating that under *operando* conditions, the effect of added supporting electrolyte is overcoming the observed decrease in electrocatalysis demonstrated by the increase in R_{ET}, which is still dominating the **$[NH_4]FeSO_4$** thermocell.

4.3.8 – Sustainability

The four iron-based thermocell redox couples clearly demonstrate their feasibility to convert thermal-to-electrical energy through thermoelectrochemistry. However, it is also important to evaluate the sustainability of the redox couples. Here, the redox couples have been evaluated both with respect to the 12 principles of green chemistry,[176] and using a simple cost-comparison. Firstly, the cost-analysis of the four thermocell systems is discussed.

It is premature to consider this a complete technoeconomic evaluation of the thermocell systems,[36] but is an informative comparison when evaluating the best thermocell system on a cost-effective basis. Table 9 describes the overall cost of both

[††] Impedance measurements of resistance values in an isothermal setup *ex situ* are expected to be significantly different to *operando* conditions at non-isothermal temperature differences. Furthermore, the internal resistance reported for the thermocell represents a steady-state discharge system; here there will be significantly altered redox ratios at the electrode surfaces, and the mass transfer in the thermogalvanic cell often involves more than simple diffusion. Therefore, quantitative comparison between such impedance measurements and actual *operando* internal resistance characteristics need to be approached with caution, but can be used as an informative qualitative tool.

the un-acidified and acidified thermocells investigated in this chapter. Along with a ratio of cost : power, where acidification typically displays a considerable cost-benefit advantage. Both the acidified **$FeSO_4$** and **$FeNO_3$** systems display excellent comparative cost-effectiveness, especially when compared to the **$FeCF_3SO_3$** systems, which are significantly less competitive due to the much higher cost of the **$FeCF_3SO_3$** salts. (Tabulated values can be found in Table A1)

The **$[NH_4]FeSO_4$** and **$FeSO_4$** systems both demonstrate significant improvements in cost-effectiveness upon acidification (*ca.* 10-fold increase for the **$[NH_4]FeSO_4$** system and an *ca.* 17-fold increase for the **$FeSO_4$** system). This is due to the significant improvement in power density of both of these systems (Figure 38), and the cheap nature of acids. A lesser increase in cost-effectiveness of the **$FeCF_3SO_3$** and **$FeNO_3$** systems are observed due to more modest improvements in power density. This provisional cost-comparison demonstrates that despite the significantly higher observed power density for the acidified **$FeNO_3$** system, the acidified **$FeSO_4$** is equivalent in cost-effectiveness, due to the significantly lower cost of materials. This demonstrates the importance of this type of analysis when considering scale up of such devices.

As discussed, economics are not the only aspect of these thermocell systems that need to be considered if they are ever to become viable for large-scale waste thermal energy harvesting. The 12 principles of green chemistry are another metric that can be used to compare the ‘greenness’ of these systems, these principles therefore represent another method of assessing and comparing the investigated redox couples.

However, only two of these principles are found to apply here, principle one (designing safer chemicals) and principle 10 (design for degradation).[176]

Table 9 – Preliminary economic comparison of the four iron systems, showing cost per reagent to fill the cell. The ratio of cost to power (£ / mW, for $\Delta T = 20$ K) is an arbitrary ratio and represents just one second of measurement; extended use of these cells would reduce this considerably.

Iron System	Cost of cell / £		Ratio of Cost : Power / £ mW^{-1}	
	Un-Acidified	Acidified	Un-Acidified	Acidified
$[NH_4]FeSO_4$	0.0074	0.0082	304	27
$FeSO_4$	0.0055	0.0063	196	12
$FeCF_3SO_3$	1.42	1.48	823	399
$FeNO_3$	0.057	0.058	19	12

All toxicity data available for the iron salts (which was admittedly not many) fall under the 'moderately toxic' range of the Gosselin, Smith, and Hodge oral toxicity rating. As all the iron salts are utilised in high concentration, they cannot be easily distinguished with respect to toxicity. The acidified samples are all also dominated by both the corrosive nature and severe ecological toxicity of strong acids;[177] these represent a more severe risk to safety and again are all essentially equal for the four systems as an undesirable property.

With respect to designing for degradation, the ions should be as benign and biodegradable as possible.[36,176] Here the $[CF_3SO_3]^-$ anion stands out as undesirable due to its highly fluorinated nature, with no evidence of biological degradation.[178] The

$[SO_4]^{2-}$ and $[HSO_4]^-$ anions are both naturally abundant and are found in many water sources, including tap water.[36] The $[NO_3]^-$ and $[NH_4]^+$ ions are also widely available in ecological environments,[179,180] and are used extensively in fertilizers as a nitrogen source for flora. However, it should be noted that a surplus of these ions can be detrimental to the ecological system, leading to problems such as eutrophication.[181]

Another important factor to consider is stability, which has been excellently described as one of the 12 principles of green engineering.[182] "Targeted durability, not immortality, should be a design goal".[182] Systems therefore should be durable, but not immortal to the point of bioaccumulation and ecological damage. As discussed, many of these ions are either bioavailable or biodegradable, however, $[NO_3]^-$ ions are known to be catalytically reduced by Fe(ii).[183] This process happens over long timescales, but does present possible risk from the degradation products such as NO_x gases. This limits the durability of the $FeNO_3$ system and could result in a possible route to atmospheric pollution.[36]

Overall, due to the cost-effectiveness of the acidified **$FeSO_4$** and **$FeNO_3$** systems, and the environmentally benign nature of the $[NO_3]^-$ and $[SO_4]^{2-}$ anions. These two systems clearly stand out from an economic standpoint, but due to the degradation of $[NO_3]^-$ by Fe(ii), acidified **$FeSO_4$** stands out as the foremost system investigated here from both an economic and ecological perspective.

4.4 – Conclusions

Four iron systems: **$[NH_4]FeSO_4$**, **$FeSO_4$**, **$FeCF_3SO_3$** and **$FeNO_3$** have been investigated for their ability to thermogalvanically convert thermal energy to electricity. Low thermoelectrochemical ability has been observed for the un-acidified sulphate-based systems, with Seebeck coefficients of +0.22 and +0.36 mV K^{-1} for the **$[NH_4]FeSO_4$** and **$FeSO_4$** systems, respectively. However, upon acidification these were both increased to *ca.* +0.95 mV K^{-1}. Significant increases in power density upon acidification have also been observed, with a 13- and 18-fold increase in respective power densities. The **$FeCF_3SO_3$** and **$FeNO_3$** systems also observe an increase in power density upon acidification, although to a much more modest degree, *ca.* 60% increase upon acidification. Acidification of these systems resulted in no appreciable increase in Seebeck coefficient, with both acidified and un-acidified **$FeCF_3SO_3$** and **$FeNO_3$** systems displaying a Seebeck coefficient *ca.* +1.55 mV K^{-1}.

A preliminary cost-comparison of the four investigated systems suggests that acidified **$FeSO_4$** and **$FeNO_3$** are the most cost-effective. Due to the high power of the **$FeNO_3$** and the low cost of **$FeSO_4$** materials. Conversely, **$FeCF_3SO_3$** is found to be hugely uncompetitive due to the significantly higher cost of **$FeCF_3SO_3$** materials. While **$FeSO_4$** and **$FeNO_3$** both stand out from an economic perspective, **$FeNO_3$** is assessed to be inherently self-decomposing over long timescales. With the bioavailability of the $[SO_4]^{2-}$ anion in **$FeSO_4$**, this system should be considered the best from a combined economic and green chemistry perspective.

4.5 – A note of caution

As discussed in the aims and objectives, the reason for this fundamental investigation of the $Fe^{2+/3+}$ redox couple was undertaken in order to obtain a reasonable S_e and power density that could be utilised in series with the extensively reported (and benchmark) $[Fe(CN)_6]^{3-/4-}$ redox couple. A combination which has been routinely used in the past.[14,15,38–40,88] However, as discussed in this chapter the inherent acidity of the $Fe^{2+/3+}$ redox couple has been demonstrated. Moreover, the electrochemical and thermoelectrochemical properties also improve upon addition of acid, and one report that used this redox couple combination has 10 % v/v of HCl.[14]

We therefore had originally planned to utilise the best performing $Fe^{2+/3+}$ system in series with $[Fe(CN)_6]^{3-/4-}$. However, during risk assessment for this, it was abundantly clear that $[Fe(CN)_6]$ is unstable towards strongly acidic conditions, releasing severely toxic $HCN_{(g)}$.[119] Therefore these two redox couples were not combined and we instead set out to design novel and inherently sustainable redox couples. This is explored in the next chapter.

Chapter 5:

n- & p-type thermocells from $FeSO_4$

Using iron sulphate to form both n-type and p-type thermogalvanic redox couples: Towards non-hazardous and 'second-life' thermogalvanic cells

The results of this chapter have been published in:

Royal Society of Chemistry journal: *Green Chemistry*, 2020, **22**, 6062-6074.[30]

5.1 – Aims and Objectives

In the previous chapters, the fundamentals of the p-type $[Fe(CN)_6]^{3-/4-}$ and the n-type $Fe^{2+/3+}$ redox couples were extensively investigated. These redox couples have been routinely utilised in-series to generate high voltage devices. However, as discussed, in preparation for a device using the same pair of redox couples, it was found that the $[Fe(CN)_6]$ molecule is highly sensitive to acidic decomposition, generating severely toxic $HCN_{(g)}$. Therefore, we did not attempt to make an n-type, p-type in series device from these redox couples. In this chapter we therefore set out to:

- Highlight this inherent danger of previously reported thermocells, calculating the potential $HCN_{(g)}$ that could be evolved from these reported devices.
- Develop an n-type and p-type combination of redox couples that could safely to utilised in series for high output voltage devices
- Quantitatively measure the sustainability of the developed redox couple combination in comparison to the routinely reported and inherently hazardous $Fe^{2+/3+}$ and $[Fe(CN)_6]^{3-/4-}$ combination.

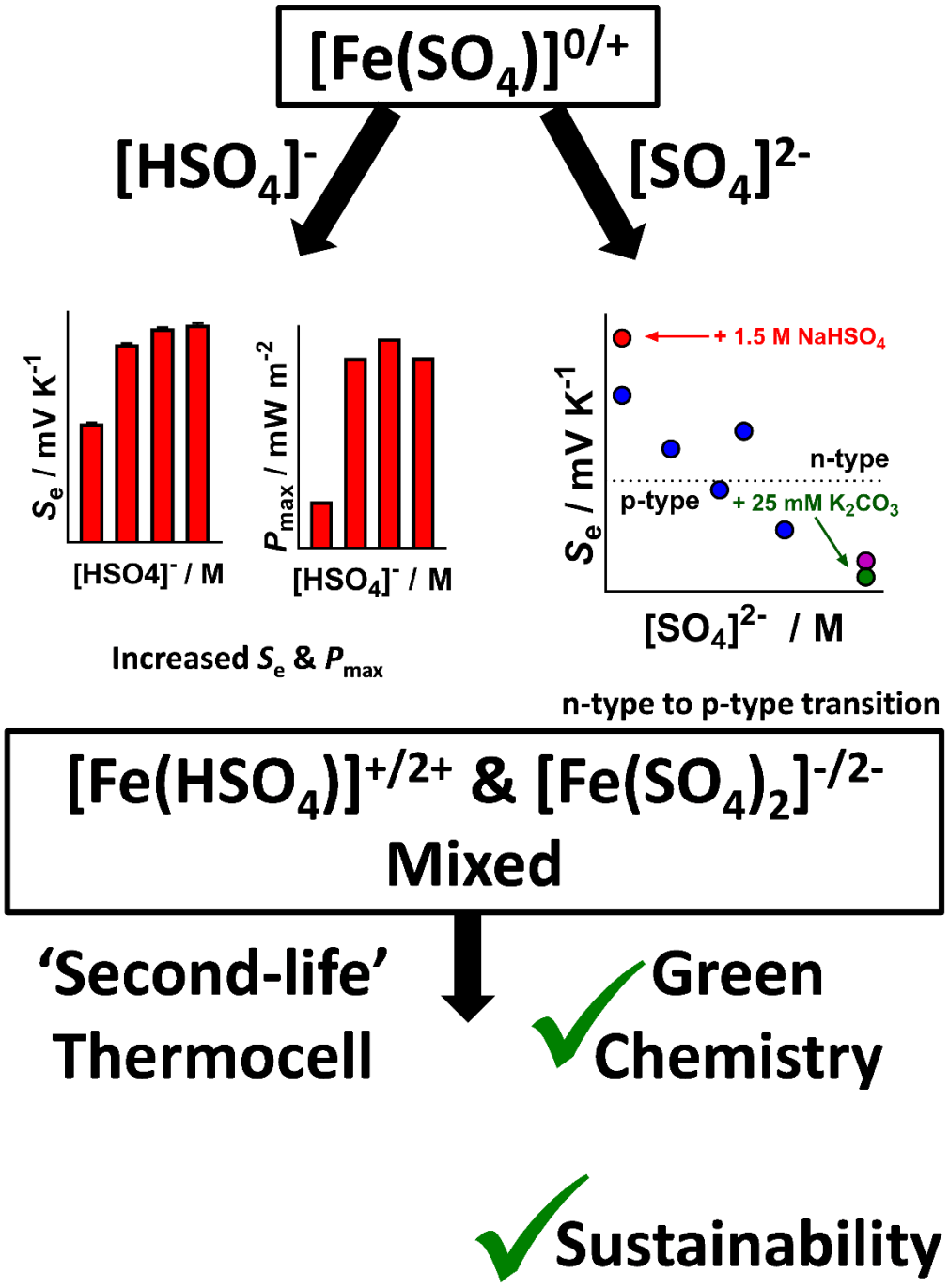
[Fe(SO4)]0/+
[HSO4]-
[SO4]2-
Se / mV K-1
[HSO4]- / M
Pmax / mW m-2
[HSO4]- / M
Increased Se & Pmax
+ 1.5 M NaHSO4
n-type
p-type
+ 25 mM K2CO3
Se / mV K-1
[SO4]2- / M
n-type to p-type transition
[Fe(HSO4)]+/2+ & [Fe(SO4)2]-/2-
Mixed
'Second-life'
Thermocell
Green
Chemistry
Sustainability

5.2 – Introduction

As discussed in the previous chapter, extensive research has been undertaken with regard to the $Fe^{2+/3+}$ n-type thermogalvanic redox couple as either aqueous,[36–39] ionic liquid[78,114,115] or gelled[14,15,164] electrolytes. In aqueous solvent, a wide range of Seebeck coefficients have been observed between +0.22 mV K^{-1} for $[NH_4]FeSO_4$ to +1.76 mV K^{-1} for $FeClO_4$.[36,38,39] The most significant factors affecting both the thermodynamics (the Seebeck coefficient) and kinetics (current density) of the $Fe^{2+/3+}$ thermocells are the counter-anion and pH.[36,39] Both the thermodynamic and kinetic aspects of thermocells are hugely important as output power of the thermocell (P_{max}) is calculated as:

$$P_{max} = 0.5V_{OCP}0.5j_{SC} \quad (13)$$

Iron-based redox couples have also demonstrated p-type thermo-electrochemical systems, observing a negative S_e. The $[Fe(Cl)_4]^{-/2-}$ and $[Fe(Br)_4]^{-/2-}$ redox couples have observed Seebeck coefficients *ca.* -0.45 mV K^{-1} in ionic liquid solvents.[78,114,115] The ferrocene | ferrocenium ($[Fc]^{0/+}$) redox couple, which is typically an n-type thermogalvanic system that displays a S_e of *ca.* +0.1 mV K^{-1} has been inverted to a p-type thermocell by covalently tethering an anionic $[NTf]^-$ group. This tethering produces the anionic $[FcNTf]^{0/-}$ redox couple, which demonstrates a p-type S_e of *ca.* -0.1 mV K^{-1}.[121] However, ionic liquid-based investigations are much less common that aqueous. The most extensively employed thermogalvanic redox couple is the aqueous p-type $[Fe(CN)_6]^{3-/4-}$, due to its relatively high Seebeck coefficient of -1.4 mV K^{-1}, and fast, reversible electrode kinetics.[17,31,34,35,67,95,120]

Despite the $[Fe(CN)_6]^{3-/4-}$ redox couple having a high Seebeck coefficient when compared to other redox couples, Seebeck coefficients in the mV K^{-1} range still represent overall low output voltages, due to low-grade temperature ranges. This is a significant challenge to effective thermogalvanic thermal-to-electrical energy conversion.[24] Due to this limitation, there have been numerous studies to increase the S_e in individual thermocells. These have focussed on introducing additives such as guanidinium, or using organic co-solvents, again, mainly utilising the $[Fe(CN)_6]^{3-/4-}$ redox couple.[17,34,35,81,82,120] Another method typically employed to increase the output voltage of thermocells is by utilising n-type and p-type thermocells electrically in-series. This has been performed in order to generate devices which produce significant voltages; in the 100s mV to several volts range (Schematically shown in Figure 41).[14,15,17,34,40] This is typically achieved using the acidic n-type $Fe^{2+/3+}$ and p-type $[Fe(CN)_6]^{3-/4-}$ redox couples.[14,15,39,40,88] The iron sulphate, chloride and perchlorate salts have been utilised to generate the n-type $Fe^{2+/3+}$ redox couple, which is often acidified, using up to 10 wt% of strong acid such as $HClO_4$ or HCl.[14,39]

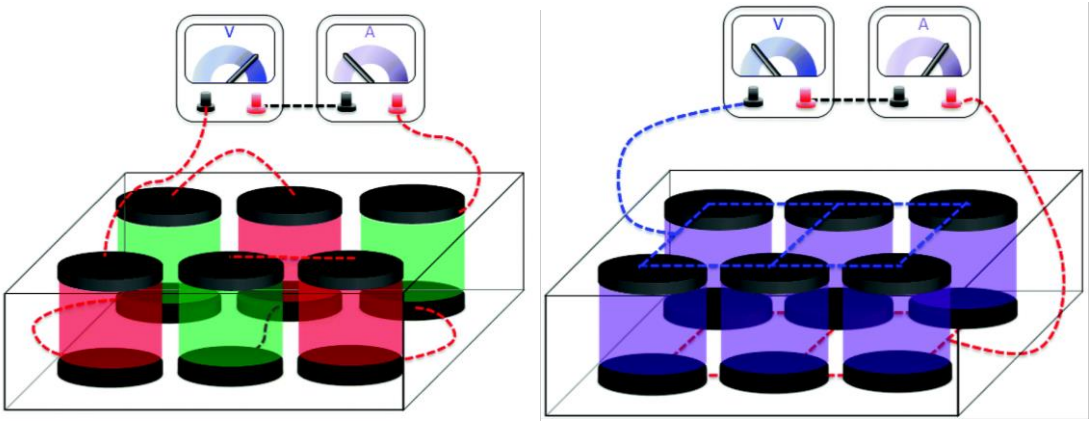

Figure 41 – Schematic of (left) n-p-n-p thermocells connected electrically in series to increase output voltage in the thermocell array. (right) n-n-n-n or p-p-p-p thermocells connected electrically in parallel to increase output current of the thermocell array.

The acidic nature of the $Fe^{2+/3+}$ redox couple is of particular concern, due to the instability of both $[Fe(CN)_6]^{3-}$ and $[Fe(CN)_6]^{4-}$ to low pH.[184,185] The $[Fe(CN)_6]^{3-/4-}$ redox couple is also unstable to UV-light,[186–188] normal tungsten or fluorescent lighting,[189] high pH[186] and high temperatures.[190–192] The main degradation product at high temperature and low pH is known to be $HCN_{(g)}$,[184,190,191,193] which is extremely toxic to humans.[119,194] This combination of acid and $[Fe(CN)_6]^{4-}$ can be tragically highlighted, where somebody committed suicide by heating $[Fe(CN)_6]^{4-}$ in under acidic conditions within a sealed vehicle environment, releasing a lethal dose of $HCN_{(g)}$.[119]

Realising the potential toxicity of inherently acidic or acidified $Fe^{2+/3+}$ and $[Fe(CN)_6]^{3-/4-}$ thermocells when used in combination, the potential $HCN_{(g)}$ evolution of reported thermocell arrays has been calculated, and is shown in Table 10.[30] Here, the potential $HCN_{(g)}$ has been calculated based on the complete decomposition of the $[Fe(CN)_6]^{4-}$ only, which represents a 50% evolution of total $HCN_{(g)}$ possible.

Therefore, to fully-comprehend the 'worst-case' scenario, the calculated values shown in Table 10 can in fact be doubled.[30] The potential concentration of $HCN_{(g)}$ has also been calculated in several defined volumes relevant to real-world applications (a medium sized car, a typical conference room for 80 people, a typical-sized UK flat, and an airbus A320). Table 10 clearly demonstrates the potential toxicity of the reported thermocell arrays, the most powerful of which demonstrates significant potential toxicity, even in a volume equivalent to an aeroplane.[30] Table 10 has been colour coded to account for the AEGL toxicity levels, with red being lethal or life-threatening, orange indicating likely irreversible health effects, yellow likely causing discomfort, and green likely no effect.[30]

Table 10 – The table demonstrates the potential hazard of $HCN_{(g)}$ evolution from published thermocell devices using multiple $Fe^{2+/3+}$ and $[Fe(CN)_6]^{3-/4-}$ cells. A 'worst case scenario' was assumed, *i.e.* that the electrolytes mixed and all $[Fe(CN)_6]^{4-}$ present completely decomposed to evolve $6HCN_{(g)}$ (full calculations detailed in Table A2). The resulting concentration in ppm (mg m^{-3}) was estimated for 5 different volumes. These were then colour-coded based upon the AEGL[195] exposure limit for $HCN_{(g)}$, where >6.5 = life-threatening or death (red); 2.5 – 6.5 = irreversible and long-lasting health effects (orange); 1 – 2.4 = discomforting but non-disabling (yellow); and < 1 = non-toxic (green), based upon exposure times of 8 hours. Table re-used from Reference[30].

Literature thermocell device (corresponding author)	Cells in thermo-cell device	HCN in mg m^{-3} (assuming HCN-evolution, within the defined volume)				
		1 m^3	3.1 – 3.4 m^3 (medium-sized car, US)	71 m^3 (typical conference room for 80 delegates)	137 m^3 (typical UK flat size)	327 m^3 (cabin volume on an airbus A320)
Zhou[14]	118	6.8	2.09	0.1	0.05	0.02
Kang[38]	2	8.4	2.59	0.12	0.06	0.03
Aldous[88]	4	16.3	5.02	0.23	0.12	0.05
Baughman[40]	112	590.3	181.61	8.31	4.31	1.84
Lee[39]	64	2185.5	624.4	30.78	16.0	6.8

It is clearly evident that the combination of the extensively employed $Fe^{2+/3+}$ and $[Fe(CN)_6]^{3-/4-}$ thermocells have significant potential toxicity, especially in sealed, small volume environments such as automobiles. It is also clearly evident from Table 10 that novel, non-hazardous redox couples need to be developed in order to be utilised in-series to generate high output voltages. Demonstrated in this chapter is a simple and benign alternative n-type and p-type redox couple combination based on iron-sulphate

and non-toxic additive electrolytes. The thermogalvanic power of these thermocell systems have been explored both individually, and in-series.

Finally, the best-performing n-type and p-type systems have been mixed, and crucially show not only inherent non-toxicity, but also the ability to maintain their thermogalvanic activity. This is described here as a 'second-life' thermogalvanic cell. The sustainability of this system *vs* the typically employed $Fe^{2+/3+}$ and $[Fe(CN)_6]^{3-/4-}$ systems have been qualitatively compared with respect to the 12 principles of green chemistry and green engineering. From this, the iron sulphate-based systems were found to be superior from a green chemistry perspective.

5.3 – Results and Discussion

5.3. 1 – Optimisation of the n-type thermocell with benign reagents

In the chapter 4, it was demonstrated that, through a combination of thermogalvanic, economic and sustainable comparisons, the acidic (acidified with 1 M H_2SO_4) $FeSO_4$ thermocell was the best candidate for cost-effective, long-term thermal energy harvesting.[36] The $FeSO_4$ thermocell has been routinely employed in the presence of H_2SO_4 to significantly improve the Seebeck coefficient (S_e), current density (j) and the power density of the redox couple.[36,39,40,88]

Addition of H_2SO_4 has been found to increase both the S_e and j_{SC}, significantly improving the performance of the thermocell.[36] This is achieved through protonation of the $[Fe(SO_4)]^{0/+}$ redox couple, resulting in the $[Fe(HSO_4)]^{+/2+}$ redox couple.[36] However, sulphuric acid is highly corrosive, and known to be toxic to ecological

environments.[177] Sodium hydrogen sulphate ($NaHSO_4$) is a less acidic (pK_a values of H_2SO_4 and $[HSO_4]^-$ are -3 and 1.99 respectively)[30] and a significantly less toxic alternative. Additionally, sodium (Na^+), hydrogen sulphate ($[HSO_4]^-$) and sulphate ($[SO_4]^{2-}$) ions are all naturally abundant in all water sources, including tap water.[36] Therefore, substituting H_2SO_4 for $NaHSO_4$ should significantly improve the sustainability of the thermocell and remove the ecological threat of subsequent thermocell solutions if they were to be released into the environment. This substitution would also make the end-of-life clean-up of the thermocell less challenging. However, no attempt has yet been made to utilise hydrogen sulphate as an acid within a thermocell.

Therefore, a two-fold systematic investigation was undertaken. Firstly, the effect of increasing equimolar concentration was undertaken from 0.4 M to 2 M $[Fe(SO_4)]^{0/+}$ in the absence of added electrolyte. Secondly, the effect of added $NaHSO_4$ to a fixed $[Fe(SO_4)]^{0/+}$ concentration of 0.6 M was investigated. Figure 42(a) shows that by increasing the concentration of $FeSO_4$ the S_e slightly reduces from *ca.* +0.38 mV K^{-1} to *ca.* +0.31 mV K^{-1}, consistent to the commonly reported S_e of *ca.* +0.3 mV K^{-1} for the $FeSO_4$ thermocell.[36,39,88]

With respect to both current and power densities, as the concentration of $FeSO_4$ was increased, an initial significant increase in current (and therefore power) density was observed (Figure 42(b & c)). Between concentrations of 0.4 M and 1.5 M, a four-fold increase in current density from 0.48 A m^{-2} to 2.04 A m^{-2} and subsequently an almost four-fold increase in power density, from 0.78 mW m^{-2} to 2.89 mW m^{-2} was observed (Tabulated values of data can be found in Table 11). However, further

increases in concentration beyond this results in a reduction in both current and power density (Figure 42(b & c)), consistent with previous reports investigating the n-type $FeClO_4$ and p-type $[Fe(CN)_6]^{3-/4-}$ systems.[15,38,94] This 'peak' in power density with concentration has been attributed to the high ionic strength environment, reducing the bulk solvent by 'fixing' all solvent water molecules in the solvation sphere,[94] and has not been investigated further here.

A modest increase in concentration from 0.4 M to 0.6 M results in a greater than 2-fold increase in power density. Therefore, 0.6 M was selected as the system to which addition of $NaHSO_4$ would be investigated. Incremental increases in $[HSO_4]^-$, in 0.5 M intervals results in an increase in S_e, from *ca.* +0.3 mV K^{-1} to *ca.* +0.5 mV K^{-1}. This achieved S_e value is significant as it is equivalent to previous reports of acidified (with H_2SO_4) $FeSO_4$ systems.[40,88] However, this is significantly lower than the S_e achieved with higher concentrations of H_2SO_4[36] (chapter 4). Even small additions (0.5 M) of $[HSO_4]^-$ was found to significantly increase the current density and power density of 2.5-fold and >3-fold, respectively.

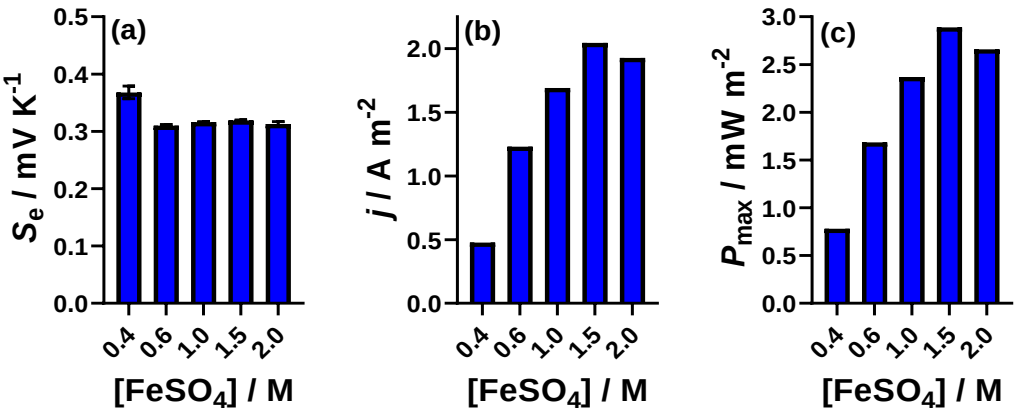

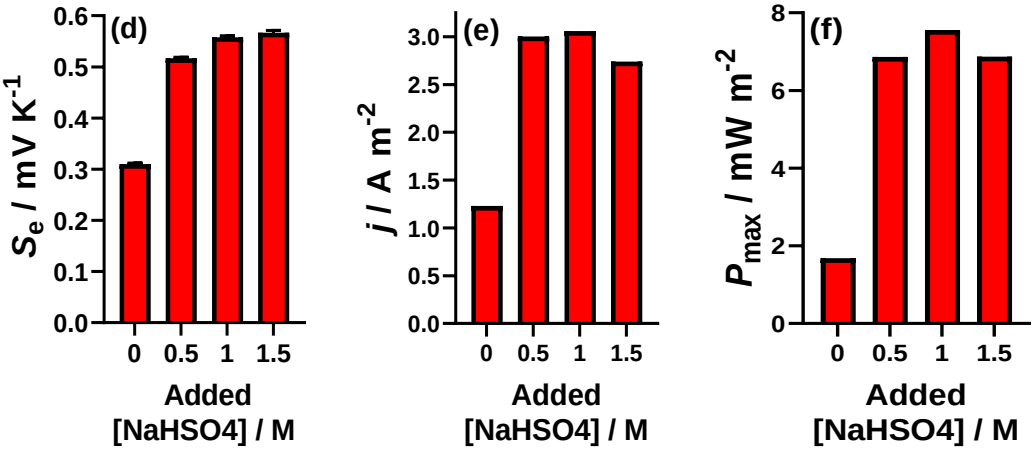

Figure 42 – Bar graphs showing the effect of increasing concentration of equimolar concentrations of (a-c) $FeSO_4$ on (a) the Seebeck coefficient (S_e), (b) the current density (j) and (c) the maximum power density (P_{max}). Also shown is (d-f) the effect of introducing various concentrations of $NaHSO_4$ to the 0.6 M $FeSO_4$ thermocell on (d) the S_e, (e) j and (f) P_{max}.

Clearly the addition of adding $[HSO_4]^-$, rather than H_2SO_4 can still yield significant improvements in the n-type $FeSO_4$ thermocell. Throughout the rest of this report the 0.6 M $FeSO_4$ thermocell will be used either in the presence or absence of 1.5 M $NaHSO_4$, which will be referred to as either **Fe(SO$_4$)** (no $[HSO_4]^-$) or **Fe(HSO$_4$)** (1.5 M $[HSO_4]^-$), respectively.

Table 11 – Table of data showing the observed S_e, j and P_{max} for all equimolar $FeSO_4$ concentrations and the 0.6 M $FeSO_4$ system in the presence of various concentrations of $NaHSO_4$, corresponding to Figure 42.

$FeSO_4$ concentration / M	**S_e / mV K^{-1}**	**j_{SC} / A m^{-2}**	**P_{max} / mW m^{-2}**
0.4	0.37 ± 0.01	0.48 ± 0.05	0.78 ± 0.09
0.6	0.31 ± 0.01	1.23 ± 0.10	1.69 ± 0.14
1.0	0.32 ± 0.01	1.69 ± 0.12	2.37 ± 0.18
1.5	0.32 ± 0.01	2.04 ± 0.12	2.89 ± 0.17
2.0	0.31 ± 0.01	1.93 ± 0.06	2.66 ± 0.12
$[HSO_4]^-$ concentration / M			
0.5	0.52 ± 0.01	3.09 ± 0.33	6.86 ± 0.79
1	0.56 ± 0.01	3.06 ± 0.43	7.55 ± 1.07
1.5	0.57 ± 0.01	2.74 ± 0.24	6.87 ± 0.60

5.3.2 – Thermodynamics of n-type to p-type transition

With the n-type **$Fe(SO_4)$** and **$Fe(HSO_4)$** systems investigated and optimised, the effect of adding a basic electrolyte, rather than acidic electrolyte, was investigated. In chapter 4 we clearly demonstrated that the $[SO_4]^{2-}$ anion is strongly coordinating to the Fe ions, resulting in a significantly reduced S_e. Therefore, it was assumed that this strong binding affinity could be exploited further to generate an anionic (and therefore p-type) system. The electrolyte chosen was thus the $[SO_4]^{2-}$ anion (obtained from Na_2SO_4). Upon addition of small concentrations of $[SO_4]^{2-}$, the S_e of the **$Fe(SO_4)$** system decreased. However, upon higher concentrations of $[SO_4]^{2-}$ (>0.6 M) the Seebeck was found to invert from a positive to a negative, demonstrating an inversion of the initial n-type thermocell to a p-type. This is proposed to be due to the increase

in $[SO_4]^{2-}$ character and the strong association of the $[SO_4]^{2-}$ anion to Fe, producing the $[Fe(SO_4)_2]^{-/2-}$ redox couple. A transition from a cationic to anionic redox couple results in an inversion of entropy upon reduction (or oxidation), which also results in an inversion of observed S_e, Equation 2 (shown again for clarity).

$$S_e = \frac{\Delta V}{\Delta T} = \frac{\Delta S_{rc}}{nF} \quad (2)$$

The observed S_e of the n-type **$Fe(SO_4)$** system was found to be *ca.* +0.3 mV K^{-1}, addition of 1.5 M $[SO_4]^{2-}$ (referred from here as **$Fe(SO_4)_2$**) was found to be equivalent, but as a p-type, exhibiting a S_e *ca.* -0.3 mV K^{-1}. 1.5 M addition of $[SO_4]^{2-}$ was found to be the limit, due to the increase in pH upon addition of basic electrolyte. Iron is known to have a rich, pH-dependent chemistry,[196,197] and Fe(iii) is known to rapidly precipitate in solutions with a pH ≥ 2.5.[30,113] The pH of the electrolyte-free 0.6 M **$Fe(SO_4)$** was found to be *ca.* 2, equivalent to the pH of a previously reported 0.2 M $FeSO_4$ thermocell in the absence of supporting electrolyte.[36] This pH can be maintained with the addition of up to 1.5 M $[SO_4]^{2-}$, but above this precipitates would form due to a pH >2.5.

The pH effect can be further demonstrated by the addition of small amounts of $[CO_3]^{2-}$ (from K_2CO_3). Addition of 25 mM $[CO_3]^{2-}$ to the 1.5 M $[SO_4]^{2-}$ solution increased the S_e of the thermocell up to -0.35 mV K^{-1} (Figure 43). However, addition of a further 25 mM to 50 mM $[CO_3]^{2-}$ resulted in rapid precipitation of the iron in solution, in line with what is expected of iron solutions in a higher pH environment.[113]

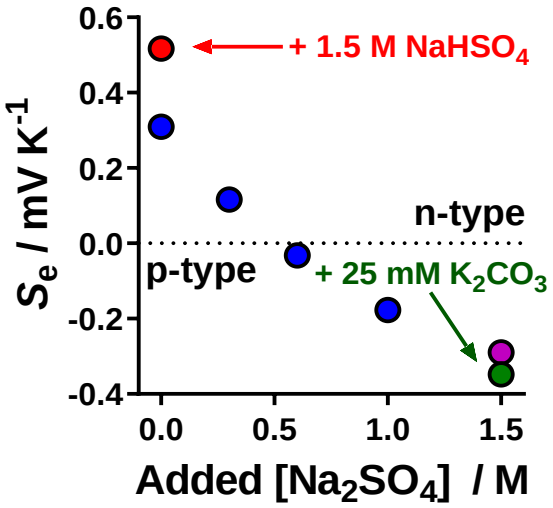

Figure 43 – Observed Seebeck coefficient (S_e) of the 0.3 M $Fe(SO_4)$ system with addition of various concentrations of added Na_2SO_4. Where presence of added $NaHSO_4$ (red) and K_2CO_3 (green) is also shown with the respective concentration added. The n-type to p-type transition is shown as a dotted line at 0.

Seebeck coefficients are theoretically temperature-independent, however, this is not always the case. This was demonstrated in the previous chapter with the $[NH_4]FeSO_4$ thermocell, which demonstrated significant temperature-dependence on the observed S_e.[36] This temperature-sensitivity was determined to be effected by the inherent equilibria present between the $Fe^{2+/3+}$ and $[SO_4]^{2-}$ ions.[36] As this equilibria is also present here, and in the case of the **$Fe(SO_4)_2$** system to an even greater extent. The temperature-dependence of the S_e on the three investigated systems **($Fe(SO_4)$**, **$Fe(HSO_4)$** and **$Fe(SO_4)_2$)** was therefore also investigated here.

Consistent with the previous investigation, (part 4.3.4) the temperature-dependence was measured by lowering the ΔT of the thermocell. Both the **$Fe(SO_4)$** and **$Fe(HSO_4)$** systems demonstrate a decrease in observed S_e, consistent with the

previous investigation on $[NH_4]FeSO_4$.[36] Due to the temperature-dependence on the S_e, the use of the term 'apparent Seebeck', or aS_e has been applied to our systems. The **$Fe(SO_4)_2$** system exhibited a more significant (and in this case beneficial) dependence in observed S_e with decreasing ΔT, increasing from -0.3 mV K^{-1} to -0.4 mV K^{-1}. All three of the investigated systems exhibit the same direction increase (towards the negative). This is observed as a decrease in aS_e for the **$Fe(SO_4)$** and **$Fe(HSO_4)$** systems. As the **$Fe(SO_4)_2$** system is a p-type thermocell, this is observed as an increase in aS_e. This observed increase or decrease in aS_e in the p-type or n-type systems is likely due to temperature-dependent speciation equilibria present in the thermocell (30).

$$[Fe(SO_4)]^{0/+} + [HSO_4]^- \rightleftharpoons [Fe(HSO_4)]^{+/2+} + [SO_4]^{2-} \quad (30)$$

$$Fe^{2+/3+} + 2[SO_4]^{2-} \rightleftharpoons [FeSO_4]^{0/+} + [SO_4]^{2-} \rightleftharpoons [Fe(SO_4)_2]^{-/2-} \quad (31)$$

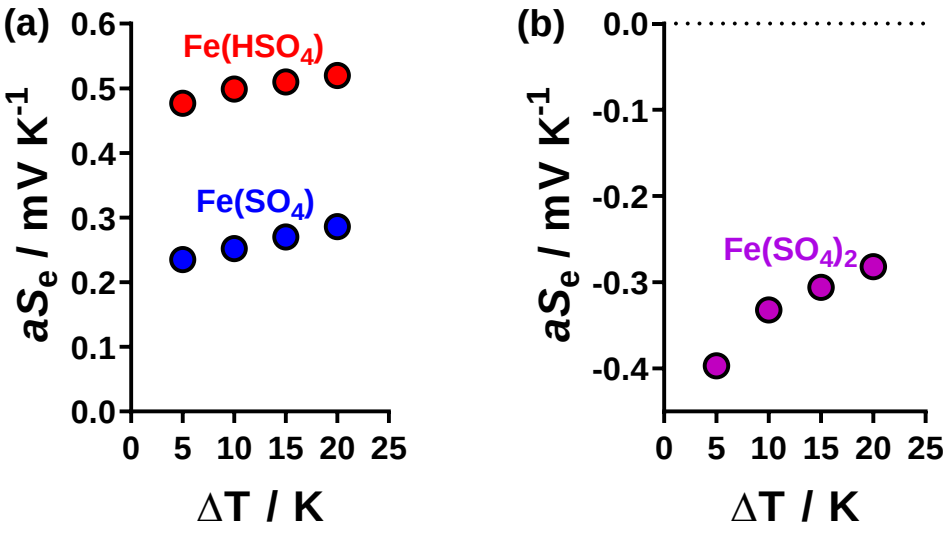

Figure 44 – Observed temperature-dependence on the apparent Seebeck 'aS_e' of (a) the n-type $Fe(SO_4)$ (brown) and $Fe(HSO_4)$ (red) systems, and (b) the p-type $Fe(SO_4)_2$ system, where the effect of decreasing ΔT, by maintaining T_{hot} (at 40°C) and increasing T_{cold}.

The decrease or increase in aS_e demonstrates a more '$FeSO_4$' or '$Fe(SO_4)_2$' character in the dynamic equilibria present. Here, it is inferred that the ion-affinity of the $[SO_4]^{2-}$ anion to the $Fe^{2+/3+}$ cations increases at higher temperatures, which is entirely consistent with the temperature investigation on the UV-Vis spectra of $FeSO_4$ in section 4.3.4. Whilst this transition from n-type to p-type thermocell observed in the aS_e is a significant observation, thermodynamics is not the only aspect of a thermocell performance. The kinetics of a thermocell are also hugely important, which has also been investigated and is discussed in the next section.

5.3.3 – Kinetics of n-type to p-type transition

The short-circuit current density (j_{SC}) and the maximum power density (P_{max}) of the $FeSO_4$ thermocell in the presence of various concentrations of $[SO_4]^{2-}$ has also been measured and are shown in Figure 45. Both of these parameters also observe the same trend as the aS_e (Figure 43), where an initial decrease with increasing addition of $[SO_4]^{2-}$ is observed, followed by an increase in the p-type direction once the transition from n-type to p-type is achieved (>0.6 M $[SO_4]^{2-}$). The n-type and p-type current and power densities can also be increased with addition of $[HSO_4]^-$ and $[CO_3]^{2-}$, respectively, as also demonstrated in Figure 45 for the 0 M $[SO_4]^{2-}$ (n-type) and 1.5 M $[SO_4]^{2-}$ (p-type).

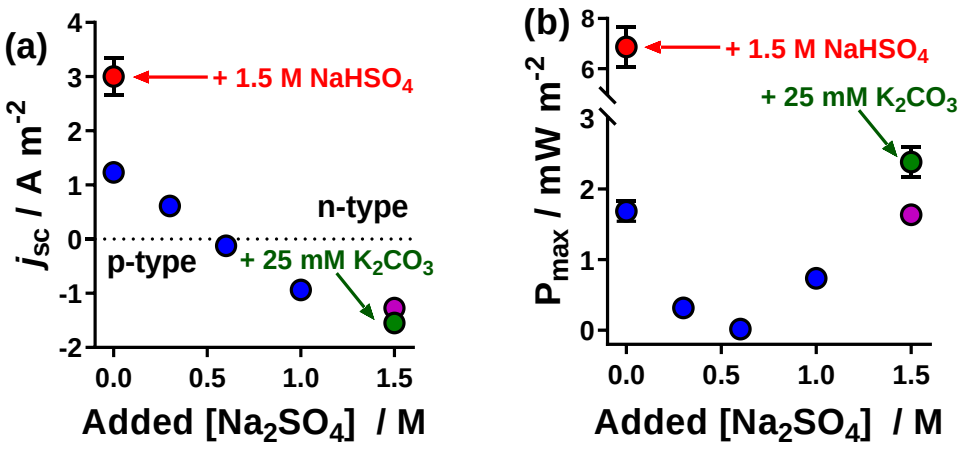

Figure 45 – Figure showing (a) the short-circuit current density (j_{SC})and (b) the maximum power density (P_{max}) of the 0.3 M $Fe(SO_4)$ system with addition of various concentrations of added Na_2SO_4. Where presence of added $NaHSO_4$ (red) and K_2CO_3 (green) is also shown with the respective concentration added. Also shown on (a) is the n-type to p-type transition is shown as a dotted line at 0 (part a).

As the thermoelectrochemical properties of the **$Fe(SO_4)_2$** system are clearly the most temperature-dependent with respect to the thermodynamics, the temperature effect on the kinetics was also investigated. The effect on kinetics with changing temperature was performed in the same manner as section 2.3.1, where ΔT is maintained, but the overall temperature was increased by raising both T_{hot} and T_{cold} simultaneously.[3] This investigation was previously undertaken for the $[Fe(CN)_6]^{3-/4-}$ redox couple, which is known to be temperature insensitive.[3,35,67] Therefore, it is important to determine how the temperature-sensitive **$Fe(SO_4)_2$** will be effected by this experiment, and compare to the temperature insensitive $[Fe(CN)_6]^{3-/4-}$ system. Figure 46 shows that as the overall temperature of the thermocell was increased, the S_e of the system doubled, from *ca.* -0.2 mV K^{-1} to *ca.* -0.4 mV K^{-1}.

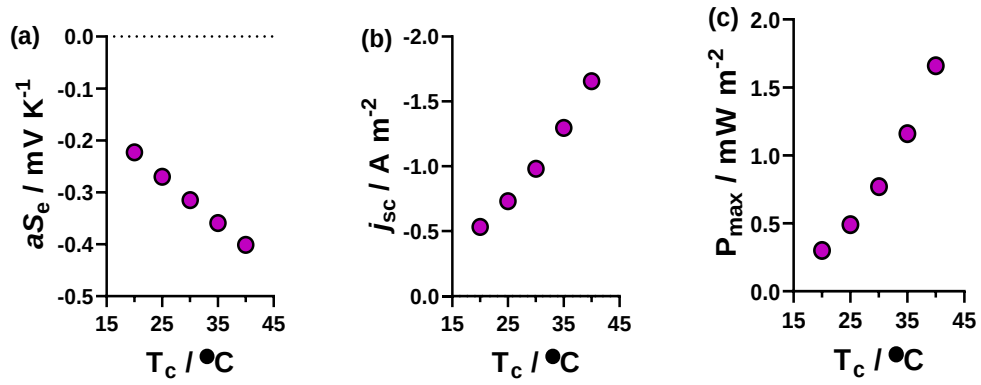

Figure 46 – Temperature-dependence on (a) apparent S_e 'aS_e' (b) short-circuit current density (j_{SC}) and (c) maximum power density (P_{max}) of the **$Fe(SO_4)_2$** system, where a constant ΔT of 10 K is maintained, and the temperature of T_{hot} and T_{cold} is increased from 30 – 50°C and 20 – 40°C respectively.

The **$Fe(SO_4)_2$** system demonstrated a significant increase in both current and power densities. In the previous study, the $[Fe(CN)_6]^{3-/4-}$ current density increased by *ca.* 155%, the current density in the **$Fe(SO_4)_2$** system here increased over 300%. Due to the significant increase in both voltage (S_e) and current, the power density increased even more significantly. In the $[Fe(CN)_6]^{3-/4-}$ thermocell an *ca.* 160% increase in power was observed, whereas the **$Fe(SO_4)_2$** system increased over 500% (Figure 46(c)). This is a significant observation as the system clearly demonstrates significantly improved performance at higher temperatures.

5.3.4 – Cyclic Voltammetry

Cyclic voltammetry (CV) can be an insightful tool for investigating redox-active species in solution, where changes in speciation,[36] electron transfer kinetics[35] and diffusion coefficients[94] can also be observed.[80,198] CVs of the three investigated systems (the **$Fe(SO_4)$**, **$Fe(HSO_4)$** and **$Fe(SO_4)_2$**) were recorded at gold electrodes, and are displayed in Figure 47. The total concentration of redox-active ions in solution is 600 mM, which represents extremely concentrated solutions, but is consistent with all other solutions in chapters 2, 3, & 4.[30,35,36]

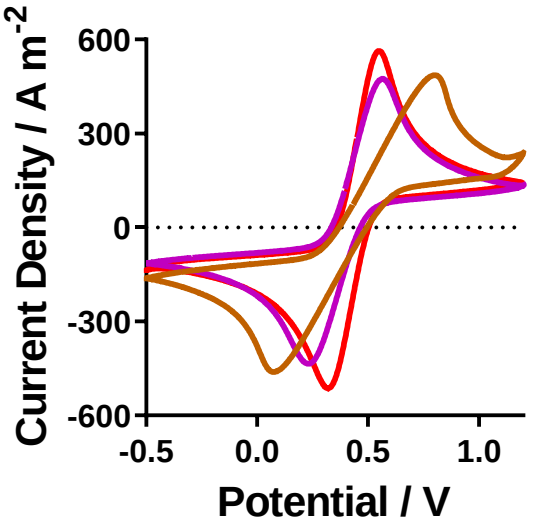

Figure 47 – Cyclic voltammograms recorded for the **$[Fe(SO_4)]^{0/+}$** (blue line), **$[Fe(HSO_4)]^{+/2+}$** (red line) and **$[Fe(SO_4)_2]^{-/2-}$** (purple line) systems. All recorded at ambient temperature using an Au working electrode, *vs* an Ag/AgCl reference electrode, at 100 mV s^{-1}. A table of data for the values can be found in the Table 12.

Figure 47 demonstrates that **$Fe(HSO_4)$** and **$Fe(SO_4)_2$** have a much smaller peak-to-peak separation than the **$Fe(SO_4)$**, consistent with an increase in electron

transfer rate.[80] These solutions contain additional $[HSO_4]^-$ and $[SO_4]^{2-}$ ions in solution, which act as a supporting electrolyte that lowers the ohmic resistance, leading to faster electrode kinetics (a deeper explanation of this effect can be found in reference[199]) (Figure 47, Tabulated values in Table 12). The inherent resistances in these systems have also been probed by electrochemical impedance spectroscopy and are discussed in part 5.3.7. However, cyclic voltammetry yields little insight into the speciation present in the solutions of the three investigated systems, in an attempt to gain a better understanding of the present speciation, these systems were all probed by UV-Vis and IR spectroscopies.

Table 12 - Table showing the potential of the oxidation peak (E_{Ox}), reduction peak (E_{Red}) and equilibrium potential (E_{eq}) and peak-to-peak separation (ΔE_p) for the voltammograms of the three $FeSO_4$ systems (0.3 M Fe(ii)SO_4 and 0.3 M Fe(iii)SO_4), in the absence of supporting electrolyte and in the presence of either 1.5 M $[SO_4]^{2-}$ or $[HSO_4]^-$. The experimental setup comprised of a 1.6 mm diameter Au working electrode, Pt wire counter electrode *vs.* Ag/AgCl reference electrode at a scan rate of 100 mVs^{-1}.

Thermocell system	E_{Ox} / V	E_{Red} / V	E_{eq} / V	ΔE_p / V
$Fe(SO_4)$	0.800	0.077	0.438	0.723
$Fe(SO_4)_2$	0.565	0.233	0.399	0.332
$Fe(HSO_4)$	0.549	0.319	0.434	0.230

5.3.5 – Spectroscopic analysis on speciation

To gain a better understanding of the speciation present within the three investigated systems, UV-Vis was initially employed. As discussed previously (part 4.3.4), Fe(ii) salts display no appreciable UV-Vis signals, and were not investigated

again here.[36] Therefore, only the Fe(iii) systems were investigated and are shown in Figure 48(a). Previous investigations into the UV-Vis of the Fe(iii)(SO_4) system observed two distinct UV-Vis peaks, one centred *ca.* 295 nm (Figure 35) attributed to the $[Fe(SO_4)]^+$ ion, and one centred *ca.* 220 nm, attributed to the $[Fe(H_2O)_6]^{3+}$ ion.[36] Both of these peaks were also observed here for the **Fe(SO_4)** system (Figure 48(a)).

Analysis of **Fe(HSO_4)**, by introducing an excess of $[HSO_4]^-$ ions resulted in a sharpening and slight shift of the 295 nm peak, consistent with the previous investigation using H_2SO_4.[36] Analysis of **Fe(SO_4)$_2$**, by introducing an excess of $[SO_4]^{2-}$ into the solution resulted in an increase of signal intensity of the 295 nm peak, without an accompanying shift, which can be attributed to a slight increase in $[SO_4]^{2-}$ association to the Fe^{3+} ion, as in equilibrium (31). The UV-Vis results are therefore also indicative of the proposed **Fe(SO_4)**, **Fe(SO_4)$_2$** and **Fe(HSO_4)** species, but UV-Vis alone is clearly not definitive.

IR spectroscopy was also employed in an attempt obtain a clearer distinction of the species present in the three systems. Unlike in UV-Vis, the Fe(ii) species can be investigated by IR, allowing the interrogation of both Fe(ii) and Fe(iii) systems.

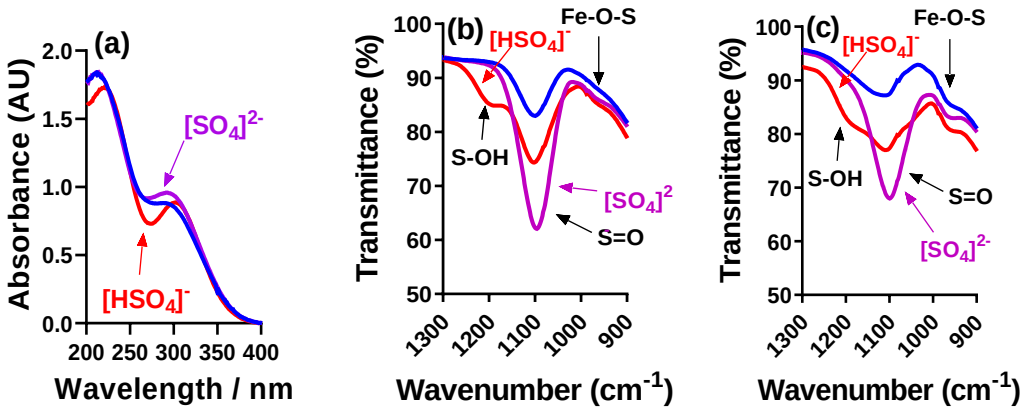

Figure 48 – (a) UV-Vis and (b & c) IR spectra of the three investigated systems: **$Fe(SO_4)$** (blue), **$Fe(SO_4)_2$** (purple, indicated by $[SO_4]^{2-}$) and **$Fe(HSO_4)$** (red, indicated by $[HSO_4]^-$). UV-Vis spectra of the Fe(III) system is shown, and IR spectra of (b) the Fe(II) systems and (c) the Fe(III) systems are shown. Blanks are shown in the Figure A3.

The sulphate anion ($[SO_4]^{2-}$) is known to have an intense IR signal centred *ca.* 1100 cm^{-1} (indicated as the S=O in Figure 48).[113] This signal was observed with both Fe(ii) and Fe(iii) (Figure 48(b & c)). This signal showed increased intensity for **$Fe(SO_4)_2$**, compared to **$Fe(SO_4)$**, due to the increased concentration of $[SO_4]^{2-}$ present. There are two other peaks present in both Fe systems, one centred *ca.* 1200 cm^{-1}, and the other *ca.* 980 cm^{-1}. The peak at 1200 cm^{-1} is observed as a shoulder on both Fe(ii) and Fe(iii) systems, which is only present with $[HSO_4]^-$, and is therefore attributed to the protonated $[HSO_4]^-$ anion (indicated by S-OH in Figure 48).[113] The peak centred around *ca.* 980 cm^{-1} is observed more strongly in the Fe(iii) system (Figure 48(c)). This peak has been attributed to $[SO_4]^{2-}$ coordination to the Fe (indicated by Fe-O-S in the spectra),[30] therefore giving direct evidence of ion-pairing, which has been indirectly evidenced in the thermoelectrochemical results.

Despite both of these spectroscopies indicating the suspected ion pairing, neither give a clear indication of the extent of ion-pairing, or the exact species present in solution. Therefore, a theoretical model based on the thermoelectrochemical results has been employed in an attempt to provide more quantitative analysis of the species present.

5.3.6 – Theoretical analysis on speciation

In order to better understand the exact speciation present within all three investigated systems (the **$Fe(SO_4)$**, **$Fe(HSO_4)$** and **$Fe(SO_4)_2$**), a theoretical model was utilised.[73,76] Fundamental work investigating the redox couple entropy (ΔS_{rc}) has reported the relationship between ΔS_{rc}, the charge of redox ions, and the ionic radius,[73] as in Equation 6:

$$\Delta S_{rc} = K_1 + K_2(AN) + K_3(Z_{ox}^2 - Z_{red}^2)/r \quad (6)$$

Where K_1, K_2 and K_3 are constants, *AN* is the acceptor number of the solvent (as water was the only solvent this is also a constant), Z_{ox}^2 and Z_{red}^2 are the ionic charge of the oxidised and reduced species respectively, and r is the ionic radius.[73,76] Due to the constants present, this relationship can be simplified to:

$$\Delta S_{rc} \propto (Z_{ox}^2 - Z_{red}^2)/r \quad (7)$$

The ΔS_{rc} can be calculated *via* the experimentally determined Seebeck coefficient, from the equation:

$$S_e = \frac{\Delta V}{\Delta T} = \frac{\Delta S_{rc}}{nF} \quad (2)$$

Using known ionic radii of the $[Fe(H_2O)_6]^{2+/3+}$,[73] and $[Fe(CN)_6]^{3-/4-}$,[76] redox couples, along with calculated ΔS_{rc} from the reported Seebeck coefficients.[35,36,67] The ΔS_{rc} of the redox couples were plotted against the $(Z_{ox}^2 - Z_{red}^2)/r$ (green squares, Figure 49). The ΔS_{rc} of the $[Fe(HSO_4)]^{+/2+}$ system has also been reported from $FeSO_4$ in the presence of 1 M H_2SO_4.[36] With respect to the systems investigated here, the charge of each investigated redox couple are proposed to be $[Fe(SO_4)]^{0/+}$, $[Fe(HSO_4)]^{+/2+}$ and $[Fe(SO_4)_2]^{-/2-}$, therefore the $(Z_{ox}^2 - Z_{red}^2)$ is proposed to be 1, 3 and -3 respectively.

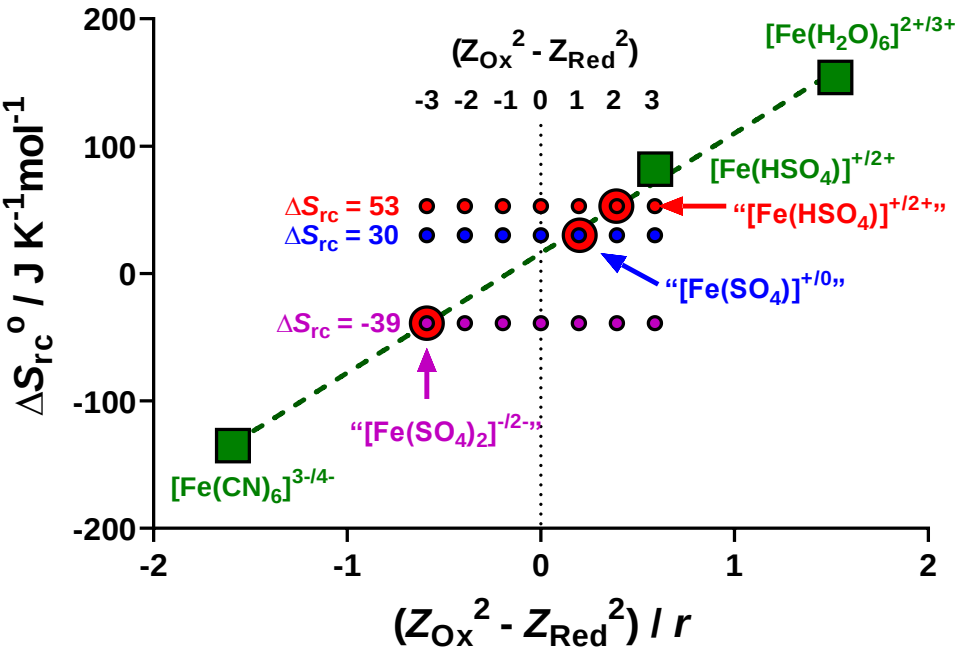

Figure 49 – Plot of ΔS_{rc} *vs* $(Z_{Ox}{}^2\text{-}Z_{Red}{}^2)/r$ for previously reported Fe(ii)/Fe(iii) redox systems (green squares) and the three Fe(ii)/Fe(iii) redox systems investigated here (red circles). Also shown are different calculated values of $(Z_{Ox}{}^2\text{-}Z_{Red}{}^2)/r$ where r was fixed as 5.1 Å, and $(Z_{Ox}{}^2\text{-}Z_{Red}{}^2)$ varied, in order to quantify which $(Z_{Ox}{}^2\text{-}Z_{Red}{}^2)$ values best represent the **$Fe(SO_4)$**, **$Fe(HSO_4)$** and **$Fe(SO_4)_2$** systems investigated here.

Figure 49 shows that for a fixed r of 5.1 Å,‡‡ the $[Fe(SO_4)]^{0/+}$ and $[Fe(SO_4)_2]^{-/2-}$ redox couples have an excellent correlation with the proposed $Z_{ox}^2 - Z_{red}^2$ (the charges of the redox couples have been included in this section for ease of the reader to follow the determination). However, the $[Fe(HSO_4)]^{+/2+}$ system is more complicated. The system is found to have an excellent correlation for ($Z_{ox}^2 - Z_{red}^2$) = 2, which is not possible given that Z_{ox} and Z_{red} are integers. The S_e of this system, and therefore ΔS_{rc} is roughly halfway between the $[Fe(SO_4)]^{0/+}$ and $[Fe(HSO_4)]^{+/2+}$ found for $FeSO_4$ and $FeSO_4 + H_2SO_4$ systems investigated previously.[36] This is due to the less acidic nature of the $[HSO_4]^-$ to H_2SO_4, where the pKa values are 1.99 and -3, respectively.[200]

Previously, the equilibrium proposed in (29) was fully driven to the right in the $FeSO_4 + H_2SO_4$ thermocell (fully generating $[Fe(HSO_4)]^{+/2+}$).[36] However, in the $NaHSO_4$-added system, this equilibria may not be fully driven to $[Fe(HSO_4)]^{+/2+}$, due to the decreased acidity. It is likely instead that there will be a mixture of both the $[FeSO_4]^{0/+}$ and $[Fe(HSO_4)]^{+/2+}$ redox couples, in competition. This suggests that our notation of **$Fe(HSO_4)$** is not strictly accurate, but will continue to be used for simplicity. This also explains the lowered observed ΔS_{rc}, and subsequent S_e for the $FeSO_4 + [HSO_4]^-$ system *vs* the $FeSO_4 + H_2SO_4$ system.[36] To demonstrate that a fully associated $[Fe(HSO_4)]^{+/2+}$ system would fit the model, the ΔS_{rc}, calculated from the reported S_e of $[Fe(HSO_4)]^{+/2+}$ (from $FeSO_4 + H_2SO_4$)[36] has also been added (Figure 49). This system is found to be an excellent fit in the proposed trend ($Z_{ox}^2 - Z_{red}^2$ = 3). The excellent correlation between two of the proposed species present in the

‡‡ 5.1 Å has been previously calculated from the ionic radii and bond length of the (H_2O)-Fe-SO_4 species.[30]

thermocell and the model determined values demonstrate the accuracy of the proposed species within the thermocells.

5.3.7 – Electrochemical impedance spectroscopic analysis

5.3.7.1 – Static (impedance) *vs* Dynamic (thermogalvanic) resistance

With the speciation of the three investigated systems determined, the kinetic limitations of the thermogalvanic power were assessed. This was performed by measuring the inherent resistances of the three systems by electrochemical impedance spectroscopy (EIS). In EIS analysis. Typically, the mass transport (or solution resistance (R_S) and electron transfer resistances (R_{ET}) can be measured and compared for various redox couples within a solution.[36,201] Comparison between *in situ vs ex situ* EIS analysis, and using the hot and cold electrodes as the working electrode have been undertaken and are discussed in the Appendix. Initially, a comparison was made between the kinetic limitations of thermocell systems through measuring the internal resistances through EIS analysis (measuring R_S and R_{ET}) and calculating the internal resistance through the *operando* resistance of the thermocell.

For the EIS analysis, the R_S and R_{ET} measured from the *in situ* thermocell are shown in Figure 50(a) & (b), also shown is the R_{cell}, calculated from Ohms law of the measured thermogalvanic data (Figure 50(c)). From this comparison, it is clear that these three systems all follow the same trend **$Fe(SO_4)$** > **$Fe(SO_4)_2$** > **$Fe(HSO_4)$**. Interestingly, the R_{cell} is calculated to be significantly higher than the combined R_S and R_{ET}, thus demonstrating that the simple break-down of all internal resistances within a thermocell into just two inherent resistances (R_S and R_{ET}) is an over-simplification.

However, this does still demonstrate that the comparison between EIS and R_{cell} is both valid and informative. The fact that R_{cell} is so much higher indicates that more factors are affecting the internal resistance of the thermocell under dynamic, *operando* thermogalvanic measurements. These factors could be due to complications at the electrode surfaces[201] or concentration gradients building up at the electrode surfaces.[35] High concentrations of electrolytes (such as those used in thermocells) have been found to have significant complexities with respect to fundamental properties such as conductivity and viscosity.[15,38,94]

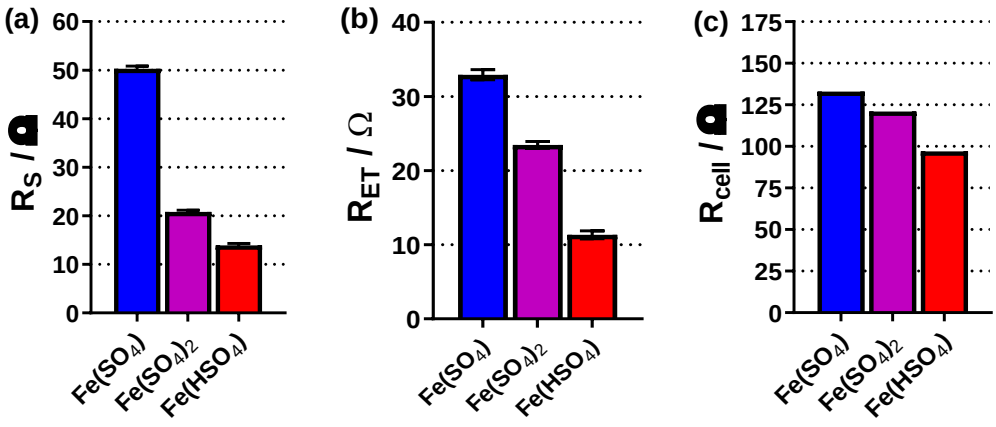

Figure 50 – Bar charts of (a) solution resistance (R_S), (b) electron transfer resistance (R_{ET}) determined through the *in-situ* non-isothermal impedance spectroscopy. Also shown is (c) calculated internal resistance (R_{cell}) of the thermogalvanic cell at a ΔT of 20 K where T_{cold} was 20°C, based upon Ohms law (V=IR) and the measured from the thermogalvanic data (Figure 45).

5.3.7.2 – Electrocatalysis of different electrode materials

A further comparison investigated in the thermocell systems is the difference in electrocatalysis of different electrode materials. This was undertaken as there has

been numerous investigations into electrode surface modification within thermocells,[40,54,93,96,201] especially with carbon nanomaterials.[54] There has even been cost-comparisons between two different types of carbon against pure platinum electrodes on the $[Fe(CN)_6]^{3-/4-}$ redox couple.[35] Gold (or more specifically, surface gold oxide) is known to be electrocatalytic towards the $Fe^{2+/3+}$ redox couple.[174] However, gold electrode passivation is also known to occur from poisoning by chemisorbed $[SO_4]^{2-}$ and $[HSO_4]^-$ species.[172]

Here, R_S was fixed for this investigation, therefore only R_{ET} was measured. Unsurprisingly, the decrease in R_{ET} also follows the same trend as that experienced previously **$Fe(SO_4)$** > **$Fe(SO_4)_2$** > **$Fe(HSO_4)$**. The R_{ET} is generally lower at gold rather than carbon, with the exception of **$Fe(SO_4)_2$**, which is found to have the same (within error) R_{ET} at both graphite and gold electrodes. This is likely due to the increased passivation of the gold surface due to the extra $[SO_4]^{2-}$ ions present in solution,[172] raising R_{ET} at Au so it is equivalent to the less electrocatalytic carbon electrode.

After undertaking an in-depth analysis into the internal resistances of the investigated thermocells comparing the measured impedance *vs* the dynamic thermocells, and comparing the electrocatalytic ability of graphite *vs* gold electrodes, the n-type and p-type thermocells were investigated in-series in order to increase the output voltage.

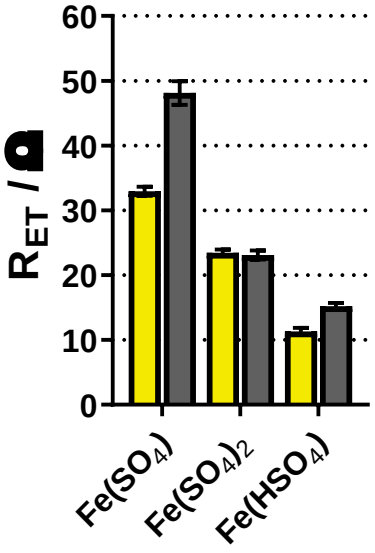

Figure 51 – Bar chart showing the electron transfer resistant (R_{ET}) of the three investigated systems ($Fe(SO_4)$, $Fe(SO_4)_2$ and $Fe(HSO_4)$) at two electrode materials gold (gold) and graphite (grey).

5.3.8 – In-parallel and in-series thermocell utilisation

Individual n-type and p-type thermogalvanic cells achieve low output voltages due to limited Seebeck coefficients[30] and the small temperature range of the utilised solvent, which is typically water. Employing n-type and p-type thermocells electrically in-series is one method of increasing the output voltage, without thermally short-circuiting the device.[88] This has often been employed using an either inherently acidic, or acidified $Fe^{2+/3+}$ n-type with a p-type $[Fe(CN)_6]^{3-/4-}$ thermocell.[14,15,38–40,88] By utilising n-type and p-type thermocells in-series (Figure 41) the output voltage is increased additively with the number of cells, where large numbers of thermocells in-series have demonstrated high output voltages in the range of 100s of mV up to several Vs.[14,15,40]

In this chapter, we demonstrate two n-type thermogalvanic systems, the **$Fe(SO_4)$** and **$Fe(HSO_4)$**, and one p-type, the **$Fe(SO_4)_2$** system. Initially, the n-type **$Fe(SO_4)$** and p-type **$Fe(SO_4)_2$** systems were examined in-series, as these individually generate similar S_e and power densities (Figure 45). Figure 52(a) demonstrates that the expected increase in voltage is observed for these combined n-type and p-type systems. Next, the superior n-type **$Fe(HSO_4)$** system was utilised in-series with the **$Fe(SO_4)_2$** system. Again, the expected additive voltage was observed (Figure 52(b)). Interestingly, the generated power of each combination was also roughly additive, where 88% was achieved for the **$Fe(SO_4)$** and **$Fe(SO_4)_2$** combination and 94% was achieved for the **$Fe(HSO_4)$** and **$Fe(SO_4)_2$** combination (where 100% represents complete additivity). The minor losses are due to increased resistances by having more electrical contacts.

While thermocells utilised in-series result in additive increases in voltage,[30,88] the current output of this method does not increase. In-fact, a slight decrease in current is typically observed due to an increase in resistance by adding electrical connections between the n-type and p-type thermocells.[30] To achieve a highly efficient thermocell array (producing high output power), both high voltage and high current is required. To compensate for this, previous investigations have utilised a combination of electrically in-series (to boost voltage) and electrically in-parallel (to boost current) thermocells to result in an array that improves both voltage and current.[88] In order to demonstrate that this is also possible with the systems investigated here, the in-parallel method was also examined with the **$Fe(HSO_4)$** thermocell, where a single thermocell is compared to two (Figure 52(c)). From this, the expected boost in power is observed,

obtained purely from the boost in current, which are both roughly double that of the one-cylinder cell.

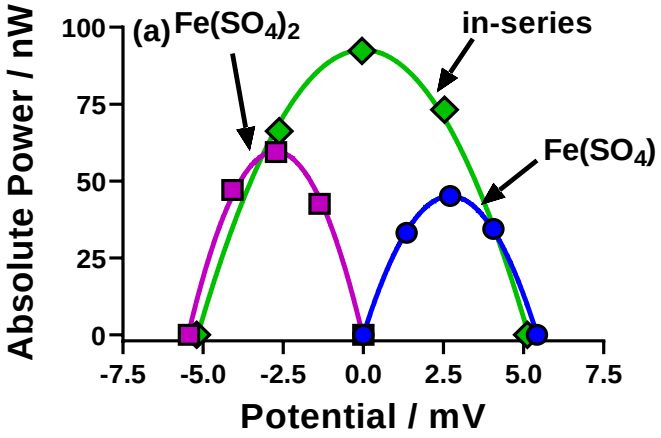

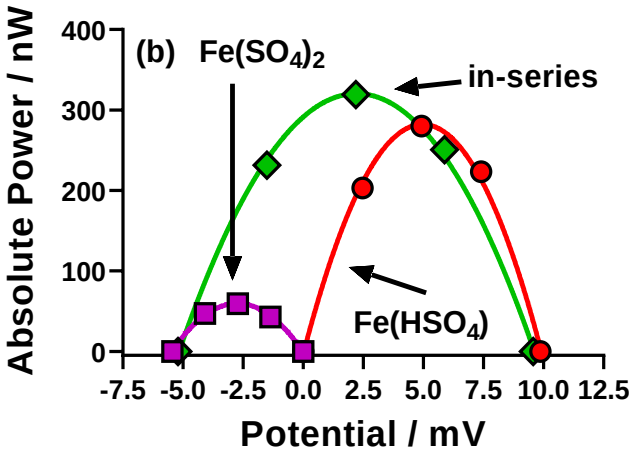

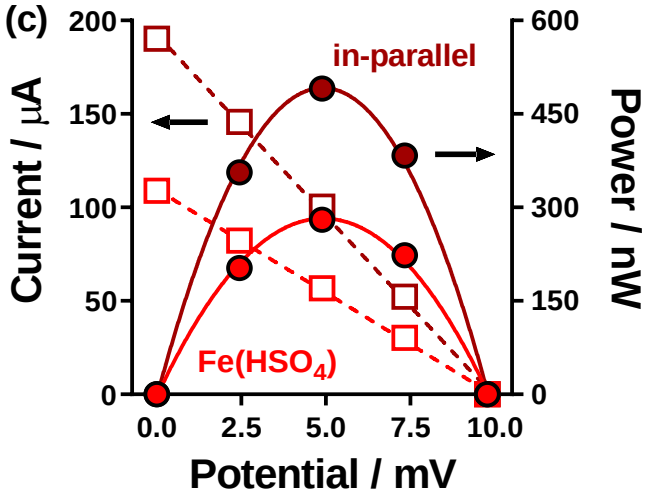

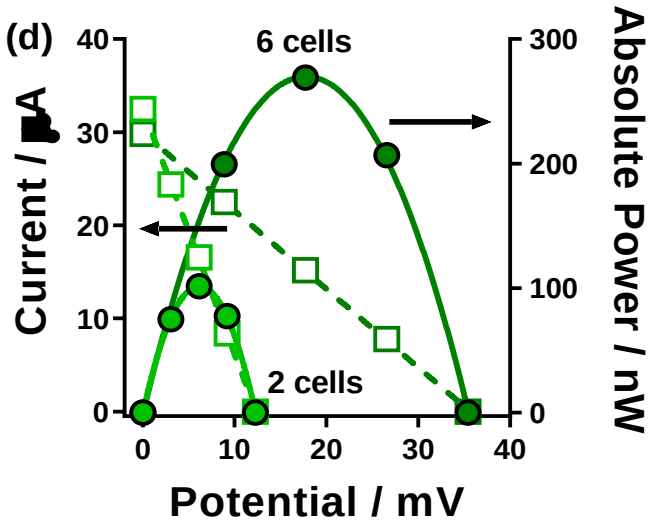

Figure 52 – Figure showing power curves of two in-series combinations (a) the n-type **$Fe(SO_4)$** and p-type **$Fe(SO_4)_2$** systems, and (b) the n-type **$Fe(HSO_4)$** and p-type **$Fe(SO_4)_2$** systems. Also shown is (c) in-parallel *I-V* plots and power curves of 1-cylinder **$Fe(HSO_4)$** and 2-cylinder **$Fe(HSO_4)$**. (d) Figure showing power curves for (a) the in-series n-type **$Fe(HSO_4)$** and p-type **$Fe(SO_4)_2$** systems where '2 cells' denote one n-p-pair and '6 cell's denotes 3 n-p-pairs.

With the success of utilising these thermocell systems both in-series and in-parallel. A larger array consisting of a 6-cylinder cell was produced and assessed. To further demonstrate the sustainability and scalability of the produced device, commercially bought graphite electrodes have been employed, rather than the gold electrodes used elsewhere. Here, the most powerful combination of the n-type **$Fe(HSO_4)$** was utilised in-series with the p-type **$Fe(SO_4)_2$**. The expected increase in output voltage was observed when utilising 6-cylinders over 2-cylinders (Figure 52(d)). The output current decreased slightly due to the increased resistance of connecting 6-thermocells, as also expected. The output power of the 6-cylinder device

also significantly increased from employing 6 cylinders, rather than 2 (a 265% increase).

5.3.9 – Towards 'unbreakable' thermocells mixing n-type and p-type systems

Table 10 demonstrates the potential toxicity of reported thermocell arrays in various volumes, where the $[Fe(CN)_6]^{3-/4-}$ system is utilised in-series with the acidic $Fe^{2+/3+}$ system. This table shows the significant quantities of $HCN_{(g)}$ that have the potential to be produced, if the two systems were to mix. Therefore, to demonstrate the inherent safety of the three investigated systems in this chapter, the two n-type systems were mixed independently with the p-type **$Fe(SO_4)_2$** system.

As demonstrated previously (Figure 52(a)) the **$Fe(SO_4)$** and **$Fe(SO_4)_2$** systems generate almost equivalent S_e, and combine excellently in-series. Therefore, these two were initially mixed. As expected, there was no issue with regard to safety upon mixing these two systems. Interestingly, upon measuring the mixed solution, it was found to still be thermogalvanically active. The resulting mixed solution had a small S_e and very low power, which is not surprising considering the solution effectively contained 0.3 M Fe(ii)SO_4, 0.3 M Fe(iii) SO_4 and 0.75 M $[SO_4]^{2-}$. This concentration of $[SO_4]^{2-}$ would be expected to yield both a low S_e and low power, as demonstrated by the initial characterisation of n-to-p-type transition of the thermocell (Figure 45).

Next, the **$Fe(HSO_4)$** and **$Fe(SO_4)_2$** systems were then mixed. Again, there was no issue concerning safety and again the resultant solution was found to be thermogalvanically active. This resulting mixed solution was found to be a much better performing n-type thermocell. Displaying a S_e of *ca.* +0.18 mV K^{-1}, which generated

a power density of 0.33 mW m^{-2}. The thermogalvanic properties of this system is shown in Figure 53, overlayed on the initial $[SO_4]^{2-}$ study from Figure 43. The ability to mix these two systems demonstrate that if these thermocell arrays are deliberately or accidentally mixed, that the resultant solution demonstrates a new 'second-life' approach to thermogalvanic cells.

To demonstrate the effectiveness of the mixed system, even after 'failure'. The array of the new mixed solution (from **$Fe(HSO_4)$** and **$Fe(SO_4)_2$**) has been utilised as an 'all n-type' array wired electrically in-parallel (as in Figure 53(b)). Due to the relatively modest S_e with respect to the other systems, and the fact that this array is 6-cylinders electrically in-parallel, a low output potential is observed in the device. However, as the mixed n-type array is electrically in-parallel, the output current increases additively (480% with respect to the one-cylinder cell) also on the more cost-effective graphite electrodes, as shown in Figure 53(d). The mixed thermocell has been fully characterised by cyclic voltammetry and electrochemical impedance spectroscopy. These analyses, along with full discussion can be found in the appendix.

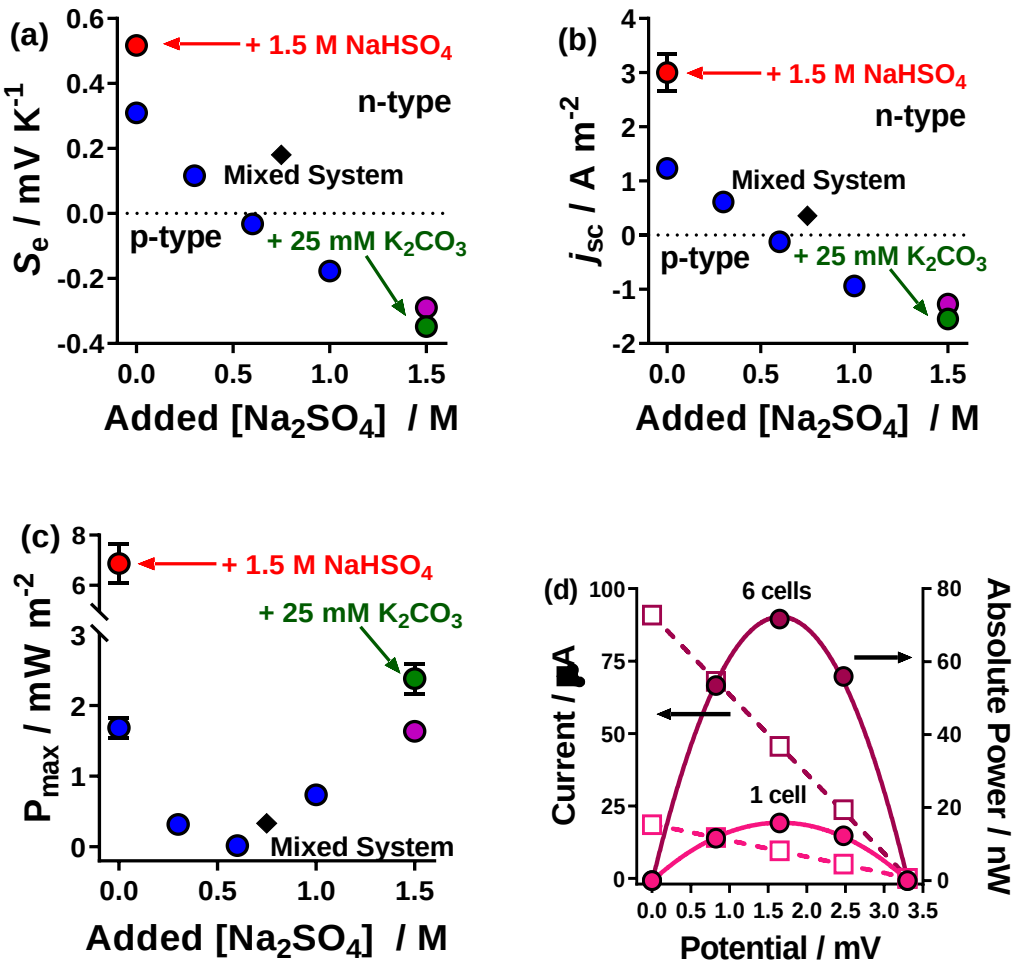

Figure 53 – (a) Plot of the Seebeck coefficient (S_e) when the thermocell was exposed to a temperature difference (ΔT) of 18 K. Adapted from Figure 43 to include the mixed system. The temperature applied to the colder electrode, T_{cold}, was fixed at 22°C. Also shown are plots of the (b) short-circuit current density (j_{SC}) and (c) maximum power density (P_{max}) generated by the thermocells as a function of Na_2SO_4 concentration; all experimental conditions same as Figure 45. Adapted from Figure 45 to include the mixed thermocell system. (d) The 'mixed' system in-parallel where '1 cell' denotes 1 cell and '6 cells' denote 6 cells.

Despite these shortcomings when compared to the **$Fe(HSO_4)$** and **$Fe(SO_4)_2$**. The mixed system represents a new class of thermocell, which we have defined as a 'second-life' thermocell.[30] This new class of thermogalvanic cell represents a

significant new advancement in the sustainability of thermoelectrochemical cells. To assess both the green and sustainable aspects of the sulphate-based thermocell systems, these were assessed compared to the typically employed $[Fe(CN)_6]^{3-/4-}$ and acidic $Fe^{2+/3+}$ systems against both the 12 principles of green chemistry and green engineering.

5.3.10 – Sustainability

We have clearly demonstrated the advantages of an 'unbreakable' thermocell that is both a safe alternative to conventional redox couples, whilst also demonstrating a thermocell which is tolerant to damage / wear and still functions when both n- and p- type thermocells have mixed. In accordance with the 12 principles of green chemistry,[176] and the 12 principles of chemical engineering,[182] comparisons can be drawn between the n- and p-type $FeSO_4$-based thermocells reported here and the typically employed $Fe^{2+/3+}$ and $[Fe(CN)_6]^{3-/4-}$ thermocells. Five of the 12 principles of green chemistry apply here: principles 1 (waste prevention), 4 (designing safer chemicals), 6 (design for energy efficiency), 10 (design for degradation) and 12 (safer chemistry for accident prevention).[176] Seven of the 12 principles of green engineering also apply here: principles 1 (non-hazardous material and energy inputs and outputs), 2 (prevention instead of treatment), 4 (maximise efficiency), 6 (conserve complexity), 7 (durability rather than immortality), 9 (minimise material diversity) and 11 (design for commercial "afterlife").[182] Many of the principles of green chemistry and engineering overlap and will be discussed together. A summary of the principles and the assessed outcome of these principles with respect to both the $FeSO_4$-based

thermocells developed here compared to the acidic $Fe^{2+/3+}$ and $[Fe(CN)_6]^{3-/4-}$ previously reported[39] are shown in Table 13. These principles have been qualitatively assessed and are discussed in more detail throughout the rest of the section.

With respect to green engineering principles 6 and 9, both complexity (in this case in chemical form) and material diversity need to be minimised when designing a greener process.[182] In this regard, the thermocells employed here contain 4 ions in total ($Fe^{2+/3+}$, Na^+, $[HSO_4]^-$ and $[SO_4]^{2-}$), whereas a typical n- and p-type in-series thermocell consists of a total of 7 ions ($Fe^{2+/3+}$, H^+, K^+, $[NH_4]^+$, $[ClO_4]^-$, Cl^- and $[Fe(CN)_6]^{3-/4-}$).[39,40] This represents a 75% increase in material diversity in the $Fe^{2+/3+}$ and $[Fe(CN)_6]^{3-/4-}$ thermocell, while also increasing complexity due to significantly different species present in the n-type and p-type thermocells. The $FeSO_4$-based systems discussed here represent both n-type and p-type thermocells that are based on similar species (**$Fe(HSO_4)$** and **$Fe(SO_4)_2$**). Hence, significantly reducing complexity within the thermocell, and thus a significant advantage with respect to scalability from a green engineering perspective.[182]

In accordance with green chemistry principles 4 and 12, and green engineering principle 1, there is a need to design safer chemicals, chemistry, and inherently safer processes. To this end, and discussed in the introduction, in the presence of acid with heating $[Fe(CN)_6]^{3-/4-}$ has the potential to degrade,[119] leading to the formation of severely toxic $HCN_{(g)}$.[119,184,193] If the $FeSO_4$-based redox couples degrade, the likely products would be species such as iron-hydroxides, or iron-oxides, due to the higher pH of the p-type thermocell.[197] Both of which are routinely treated with strong acids to produce the subsequent iron-salt and water. Thus, the possible degradation products

can be easily recycled.[197] The Na^+, $[HSO_4]^-$ and $[SO_4]^{2-}$ ions are also all naturally abundant and found in all water sources, including tap water.[36] These ions therefore are inherently much safer than the $[Fe(CN)_6]^{3-/4-}$ and acidic $Fe^{2+/3+}$ thermocells typically employed.

Table 13 - Table considering the 'All-$FeSO_4$ in-series thermocell' reported here, *vs* the most recently published ferricyanide-based in-series thermocell from Table 10.[39] The two have been compared using relevant '12 Principles of Green Chemistry' and the '12 Principles of Green Engineering', considering (i) efficacy during use, and the scenario if (ii) the electrolytes are accidentally mixed, and/or (iii) released into the environment.

Principles of Green Chemistry (GC) & Green Engineering (GE) Adapted from ref [176,182]	**HCl-acidified $FeClO_4$ and $K_3/[NH_4]_4[Fe(CN)_6]$ in-series thermocell** (exemplified by [39])	**All-$FeSO_4$ in-series thermocell** (this work)
- Minimise material diversity (**GE 9**) - Conserve complexity (**GE 6**)	7 elements/molecules; complexity lost on mixing ($Fe^{2+/3+}$, H^+, K^+, $(NH_4)^+$, $[ClO_4]^-$, Cl^-, $[Fe(CN)_6]^{3-/4-}$) ✗	4 elements/molecules; complexity retained on mixing ($Fe^{2+/3+}$, Na^+, $[HSO_4]^-$, $[SO_4]^{2-}$) ✓
- Designing safe chemicals (**GC 4**) - Safer chemistry for accident prevention (**GC 12**) - Inputs/outputs inherently non-hazardous (**GE 1**)	Individually safe, hazardous if mixed; $[Fe(CN)_6]^{4-}$ harmful to aquatic life (long lasting effects) ✗	Safe, both individually and mixed ✓
- Design for degradation (**GC 10**) - Durability *vs* Immortality (**GE 7**)	Ecologically damaging acids present if released into the environment ✗	Biodegradable or already elemental elements in the solution ✓
- Design for commercial 'afterlife' (**GE 11**)	Mixing cannot be reversed; results in 'end-of-life' ✗	Mixing enables 'second life' of thermocell ✓
- Waste prevention (**GC 1**) - Waste prevention instead of treatment (**GE 2**)	Insoluble and toxic waste generated if mixed ✗	'Second life' can prevent waste ✓
- Design energy efficiency (**GC 6**) - Maximise efficiency (**GE 4**)	S_e = 1.7 + 1.3 mV K^{-1} = 3.0 mV K^{-1} ✓	aS_e = 0.4 + 0.6 mV K^{-1} = 1.0 mV K^{-1} ✗
TOTAL number of rows thermocell is superior in	**1**	**5**

There is a current drive to prevent long-life waste such as non-biodegradable plastics. Green chemistry principle 10 and green engineering principle 7 are both meant to address this. These are concerned with making degradable rather than immortal systems, where waste will be minimised (discussed in more detail with regard to waste prevention below). With respect to degradation of the thermocell, we consider here the scenario if the thermocell degradation results in the individual elements being released into the environment. For example, if the thermocell itself is made of a biodegradable material which fails with extended time and the solution is released into the environment. The only important factor here is the presence of concentrated acid which poses a significant ecological threat.[177] As already mentioned, the $[SO_4]^{2-}$ and $[HSO_4]^-$ anions are both naturally abundant and are found in many water sources.[36] There is no data on the other elements in these systems.

With respect to green engineering principle 11, there is a desire for products and systems to perform in a commercial 'afterlife'. In this regard, the $FeSO_4$-based systems showcase an 'afterlife' demonstrated as the 'second-life' continued thermogalvanic activity upon mixing of the solutions (Figure 53). The $Fe^{2+/3+}$ and $[Fe(CN)_6]^{3-/4-}$ systems fail in this aspect as the potential 'afterlife' of mixing of these systems is the evolution of severely toxic $HCN_{(g)}$.[119] Therefore, in this aspect the $FeSO_4$-based thermocells demonstrate a significant advantage due to the 'second-life' capability.

Due to this 'second-life' ability the $FeSO_4$-based thermocells also show an advantage over the $Fe^{2+/3+}$ and $[Fe(CN)_6]^{3-/4-}$ systems with respect to green chemistry principle 1 and green engineering principle 2, both concerning the prevention of waste.

If the $Fe^{2+/3+}$ and $[Fe(CN)_6]^{3-/4-}$ thermocells were to mix, in addition to the toxic substances, the insoluble $Fe[Fe(CN)_6]_{(s)}$ (or Prussian blue) would be produced, which would be completely wasted and need to be removed. Our $FeSO_4$-based thermocell redox couples demonstrate a 'second-life' which removes the need to remove any waste as the 'waste' would maintain activity and can still be used.[182]

Despite all these shortcomings of the $[Fe(CN)_6]^{3-/4-}$ and $Fe^{2+/3+}$-based thermocells, they do have one favourable aspect in accordance to the twelve principles of green chemistry and green engineering, principles 6 and 4, respectively. This is to maximise energy efficiency. Where both the n-type and p-type $FeSO_4$ systems employed here exhibit lower Seebeck coefficients of -0.4 and +0.6 mV K^{-1} *vs* -1.4[35,67] and between +1.35 and +1.78[36,38,39] mV K^{-1} for the $[Fe(SO_4)_2]^{-/2-}$, $[Fe(HSO_4)]^{+/2+}$ and the $[Fe(CN)_6]^{3-/4-}$ and $Fe^{2+/3+}$ redox couples, respectively. The $Fe^{2+/3+}$ and $[Fe(CN)_6]^{3-/4-}$ combination also exhibits higher power densities in similar conditions.[3,35,36] However, there are usually compromises made with respect to increasing the sustainability of any process. Here, the compromise is between the greater power density of the $Fe^{2+/3+}$ and $[Fe(CN)_6]^{3-/4-}$ array *vs* the much improved safety, significantly lower complexity and ability to have a 'second-life' of the $FeSO_4$-based thermocells.

5.4 – Conclusion

To conclude, an in-depth study has been conducted on the $FeSO_4$ thermocell, in the absence and presence of added electrolytes (the $[HSO_4]^-$ and $[SO_4]^{2-}$ anions). Where the presence of acidic $[HSO_4]^-$ anions was found to improve the n-type thermocell with respect to S_e, j_{SC} and P_{max}. Significantly, with increasing concentration of $[SO_4]^{2-}$ anions the n-type **Fe(SO₄)** thermocell was found to transition into a p-type **Fe(SO₄)₂** system. The three investigated systems have been explored for temperature- and speciation-dependent thermogalvanic properties. Where the S_e of all three species was found to be affected by altering the temperature of the system, most significantly observed with **Fe(SO₄)₂** (where the S_e increased from *ca.* -0.28 mV K^{-1} to *ca.* -0.4 mV K^{-1}).

The speciation of the three systems was analysed experimentally by IR and UV-Vis spectroscopies, and theoretically by a model based on the thermogalvanic properties observed (ΔS_{rc}). This analysis confirmed the proposed speciation of the $[Fe(SO_4)]^{0/+}$ and $[Fe(SO_4)_2]^{-/2-}$ redox couples, and determined that different equilibria are present in the **Fe(HSO₄)** system. For which, there is both $[Fe(SO_4)]^{0/+}$ and $[Fe(HSO_4)]^{+/2+}$ character in solution. The electrochemical properties of the three investigated systems have been probed by cyclic voltammetry and electrochemical impedance spectroscopy, where the clear advantage of having excess electrolyte (the $[HSO_4]^-$ and $[SO_4]^{2-}$ anions) is observed in both the lower peak-to-peak separation of the **Fe(SO₄)** and **Fe(HSO₄)** systems, and the consistently lower R_S and R_{ET} in these systems, when measured *in situ vs ex situ*, and comparing different electrode materials.

The n-type and p-type thermocell systems have been utilised in-series and in-parallel to increase output voltage and current, respectively. These systems have even been mixed and are found to maintain thermoelectrochemical activity, where the mixed system has also been fully characterised. This 'second-life' ability of the $FeSO_4$-based systems demonstrates a whole new class of thermogalvanic cell, which represents a much safer alternative to the currently extensively employed $Fe^{2+/3+}$ and $[Fe(CN)_6]^{3-/4-}$ systems, which have the potential to generate severely toxic $HCN_{(g)}$ if mixed. Finally, the sustainability of the $FeSO_4$-based systems have been compared to a typical $Fe^{2+/3+}$ and $[Fe(CN)_6]^{3-/4-}$ system with respect to the 12 principles of green chemistry and green engineering. This qualitative analysis has demonstrated the significant advantage of the $FeSO_4$-based systems due to less complexity in the system, alongside environmentally benign or biodegradable redox couples, and the ability to maintain activity in a 'second-life' thermocell when mixed.

Chapter 6:

Fe-ligand-complex Thermoelectrochemistry

High performance p-type thermogalvanic redox couples developed from Fe(ligand) complexes

The results of this chapter have been published in:

Royal Society of Chemistry journal: *Green Chemistry*, 2021, **23**, 8901-8915.[79]

6.1 – Aims and Objectives

In the previous chapter we developed an inherently safe combination of n-type and p-type redox couples based on iron sulphate. This combination was shown to be significantly more sustainable than the commonly utilised, but significantly hazardous combination of inherently acidic or acidified $Fe^{2+/3+}$ and $[Fe(CN)_6]^{3-/4-}$. However, the iron sulphate-based combination only produced *ca.* 33% of the output voltage of the $Fe^{2+/3+}$ and $[Fe(CN)_6]^{3-/4-}$ combination, due to the smaller charge on the redox couples. The other issue observed with the iron sulphate-based redox couples was the significant temperature dependence on the thermoelectrochemical properties, due the reliance on a cation-anion association. Therefore, in this chapter we set out to:

- Exploit the stronger binding of charged anionic ligands to the Fe cation centre to investigate a range of anionic carboxylate-based species as ligands to generate anionic (and therefore p-type) redox couples.
- Develop anionic redox couples that have a higher charge than $[Fe(SO_4)_2]^{-/2-}$, and will thus observe a higher p-type S_e.
- Combine the developed high-performance Fe(ligand) p-type redox couple with an n-type redox couple based on Fe salts for a better performing (in both voltage and power) device than the one developed using iron sulphate-based redox couples.

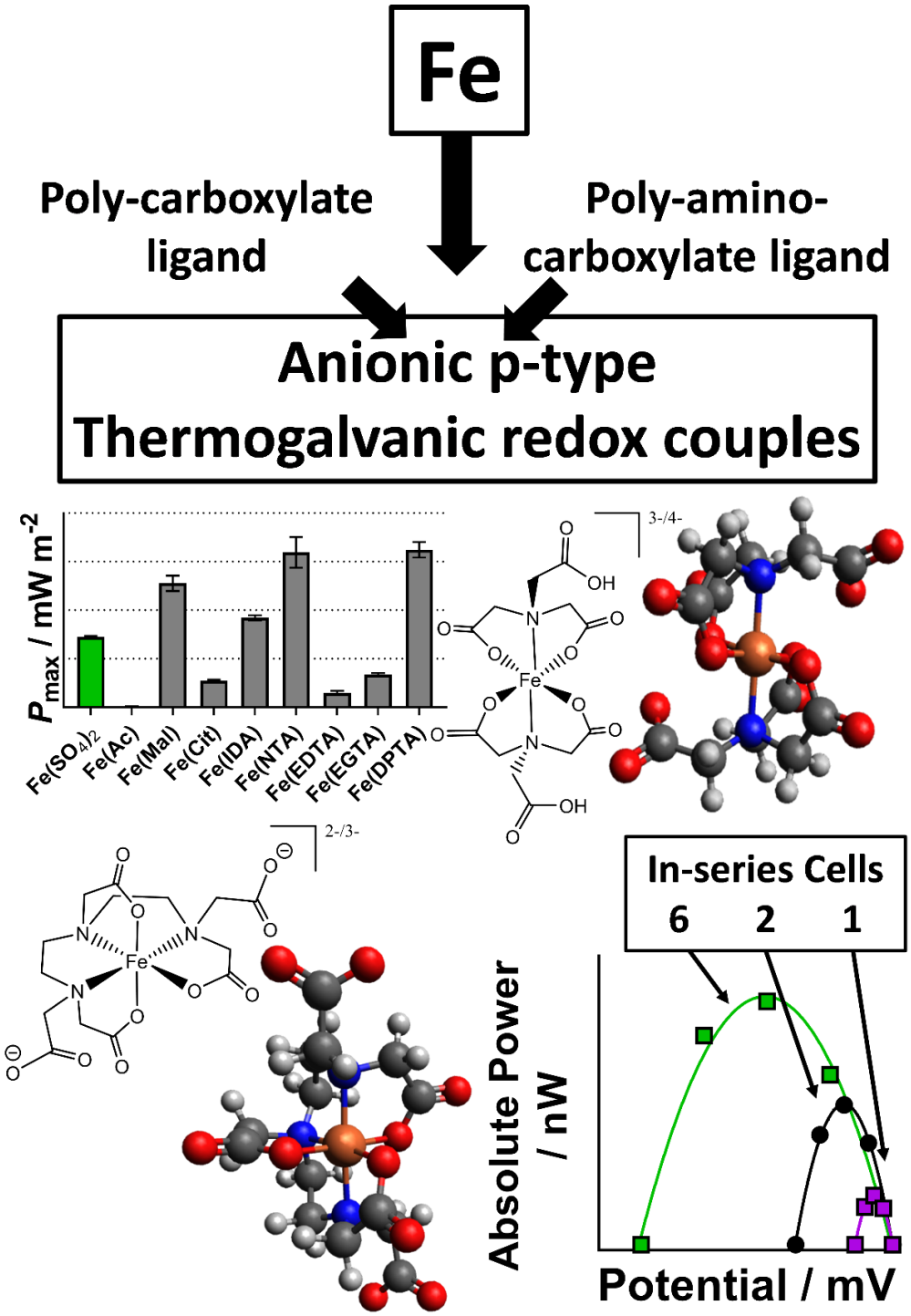
Fe
Poly-carboxylate ligand
Poly-amino-carboxylate ligand
Anionic p-type Thermogalvanic redox couples
P_{max} / mW m^{-2}
Fe(SO4)2
Fe(Ac)
Fe(Mal)
Fe(Cit)
Fe(IDA)
Fe(NTA)
Fe(EDTA)
Fe(EGTA)
Fe(DPTA)
3-/4-
2-/3-
In-series Cells
6 2 1
Absolute Power / nW
Potential / mV

6.2 – Introduction

In the previous chapter, we demonstrated the requirement for developing both n-type and p-type thermocells, which can be used in series to significantly increase the output voltage of devices. The requirement for inherent sustainability was also demonstrated as the inherent sustainability of the iron sulphate-based n-type and p-type redox couple was far superior when compared to the typically employed acidic $Fe^{2+/3+}$ and $[Fe(CN)_6]^{3-/4-}$.[30] However, the combined S_e of the more sustainable iron sulphate-based redox couples was significantly lower than the potentially hazardous combined S_e of the $Fe^{2+/3+}$ and $[Fe(CN)_6]^{3-/4-}$ redox couples (0.8 and 3.2 mV K^{-1}, respectively).[30]

The p-type $[Fe(SO_4)_2]^{-/2-}$ redox couple was generated from the high affinity of the $[SO_4]^{2-}$ anion to the $Fe^{2+/3+}$ metal centre,[30] producing an anionic redox couple which exhibits a negative Seebeck coefficient. However, as this is an ion-anion association, rather than ion-ligand coordination bonding, such as $[Fe(CN)_6]^{3-/4-}$,[25,67] these systems exhibited significant variation with changes in conditions such as temperature.[30] Therefore, more sustainable (compared to $[Fe(CN)_6]^{3-/4-}$) negatively charged redox couples need to be designed using species with strong coordination ability. The Fe ion is known to be oxophilic,[197] and strong coordination ability from ligands can be obtained from using having multidentate ligands, which exploit the chelate effect.[202]

Ligands are commonly employed to generate stable, and charged metal-ligand complexes, this strategy has also been reported in thermocells. With respect to iron complexes, as previously discussed the hexacyano (6$[CN]^-$) ligand complex $[Fe(CN)_6]^{3-/4-}$ is the most extensively explored redox couple in thermogalvanic cells.

This system has also been incorporated with a phenanthroline ligand to form the $[Fe(phen)(CN)_4]^{-/2-}$ redox couple, reducing the Seebeck coefficient from a reported -1.6 mV K^{-1} to -1.0 mV K^{-1}, at very low concentrations.[31] Other Fe(ligand) complexes investigated in thermocells have all been studied in ionic liquids, the $Fe(Cp)_2$ (known as ferrocene / ferrocenium ($[Fc]^{0/+}$)) have reported a S_e of *ca.* +0.1 mV K^{-1}, in a wide range of solvents.[78] As discussed in the previous chapter introduction, this redox couple has had both an $[Emim]^+$ and $[NTf]^-$ group covalently bonded to yield S_e of *ca.* +0.2 and -0.1 mV K^{-1}, respectively.[121] The $[Fe(bpy)_3]^{2+/3+}$ redox couple has reported a S_e of +0.48 mV K^{-1},[114] and the $[Fe(Cl)_4]^{-/2-}$ and $[Fe(Br)_4]^{-/2-}$ redox couples have reported S_e of -0.48 and -0.42 mV K^{-1}, respectively.[114]

In this chapter, a number of anionic ligands (shown in Figure 54) have been investigated, these have been complexed to the $Fe^{2+/3+}$ redox couple, generating anionic iron-ligand complexes. These complexes have been found to exhibit p-type, negative Seebeck coefficients in the range of -0.07 mV K^{-1} up to -1.35 mv K^{-1}. Demonstrating Seebeck coefficients on-par with the state-of-the-art $[Fe(CN)_6]^{3-/4-}$ redox couple, but which can be used safely in combination with $Fe^{2+/3+}$. The p-type Fe(DEPTA) has been utilised in-series with $Fe^{2+/3+}$, generated from iron chloride, to produce a device that is significantly better performing than the previous $[Fe(SO_4)_2]^{-/2-}$ and $[Fe(HSO_4)]^{+/2+}$ combination, whilst maintaining the inherent safety and green chemistry credentials.

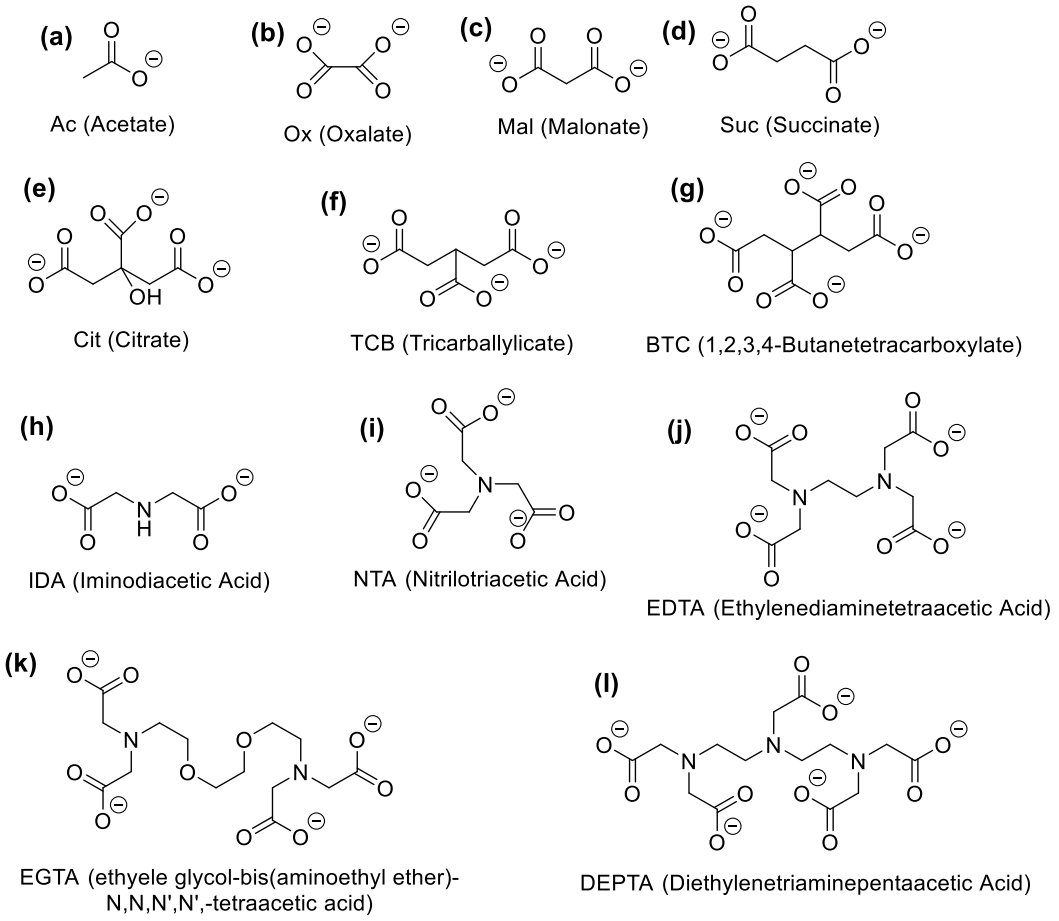

Figure 54 – Figure showing the chemical structures of the fully-anionic form of all ligands which have been investigated in this chapter.

6.3 – Results and Discussion

6.3.1 – Thermoelectrochemistry of Fe-ligand complexes

All ligands in Figure 54 were tested for their ability to generate anionic iron redox couples. This was ultimately successful for a number of ligands (acetate, malonate, citrate, IDA, NTA, EDTA, EGTA and DEPTA). The Fe(ligand) complexes were synthesised *via* one of three methods (full explanation in experimental chapter). Method 1 was used to synthesise the acetate, malonate and citrate, method 2 for IDA, and method 3 for NTA, EDTA, EGTA and DEPTA. Method 2 was used (*i.e.* in the absence of the protonated acid solid, due to the significant insolubility of these compounds, where they had to be deprotonated with NaOH before addition to the Fe solution was possible.

The poly-carboxylate redox couples were initially screened by adding an equimolar ratio of ligand (protonated, as the carboxylic acid) and ligand (deprotonated, as the sodium carboxylate). The acetate, malonate and citrate-based systems were found to form coloured solutions. Due to complications with instability, all other poly-carboxylate systems were not investigated further. The oxylate and succinate carboxylic acids and carboxylate salts were found to be sparingly soluble and could not be used. The TCB and BTC were soluble when deprotonated to the carboxylate, but immediately formed a precipitate upon addition of to the iron-solution. Likely forming a rigid structured metal-organic framework. These systems were therefore no longer investigated, and the acetate, malonate and citrate were taken forward for further testing.

IDA was the only poly-aminocarboxylate system to have a soluble carboxylic acid (and could be synthesised using method 2, where the carboxylate species required deprotonation with NaOH), all others were synthesised using the fully deprotonated carboxylate solution only (method 3). All these systems, along with the acetate, malonate and citrate were found to form a complex that demonstrated thermogalvanic activity. Therefore, the thermoelectrochemical properties of all Fe(ligand) complexes were initially investigated.

All stable poly-carboxylate and poly-aminocarboxylate systems were (semi)-optimised with respect to metal, carboxylic acid, and carboxylate ratio (discussed in Tables A3-A5), and the resultant thermoelectrochemical properties are displayed in Figure 55 for (a) S_e, (b) j_{SC} and (c) P_{max}, respectively (Tabulated data shown in Table 14). Despite the ligands being shown in order of ascending charge of ligand for both poly-carboxylate (Ac (-1), Mal (-2), Cit (-3)) and poly-aminocarboxylate (IDA (-2), NTA (-3), EDTA (-4), EGTA (-4), DEPTA (-5)), there appears to be no observable trend in any of the three thermoelectrochemical properties measured. However, four candidates stand out with superior power density (the Mal, IDA, NTA and DEPTA). Two other systems (citrate and EGTA) also display a higher observed S_e than the $[Fe(SO_4)_2]^{-/2-}$ system developed in the previous chapter.

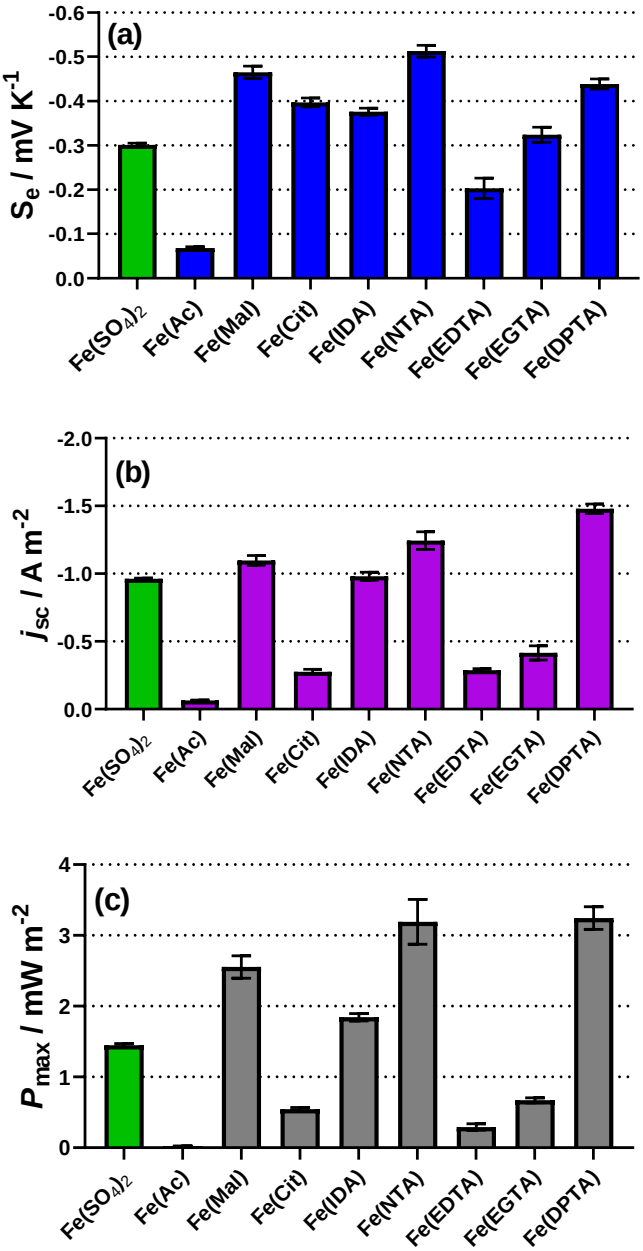

Figure 55 – Figure showing the (a) S_e, (b) j_{SC} and (c) P_{max} of the various Fe(ligand) complexes investigated in this chapter, compared to the $[Fe(SO_4)_2]^{-/2-}$ investigated in the previous chapter.

The distinct lack of trend between ligand charge and thermoelectrochemical properties (or primarily, the S_e) is an intriguing and unexpected outcome, which

requires much deeper investigation into these novel redox systems. Therefore, the electrochemistry of these systems was measured and is discussed below.

Table 14 – Table of data showing all investigated ligands from Figure 56 at the (semi)-optimised ratio of ligand acid to ligand base, pH of these produced solutions is also shown.

Ligand	Soluble / Thermo-galvanically active	Semi-optimised ratio of acid : base*	S_e / mV K^{-1}	j_{SC} / A m^{-2}	P_{max} / mW m^{-2}	pH
$[Ac]^-$	✓	5 : 5	-0.07 ± 0.01	-0.06 ± 0.01	0.02 ± 0.01	4.4
$[Ox]^{2-}$	✘**	-	-	-	-	-
$[Mal]^{2-}$	✓	5 : 10	-0.47 ± 0.01	-1.09 ± 0.04	2.55 ± 0.16	4.5
$[Suc]^{2-}$	✘**	-	-	-	-	-
$[Cit]^{3-}$	✓	5 : 5	-0.40 ± 0.01	-0.28 ± 0.02	0.55 ± 0.02	3.8
$[TCB]^{3-}$	✘***	-	-	-	-	-
$[BTC]^{4-}$	✘***	-	-	-	-	-
$[IDA]^{2-}$	✓	2 : 4	-0.38 ± 0.01	-0.98 ± 0.03	1.84 ± 0.05	3.5
$[NTA]^{3-}$	✓	0 : 5**	-0.51 ± 0.01	-1.24 ± 0.07	3.19 ± 0.32	8.9
$[EDTA]^{4-}$	✓	0 : 2**	-0.20 ± 0.02	-0.29 ± 0.01	0.29 ± 0.04	6.8
$[EGTA]^{4-}$	✓	0 : 2**	-0.32 ± 0.02	-0.42 ± 0.05	0.67 ± 0.04	8.9
$[DPTA]^{5-}$	✓	0 : 2**	-0.44 ± 0.01	-1.48 ± 0.04	3.25 ± 0.16	8.9

*Optimisation data can be found in Appendix

**Solubility issues.

***Precipitation was formed on mixing of Fe and Base.

6.3.2 – Cyclic Voltammetry

Throughout this thesis, cyclic voltammetry (CV) has already been demonstrated to be a hugely powerful tool in understanding the redox couple behaviour in thermoelectrochemical systems. Therefore, this was also employed here for all the (semi)-optimised redox couples shown above. Figure 56(a-c) shows the representative CVs of all the redox couples at a Au working electrode *vs* an Ag/AgCl reference. Also shown is the parent FeCl in the absence of any acid or ligand, as a 'blank' comparison.

The investigated redox couples display a wide range of peak-to-peak separations (ΔE). The Fe(Ac) and Fe(Cit) systems displayed a significantly high ΔE (in the range of *ca.* 600 – 800 mVs), demonstrating electrochemical irreversibility of the redox couple. Many of the redox couples such as the Fe(NTA), Fe(EDTA), Fe(EGTA) and Fe(DEPTA) all displayed a ΔE on par with the FeCl at *ca.* 200 mV. Demonstrating good electrochemical kinetics with an electrochemical *pseudo*-reversibility of the redox couple, with Au being a good electrocatalyst for the Fe(ii)/Fe(iii) redox couple.[174]

Next, the peak current (I_p) of the redox couples were compared from the CVs. Of all the systems investigated, only the Fe(EDTA) and Fe(DEPTA) display an I_p on par with the FeCl system in the absence of ligand. Several of the investigated redox couples demonstrated a significantly lower I_p than FeCl. The systems that demonstrate a high ΔE with low I_p (the Fe(Ac) and Fe(Cit)) also have a low j_{SC}, compared to the other investigated systems, which can be explained by the poor electrochemical reversibility. However, a system such as Fe(EDTA) demonstrates good

electrochemical reversibility and I_p, but a low S_e (unexpected for a 4^- ligand) and a low j_{SC}. There are therefore clearly other factors occurring in these systems that cannot be explained by the electrochemical and thermoelectrochemical properties alone. Therefore, electrochemical impedance spectroscopy was employed to probe the inherent resistances of the redox couples.

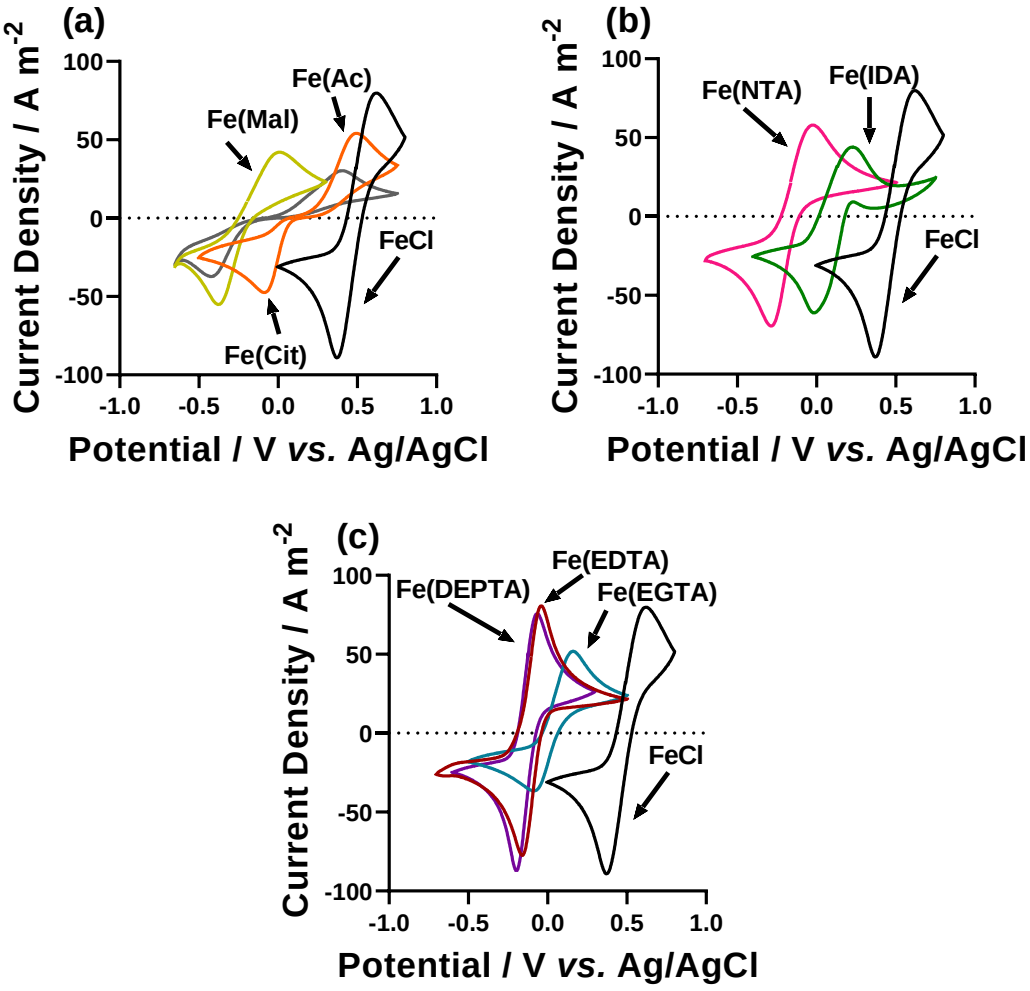

Figure 56 – Figure showing (a-c) cyclic voltammograms of the Fe(ligand) redox couples investigated in this report, all compared to the $FeCl_{2/3}$ system in the absence of ligand.

6.3.3 – Electrochemical Impedance Spectroscopy

Electrochemical impedance spectroscopy (EIS) is another useful analysis technique for electrochemical systems, which has been previously utilised to measure the inherent resistances within thermogalvanic cells[30,36,168,169,201] and was discussed extensively in the previous chapter. Therefore, this technique was also employed here on the Fe(ligand) systems.

EIS analysis was performed *ex-situ* in a three-electrode setup where the CVs were also recorded, using a Pt working electrode. Attempts to perform this technique on the Fe(Ac) system proved too difficult and is therefore left out of the discussion in this section. Figure 57 shows both the measured solution (or mass transport, (R_S)) and electron transfer (R_{ET}) resistances of the investigated systems. Interestingly, the R_S of the ligand systems are all found to be lower than that of FeCl in the absence of ligand. This is due to the excess of charged ligand and in some cases also acidic ligand all acting as a supporting electrolyte, reducing the ohmic resistance of the systems (and therefore R_S).[30,36]

Regarding the R_{ET}, only two systems (the Fe(IDA) and Fe(DEPTA)) were found to have lower R_{ET} than FeCl (Figure 57(b)), and four systems (Fe(Mal), Fe(IDA), Fe(NTA), Fe(DEPTA)) were found to have a significantly lower R_{ET} than the others. Unsurprisingly, these four systems are also those that generate high power density. The Fe(EGTA), Fe(EDTA) and Fe(Cit) were all found to have significantly higher R_{ET} than the parent FeCl, indicating that a high resistance to electron transfer at the electrode surface is the cause of the lower thermogalvanic current (and subsequently lower power density) observed in Figure 55(b & c) respectively. Table

15 shows both the electrochemical and EIS parameters extracted from the analysis of all the Fe(ligand) systems.

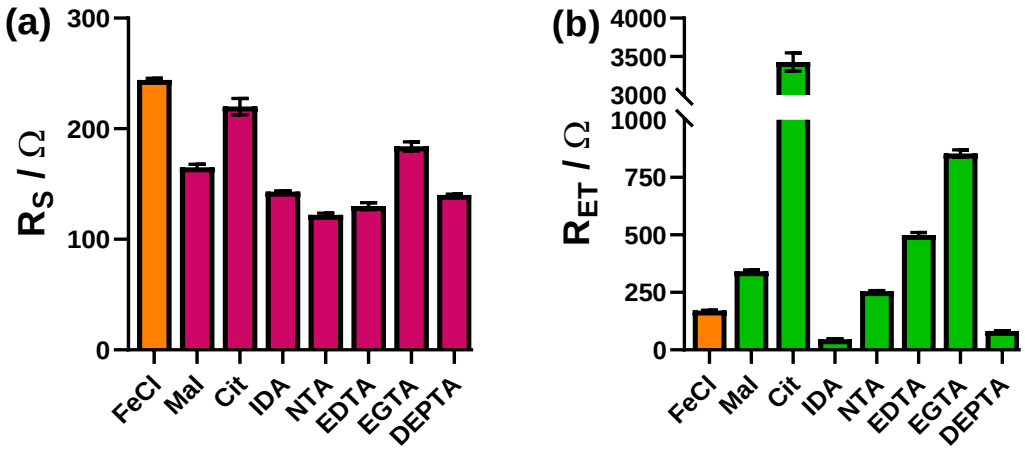

Figure 57 – Figure showing the electrochemical impedance spectroscopy measured (a) solution resistance (R_S) and electron transfer resistance (R_{ET}) for all investigated Fe(ligand) systems.

Due to the presence of acid and base in systems such as Fe(Mal) and Fe(IDA), and the excess of ligand required for systems such as Fe(NTA) and Fe(DEPTA), complicated speciation must be present in these systems. None of the previous characterisation yields information such as the number and charge of bound ligands to each Fe centre. The determination of overall charge of the bound ligands can yield the overall charge of the complex and predict the observed Seebeck coefficient. To examine this further, spectroscopic analysis was undertaken.

Table 15 – Table of data summarising values extracted from cyclic voltammograms (Figure 56) and electrochemical impedance spectroscopy (Figure 56) of the semi-optimised Fe(ligand) complexes. These have been compared against the parent $FeCl_{2/3}$ species (*i.e.* 50 mM $FeCl_2$ and 50 mM $FeCl_3$, in the absence of any ligand). The values are the equilibrium potential (E_{eq}), peak-to-peak separation (ΔE), peak current density for the oxidation and reduction peaks ($I_{p(Ox)}$ and $I_{p(Red)}$), solution resistance (R_S), and electron transfer resistance (R_{ET}).

Fe(ligand) solution	E_{eq} / V *vs* Ag/AgCl	ΔE / V	$I_{p(Ox)}$ / Am^{-2}	$I_{p(Red)}$ / Am^{-2}	R_S / Ω	R_{ET} / Ω
Parent $FeCl_{2/3}$	0.460	0.249	80	-89	244 ± 2	171 ± 2
Fe(Ac)	0.102	0.579	54	-47	-	-
Fe(Mal)	-0.198	0.383	42	-55	165 ± 3	342 ± 6
Fe(Cit)	-0.070	0.828	30	-37	220 ± 7	3430 ± 117
Fe(IDA)	0.128	0.242	44	-61	143 ± 1	46 ± 1
Fe(NTA)	-0.167	0.310	58	-70	122 ± 2	255 ± 3
Fe(EDTA)	-0.104	0.201	81	-77	130 ± 3	499 ± 11
Fe(EGTA)	-0.003	0.247	52	-37	184 ± 4	854 ± 16
Fe(DEPTA)	-0.125	0.262	76	-87	140 ± 1	83 ± 1

6.3.4 – UV-Vis Spectroscopy of the Fe(ligand) complexes

UV-Vis spectroscopy has been routinely employed in inorganic chemistry to understand the nature of metal-ligand binding interactions, where functional groups such as carboxylates are routinely investigated. This technique has also been used in thermogalvanic cells to measure the character of iron species in solution such as $[Fe(OH)_x(H_2O)_{6-x}]^{2+/3+-x}$ and $[Fe(SO_4)]^{0/+}$,[36,39] as also demonstrated in chapters 4 and 5. However, one consistent issue with this type of analysis is the high extinction coefficients, which requires low concentrations of electrolyte to be investigated. This concentration is therefore significantly lower than those investigated in the

electrochemical and thermoelectrochemical analysis, and is therefore not necessarily wholly representative.

This problem is also observed here, where 50 mM of both Fe(ii) and Fe(iii) are used in thermocells, but only 2.5 mM of either Fe(ii) or Fe(iii) or 1.25 mM of both Fe(ii) and Fe(iii) can be investigated. Previously, the Fe(ii) of aqueous salt systems was found to produce no measurable UV-Vis signal.[36] However, as the colours of these systems would be produced from the carboxylate – metal interaction, the Fe(ii) was predicted to demonstrate a UV-Vis signal. Figure 58(a-c) shows the Fe(ii), Fe(iii) and Fe(ii) and Fe(iii) systems for Fe(Mal), Fe(IDA) and Fe(DEPTA). This analysis simply demonstrates that despite the Fe(ii) yielding a UV-Vis signal, it is a weaker version of the Fe(iii), this was confirmed by the combination of Fe(ii) and Fe(iii), which produced a signal exactly in between the two.

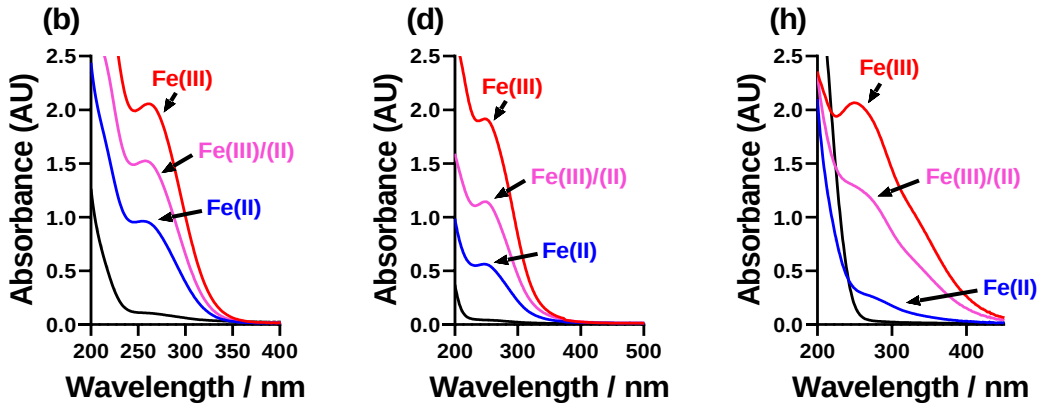

Figure 58 – UV-Vis spectra for the Fe(ii), Fe(ii)/Fe(iii) and Fe(iii) for (a) Fe(Mal), (b) Fe(IDA) and (c) Fe(DEPTA). The black line represents the ligand in the absence of Fe, all Fe concentrations in these systems was 2.5 mM overall.

Due to the weak nature of the Fe(ii) signal, which is also equivalent to the Fe(iii), only the Fe(iii) was investigated at 2.5 mM concentration for all species. The resultant obtained spectra are shown in Figure 59. All these systems demonstrate (to some extent) a peak centred *ca.* 250 nm, which is consistent with a π to π^* transition. This peak is observed to varying degrees of sharpness. The reason for this is unknown, but as this clearly yields no significant insight into the speciation of the systems it was not investigated any further. Therefore, the speciation of the Fe(ligand) systems were investigated by another method, namely using the theoretical Weaver model.

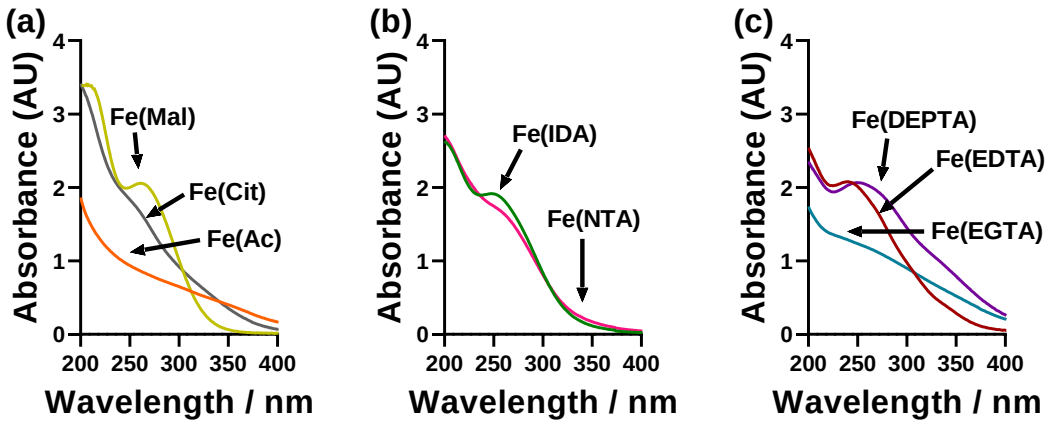

Figure 59 – Fe(ligand) UV-Vis spectra of 2.5 mM of Fe(iii) for the (a) Fe(Ac), Fe(Cit) and Fe(Mal) (b) Fe(IDA) and Fe(NTA) and (c) Fe(EDTA), Fe(EGTA) and Fe(DEPTA) systems.

6.3.5 – Speciation determination

The UV-Vis can clearly not offer any insight into a quantitative assessment of the number of ligands bound to the metal centre and the respective charge of these

ligands. The Weaver model (Equation 7, shown again for clarity) was again employed to understand the charged Fe(ligand) complexes investigated in this chapter. Using the thermodynamic information obtained from part 6.3.1.

$$\Delta S_{rc} \propto (Z_{ox}^2 - Z_{red}^2)/r \quad (7)$$

An initial assessment using the thermodynamic information in Figure 55(a) predicted the Fe(Ac), Fe(Mal), Fe(Cit), Fe(IDA) and Fe(EGTA) to be $[Fe(Ac)_3]^{0/-}$ (correlating with a $Z_{ox}^2 - Z_{red}^2$ of -1), and $[Fe(Mal)_2]^{-/2-}$, $[Fe(Cit)]^{-/2-}$, $[Fe(IDA)_2]^{-/2-}$ and $[Fe(EGTA)]^{-/2-}$ (all correlating with a $Z_{ox}^2 - Z_{red}^2$ of -3). As these complexes have rational $Z_{ox}^2 - Z_{red}^2$ values, which correlate excellently with rational complexes that have 6-coordinate binding towards the metal centre (discussed further in the next section). These systems also correlate excellently in the Weaver plot for aqueous iron-based systems (Figure 60(a)).

The Fe(DEPTA) was found to be an outlier with $Z_{ox}^2 - Z_{red}^2$ value of -5, which is irrational when Z_{ox} and Z_{red} are integers. The Fe(EDTA) system and Fe(NTA) systems also appear to be (slightly) low and high of the -3 value expected for a $[Ligand]^{4-}$ system.[§§] Therefore, a pH investigation of these three systems was undertaken in a purely thermodynamic context (Figure 60(b-d)), which demonstrated that as the pH was increased, the S_e of all three-systems increased.

There are some important things to highlight from this pH-study. Firstly, the observed S_e of the Fe(EDTA) roughly doubles to be equivalent to the Fe(Cit), Fe(Mal),

[§§] It should also be noted here that an [NTA] ligand should have a maximum charge of -3, yielding a $[NTA]^{3-}$ ligand. Therefore, as this was significantly closer to $[Fe(NTA)]^{-/2-}$ overall complex than $[Fe(NTA)]^{0/-}$ overall complex, it is predicted that two $[NTA]^{3-}$ ligands bind to the iron centre.

Fe(IDA) and Fe(EGTA), to also correlate well with the $[EDTA]^{4-}$ and the expected $[Fe(EDTA)]^{-/2-}$ redox couple. Secondly, the observed S_e of the Fe(DEPTA) also increases significantly to the expected $[DEPTA]^{5-}$ ligand, and the $[Fe(DEPTA)]^{2-/3-}$ redox couple, as demonstrated in Figure 60(a).

As it is predicted that two NTA ligands have bound to one Fe centre (forming a predicted $[Fe(NTA)_2]^{3-/4-}$ system), a significant pH-optimised increase in S_e was expected. This expected increase was observed upon increasing the pH, and a high S_e of *ca.* -1.35 mV K^{-1} was observed for the $[Fe(NTA)_2]^{3-/4-}$ redox couple. This is a very significant observation as a redox couple demonstrates a high S_e on-par with the universally utilised $[Fe(CN)_6]^{3-/4-}$ redox couple. All three optimised species were then also plotted on the Weaver plot, which now shows the excellent correlation of all redox couples investigated in this chapter, the unoptimized plot is shown in Figure A11.

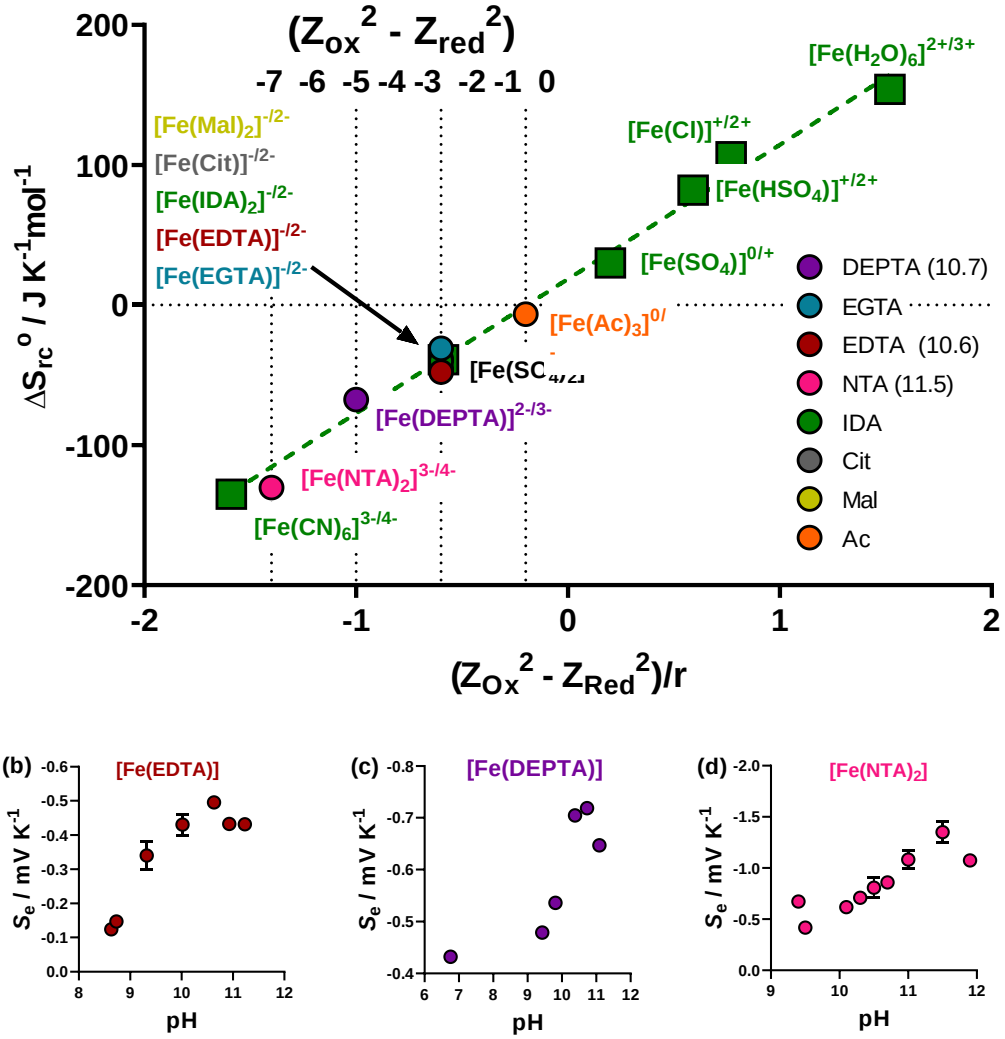

Figure 60 – Showing (a) a plot of ΔS_{rc} *vs* $(Z_{Ox}^2 - Z_{Red}^2)/r$ for all reported aqueous Fe(ii)/Fe(iii) redox systems (green squares) and all investigated Fe(ligand) solutions investigated here (coloured circles). The dotted lines indicate the $(Z_{Ox}^2 - Z_{Red}^2)$ values to 0/-1, -1/-2, -2/-3 and -3/-4 redox couples (using r = 5 Å). From these the likely ionic charge changes in the redox couples have been put next to the complex, *e.g.* $[Fe(NTA)_2]^{3-/4-}$. The values for Fe(EDTA), Fe(DEPTA) and Fe(NTA) were the pH optimised values; (b), (c) and (d) plot the observed trends in S_e *vs* pH for these three, respectively, using an applied ΔT = 18 K. pH modification was achieved by the direct addition of solid K_2CO_3 to the semi-optimised systems, the optimised pH used in this figure for Fe(EDTA), Fe(DEPTA) and Fe(NTA) are shown in brackets in the figure legend.

As the speciation model from the Weaver plot clearly indicates the number of ligands bound to the metal centre and the charge of these ligands it is possible to predict the speciation as 3D model structures.

6.3.6 – Fe(ligand) complex structures

With the speciation determined with respect to the redox couples, the next investigation was to determine the exact 3D structure of these systems. This work was conducted by Dr. Kristine Laws in our group on Avagadro 3D software, it is used here with permission as it significantly contributes to the discussion on speciation. The lowest energy (and therefore more favourable) structures for all Fe(ligand) species are shown in Figure 61. These correspond to the 3D structures shown in Figure 62.

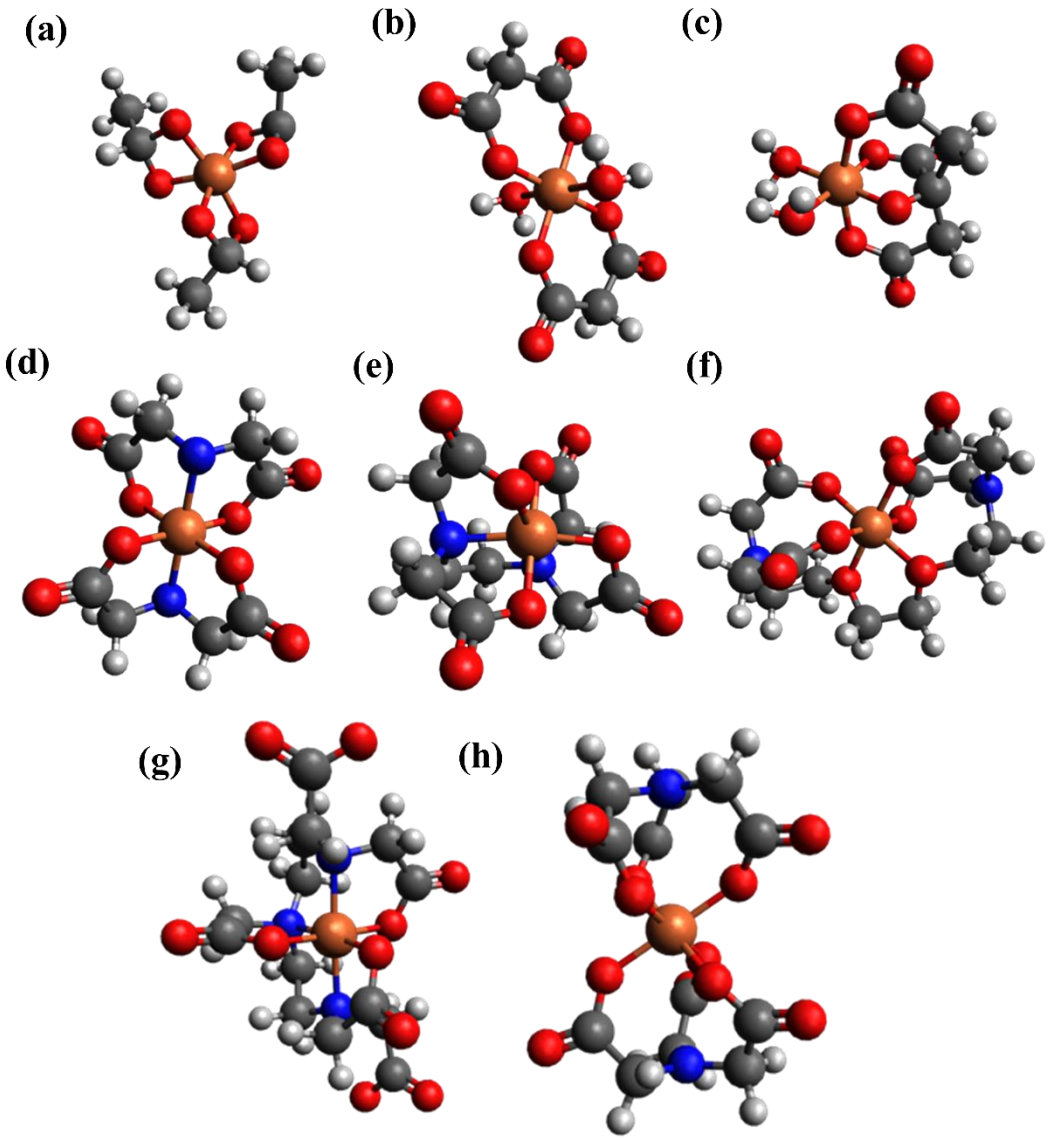

Figure 61 – energy minimised conformational structures a) $[Fe(Ac)_3]^{0/-}$ b) $[Fe(Mal)_2(OH_2)_2]^{-/2-}$ c) $[Fe(Cit)(OH_2)_2]^{-/2-}$ d) $[Fe(IDA)_2]^{-/2-}$ e) $[Fe(EDTA)]^{-/2-}$ f) $[Fe(EGTA)]^{-/2-}$ g) $[Fe(DETPA)]^{2-/3-}$ h) $[Fe(NTA)_2]^{3-/4-}$.

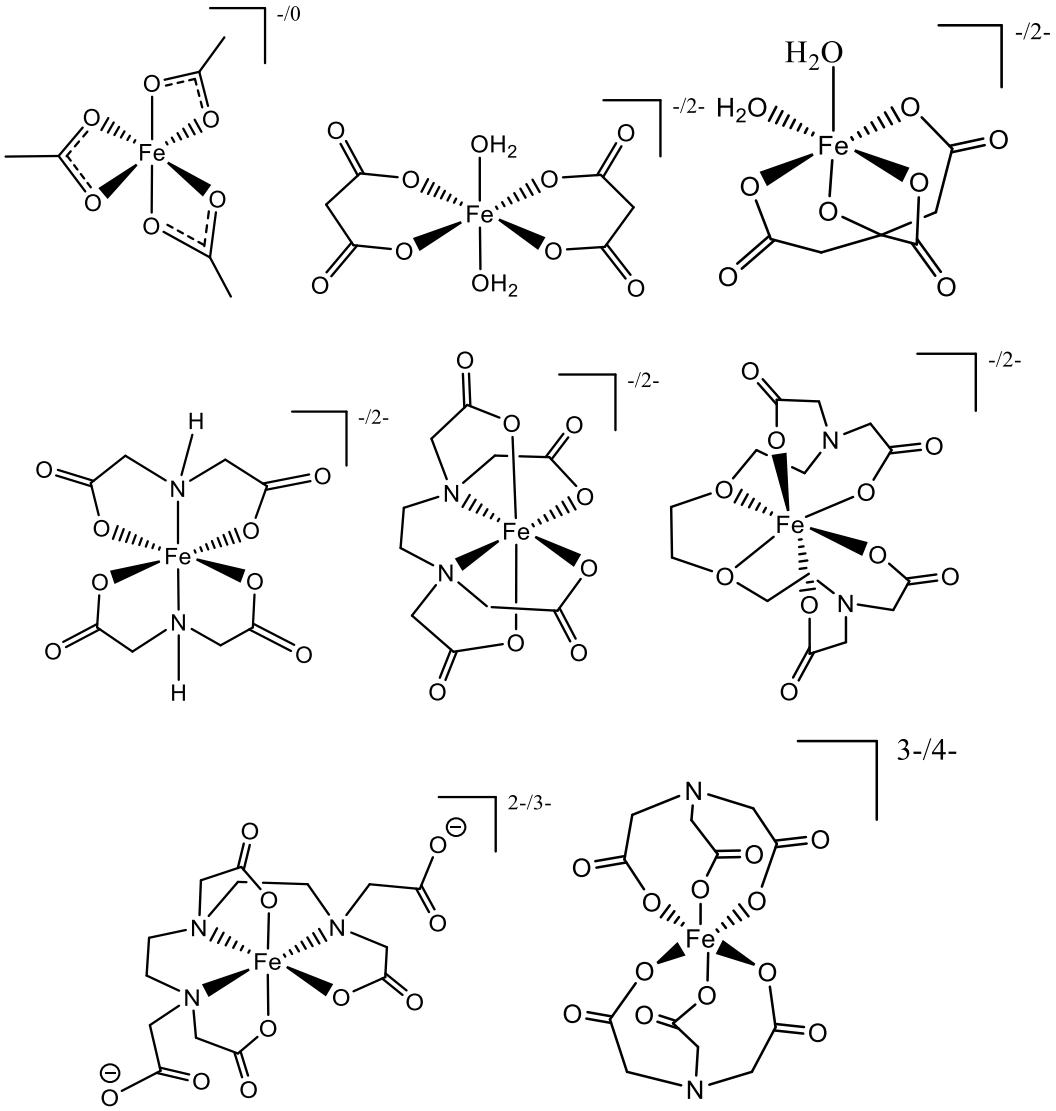

Figure 62 – Structures of the energy optimised Fe(ligand) systems investigated here, ordered the same as Figure 61.

With the success of the speciation modelling from the Weaver plot, and the high achieved S_e from the $[Fe(NTA)_2]^{3-/4-}$ and $[Fe(DEPTA)]^{2-/3-}$ redox couples upon pH-optimisation, these were further investigated. This was undertaken to determine both the thermoelectrochemical kinetics and cyclic voltametric responses with increasing pH of these species.

6.3.7 – pH effect on the kinetics of Fe(NTA) and Fe(DEPTA)

Having required a pH correction to accurately determined the speciation through the thermodynamics and the Weaver model, the kinetics and electrochemistry of the Fe(NTA) and Fe(DEPTA) species were also investigated under various pH's, where the pH was increased with addition of $[CO_3]^{2-}$. Therefore, the thermogalvanic current and power densities were also measured with altering pH. The Fe(DEPTA) and Fe(NTA) are shown in Figure 63(a & b) and Figure 63(c & d), respectively. As can be observed, the j_{SC} of the Fe(DEPTA) remains roughly constant with increasing pH, up until *ca.* pH 10, followed by a sharp drop in j_{SC} above this pH. As the observed S_e increases with increasing pH, peaking around pH 10.5, these combined factors lead to a peak in power density, at a pH of *ca.* 10.25 (Figure 63(b)).

For the Fe(NTA) system, the j_{SC} was found to sharply decrease with increasing pH, followed by a more gradual decrease beyond *ca.* pH 10. With respect to the power density, a sharp decrease followed by a plateau in low power density was observed. Demonstrating that the increase in S_e is equivalent to the decrease in current observed, leading to a plateau in power. Another noteworthy aspect of this system is the instability of the power density with high pH (above pH 11). When these solutions were left overnight a precipitate was formed, which is likely $Fe(OH)_x$ species, consistent with the observations in the previous chapter.[30]

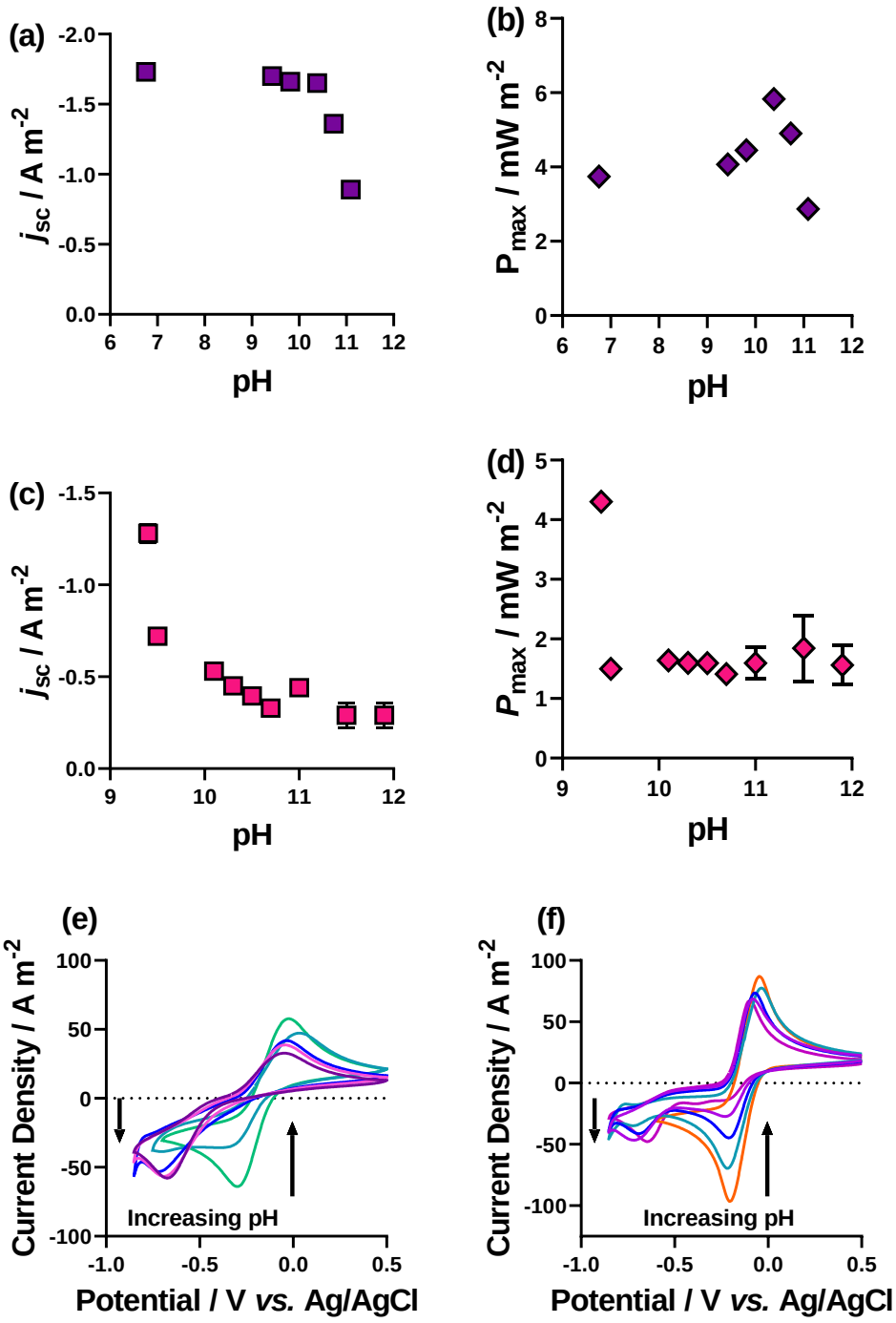

Figure 63 – Figure showing the j_{SC} and P_{max} for the (a & b) Fe(DEPTA) and (c & d) Fe(NTA) systems at various pH's. Also shown are the cyclic voltametric responses recorded at the same pH range, demonstrated as increasing pH.

With these interesting pH observations, cyclic voltammograms were also recorded for these various pH solutions. As observed previously, the un-modified pH solution for Fe(DEPTA) has fast, reversible electrode kinetics. However, when increasing pH, the reduction peak of the redox couple reduces in current. This is observed concurrently with an increase in another reduction peak *ca.* 500 mV more cathodic, with a much higher ΔE. It can be deduced therefore, that $[Fe(DEPTA)]^{-/2-}$ has the faster redox kinetics and $[Fe(DEPTA)]^{2-/3-}$ has slower, irreversible redox kinetics. Therefore, at the maximum power density, it is assumed that a combination of the $[Fe(DEPTA)]^{-/2-}$ and $[Fe(DEPTA)]^{2-/3-}$ species are present, yielding both the fast kinetics for high j_{SC} and high thermodynamics for the high S_e.

With respect to the Fe(NTA) system, increasing pH also reduces the reversible redox couple, similar to the Fe(DEPTA). The reduction peak reduces with increasing pH, again concurrently with an increase in an irreversible reduction peak at *ca.* 500 mV more cathodic. This transition occurs much faster in the Fe(NTA) system than the Fe(DEPTA) system, which explains why the current density immediately decreases so dramatically with even small increases in pH. Any increase above the (semi)-optimised value therefore severely decreases the performance of this system, as clearly observed by the j_{SC} and P_{max} (Figure 63(c & d)).

6.3.8 – In-series devices of FeCl & Fe(DEPTA)

Having achieved a high S_e, whilst maintaining a high current in the Fe(DEPTA) system, leading to high power density, this system was taken forward and investigated in-series with the n-type FeCl system typically investigated in thermocells.[14,15,164]

Figure 64 shows that despite the higher S_e (and therefore voltage) of the FeCl system (Figure 64(a, black)), the Fe(DEPTA) observes equivalent power density (Figure 64(a, purple)) due to the higher current in the Fe(DEPTA) than the FeCl (Figure 64(b)).

Due to these equivalent observed power densities, these are excellent candidates to be utilised in-series. In the previous chapter, the superior n-type $[Fe(HSO_4)]^{+/2+}$ system was investigated in series with the inferior p-type $[Fe(SO_4)_2]^{-/2-}$ system. This led to a marginal increase in power of the in-series combination than the $[Fe(HSO_4)]^{+/2+}$ alone, but a large increase in potential. Since the power densities of the FeCl and Fe(DEPTA) are equivalent, this should significantly increase the power of both the individual FeCl and Fe(DEPTA) thermocells, as well as significantly increase the potential.

Interestingly, the FeCl and Fe(DEPTA) combination has a higher power density than both individual elements combined, 249% and 284% with respect to FeCl and Fe(DEPTA) individually. This is likely due to the unique combination of a high overpotential from the FeCl system driving the faster kinetics in the Fe(DEPTA) system, resulting in overall greater performance.

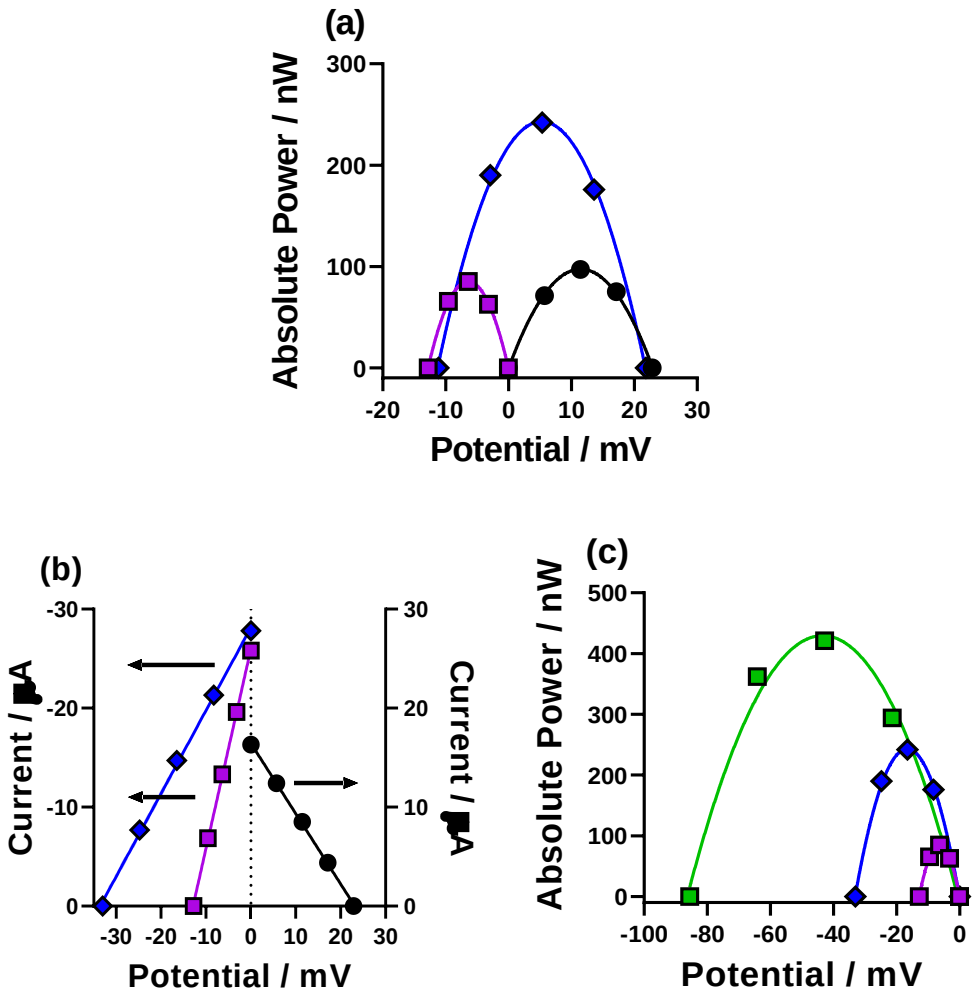

Figure 64 – Figure showing (a) the output power and (b) the output current of FeCl (●), Fe(DEPTA) (■) both individually and in series (◆). (c) The Fe(DEPTA) (■), FeCl and Fe(DEPTA) in series as both 2 (◆) and 6 chamber (■) devices.

The in-series combination generated 33 mV, this is significantly higher than the 12 mV produced from the Fe-SO_4 based (2-chamber) combination in the previous chapter. With this significantly promising 2-chamber n-type and p-type combination, another 6-cyliner device was assembled and measured. This 6-chamber cell was found to produce 85 mV and 421 nW, again significantly higher than the 35 mV and 269 nW produced by the $FeSO_4$-based 6-chamber thermocell, on the same electrode material.

This result is a significant saving in material to generate 1 V (35 pairs as opposed to 86 pairs) or 10 μW (71 pairs as opposed to 112 pairs). This is found to be a significant improvement on the proof-of-concept $FeSO_4$-based combination in the previous chapter. With these very encouraging results from the power density, the sustainability and cost-effectiveness of all the Fe(ligand) systems were evaluated and are discussed in the following sections.

6.3.9 – Sustainability of the Fe(ligand) complexes

The sustainability of generating both n-type and p-type redox couples from iron-sulphate was previously highlighted.[30] Demonstrating that a combination of less complexity in the system, use of benign reagents and the inherent non-hazardous ability to mix the thermocell solutions was superior to the inherently hazardous but typically-employed $Fe^{2+/3+}$ and $[Fe(CN)_6]^{3-/4-}$ redox couples. These two combinations could be quantitatively evaluated using the 12 principles of green chemistry and 12 principles of green chemical engineering.[30]

However, the $Fe(SO_4)$-based thermocells were unable to excel in 'maximising energy efficiency' green chemistry principle 6,[176] and green engineering principle 4.[182] Due to the much lower combined S_e of the $Fe(SO_4)$-based systems than the current state-of-the-art reported system[39] (0.8 mV K^{-1} *vs* 3.0 mV K^{-1}).[30] Here, we have demonstrated that a p-type redox couple ($[Fe(NTA)_2]^{3-/4-}$) has a S_e comparable to that of the $[Fe(CN)_6]^{3-/4-}$. In addition, our results show a significantly higher combined S_e using Fe(DEPTA) and Fe(Cl) combination (1.8 mV K^{-1}), which has more than doubled

that of our previously reported sustainable and non-hazardous redox couple combination based on $Fe(SO_4)$.[30]

Assessing the systems developed here by other principles of green chemistry and green engineering also compared favourably to the current state-of-the-art system. The combination of Fe(DEPTA) and Fe(Cl) thermocells have as little inherent complexity as the $FeSO_4$-based thermocells as these also comprise of 4 elements (the $Fe^{2+/3+}$, Cl^-, Na^+ and $[DEPTA]^{5-}$), less than the 7 elements of the $Fe^{2+/3+}$ and $[Fe(CN)_6]^{3-/4-}$ thermocells.[30] The combined Fe(DEPTA) and Fe(Cl) are also inherently safe when combined, this has already been highlighted as a significant advantage to the current state-of-the-art combination due to the potential to produce lethal quantities of severely toxic $HCN_{(g)}$, even in an aeroplane volume.[30]

Having assessed the Fe(DEPTA) and Fe(Cl) combination also has the advantages of little complexity and inherent safety, but demonstrates significantly higher energy efficiency in terms of both voltage and power. The cost-effectiveness of these systems were determined and compared to the $[Fe(SO_4)]^{-/2-}$ thermocell.

6.3.10 – Cost-comparison of Fe(ligand) systems *vs* $Fe(SO_4)_2$

If thermogalvanic systems are going to be feasible for large-scale, low-grade waste heat harvesting, then they must blend inherent safety, efficiency, scalability, and cost-effectiveness. We have previously demonstrated the inherent safety of $FeSO_4$-based systems but with the (relatively) significant-compromise on efficiency.[30] Here we have demonstrated the inherent safety of the Fe(DEPTA) and Fe(Cl) combination

with much higher efficiency (higher Seebeck coefficient and higher power output in a 6-cylinder device).

Therefore, the cost-effectiveness of the investigated iron salts was assessed, and compared to that of the $Fe(SO_4)_2$ redox couple at equivalent concentration. The output power of each thermocell here is taken from Figure 55(c), with the exception of Fe(DEPTA), which was also taken from optimised pH as in Figure 63(b). This kind of provisional techno-economic evaluation has already been reported for acidified n-type iron salts (as in chapter 4),[36] which found that despite significantly less power density being produced by acidified $FeSO_4$ when compared to $FeNO_3$, the significantly cheaper materials demonstrated that acidified $FeSO_4$ was equivalent in a cost-effective basis. This kind of balance between cost and power is hugely significant when considering scalability.[36]

Here we analyse the Fe(ligand) systems under two separate conditions, if both the ligand carboxylic acid and carboxylate salt were purchased, and if only the carboxylic acid form was purchased (as this is typically cheaper) and the deprotonated form was synthesised by chemically neutralising with sodium hydroxide (Table 16). The Fe(Ac), Fe(Mal) and Fe(EGTA) systems have extremely high cost : power ratios. This is due to the very low power produced by the Fe(Ac) system, and high cost of the Fe(Mal) and Fe(EGTA) systems (for the purchased carboxylic acid and carboxylate salt for the Fe(Mal)). However, from this analysis some viable candidates stand out as the most cost-effective. For example, the Fe(DEPTA), Fe(IDA) (using sodium hydroxide deprotonation) and Fe(NTA). All of which are *ca.* half the cost : power of the $Fe(SO_4)_2$.

Table 16 – Cost analysis of the power of each of the investigated Fe(ligand) complexes. The table of costing of all the materials can be found in Table A6.

Fe(Ligand)	Power / mW ($x10^{-5}$)	Cost of Materials per thermo-cell / £	Cost of Materials per thermocell (NaOH neutralised) / £	Cost : Power Ratio / £ mW^{-1}	Cost : Power Ratio (NaOH Neutralised) / £ mW^{-1}
Fe(Ac)	0.08	0.0019	0.0013	2416	1732
Fe(Mal)	9.00	0.1133	0.0047	1258	53
Fe(Cit)	1.93	0.0043	0.0038	225	199
Fe(IDA)	5.17	0.0224	0.0017	432	33
Fe(NTA)	1.52	0.0053	0.0051	35	34
Fe(EDTA)	1.03	-	0.0048	-	468
Fe(EGTA)	2.37	-	0.0461	-	1951
Fe(DEPTA)	11.46	0.0047	0.0059	41	52
Fe(DEPTA) (pH optimised)	20.55	0.0058	0.0070	28	34
$Fe(SO_4)_2$	5.11	0.0032	-	64	-

Several of these systems demonstrate more cost-effective power than the $[Fe(SO_4)_2]^{-/2-}$, these are the Fe(IDA) and Fe(Mal) (when the carboxylic acids are neutralised with NaOH), both methods for the Fe(NTA) and both methods for the Fe(DEPTA) (both with and without pH optimisation). From this analysis it is also clear that several of the Fe(ligand) species developed in this chapter demonstrate a significant improvement in cost-effectiveness over the $FeSO_4$-based redox couples developed in the previous chapter.

6.4 – Conclusions

In conclusion, the iron-ligand complexes developed in this chapter are a significant advancement on the proof-of-concept $FeSO_4$-based thermocell developed in the previous chapter. These complexes maintain the inherent sustainability and green chemistry advantages over the inherently hazardous acidic $Fe^{2+/3+}$ and $[Fe(CN)_6]^{3-/4-}$ combination, but are significantly more powerful than the $FeSO_4$-based combination exhibiting a combined S_e of 1.8 mV K^{-1} when the Fe(DEPTA) and Fe(Cl) redox couples are utilised in series, over double that of the $FeSO_4$-based combination of 0.8 mV K^{-1}.

Interrogating the speciation by CV, UV-Vis and a theoretical Weaver model determined the speciation and charge (once accounted for pH). The 3D structures have also been determined for their lowest energy conformations. The sustainability of these p-type redox couples have been qualitatively assessed and are equivalent to the $FeSO_4$-based redox couples in the previous chapter and are again significantly more sustainable than the $Fe^{2+/3+}$ and $[Fe(CN)_6]^{3-/4-}$ redox couples combination. A provisional techno-economic comparison also demonstrated the inherent cost-effectiveness of some of the Fe(ligand) complexes when compared to the $[Fe(SO_4)_2]^{-/2-}$ systems, with several demonstrating around half the £ / mW^{-1} of the latter. Overall, these redox couples demonstrate a significant step towards sustainable, high-performance redox couples for thermogalvanic energy harvesting.

Conclusions

As each chapter has a respective, detailed conclusion, the conclusions in this chapter will be limited and more of a summary / overview of the thesis research.

In this thesis, a wide range of fundamental physiochemical, electrochemical and thermoelectrochemical research was initially investigated for a model redox couple (namely $[Fe(CN)_6]^{3-/4-}$) with respect to both absolute temperature and temperature difference, both equimolar and non-equimolar concentration, homogeneous electrochemistry, conductivity, viscosity, cyclic voltammetry at both a static and rotating disc electrode, kinetic rate constant and diffusion coefficients of the redox ions at various solutions.

This fundamental investigation demonstrated that with increasing concentration to super-concentrated and even 'water-in-salt' concentrations severely limits the apparent kinetic rate constant and the diffusion coefficient of the $[Fe(CN)_6]^{3-/4-}$ ions in solution. This is caused by both an increase in ion-pairing and viscosity with increasing concentration. It is assumed that these effects are not only limited to the $[Fe(CN)_6]^{3-/4-}$ redox couple in thermogalvanic cells but also for many redox couples in aqueous solutions. These inherent limitations could therefore be important towards a wide array of redox-based electrochemical energy technologies such as redox-flow batteries.

The $[Fe(CN)_6]^{3-/4-}$ redox couple is a p-type (negative S_e) thermogalvanic redox couple. To develop high voltage output thermogalvanic devices, both n-type (positive S_e) and p-type redox couple systems need to be developed. Therefore, the n-type $Fe^{2+/3+}$ redox couple was also fundamentally investigated for both counter-anion and pH, this

investigation also extended towards both sustainability and cost-effective power generation of the investigated systems. This combination of criteria demonstrated that the most powerful system was not necessarily the most sustainable or cost-effective.

Unfortunately, once the $[Fe(CN)_6]^{3-/4-}$ and $Fe^{2+/3+}$ redox couples were fundamentally investigated with the idea of utilising these two redox couples in series to generate a high voltage device. It was determined that this particular combination could lead to potentially hazardous consequences due to the instability of the $[Fe(CN)_6]$ towards acidic decomposition, leading to severely toxic $HCN_{(g)}$.

Therefore, the rest of the thesis was concerned with developing a sustainable and more importantly safe n-type and p-type combination. This was initially achieved by generating both n-type and p-type redox couples from iron sulphate. This proof-of-concept device demonstrated significant improvements in the sustainability over the $[Fe(CN)_6]^{3-/4-}$ and $Fe^{2+/3+}$ redox couples, due to less complexity in the system, alongside environmentally benign or biodegradable redox couples, and the ability to maintain activity in a 'second-life' thermocell when mixed.

However, the redox couples based on iron sulphate was significantly less powerful that the $[Fe(CN)_6]^{3-/4-}$ and $Fe^{2+/3+}$ combination. Therefore, a wide range of anionic ligands was investigated in order to generate anionic Fe(ligand) complexes that observe a p-type S_e. Ultimately, this was successful with a range of Fe(ligand) complexes developed. Under the right conditions (pH-optimisation) one Fe(ligand) complexes demonstrated equivalent S_e to the potentially hazardous $[Fe(CN)_6]^{3-/4-}$ redox couple. Another of the redox couples demonstrated reasonable S_e, with good kinetics and was thus utilised in series with the $Fe^{2+/3+}$ redox couple generated from iron chloride. This proof-of-concept device was found to be significantly better

performing than the equivalent device based on the iron sulphate redox couples, producing both higher voltage and power output, whilst maintaining the sustainability and green chemistry credentials.

References

1 E. D. Coyle and R. A. Simmons, *Understanding the Global Energy Crisis*, Perdue University Press, 2014.

2 R. M. Elavarasan, *Eur. J. Sustain. Dev. Res.*, 2018, **3**, 1–19.

3 M. A. Buckingham and L. Aldous, *J. Electroanal. Chem.*, 2020, **872**, 114280.

4 Fitriani, R. Ovik, B. D. Long, M. C. Barma, M. Riaz, M. F. M. Sabri, S. M. Said and R. Saidur, *Renew. Sustain. Energy Rev.*, 2016, **64**, 635–659.

5 R. Law, A. Harvey and D. Reay, *Appl. Therm. Eng.*, 2013, **53**, 188–196.

6 D. H. Kwak, M. Binns and J. K. Kim, *Appl. Energy*, 2014, **131**, 307–322.

7 G. Oluleye, M. Jobson and R. Smith, *Energy*, 2015, **90**, 5–23.

8 G. Oluleye, M. Jobson, R. Smith and S. J. Perry, *Appl. Energy*, 2016, **161**, 627–646.

9 E. Woolley, Y. Luo and A. Simeone, *Sustain. Energy Technol. Assessments*, 2018, **29**, 50–59.

10 S. Chu and A. Majumdar, *Nature*, 2012, **488**, 294–303.

11 M. H. Dickson and M. Fanelli, *Geothermal energy: Utilization and technology*, Routledge, 2013.

12 B. Rodríguez-Soria, J. Domínguez-Hernández, J. M. Pérez-Bella and J. J. Del Coz-Díaz, *Renew. Sustain. Energy Rev.*, 2014, **34**, 78–90.

13 O. Kaynakli, *Renew. Sustain. Energy Rev.*, 2012, **16**, 415–425.

14 P. Yang, K. Liu, Q. Chen, X. Mo, Y. Zhou, S. Li, G. Feng and J. Zhou, *Angew. Chem. Int. Ed.*, 2016, **55**, 12050–12053.

15 Y. Liu, S. Zhang, Y. Zhou, M. A. Buckingham, L. Aldous, P. C. Sherrel, G. G. Wallace, G. Ryder, S. Faisal, D. L. Officer, S. Beirne and J. Chen, *Adv. Energy Mater.*, 2020, **10**, 2002539.

16 H. Im, H. G. Moon, J. S. Lee, I. Y. Chung, T. J. Kang and Y. H. Kim, *Nano Res.*, 2014, **7**, 443–452.

17 C. Han, X. Qian, Q. Li, B. Deng, Y. Zhu, Z. Han, W. Zhang, W. Wang, S. Feng, G. Chen and W. Liu, *Science (80-.).*, 2020, **368**, 1091–1098.

18 S. Brückner, S. Liu, L. Miró, M. Radspieler, L. F. Cabeza and E. Lävemann, *Appl. Energy*, 2015, **151**, 157–167.

19 H. Jouhara, N. Khordehgah, S. Almahmoud, B. Delpech, A. Chauhan and S. A. Tassou, *Therm. Sci. Eng. Prog.*, 2018, **6**, 268–289.

20 J. M. Beér, *Prog. Energy Combust. Sci.*, 2007, **33**, 107–134.

21 B. F. Tchanche, G. Lambrinos, A. Frangoudakis and G. Papadakis, *Renew. Sustain. Energy Rev.*, 2011, **15**, 3963–3979.

22 B. Saleh, G. Koglbauer, M. Wendland and J. Fischer, *Energy*, 2011, **36**, 199–211.

23 T. C. Hung, S. T. Y and S. K. Wang, *Energy*, 1997, **22**, 661–667.

24 M. F. Dupont, D. R. MacFarlane and J. M. Pringle, *Chem. Commun.*, 2017, **53**, 6288–6302.

25 T. I. Quickenden and Y. Mua, *J. Electrochem. Soc.*, 1995, **142**, 3985–3994.

26 E. . Bouty, *J. Phys. Theor. Appl.*, 1880, **9**, 306–320.

27 T. W. Richards, *Proc. Am. Acad. Arts Sci.*, 1897, **33**, 3–20.

28 T. W. Richards, *Zeitschrift für Phys. Chemie*, 1897, **24**, 39–54.

29 H. Julian Goldmid, *Introduction to Thermoelectricity*, Springer Berlin Heidelberg, Second Edi., 2016.

30 M. A. Buckingham, K. Laws, J. T. Sengel and L. Aldous, *Green Chem.*, 2020, **22**, 6062.

31 T. I. Quickenden and C. F. Vernon, *Sol. Energy*, 1986, **36**, 63–72.

32 Y. Mua and T. I. Quickenden, *J. Electrochem. Soc.*, 1996, **143**, 2558–2564.

33 T. I. Quickenden and Y. Mua, *J. Electrochem. Soc.*, 1995, **142**, 3652–3659.

34 B. Yu, J. Duan, H. Cong, W. Xie, R. Liu, X. Zhuang, H. Wang, B. Qi, M. Xu, Z. L. Wang and J. Zhou, *Science (80-.).*, 2020, **370**, 342–346.

35 M. A. Buckingham, S. Hammoud, H. Li, C. J. Beale, J. T. Sengel and L. Aldous, *Sustain. Energy Fuels*, 2020, **4**, 3388.

36 M. A. Buckingham, F. Marken and L. Aldous, *Sustain. Energy Fuels*, 2018, **2**, 2717.

37 B. W. Burrows, *Proc. 10th Intersoc. Energy Convers. Eng. Conf.*, 1975, 821–827.

38 J. H. Kim, J. H. Lee, R. R. Palem, M. S. Suh, H. H. Lee and T. J. Kang, *Sci. Rep.*, 2019, **9**, 8706.

39 K. Kim, S. Hwang and H. Lee, *Electrochim. Acta*, 2020, **335**, 135651.

40 L. Zhang, T. Kim, N. Li, T. J. Kang, J. Chen, J. M. Pringle, M. Zhang, A. H. Kazim, S. Fang, C. Haines, D. Al-Masri, B. A. Cola, J. M. Razal, J. Di, S. Beirne, D. R. MacFarlane, A. Gonzalez-Martin, S. Mathew, Y. H. Kim, G. Wallace and R. H. Baughman, *Adv. Mater.*, 2017, **29**, 1605652.

41 T. J. Abraham, D. R. Macfarlane and J. M. Pringle, *Energy Environ. Sci.*, 2013, **6**, 2639–2645.

42 N. Jiao, T. J. Abraham, D. R. MacFarlane and J. M. Pringle, *J. Electrochem. Soc.*, 2014, **161**, D3061–D3065.

43 T. J. Abraham, N. Tachikawa, D. R. MacFarlane and J. M. Pringle, *Phys. Chem. Chem. Phys.*, 2014, **16**, 2527–2532.

44 R. Koerver, D. R. MacFarlane and J. M. Pringle, *Electrochim. Acta*, 2015, **184**, 186–192.

45 J. He, D. Al-Masri, D. R. MacFarlane and J. M. Pringle, *Faraday Discuss.*, 2016, **190**, 205–218.

46 M. A. Lazar, D. Al-Masri, D. R. Macfarlane and J. M. Pringle, *Phys. Chem. Chem. Phys.*, 2016, **18**, 1404–1410.

47 H. Li, A. Gunawan, P. E. Phelan, D. A. Buttry, V. Mujica, R. A. Taylor and R. S. Prasher, *Nanoscale Microscale Thermophys. Eng.*, 2013, **17**, 304–323.

48 J. J. Black, A. Dolan, J. B. Harper and L. Aldous, *Phys. Chem. Chem. Phys.*, 2018, **20**, 16558–16567.

49 K. Kim and H. Lee, *Energy Technol.*, 2019, **7**, 3–7.

50 J. J. Black, T. Murphy, R. Atkin, A. Dolan and L. Aldous, *Phys. Chem. Chem.*

Phys., 2016, **18**, 20768–20777.

51 A. J. deBethune, T. S. Licht and N. Swendeman, *Temp. Coefficients Electrode Potentials Isothermal Therm. CoefficientsmThe Stand. Ion. Entropy Electrochem. Transp. Hydrog. Ion*, 1959, **106**, 626–627.

52 R. Hu, B. A. Cola, N. Haram, J. N. Barisci, S. Lee, S. Stoughton, G. Wallace, C. Too, M. Thomas, A. Gestos, M. E. Dela Cruz, J. P. Ferraris, A. A. Zakhidov and R. H. Baughman, *Nano Lett.*, 2010, **10**, 838–846.

53 J. Wu, J. J. Black and L. Aldous, *Electrochim. Acta*, 2017, **225**, 482–492.

54 M. S. Romano, J. M. Razal, D. Antiohos, G. Wallace and J. Chen, *J. Nanosci. Nanotechnol.*, 2015, **15**, 1–14.

55 G. R. Salvi and A. J. DeBethune, *J. Electrochem. Soc.*, 1961, **108**, 672.

56 H. G. Hertz and S. K. Ratkje, *J. Electrochem. Soc.*, 1989, **136**, 1698–1704.

57 W. . G. Breck and J. Lin, *Trans. Faraday Soc.*, 1965, **61**, 744–748.

58 A. J. deBethune, *J. Electrochem. Soc.*, 1960, **107**, 829.

59 E. D. Eastman, *J. Am. Chem. Soc.*, 1926, **48**, 1482–1493.

60 W. G. Breck and J. Lin, *Trans. Faraday Soc.*, 1965, **61**, 1511–1515.

61 J. N. Agar and W. G. Breck, *Nature*, 1955, **175**, 298–299.

62 J. N. Agar, *Rev. Pure Appl. Chem.*, 1958, **8**, 1.

63 J. N. Agar, *Annu. Rev. Phys. Chem.*, 1964, **15**, 469–488.

64 W. G. Breck and E. King, *Can. J. Chem.*, 1969, **47**, 3480–3482.

65 E. D. Eastman, *J. Am. Chem. Soc.*, 1928, **50**, 283–291.

66 D. Zhao, H. Wang, Z. U. Khan, J. C. Chen, R. Gabrielsson, M. P. Jonsson, M. Berggren and X. Crispin, *Energy Environ. Sci.*, 2016, **9**, 1450–1457.

67 B. Burrows, *J. Electrochem. Soc.*, 1976, **123**, 154–159.

68 P. Atkins and J. de Paula, *Atkins' Physical Chemistry*, Oxford University Press, Oxford [England], 9th Editio., 2010.

69 E. L. Yee, R. J. Cave, K. L. Guyer, P. D. Tyma and M. J. Weaver, *J. Am. Chem. Soc.*, 1979, **101**, 1131–1137.

70 E. L. Yee and M. J. Weaver, *Inorg. Chem.*, 1980, **19**, 1077–1079.

71 N. Sutin, M. J. Weaver and E. L. Yee, *Inorg. Chem.*, 1980, **19**, 1096–1098.

72 J. T. Hupp and M. J. Weaver, *J. Electrochem. Soc.*, 1984, **131**, 619–622.

73 J. T. Hupp and M. J. Weaver, *J. Phys. Chem.*, 1984, **88**, 1860–1864.

74 S. Sahami and M. J. Weaver, *J. Electroanal. Chem.*, 1981, **122**, 155–170.

75 S. Sahami and M. J. Weaver, *J. Electroanal. Chem.*, 1981, **122**, 171–181.

76 J. T. Hupp and M. J. Weaver, *Inorg. Chem.*, 1984, **23**, 3639–3644.

77 M. J. Kamlet, J. L. M. Abboud and R. W. Taft, *An Examination of Linear Solvation Energy Relationships*, John Wiley & Sons, INC., 1981, vol. 13.

78 Y. Yamato, Y. Katayama and T. Miura, *J. Electrochem. Soc.*, 2013, **160**, H309–H314.

79 M. A. Buckingham, K. Laws, E. Cross, A. Surman and L. Aldous, *Green Chem.*, 2021, **23**, 8901.

80 A. J. Bard and L. R. Faulkner, *Electrochemical Methods: Fundamentals and*

Applications, John Wiley & Sons, INC., Second Edi., 2001.

81 T. Kim, J. S. Lee, G. Lee, H. Yoon, J. Yoon, T. J. Kang and Y. H. Kim, *Nano Energy*, 2017, **31**, 160–167.

82 D. Inoue, Y. Fukuzumi and Y. Moritomo, *Jpn. J. Appl. Phys.*, 2020, **59**, 11–16.

83 B. Huang, S. Muy, S. Feng, Y. Katayama, Y. C. Lu, G. Chen and Y. Shao-Horn, *Phys. Chem. Chem. Phys.*, 2018, **20**, 15680–15686.

84 H. Zhou, T. Yamada and N. Kimizuka, *J. Am. Chem. Soc.*, 2016, **138**, 10502–10507.

85 Y. Liang, T. Yamada, H. Zhou and N. Kimizuka, *Chem. Sci.*, 2019, **10**, 773–780.

86 H. Zhou, T. Yamada and N. Kimizuka, *Sustain. Energy Fuels*, 2018, **2**, 472–478.

87 H. Inoue, Y. Liang, T. Yamada and N. Kimizuka, *Chem. Commun.*, 2020, **56**, 7013–7016.

88 M. Al Maimani, J. J. Black and L. Aldous, *Electrochem. commun.*, 2016, **72**, 181–185.

89 J. Duan, B. Yu, K. Liu, J. Li, P. Yang, W. Xie, G. Xue, R. Liu, H. Wang and J. Zhou, *Nano Energy*, 2019, **57**, 473–479.

90 P. F. Salazar, S. Kumar and B. A. Cola, *J. Appl. Electrochem.*, 2014, **44**, 325–336.

91 J. M. Hornut and A. Storck, *J. Appl. Electrochem.*, 1991, **21**, 1103–1113.

92 A. V. Sokirko, *Electrochim. Acta*, 1994, **39**, 597–609.

93 T. J. Kang, S. Fang, M. E. Kozlov, C. S. Haines, N. Li, Y. H. Kim, Y. Chen and R. H. Baughman, *Adv. Funct. Mater.*, 2012, **22**, 477–489.

94 M. A. Buckingham, K. Laws, H. Li, Y. Kuang and L. Aldous, *Cell Reports Phys. Sci.*, 2021, **2**, 100510.

95 G. Qian, X. Yu, Z. Li, J. Wu, R. Huang and Y. Lu, *Energy Convers. Manag.*, 2020, **217**, 113005.

96 M. S. Romano, N. Li, D. Antiohos, J. M. Razal, A. Nattestad, S. Beirne, S. Fang, Y. Chen, R. Jalili, G. G. Wallace, R. Baughman and J. Chen, *Adv. Mater.*, 2013, **25**, 6602–6606.

97 P. Yang and H. Fan, *Chem. Res. Chinese Univ.*, 2020, **36**, 420–424.

98 H. Zhou and P. Liu, *ACS Appl. Energy Mater.*, 2018, **1**, 1424–1428.

99 T. Ikeshoji, *Bull. Chem. Soc. Jpn.*, 1987, **60**, 1505–1514.

100 H. Im, T. Kim, H. Song, J. Choi, J. S. Park, R. Ovalle-Robles, H. D. Yang, K. D. Kihm, R. H. Baughman, H. H. Lee, T. J. Kang and Y. H. Kim, *Nat. Commun.*, 2016, **7**, 10600.

101 Nicolas Léonard Said Carnot, *Réflexions sur la puissance motrice du feu et sur les machines propres à développer cette puissance*, Bachelier, Paris, First Edit., 1824.

102 F. Zhao, W. Qian, M. Li, W. Li, L. Chen, F. Zhong, W. Huang and C. Dong, *RSC Adv.*, 2017, **7**, 23890–23895.

103 G. Li, D. Dong, G. Hong, L. Yan, X. Zhang and W. Song, *Adv. Mater.*, 2019, **31**, 1901403.

104 S. Gupta and R. Meek, *Appl. Phys. A*, 2020, **126**, 704.

105 M. S. Romano, S. Gambhir, J. M. Razal, A. Gestos, G. G. Wallace and J. Chen, *J. Therm. Anal. Calorim.*, 2012, **109**, 1229–1235.

106 D. Dong, H. Guo, G. Li, L. Yan, X. Zhang and W. Song, *Nano Energy*, 2017, **39**, 470–477.

107 W. Qian, M. Li, L. Chen, J. Zhang and C. Dong, *RSC Adv.*, 2015, **5**, 97982–97987.

108 W. Qian, M. Cao, F. Xie and C. Dong, *Nano-Micro Lett.*, 2016, **8**, 240–246.

109 Y. Zhou, W. Qian, W. Huang, B. Liu, H. Lin and C. Dong, *Nanomaterials*, 2019, **9**, 1450.

110 W. Huang, J. Xu, K. He, Z. Li, W. Qian and C. Dong, *IOP Conf. Ser. Earth Environ. Sci.*, 2018, **121**, 042027.

111 W. D. G. Gonçalves, C. Caspers, J. Dupont and P. Migowski, *Curr. Opin. Green Sustain. Chem.*, 2020, **26**, 100404.

112 Y. Zhou, Y. Liu, M. A. Buckingham, S. Zhang, L. Aldous, S. Beirne, G. G. Wallace and J. Chen, *Electrochem. commun.*, 2021, **124**, 106938.

113 J. Majzlan and S. C. B. Myneni, *Environ. Sci. Technol.*, 2005, **39**, 188–194.

114 T. Migita, N. Tachikawa, Y. Katayama and T. Miura, *Electrochemistry*, 2009, **77**, 639–641.

115 Y. Yamato, Y. Katayama and T. Miura, *ECS Trans.*, 2012, **50**, 167–174.

116 A. Taheri, D. R. MacFarlane, C. Pozo-Gonzalo and J. M. Pringle, *Electrochim. Acta*, 2019, **297**, 669–675.

117 T. Ikeshoji and F. N. B. de Nahui, *J. Electroanal. Chem.*, 1990, **296**, 19–36.

118 T. Ikeshoji and R. S. Gonçalves, *J. Appl. Electrochem.*, 1993, **23**, 516–519.

119 F. Musshoff, K. M. Kirschbaum and B. Madea, *Forensic Sci. Int.*, 2011, **204**, e4–e7.

120 J. Duan, G. Feng, B. Yu, J. Li, M. Chen, P. Yang, J. Feng, K. Liu and J. Zhou, *Nat. Commun.*, 2018, **9**, 1–8.

121 L. Aldous, J. J. Black, M. C. Elias, B. Gélinas and D. Rochefort, *Phys. Chem. Chem. Phys.*, 2017, **19**, 24255–24263.

122 E. H. B. Anari, M. Romano, W. X. Teh, J. J. Black, E. Jiang, J. Chen, T. Q. To, J. Panchompoo and L. Aldous, *Chem. Commun.*, 2016, **52**, 745–748.

123 B. T. Huang, M. Roger, M. Bonetti, T. J. Salez, C. Wiertel-Gasquet, E. Dubois, R. Cabreira Gomes, G. Demouchy, G. Mériguet, V. Peyre, M. Kouyaté, C. L. Filomeno, J. Depeyrot, F. A. Tourinho, R. Perzynski and S. Nakamae, *J. Chem. Phys.*, 2015, **143**, 054802.

124 T. J. Salez, M. Kouyaté, C. Filomeno, M. Bonetti, M. Roger, G. Demouchy, E. Dubois, R. Perzynski, A. Cēbers and S. Nakamae, *Nanoscale Adv.*, 2019, **1**, 2979–2989.

125 T. Yamada, X. Zou, Y. Liang and N. Kimizuka, *Polym. J.*, 2018, **50**, 771–774.

126 A. Kundu and T. S. Fisher, *Electrochim. Acta*, 2018, **281**, 357–369.

127 S. Pu, Y. Liao, K. Chen, J. Fu, S. Zhang, L. Ge, G. Conta, S. Bouzarif, T. Cheng, X. Hu, K. Liu and J. Chen, *Nano Lett.*, 2020, **20**, 3791–3797.

128 Z. Ahmad, J. Bhadra, F. Touati, A. Alashraf, R. A. Shakoor and N. J. Al-Thani,

RSC Adv., 2016, **6**, 71370–71374.

129 C. Sealy, *Nano Today*, 2010, **5**, 163.

130 A. Gunawan, N. W. Fette and P. E. Phelan, *Am. Soc. Mech. Eng. Power Div. POWER*, 2015, **1**, 1–8.

131 A. H. Kazim, A. S. Booeshaghi, S. T. Stephens and B. A. Cola, *Sustain. Energy Fuels*, 2017, **1**, 1381–1389.

132 G. Shin, J. G. Jeon, J. H. Kim, J. H. Lee, H. J. Kim, J. Lee, K. M. Kang and T. J. Kang, *Molecules*, 2020, **25**, 1928.

133 M. Inagaki and E. Itoh, *Synth. Met.*, 2000, **35**, 383–385.

134 Y. Maeda, E. Itoh and M. Inagaki, *Synth. Met.*, 1987, **20**, 73–78.

135 Q. Shen, Z. Ning, B. Fu, S. Ma, Z. Wang, L. Shu, L. Zhang, X. Wang, J. Xu, P. Tao, C. Song, J. Wu, T. Deng and W. Shang, *J. Mater. Chem. A*, 2019, **7**, 6514–6521.

136 M. Schönig and R. Schuster, *Appl. Phys. Lett.*, 2020, **116**, 091601.

137 K. Liu, Y. Zhou, F. Yuan, X. Mo, P. Yang, Q. Chen, J. Li, T. Ding and J. Zhou, *Angew. Chemie - Int. Ed.*, 2016, **55**, 15864–15868.

138 Y. Ikeda, K. Fukui and Y. Murakami, *Phys. Chem. Chem. Phys.*, 2019, **21**, 25838–25848.

139 A. Gunawan, C. H. Lin, D. A. Buttry, V. Mujica, R. A. Taylor, R. S. Prasher and P. E. Phelan, *Nanoscale Microscale Thermophys. Eng.*, 2013, **17**, 304–323.

140 W. Liu, X. Qian, C. G. Han, Q. Li and G. Chen, *Appl. Phys. Lett.*, 2021, **118**, 020501.

141 W. G. Breck and J. Lin, *Trans. Faraday Soc.*, 1965, **61**, 1511–1515.

142 B. X. Shi and J. He, *Science (80-.).*, 2021, **371**, 343–344.

143 A. Gunawan, H. Li, C. H. Lin, D. A. Buttry, V. Mujica, R. A. Taylor, R. S. Prasher and P. E. Phelan, *Int. J. Heat Mass Transf.*, 2014, **78**, 423–434.

144 P. Blanc and C. Madic, *Inorganica Chim. Acta*, 1984, **94**, 134–136.

145 T. J. Abraham, D. R. Macfarlane, R. H. Baughman, L. Jin, N. Li and J. M. Pringle, *Electrochim. Acta*, 2013, **113**, 87–93.

146 T. Ikeshoji, F. N. B. de Nahui, S. Kimura and M. Yoneya, *J. Electroanal. Chem.*, 1991, **312**, 43–56.

147 P. H. Daum and C. G. Enke, *Anal. Chem.*, 1969, **41**, 653–656.

148 K. Winkler, *J. Electroanal. Chem.*, 1995, **388**, 151–159.

149 L. M. Peter, W. Dürr, P. Bindra and H. Gerischer, *J. Electroanal. Chem.*, 1976, **71**, 31–50.

150 A. J. Esswein, J. Goeltz, D. Amadeo, High solutibilty iron hexacyanides, US 2014/0051003 A1, 2014, 14.

151 L. Suo, O. Borodin, T. Gao, M. Olguin, J. Ho, X. Fan, C. Luo, C. Wang and K. Xu, *Science (80-.).*, 2015, **350**, 938–943.

152 T. Liang, R. Hou, Q. Dou, H. Zhang and X. Yan, *Adv. Funct. Mater.*, 2020, 2006749.

153 L. Suo, F. Han, X. Fan, H. Liu, K. Xu and C. Wang, *J. Mater. Chem. A*, 2016, **4**, 6639–6644.

154 P. Iamprasertkun, A. Ejigu and R. A. W. Dryfe, *Chem. Sci.*, 2020, **11**, 6978–

6989.

155 S. A. Campbell and L. M. Peter, *J. Electroanal. Chem.*, 1994, **364**, 257–260.

156 J. C. James, *Trans. Faraday Soc.*, 1949, **45**, 855–861.

157 R. S. Kühnel, D. Reber, A. Remhof, R. Figi, D. Bleiner and C. Battaglia, *Chem. Commun.*, 2016, **52**, 10435–10438.

158 M. R. Lukatskaya, J. I. Feldblyum, D. G. Mackanic, F. Lissel, D. L. Michels, Y. Cui and Z. Bao, *Energy Environ. Sci.*, 2018, **11**, 2876–2883.

159 K. R. J. Lovelock, A. Ejigu, S. F. Loh, S. Men, P. Licence and D. A. Walsh, *Phys. Chem. Chem. Phys.*, 2011, **13**, 10155–10164.

160 J. T. Edward, *J. Chem. Educ.*, 1970, **47**, 261–270.

161 Y. Marcus, *Chem. Rev.*, 2009, **109**, 1346-1370.

162 Y. Marcus, *Chem. Rev.*, 1988, **88**, 1475–1498.

163 G. Prampolini, P. Yu, S. Pizzanelli, I. Cacelli, F. Yang, J. Zhao and J. Wang, *J. Phys. Chem. B*, 2014, **118**, 14899–14912.

164 Y. Zhou, Y. Liu, M. A. Buckingham, S. Zhang, L. Aldous, S. Beirne, G. G. Wallace and J. Chen, *Electrochem. commun.*, 2021, **124**, 106938.

165 R. Diaz-Torrez and S. Alvarez, *Dalt. Trans.*, 2011, **40**, 10742–10750.

166 S. G. Bratsch, *J. Phys. Chem. Ref. Data*, 1989, **18**, 1–21.

167 T. Ding, L. Zhu, X.-Q. Wang, K. H. Chan, X. Lu, Y. Cheng and G. W. Ho, *Adv. Energy Mater.*, 2018, **8**, 1802397.

168 J. H. Kim and T. J. Kang, *ACS Appl. Mater. Interfaces*, 2019, **11**, 28894–28899.

169 J. H. Lee, Y. Jung, J. H. Kim, S. J. Yang and T. J. Kang, *Carbon N. Y.*, 2019, **147**, 559–565.

170 C. C. Loures, M. A. K. Alcântara, H. J. Izario Filho, A. C. S. C. Teixeira, F. T. Silva, T. C. B. Paiva and G. R. L. Samanamud, *Int. Rev. Chem. Eng.*, 2013, **5**, 102–120.

171 M. A. Buckingham, S. Zhang, Y. Liu, J. Chen, F. Marken and L. Aldous, *ACS Appl. Energy Mater.*, 2021, **4**, 11204.

172 H. Angerstein-Kozlowska, B. E. Conway, A. Hamelin and L. Stoicoviciu, *J. Electroanal. Chem.*, 1987, **228**, 429–453.

173 M. Philippe, B. Didillon and L. Gilbert, *Green Chem.*, 2012, **14**, 952–956.

174 R. L. McCreery, *Chem. Rev.*, 2008, **108**, 2646–2687.

175 F. G. Bordwell, *Acc. Chem. Res.*, 1988, **21**, 456–463.

176 P. Anastas and J. Warner, *Green Chemistry: Theory and Practice*, Oxford University Press, Oxford [England], 2000.

177 L. L. Trent, R. S. Hestand and C. C. Carter, *J. Aquat. Plant Manag.*, 1978, **16**, 40–43.

178 D. Coleman and N. Gathergood, *Chem. Soc. Rev.*, 2010, **39**, 600–637.

179 Y. Xue, J. Song, Y. Zhang, F. Kong, M. Wen and G. Zhang, *Water (Switzerland)*, 2016, **8**, 328.

180 C. Kabala, A. Karczewska, B. Galka, M. Cuske and J. Sowinski, *Envionmental Monit. Assess.*, 2017, **189**, 304.

181 P. J. A. Withers, C. Neal, H. P. Jarvie and D. G. Doody, *Sustainability*, 2014, **6**,

5853.

182 P. T. Anastas and J. B. Zimmerman, *Environ. Sci. Technol.*, 2003, **37**, 94A-101A.

183 C. J. Ottley, W. Davison and W. M. Edmunds, *Geochim. Cosmochim. Acta*, 1997, **61**, 1819–1828.

184 P. L. Domingo, B. Garcia and J. M. Leal, *Can. J. Chem.*, 1990, **68**, 228–235.

185 H. Basset and A. S. Corbet, *J. Chem. Soc. Trans.*, 1924, 1358–1366.

186 C. A. P. Arellano and S. S. Martínez, *Sol. Energy Mater. Sol. Cells*, 2010, **94**, 327–332.

187 S. Asperger, *Trans. Faraday Soc.*, 1952, **48**, 617–624.

188 S. Asperger, I. Murati and D. Pavlovic, *J. Chem. Soc.*, 1953, 730–736.

189 J. M. Kruse and L. E. Thibault, *Anal. Chem.*, 1973, **45**, 2260–2261.

190 A. S. Brar, H. S. Sandhu and S. S. Sandhu, *J. Therm. Anal.*, 1983, **26**, 7–15.

191 A. S. Brar, H. S. Sandhu and H. S. Sandhu, *Thermochim. Acta*, 1980, **41**, 253–256.

192 A. S. Brar, H. Singh, S. Brar and B. S. Randhawa, *J. Therm. Anal.*, 1981, **21**, 77–88.

193 M. Ruiz-Bermejo, C. Rogero, C. Menor-Salván, S. Osuna-Esteban, J. Á. Martín-Gago and S. Veintemillas-Verdaguer, *Chem. Biodivers.*, 2009, **6**, 1309–1322.

194 A. H. Hall and B. H. Rumack, *Ann. Emerg. Med.*, 1986, **15**, 1067–1074.

References

195 Hydrogen Cyanide, https://www.cdc.gov/niosh/ershdb/emergencyresponsecard_29750038.html.

196 N. N. Greenwood and A. Earnshaw, *Chemistry of the Elements*, Pergamon Press Ltd., Leeds, 1984.

197 R. J. Lemire, U. Berner, C. Musikas, D. A. Palmer, P. Taylor and O. Tochiyama, *Chemical thermodynamics of iron Part 1*, OECD, 2013, vol. 13a.

198 R. G. Compton and C. E. Banks, *Understanding Voltammetry*, Imperial College Press, Second Edi., 2010.

199 E. J. F. Dickinson, J. G. Limon-petersen, N. V Rees and R. G. Compton, *J. Phys. Chem. C*, 2009, **113**, 11157–11171.

200 D. H. Ripin and D. A. Evans, pKa's of Inorganic and Oxo-Acids.

201 H. A. H. Alzahrani, M. A. Buckingham, F. Marken and L. Aldous, *Electrochem. commun.*, 2019, **102**, 41.

202 C. E. Housecroft and A. G. Sharpe, *Inorganic Chemistry*, Pearson Education Limited, Fourth Edi., 2012.

Thesis Appendix

Appendix to Chapter 4

Data for UV-Vis

UV-Vis spectra for a solution of 100 mM $NaNO_3$ showing the strong intensity peak centred on 220 nm is attributed to the $[NO_3]^-$ anion.

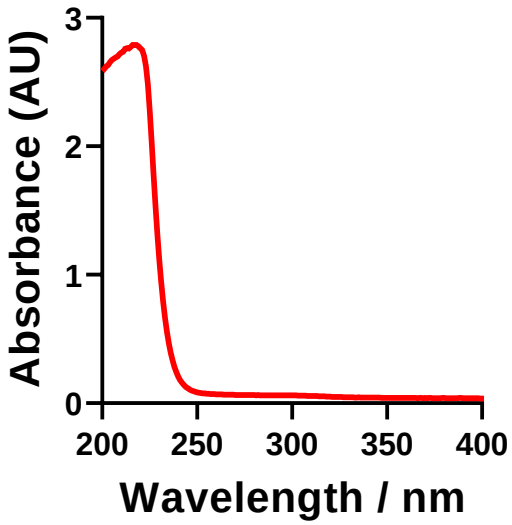

Figure A65 – UV-Vis spectra of 100 mM $NaNO_3$.

Table of costing for techno-economic evaluation

Table A17 – List of compounds, their pack sizes and the cost used in the cost analysis, as found on the Sigma Aldrich website (sigmaaldrich.com; country set to United Kingdom) on 10th August 2018.

Iron Salt	**Grade (purity / %)***	**Cost / £**	**Pack size / g**
Ammonium iron(ii) sulphate hexahydrate	ACS (99)	83.50	500
Ammonium iron(iii) sulphate dodecahydrate	ACS (99)	41.00	500
Iron(ii) sulphate	ACS (≥99)	20.00	250**
Iron(iii) sulphate****	n/a (97)	100.00	500
Iron(ii) chloride tetrahydrate	Puriss (≥99.0)	43.50	250**
Silver(i) nitrate	ACS (≥99.0)	1090.00	500
Iron(iii) nitrate nonahydrate	ACS (≥98)	59.50	500
Iron(ii) trifluoromethanesulphonate	n/a (≥85)	65.30	5**
Iron(iii) trifluoromethanesulphonate	n/a *90)	30.80	1**
Acid	**Grade (purity / %)**	**Cost / £**	**Pack size / L**
Nitric acid	ACS (70)	204.10	2.5
Sulphuric acid	ACS (95-98)	108.00	2.5
Trifluoromethanesulphonic acid	n/a (98)	117.00	0.059***

* The purity of the solid samples was not included when calculating the cost per cell; purity was simply used to ensure comparison of materials of similar grades

** Pack sizes of 500 g were not available; these represent the nearest pack size available on the Sigma Aldrich website

*** Only 100 g (or 59 mL) was available

Appendix to Chapter 5

Tables for calculation of $HCN_{(g)}$ evolution

Table A18 - Experimental details and calculations of potential $HCN_{(g)}$ evolved from $[Fe(CN)_6]^{4-}$ used in in-series thermocell devices (used to prepare Table 1 in chapter 5).

Corresponding author (reference)	**Total thermocells | Total half-cells**	**Thermocell dimensions area (cm^2) x height (cm) (volume per thermocell / cm^3) | Total volume (cm^3)**	**$[Fe(CN)_6]^{4-}$ concentration / M**	**Potential $HCN_{(g)}$ from $[Fe(CN)_6]^{4-}$ / mg**
Zhou (2016)[1]	118 | 59	0.07 x 0.1 (0.007) | 0.42	0.1	6.8
Kang (2019)[2]	2 | 1	1 x 0.26 (0.26) | 0.26	0.2	8.4
Aldous (2016)[3]	4 | 2	2 x 0.25 (0.5) | 1	0.1	16.3
Baughman (2017)[4]	112 | 56	1 x 0.26 (0.26) | 14.56	0.25	590.25
Lee (2020)[5]	64 | 32	0.78 x 1.2 (0.94) | 29.95	0.45	2185.5

Data for IR in the absence of Fe

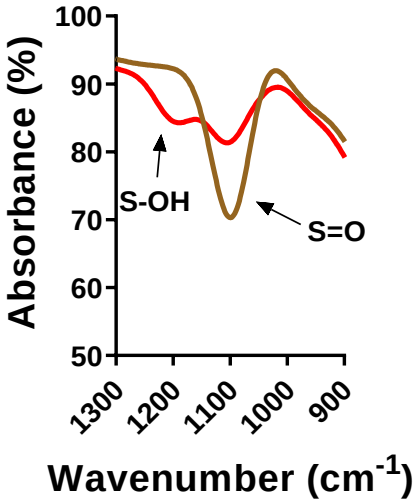

Figure A66 – IR spectra of 0.075 M Na_2SO_4 (green) and 0.075 M $NaHSO_4$ (red). NB: These are measured in the absence of iron sulphate.

***Ex-situ vs in-situ* Electrochemical Impedance Spectroscopy analysis**

EIS analysis is typically performed *ex-situ* under isothermal conditions. Conditions that are clearly different from the non-isothermal *in-situ* thermocell. Whilst this yields an informative and interesting comparison between separate redox couples,[6] or yields significant insight into the complexities of electrode surface interactions,[7] EIS analysis could potentially be even more informative if performed *in-situ* in the non-isothermal thermocell setup.[8] To this end, a comparison between the typically employed *ex-situ* isothermal EIS analysis and an *in-situ*, non-isothermal EIS analysis was initially undertaken for the three investigated systems.

The solution resistance, R_S of the *ex-situ* thermocells are significantly higher than the *in-situ* (Figure A3). This is not surprising as the presence of a temperature gradient between the electrodes will induce convection in solution, significantly reducing the *in-situ* R_S over the static solution *ex-situ* R_S. In both the *in-situ* and *ex-situ* R_S, the same trend is followed, where

Fe(SO4) >> **Fe(SO4)2** > **Fe(HSO4)**. This can be explained by a supporting electrolyte effect reducing the ohmic resistance of the solution, where supporting electrolyte is present in the **Fe(SO4)2** and **Fe(HSO4)** systems. The lower pH of the **Fe(HSO4)** system showcases increased proton concentration in the system, further decreasing ohmic resistance due to the high mobility of the H^+ ion in water.

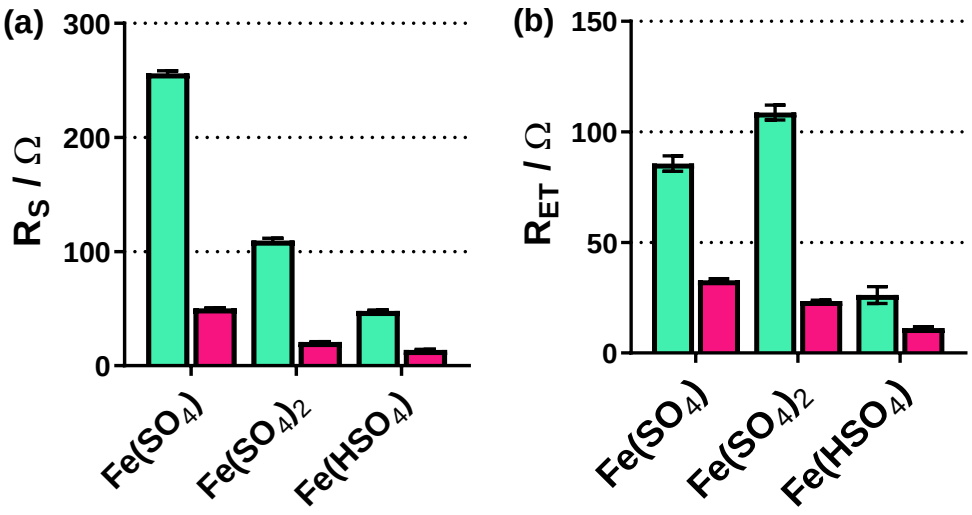

Figure A67 – Bar charts showing (a) mass transport (or solution) resistance (R_S) and (b) electron transfer resistances (R_{ET}) of the **Fe(SO4)**, **Fe(SO4)2** and **Fe(HSO4)** systems, from the isothermal *ex-situ* setup (turquoise, the same as the cyclic voltametric setup) and the non-isothermal *in-situ* setup (pink, the same as the thermoelectrochemical setup).

With respect to R_{ET}, again the *in-situ* R_{ET} is significantly lower than the *ex-situ*. However, the *ex-situ* R_{ET} trend is different to the *in-situ* (which follows the R_S described above). For the *ex-situ* R_{ET}, the trend follows: **Fe(SO4)2** > **Fe(SO4)** > **Fe(HSO4)**. $FeSO_4$ has previously been demonstrated to have a far higher R_{ET} than $FeNO_3$ or $FeCF_3SO_3$, (part 4.3.7).[6] This has been proposed to be due to sulphate-poisoning of the gold electrode surface, as the $[SO_4]^{2-}$ and

$[HSO_4]^-$ ions strongly chemisorb on the gold electrode surface. This process hinders the formation of electrocatalytic gold oxide,[9] significantly increasing the R_{ET}.[6]

Overall, the *ex-situ* and *in-situ* EIS analysis show the same trends in both R_S and R_{ET}. But there is a significant difference in the observed values, stemming from a significant difference in the investigated setups. This discrepancy typifies the importance of *in-situ* measurements, in order to obtain a more realistic comparison of various systems within any thermocell.

Hot *vs* cold electrode comparison

Due to the unique non-isothermal thermoelectrochemical setup utilised for the *in-situ* EIS analysis, further comparisons can be made within this measurement. In the *in-situ* measurements above (Figure A3) the hotter electrode was solely used as a working electrode, the colder electrode as a counter and a Pt wire *pseudo*-reference in solution. A simple, but necessary comparison is between using either the hotter or colder electrode as the working electrode.

Therefore, this comparison, has also been undertaken. Figure A4 shows that by altering the working from the hot to cold, the R_{ET} is consistently lower for all three redox systems when using the hot working electrode. This is reasonable as a decrease in kinetic energy of the cold electrode (by being held at a lower temperature) would increase the energy required to undertake redox processes at the electrode surface.

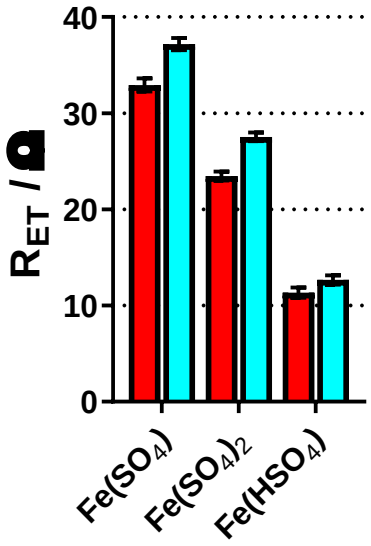

Figure A68 – Bar charts showing the electron transfer resistances (R_{ET}) of the **$Fe(SO_4)$**, **$Fe(SO_4)_2$** and **$Fe(HSO_4)$** systems. During fitting the R_S was fixed to those of the previous investigation (Figure A3), and the R_{ET} fit. Here, the hot (red) and cold (blue) electrodes were used as the working, with the other as the counter and a Pt-wire as a *pseudo*-reference.

It is important to note that only R_{ET} is shown here as R_S is fixed during fitting, the value for this is fixed from those measured in Figure A3(a). This was fixed as R_S should be equivalent, independent of which electrode is being used as the working electrode, or even the electrode material used (discussed in section 5.3.7.2). From these investigations it is clearly important that the measurement should be made *in-situ*, and that the hot or cold electrode should be fixed throughout all further investigations as it has an effect on the outcome of the EIS analysis.

Nyquist Plots for Electrochemical Impedance Spectroscopy analysis

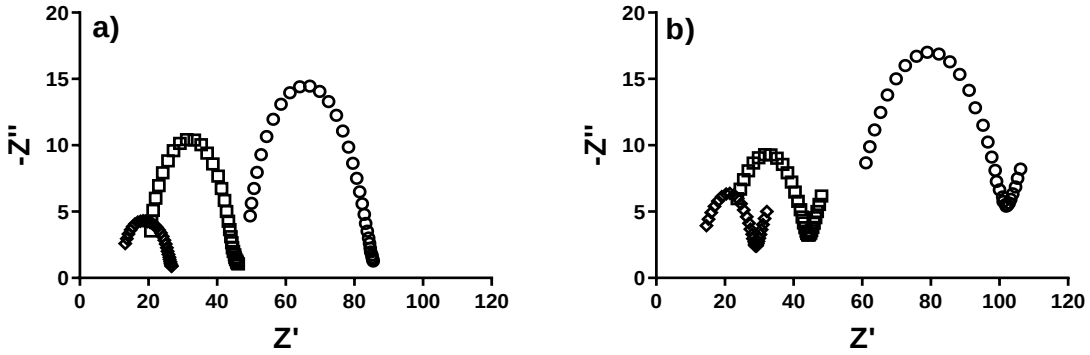

Figure A69 – Nyquist and fitting plots for the impedance data for the **$[Fe(SO_4)]^{0/+}$** (circle), **$[Fe(SO_4)_2]^{-/2-}$** (square) and **$[Fe(HSO_4)]^{+/2+}$** (diamond) systems, at (a) gold electrodes and (b) graphite electrodes. All measured *in situ* in the thermogalvanic cell, with T_c = 22°C and T_h = 40°C (applied ΔT = 18 K).

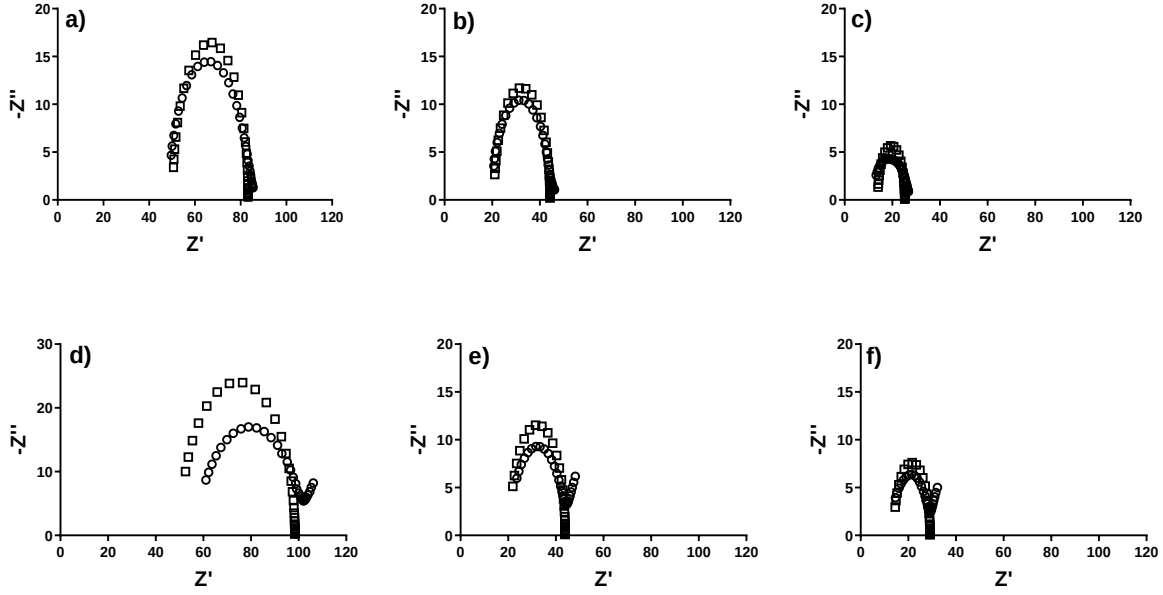

Figure A70 – Nyquist and fitting plots for the impedance data for the **$[Fe(SO_4)]^{0/+}$** (a & b), **$[Fe(SO_4)_2]^{-/2-}$** (c & d) and **$[Fe(HSO_4)]^{+/2+}$** (e & f) systems, where the working electrode was either gold (a-c) or graphite (d-f). All experimental data is shown as circles and all fitting data in shown as squares.

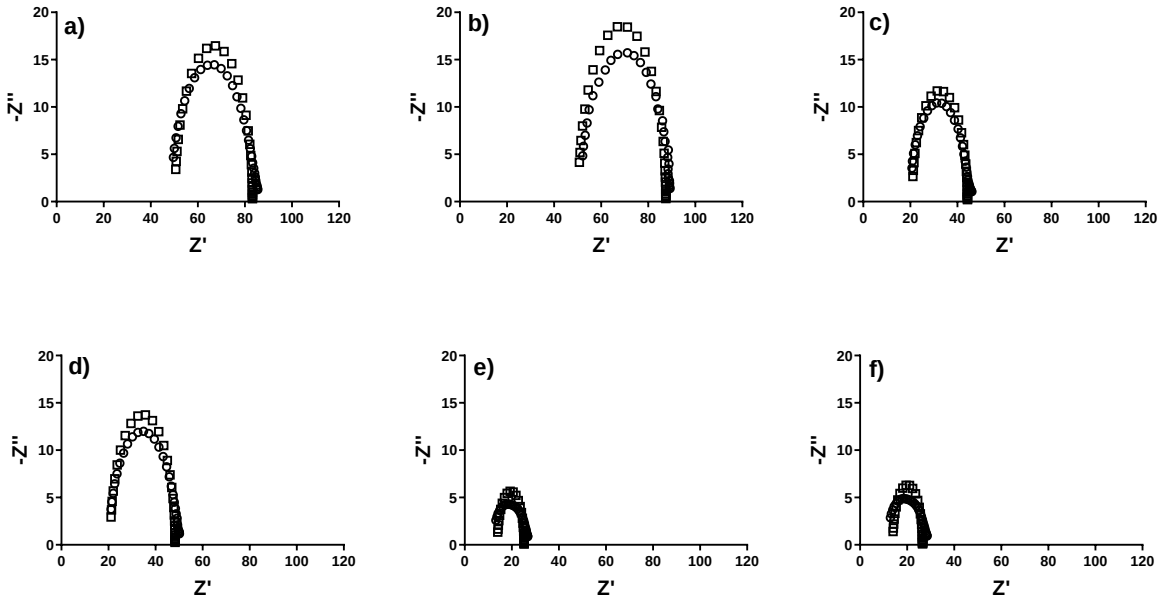

Figure A71 – Nyquist and fitting plots for the impedance data for the **[Fe(SO$_4$)]$^{0/+}$** (a & b), **[Fe(SO$_4$)$_2$]$^{-/2-}$** (c & d) and **[Fe(HSO$_4$)]$^{+/2+}$** (e & f) systems, where the working electrode was either the hot (a, c & e) or the cold (b, d & f) electrode. All experimental data is shown as circles and all fitted data shown as squares.

Characterising the mixed thermocell system

The mixed or 'second-life' system has been characterised by cyclic voltammetry, EIS analysis (coupled to the calculated R_{cell}) and for its thermogalvanic properties (which are shown in Figure A8 and A9). Firstly, the cyclic voltammetry was assessed with respect to the three un-mixed systems. Figure A8 shows that the mixed system is electrochemically indistinct from the **Fe(HSO$_4$)** and **Fe(SO$_4$)$_2$** systems. Due to this, EIS analysis was performed in an attempt to better understand the system.

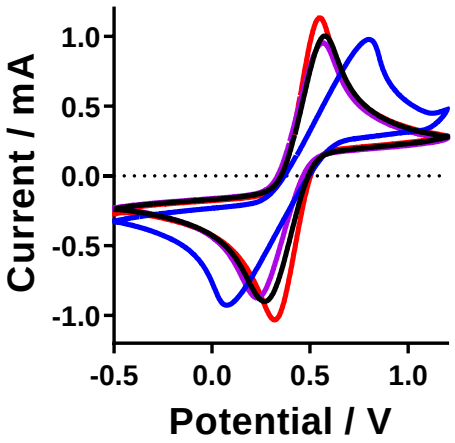

Figure A72 – Cyclic voltammograms recorded for the (blue) **$Fe(SO_4)$** (purple) **$Fe(SO_4)_2$** (red) **$Fe(HSO_4)$** (all taken from Figure 47) and (black) the 'mixed' systems recorded using a Au working electrode with a Ag/AgCl reference electrode at a scan rate of 100 mV s^{-1}.

The electrochemical impedance analysis for the mixed system was observed to match the general trend in the R_S and R_{ET} analysis (Figure A9) observed for the individual thermocell systems. Where a lower R_S is observed than the **$Fe(SO_4)$** system due to the decreased ohmic resistance from the presence of supporting electrolyte in the system. The R_{cell} however did not follow this trend and was much larger than expected. The cause of the difference is unclear, however, a number of factors are likely contributing. Firstly, the smaller driving force in the thermocell (observed as a low S_e, as the driving force is known to be proportional to S_e^2).[10] Secondly, some of the species present in solution could be redox-inactive.[6] Thirdly, by virtue of being a mixed system, there is likely a mixture of species from several equilibria competing simultaneously (Equilbria 27 & 28 & 29) (discussed in the main text). This could lead to the presence of some non-thermogalvanically active species, which would lead to higher resistance in the non-isothermal active thermogalvanic cell, when compared to the passive impedance analysis. From the impedance analysis, R_S and R_{ET} measure all species present, whether redox-active or thermogalvanically active. Whereas R_{cell} only represents redox-active molecules

undergoing thermogalvanic processes under active conditions. As R_{cell} is calculated from the *I-V* plots from the measured thermocell.

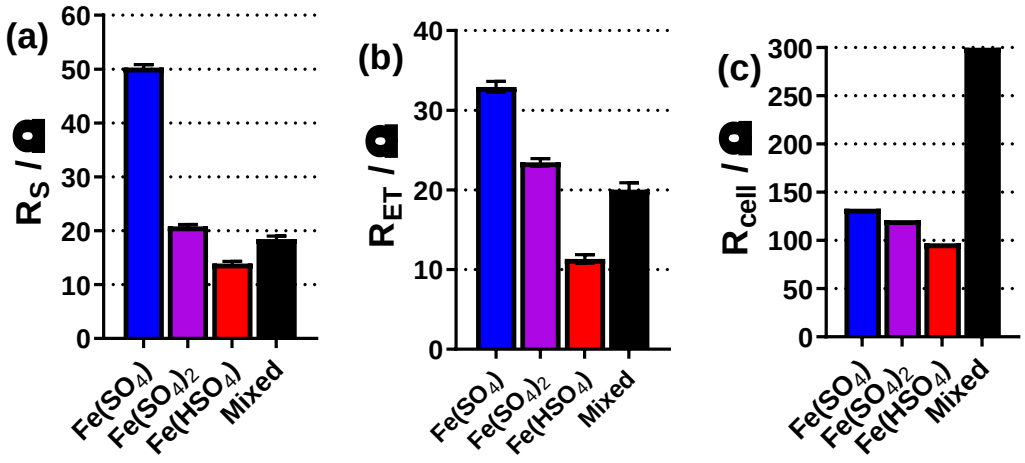

Figure A73 – Bar chats of a) solution resistance, R_S and b) electron transfer resistance, R_{ET} of the non-isothermal thermocell determined through impedance spectroscopy. Also shown is c) the calculated total thermocell resistance, R_{cell} of the thermogalvanic cell, based upon ohms law ($V = IR$) from the *I-V* plots measured from the thermocell. All measurements were taken at a ΔT of 20°C. This figure has the data of Figure 50 but with the included mixed.

Appendix to Chapter 6

Tables of (semi)optimisation

In thermogalvanic cells, anionic redox couples have been prepared by the coordination of $Fe^{2+/3+}$ with the anionic ligands CN^- and $[SO_4]^{2-}$, to form the $[Fe(CN)_6]^{3-/4-}$ and $[Fe(SO_4)_2]^{-/2-}$ redox couples, respectively. The former possesses inherent risk due to the potentially lethal toxicity of the ligand,[11] whereas the low charge density on the latter results in a significantly lower Seebeck coefficient (S_e).[11] In an effort to generate highly charged but sustainable and safe redox couples, a range of poly-carboxylate (Figure A10(a – g)) and poly-aminocarboxylate (Figure A10(h – l) ligands were screened.

The poly-carboxylate redox couples were screened by evaluating 50 mM $FeCl_2$ and 50 mM $FeCl_3$ in the presence of 10 equivalents (500 mM) of the carboxylate ligand, with 5 equivalents as the free acid and 5 equivalents as the conjugate sodium carboxylate. Of the 7 ligands, only 3 passed this initial screening; the thermogalvanic results for these systems are summarised in Table 1. Acetate, malonate and citrate visually complexes with the iron (based upon colour change) and importantly significant changes in the thermoelectrochemistry was observed, with acetate and citrate both demonstrating an inversion in the entropy difference, *e.g.* the positive S_e of 0.1 M $FeCl_{2/3}$ (+1.1 mV K^{-1}) inverted to negative S_e of -0.40 mV mV K^{-1} upon addition of the citrate. This compares favourably with the previously reported $[Fe(SO_4)_2]^{-/2-}$ system (S_e = *ca.* -0.29 mV K^{-1} for 0.3 M $Fe(SO_4)$, 0.3 M $Fe(SO_4)_{1.5}$ and 1.5 M Na_2SO_4).[11] However, the oxalate and succinate ligands were found to be sparing soluble, whereas the TBC and BTC ligands were soluble but their iron complexes were not; these 4 were discounted from further exploration.

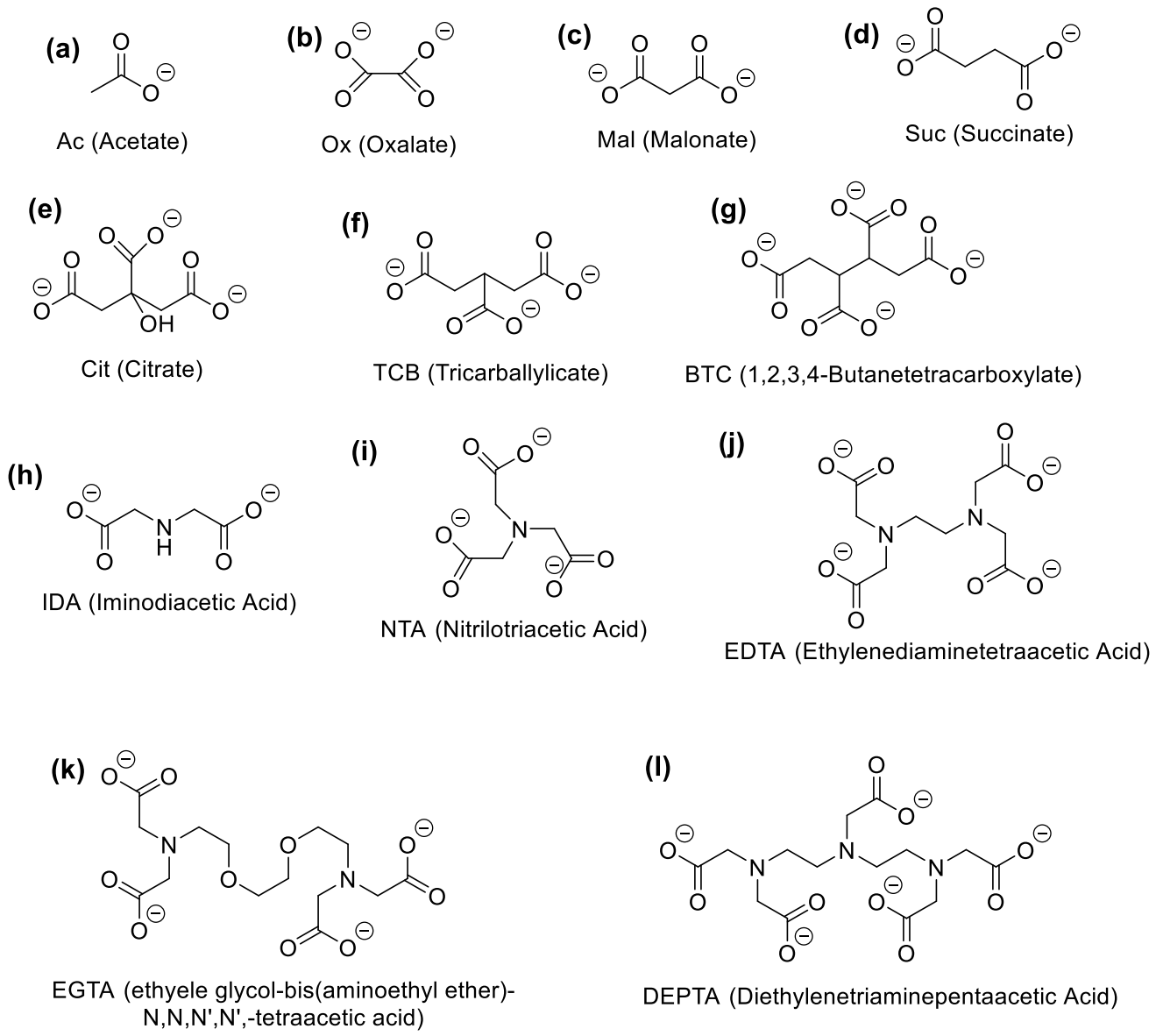

Figure A74 – Chemical structures, abbreviated name (full common name) for the anionic ligands investigated in this study.

Moving onto the poly-aminocarboxylate ligands, the free acids were consistently found to be poorly soluble; the numerous binding sites also meant less of the carboxylate conjugate base (as the sodium salt) was required. Therefore 50 mM $FeCl_2$ and 50 mM $FeCl_3$ was initially screened in the presence of 2 equivalents (100 mM) of the fully deprotonated carboxylate salts. Here, all 5 visually appeared to complex, and reassuringly 5 demonstrated negative S_e values.

Table A19 – Table of data showing the corresponding thermogalvanic properties (Seebeck coefficient, S_e, short circuit current density, j_{sc}, and maximum power density, P_{max}) measured for the as-prepared Fe(ligand) solutions. These were prepared from 50 mM $FeCl_2$ and 50 mM $FeCl_3$; all polycaboxylate ligands (Ac to BTC) were measured with 5 equivalents of the carboxylic acid form and 5 equivalents of the carboxylate salt, while the polyaminocarboxylate (IDA to DEPTA) were measured using 2 equivalents of the carboxylate salt. Thermogalvanic properties were quantified in the thermogalvanic cell at an applied ΔT = 18 K; (a dash indicates solubility issues precluded thermogalvanic measurement).

Ligand	Se	j	P
Ac	-0.07	-0.06	0.02
Ox	-	-	-
Suc	-	-	-
Mal	+0.03	+0.07	0.01
TCB	-	-	-
Cit	-0.40	-0.28	0.55
BTC	-	-	-
IDA	-0.38	-0.98	1.84
NTA	-0.09	-0.20	0.09
EDTA	-0.20	-0.29	0.29
EGTA	-0.32	-0.42	0.67
DEPTA	-0.44	-1.48	3.25

Semi-optimisation of the poly-carboxylate systems

Acetate, malonate, and citrate were subjected to semi-optimisation; since the goal was a more negative S_e value, more of the conjugate base was added. As shown in Table A4, this was unsuccessful for acetate, with the resulting complex being insoluble. Malonate was dramatically improved by doubling the quantity of the carboxylate salt, with the S_e inverting from +0.03 mV K-1 to -0.47 mV K^{-1}, and the power increasing 260-fold. Conversely, citrate demonstrated a decrease in performance after doubling the quantity of the carboxylate salt. The

semi-optimised malonate system displayed by far the highest thermogalvanic power production for the poly-carboxylate-based systems.

Table A20 – Table of data summarising the thermogalvanic properties for semi-optimised polycarboxylate ligand systems, achieved *via* varying the number of equivalents per Fe(ii/iii) and the acid : carboxylate ratio.

Ligand	Charge	Eq. Acid	Eq. Base	Se	j	P
Ac	1-	5	5	-0.07	-0.06	0.02
Ac	1-	5	10	-	-	-
Ac	1-	10	10	-	-	-
Mal	2-	5	5	+0.03	+0.07	0.01
Mal	2-	5	10	-0.47	-1.1	2.6
Cit	3-	5	5	-0.40	-0.28	0.55
Cit	3-	5	10	-0.32	-0.17	0.27

Semi-optimisation of the poly-aminocarboxylate systems

The 5 successful poly-aminocarboxylate systems were subjected to considerably more optimisation, both by increasing the quantity of the carboxylate salt, and by adding some of the free acid; the results are summarised in Table A5.

Table A21 - Table of data summarising the thermogalvanic properties for semi-optimised polyaminocarboxylate ligand systems, achieved *via* varying the number of equivalents per Fe(ii/iii) and the acid : carboxylate ratio.

Ligand	Eq.Acid	Eq. Base	Se	j	P	Semi-optimised?
Gly	0	2	Insoluble			
	2	2				
	5	5				
	5	2	+0.52	+0.18	0.50	
IDA	0	2	-0.31	-0.53	0.83	
	0	4	-0.18	-0.09	0.10	
	0	6	-0.30	-0.13	0.21	
	2	2	-0.43	-0.81	1.73	
	2*	4*	-0.38	-0.98	1.84	*
	2	6	+0.35	+0.86	1.50	
NTA	0	6	-0.45	-1.21	2.7	
	0*	5*	-0.51	-1.24	3.2	*
	0	4	-0.43	-1.13	2.4	
	0	3	-0.26	-0.45	0.59	
	0	2	-0.09	-0.20	0.09	
EDTA	0*	2*	-0.20	-0.30	0.27	*
	0	3	0	0	0	
EGTA	0*	2*	-0.31	-0.45	0.70	*
	0	3	-0.48	-0.20	0.50	
DEPTA	0	3	-0.45	-1.5	3.34	
	0*	2*	-0.44	-1.5	3.24	*

IDA was the only poly-aminocarboxylate system that benefited from the addition of the corresponding acid; the S_e values varied between +0.35 and -0.43 mV K^{-1}, with the highest power achieved for when there was twice as much carboxylate salt present as the free acid. NTA reached peak performance with 5 equivalents of the carboxylate, whereas the larger EDTA ligand was optimised with 2 equivalents; EGTA had a higher S_e with 3 equivalents, but higher power (likely due to faster kinetics) with only 2. The largest ligand, DEPTA, displayed excellent performance with either 2 or 3 equivalents; it yielded consistently high negative S_e values, and the highest power.

Unmodified Weaver plot

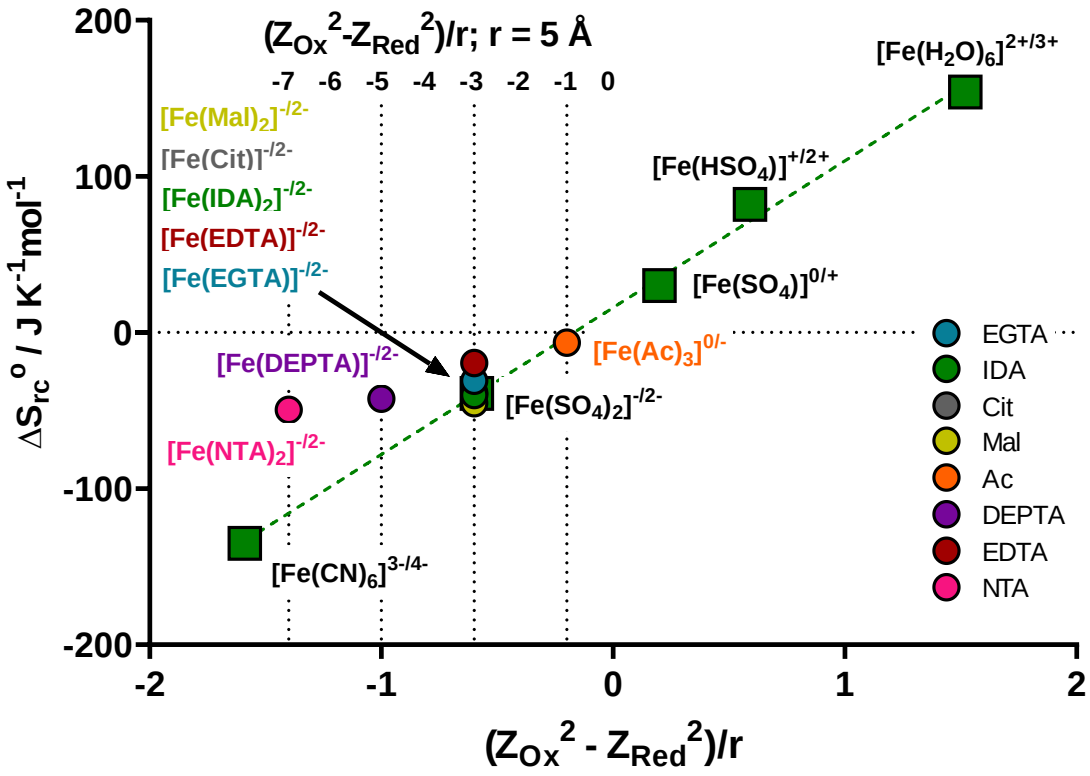

Figure A75 – Figure showing a plot of ΔS_{rc} vs. $(Z_{Ox}^2 - Z_{Red}^2)/r$ for all reported aqueous Fe(ii)/Fe(iii) redox systems (red circles) and all investigated Fe(ligand) solutions investigated here (coloured squares). The dotted lines indicate the $(Z_{Ox}^2 - Z_{Red}^2)$ values to 0/-1, -1/-2, -2/-3 and -3/-4 redox couples (using r = 5 Å). From these the likely ionic charge changes in the redox couples have been put next to the complex, *e.g.* $[Fe(NTA)_2]^{3-/4-}$. The values for Fe(EDTA), Fe(DEPTA) and Fe(NTA) were the pH unoptimised values taken from Table 1 in the main text.

Table of cost analysis parameters

Table A22 – Table of data for the cost analysis which is shown in Table 3 in the main text, showing the chemical, pack size and cost used. These were all taken from sigma Aldrich website accessed 17th of June 2021.

Chemical	Grade (purity)	Cost / £	Pack size / g (or mL is specified)
Iron(iii) chloride	Reagent Grade (97%)	46.50	1000
Iron(ii) chloride tetrahydrate	ReagentPlus (98%)	114.00	1000
Iron(iii) sulphate	ACS Reagent (>99.0%)	55.40	1000
Iron(ii) sulphate	(97%)	107.00	500
Acetic acid	Glacial, ACS (>99.7%)	49.80	2500 (mL)
Sodium acetate trihydrate	ReagentPlus (>99.0%)	47.70	1000
Malonic acid	ReagentPlus (99%)	82.50	500
Disodium malonate hydrate	BioXtra	47.20	25
Citric acid hydrate	ACS (>99.0%)	40.60	1000
Trisodium citrate trihydrate	ACS (>99.0%)	44.70	1000
IDA(H_2)	(98%)	36.70	500
IDA(Na_2)	(>95.0%)	38.70	50
NTA(H_3)	ACS (>99.0%)	41.50	500
NTA(Na_3)	Sigma grade (>98%)	45.40	1000
EDTA(H_4)	ACS Reagent (99.4-100.6%)	163.00	1000
EGTA(H_4)	(>97.0%)	838.00	500
DEPTA(H_5)	(>98%)	151.00	1000
DEPTA(Na_5)	40% in water	35.50	500 (mL)
Sodium hydroxide	ACS (97%)	86.50	1000
Sodium sulphate	ACS (>99%)	89.60	1000
Potassium carbonate	ACS (>99%)	52.40	1000

Appendix References

1 P. Yang, K. Liu, Q. Chen, X. Mo, Y. Zhou, S. Li, G. Feng and J. Zhou, *Angew. Chem. Int. Ed.*, 2016, **55**, 12050–12053.

2 J. H. Kim, J. H. Lee, R. R. Palem, M. S. Suh, H. H. Lee and T. J. Kang, *Sci. Rep.*, 2019, **9**, 8706.

3 M. Al Maimani, J. J. Black and L. Aldous, *Electrochem. commun.*, 2016, **72**, 181–185.

4 L. Zhang, T. Kim, N. Li, T. J. Kang, J. Chen, J. M. Pringle, M. Zhang, A. H. Kazim, S. Fang, C. Haines, D. Al-Masri, B. A. Cola, J. M. Razal, J. Di, S. Beirne, D. R. MacFarlane, A. Gonzalez-Martin, S. Mathew, Y. H. Kim, G. Wallace and R. H. Baughman, *Adv. Mater.*, 2017, **29**, 1605652.

5 K. Kim, S. Hwang and H. Lee, *Electrochim. Acta*, 2020, **335**, 135651.

6 M. A. Buckingham, F. Marken and L. Aldous, *Sustain. Energy Fuels*, 2018, **2**, 2717.

7 H. A. H. Alzahrani, M. A. Buckingham, F. Marken and L. Aldous, *Electrochem. commun.*, 2019, **102**, 41.

8 P. Yang and H. Fan, *Chem. Res. Chinese Univ.*, 2020, **36**, 420–424.

9 H. Angerstein-Kozlowska, B. E. Conway, A. Hamelin and L. Stoicoviciu, *J. Electroanal. Chem.*, 1987, **228**, 429–453.

10 M. A. Buckingham, S. Hammoud, H. Li, C. J. Beale, J. T. Sengel and L. Aldous, *Sustain. Energy Fuels*, 2020, **4**, 3388.

11 M. A. Buckingham, K. Laws, J. T. Sengel and L. Aldous, *Green Chem.*, 2020, **22**, 6062.